Theoretical Investigation of Core-collapse Supernovae with Boltzmann Neutrino Transport Simulations

ボルツマンニュートリノ輸送計算による重力崩壊型超新星爆発の理論的研究

February, 2024

Ryuichiro AKAHO
赤穂　龍一郎

Theoretical Investigation of Core-collapse Supernovae with Boltzmann Neutrino Transport Simulations

ボルツマンニュートリノ輸送計算による重力崩壊型超新星爆発の理論的研究

February, 2024

Waseda University Graduate School of Advanced Science and Engineering

Department of Pure and Applied Physics, Research on Theoretical Astrophysics

Ryuichiro AKAHO
赤穂　龍一郎

Abstract

Massive stars are known to end their lives with core-collapse supernovae (CCSNe) and form neutron stars (NSs) or black holes (BHs). It is governed by nonlinear equations, and numerical simulations are necessary to obtain the theoretical understanding. CCSN simulations have been performed extensively around the world, and the successful explosion have been reproduced. However, there are still conflicts with the observations, and many uncertainties are remaining. This is attributed to the various approximations or the simplifications employed in the simulations, and the accurate theoretical understanding can be only obtained by the first-principle simulations.

This thesis puts emphasis on neutrino, which plays a crucial role in CCSNe. Actually, more than 99% of the energy released by the gravitational collapse will be converted into neutrinos, and about 1% of the neutrino energy is transferred to the surrounding matter. Hence the neutrinos completely govern CCSN dynamics. In addition, neutrinos are important observational signal from CCSNe. It is emitted from much more inside than the electromagnetic signals, and it provides important information of the CCSN core. Its detection may provide astrophysics tests for physics, such as the nuclear matter equation of state. Significant progress have been made in neutrino detection techniques, and the construction of more advanced detectors are planned. Accurate numerical simulation should be performed in preparation for future observations.

Treating neutrinos is numerically difficult. At the center, the matter is optically thick and the neutrino distribution is in thermal equilibrium and isotropic. On the other hand, at larger radii, neutrinos flows freely. The most nontrivial part is the intermediate semi-transparent region, and whole momentum space distribution should be treated for the neutrino transport. However, most of previous studies have used approximate neutrino transport. Previous studies have reported deviation of the results due to the use of approximate neutrino transport, hence the rigorous method is crucial.

This thesis focuses on the Boltzmann neutrino transport, which directly solves the neutrino distribution function in phase space. There are actually few examples of previous studies on the multi-dimensional Boltzmann neutrino transport simulation. However, these studies are limited to Newtonian gravity, while the general relativistic effect is important in CCSNe due to its strong gravity. Previous study showed that general relativity can dramatically change CCSN dynamics even for NS forming case, and let alone in BH formation. For that reason, I first develope general relativistic (GR) Boltzmann neutrino radiation hydrodynamics code.

With the GR version of the code, three kinds of simulations are performed. First, I perform 2D CCSN simulation and investigated the early postbounce phase of CCSNe. By directly comparing the results with the simulation performed with the Newtonian gravity, GR effect on CCSN dynamics is discussed. It is confirmed that the central density and the temperature are clearly higher in GR, due to the stronger gravity. However, the neutrino luminosities and the shock wave evolution do not show large difference because the high temperature matter are confined at the center.

Second and third parts focus on the late time evolution of the protoneutron star (PNS), which is the remnant of CCSNe. The second part consider how the convection can affect the PNS evolution. The late time evolution of PNS is usually considered in 1D, and this study aims to discuss how multi-dimensionality affect the result. By setting the PNS evolved in 1D as a initial model, I perform 2D PNS convection simulation. It is found that the negative lepton gradient causes the convection, which

raises the temperature at the neutrino sphere. As a result, the neutrino luminosity and the mean energy are clearly higher than 1D. The third part consider how the fallback accretion onto PNS affects the neutrino emission. The fallback accretion is usually ignored in the PNS evolution, and this study quantify how it affects the neutrino emission and detectability. By setting a cold, deleptonized PNS at the center and parametrically changing the fallback accretion rates, I investigate the neutrino emission due to fallback. The neutrino mean energy due to fallback is found to be clearly higher than the late-time thermal emission from PNS. It is also found that the event rates can be high enough for the galactic events with the realistic amount of the accretion rates.

Fourth part of this thesis consider the quantum aspect of neutrinos in CCSNe, the neutrino oscillation. Especially, I focus on the collective neutrino oscillation, which is induced by the neutrino self-interaction. Its occurrence is nonlinear and also depend on the neutrino momentum space distribution, and its behavior is still not well understood. I perform post-process analysis of two modes of the collective neutrino oscillation, namely fast flavor instability (FFI) and the collisional flavor instability (CFI). I confirm that both FFI and CFI occur in CCSNe, and the condition for their occurrence are discussed in detail. By comparing the linear growth rates, it is found that FFI would be dominant over CFI.

Contents

Acknowledgements

I would like to thank my supervisor, Prof. Shoichi Yamada, for supporting my research activity. My research would not be feasible without my collaborators; Akira Harada, Hiroki Nagakura, Wakana Iwakami, Hideo Matsufuru, Hirotada Okawa, Kohsuke Sumiyoshi, Jiabao Liu, Masamichi Zaizen. I am also grateful for Yudai Suwa, Ken'ichiro Nakazato, Hideyuki Suzuki for providing useful comments. I also got positive stimulations by members in the Yamada laboratory.

I am supported by JSPS Grant-in-Aid for JSPS Fellows (Grant No. 22J10298) from the Ministry of Education, Culture, Sports, Science, and Technology (MEXT), Japan. For providing high performance computing resources, following institutions are acknowledged; K and Fugaku supercomputers provided by RIKEN, the FX10 provided by Tokyo University, the FX100 provided by Nagoya University, the Grand Chariot provided by Hokkaido University, and Oakforest-PACS provided by JCAHPC through the HPCI System Research Project (Project ID: hp130025, 140211, 150225, 150262, 160071, 160211, 170031, 170230, 170304, 180111, 180179, 180239, 190100, 190160, 200102, 200124, 210050, 210051, 210164, 220047, 220173, 220047, 220223 and 230033), Cray XC50 at Center for Computational Astrophysics, National Astronomical Observatory of Japan (NAOJ), Computing Research Center at KEK, JLDG on SINET of NII, Research Center for Nuclear Physics, Osaka University, Yukawa Institute of Theoretical Physics, Kyoto University, Nagoya University, and Information Technology Center of University of Tokyo.

Chapter 1

Introduction

1.1 Outline of This Thesis

This thesis is devoted to the theoretical study of core-collapse supernovae (CCSNe) and relevant phenomena using numerical simulations. Especially, I put special emphasis on neutrinos, and stick to the rigorous simulations using the Boltzmann neutrino transport. This chapter briefly reviews the basics of CCSNe and explain the remaining issues. Chapter 2 explains the neutrino transport, which is important throughout this thesis. Chapter 3 explains the numerical method of the Boltzmann-radiation hydrodynamics code. General relativistic version of the code is newly developed by myself, and they are employed in the simulations performed in chapters 4, 5 and 6. Chapter 4 show the result of CCSN simulation, and directly compare the results with existing result performed in Newtonian gravity. Chapters 5 and 6 show the results of the investigation about the late-time evolution of Protoneutron star (PNS), which is the remnant PNS after the successful CCSN explosion. The former focuses on the effect of the convection inside PNS, and the latter focuses on the effect of the fallback accretion onto PNS. Chapter 7 focuses on the collective neutrino flavor conversion inside CCSNe. This thesis is concluded in chapter 8. Appendices A and B explains the discretization methods of the Boltzmann and hydrodynamics solvers, respectively and show the explicit formulae used for the finite difference. The code verification tests of the GR codes are performed in appendices C and D.

1.2 Definitions and Notations

In this thesis, the natural unit is employed unless otherwise stated; the unit is chosen so that the the gravitational constant G and the speed of light c are set to 1. The signature of the metric is $-+++$ except for chapter 7, where the opposite sign is used. This is due to different convention; the former sign is typically used in astrophysics, and the latter is typically used in the particle physics. There is no inconsistencies nor confusions due to this difference. The Greek indices (e.g. μ) runs from 0 to 3 and Latin indices (e.g. i) run from 1 to 3.

The spacetime metric is denoted as $g_{\mu\nu}$, and the variables for the 3+1 decomposition are written as α, β^i, γ_{ij}, which correspond to the lapse function, shift vector, and the spatial metric, respectively. The timelike unit vector perpendicular to the constant-time hypersurface n^μ is given as

$$n^\mu = (1/\alpha, -\beta^i/\alpha). \tag{1.1}$$

The symbols g and $\Gamma^\alpha_{\mu\nu}$ represent the determinant of the metric and the Christoffel symbols, respectively.

The neutrino flavor is referred as follows; electron-type neutrino ν_e, anti-electron type $\bar{\nu}_e$, and heavy-leptonic type neutrinos ν_x. Note that three-species assumption is used in this study. This assumption

is valid as long as the muon and tauon fractions are small, and also the neutrino oscillation does not occur.

1.3 Stellar Evolution, Core-collapse Supernovae, and Formation of Compact Objects

Here, I briefly review the astrophysical phenomena associated with CCSNe. The story begins with the stellar formation. In the galaxies, dilute gas named interstellar medium exists, and they are gradually accumulated by the self gravity. They eventually experience a gravitational collapse, which forms a protostar. Similarly as an "ordinary star", protostar are also bright, but with the different mechanism, the released gravitational energy. The protostar gradually shrinks and the temperature gradually rises. At some point, the temperature gets high enough to trigger the nuclear fusion of hydrogen, and enters the main-sequence stage.

Main sequence stars are initially composed of light elements, mostly hydrogen or helium. The nuclear fusion inside the star generates heavier and heavier elements. The fate of the star strongly depends on its mass; heavier star uses up the fuel faster, which makes its life shorter. My focus is the massive star $10M_\odot \lesssim M \lesssim 100M_\odot$ that will experience CCSNe, and the typical lifetime is $\sim 10^7$ yrs. Lighter stars with mass $o(1)M_\odot$ will not end its life dramatically; they use up the fuel slowly and eventually form white dwarfs (WDs). More massive stars with mass $o(10^2)M_\odot$ are likely to undergo pair-instability supernovae, whose explosion mechanism is different from CCSNe.

Inside the progenitor stars of CCSNe, nuclear fusion continues up to ^{56}Fe, which has the lowest binding energy of $\sim 8.8\,$MeV. Since it is the most stable element, heavier elements beyond ^{56}Fe is not generated by the stellar nucleosynthesis. Thus the iron core is formed at the center and its mass grows with time. It is supported by the degenerate pressure of electron, and there is a possible maximum mass, called the Chandrasekhar limit (Chandrasekhar, 1931). If the iron core gets more massive than this limit, self-gravity causes the gravitational collapse.

The gravitational collapse is halted when the central density reaches the nuclear density because the repulsive force due to the strong interaction takes place. The inner core suddenly gets stiff, where the outer core is still free-falling. The discontinuity of the velocity between them creates a shock wave that propagates outward. If the shock wave reaches the outer envelope of the stellar surface, the explosion occurs, regarded as the successful CCSN.

The propagation of the shock wave up to the stellar surface is not an easy journey. There are several negative effects that stops the shock propagation; such as the ram pressure due to mass accretion, energy loss by the neutrino cooling and the photodissociation of nuclei. As explained later, neutrinos emitted from the central protoneutron star (PNS) heats up the matter behind the shock wave, which eventually helps the explosion. This is the delayed-explosion scenario by the neutrino heating mechanism.

CCSNe is accompanied by the formation of compact objects at the center, which is either neutron stars (NSs) or black hole (BH). In a typical CCSN with successful explosion, NS is likely to be formed. In the NS formation case, the hot NS named the protoneutron star (PNS) is formed at first, and gradually cools down by the neutrino emission and form the cold NS. In the failed case, on the other hand, the endless mass accretion makes the BH at the center. Simulation in Burrows et al. (2023a) showed that successful explosion can also accompany BH formation, but it is still a debate whether such phenomena is common. In the BH formation case, the accretion disk formed around the BH can be a site of the long gamma ray burst (LGRB).

1.4 Observational Signals of CCSNe

CCSNe can be observed in various ways, which is very important for validating the theoretical predictions and probing the high energy physics. Following sections review three kinds of observational signals, namely electromagnetic, neutrino, and the gravitational wave (GW).

1.4.1 Electromagnetic Signal

Electromagnetic signal is naturally the most ancient but still yet very important observable of CCSNe. The advantage of the electromagnetic observation is that it can detect much distant events than neutrinos than GWs. It is also advantageous that there are many optical telescopes in the world, in contrast to the neutrino or GW detectors. CCSNe (and other types) are extensively searched by the electromagnetic observations and found in a rate of $o(10)$ per month (Latest Supernovae, 2024).

There are many channels of possible electromagnetic signals from CCSNe, and this review do not cover all of them. There are two important observational implications to CCSN theory; the explosion energy, and the ^{56}Ni mass. First, the explosion energy is very important quantity to probe CCSN engine. There are several methods to estimate the explosion energy such as the fitting formula (Goldberg et al., 2019). Observation suggest that the typical explosion energy is $o(10^{51})$ erg (but also see Martinez et al. (2022), where the median is somewhat lower). Second, the synthesized mass of ^{56}Ni is also important. ^{56}Ni has a half time of ~ 6 days, and the electromagnetic emission from the decay can be observed, where the synthesized mass mass can be rather accurately estimated among various elements. In the field of CCSN simulations, reproducing these two observables is a very important objective. Remaining issues related to these observations is discussed in section 1.5.2.

1.4.2 Neutrino Signal

More than 99% of the released gravitational energy is converted into neutrinos and if the distance of CCSNe is close enough, they are observable. So far, there is only one example of the direct neutrino detection from a CCSN event, which is SN1987A. It occurred in ~ 50 kpc away, and resided in the Large Magellanic Cloud (LMC). Kamiokande-II detector detected 12 $\bar{\nu}_e$ (Hirata et al., 1987) and Irvine–Michigan–Brookhaven (IMB) detector detected 8 $\bar{\nu}_e$'s (Bionta et al., 1987). This observation supports the theoretical model that most ($\gtrsim 99\%$) of the released gravitational wave is emitted in the form of neutrinos.

After the successful observation from SN1987A, significant progress has been made in the last decades in neutrino detection techniques. Various types of neutrino detectors such as water Cherenkov (Ikeda et al., 2007; Hyper-Kamiokande Proto-Collaboration et al., 2018; Abbasi et al., 2011), liquid argon (Abi et al., 2021), liquid scintillators (Asakura et al., 2016; An et al., 2016), and dark-matter detectors (Lang et al., 2016) are currently operating or planned, offering the means to distinguish neutrino flavors (Horiuchi & Kneller, 2018).

Currently, largest water-Cherenkov detector Super-Kamiokande (Super-K) is operating, and its successor Hyper-Kamiokande (Hyper-K), which will have a volume more than 10 times larger, began construction. There are also detectors under construction such as Jiangmen Underground Neutrino Observatory (JUNO) (An et al., 2016) and Deep Underground Neutrino Experiment (DUNE) (Abed Abud et al., 2023). Different neutrino detectors have different preferred energy range; ice-Cherenkov detector IceCube (Aartsen et al., 2017) is useful for detecting higher energy neutrinos, and liquid-scintillator KamLAND (Abe et al., 2023) is useful for lower energy neutrinos.

There are several emission mechanism from CCSNe, which are individually explained below.

Pre-supernova Neutrinos

If the CCSN distance is close enough, pre-supernova neutrino would be detected prior to the explosion, called "pre-supernova neutrinos". It was first proposed in Odrzywolek et al. (2004), and many theoretical studies have been performed (Kato et al., 2015; Yoshida et al., 2016; Patton et al., 2017; Kato et al., 2017, 2020). The pioneering paper (Odrzywolek et al., 2004) only considered the electron-positron pair annihilation, but later studies pointed out that other reactions such as the plasmon decay or the nuclear weak processes may be also important. Since it will be detectable before any other kinds of observational signals, if available, it will be very useful for preparing the optical telescopes for the imminent event.

Burst Neutrino

As explained earlier, the shock wave generated at the interface between the inner and the outer cores propagate outward. At that time, shock wave position is completely optically thick and most of the neutrinos are trapped inside the core. However, when the shock wave propagates outward and the goes out of the neutrino sphere, large amount of neutrinos are emitted from the shock-heated material. This is the neutronization burst, and the luminosity of the electron-type neutrinos exceed $10^{53}\,\mathrm{erg\,s^{-1}}$. The luminosity is clearly higher than other phases.

PNS Cooling

After the explosion, hot PNS is formed at the center, which slowly gets cooled down by neutrino emission. The duration strongly depends on the EOS, but it is estimated to continue for $\sim 100\,\mathrm{s}$ (Nakazato & Suzuki, 2019). Although the luminosity is much lowered than the burst signal, thanks to its long duration, detection prospects is not low. Furthermore, this phase will be less chaotic than the signals from the early postbounce where the turbulence dominates, and will be useful for purely extracting the NS properties.

The PNS cooling phase can be further categorized into three phases (Roberts, 2012; Nakazato & Suzuki, 2019). The first phase in $t \lesssim 10\,\mathrm{s}$ is named the mantle contraction phase, where PNS rapidly shrinks and loses a lot of energy by neutrino emission. This is characterized as the rapid decline of the neutrino luminosity as shown in the simulations (Nakazato & Suzuki, 2019). The preceding phase $10 \lesssim t \lesssim 60\,\mathrm{s}$ is named as the shallow decay phase, where the PNS morphology does not change rapidly, and gradually cools down by the neutrino emission. This characterized as the rather moderate decline of the luminosity (Nakazato & Suzuki, 2019). The neutrino sphere gradually gets inward, and if the entire PNS gets semi-transparent to neutrinos, it enters the next stage. The later phase in $t \gtrsim 60\,\mathrm{s}$ is called the volume cooling phase, when and the entire volume of the PNS gets cooled down. This is characterized as the final rapid decline of the luminosity (Nakazato & Suzuki, 2019).

Primarily due to its long duration, it is difficult to track its entire lifetime in multi-dimension with sophisticated numerical schemes. As a result, there are a lot of uncertainties in the PNS evolution phase. Further details of the current understandings are explained in the first parts of chapters 5 and 6.

Diffuse Supernova Neutrino Background

I finally introduce the diffuse supernova neutrino background (DSNB), which is systematically different from previous three examples. In the history of the universe, uncountable number of CCSNe have occurred, and most of the emitted neutrinos still roam around in the universe, and called DSNB. The advantage of DSNB is that we do not wait for next nearby CCSN, unlike previous three examples. So far, there is no direct detection of DSNB, and the observational upper limit on the DSNB flux is provided by the non-detection. By combining the data for Kamiokande and Super-K the upper limit is $2.7\,\mathrm{cm^{-2}\,sec^{-1}}$ for $\bar{\nu}_e$'s with energy 17.3 MeV (Abe et al., 2021). Longer duration observation

with current SK-Gd (Gadolinium-loaded version of Super-K) and Hyper-K will provide upper limit or direct detection of DSNB. The theoretical modeling of DSNB is also ongoing (see Ashida et al. (2023) and references therein). The theoretical modelling depends on various uncertain parameters such as the stellar initial mass function (IMF), total amount of emitted neutrinos for a given progenitor, and EOS. Current observational constraint only excludes the most optimistic model, and future DSNB observation will be useful to probe the aforementioned uncertainties.

1.4.3 Gravitational Wave

Although actual observation is not yet realized, GWs can also be a observable of CCSNe (see Abdikamalov et al. (2022) for a review). There are currently operating detectors such as Laser Interferometer Gravitational-Wave Observatory (LIGO) (Abbott et al., 2009) , Virgo (Accadia et al., 2012) , Kamioka Gravitational Wave Detector (KAGRA) (Akutsu et al., 2021), and there are also future-planned detectors such as the space bourne GW detectors; Laser Interferometer Space Antenna (LISA) and the Deci-hertz Interferometer Gravitational wave Observatory (DECIGO) (Seto et al., 2001). There are two kinds of GW emission mechanism from CCSNe; from fluid motion and from neutrinos.

GW from Fluid Motion

In the similar way as other astrophysical phenomena such as the compact binary mergers, violent fluid motion can emit GWs. At early postbounce phase $t \lesssim 100\,\mathrm{ms}$, prompt convection will be a main emitter of GW. Later at $t \gtrsim 100\,\mathrm{ms}$, the GW emitter will be bifurcate into two; (1) fluid motion inside the PNS, and (2) the turbulent fluid motion behind the shock wave. (1) PNS oscillation or the convection inside it will naturally emit GW. The GW from PNS has a unique characteristics; the frequency increase with time, as demonstrated by numerical simulations Murphy et al. (2009); Müller et al. (2013); Kuroda et al. (2016). This is because the PNS contracts with time and the characteristic length is shortened. (2) The turbulent fluid motion behind the shock wave, namely the neutrino-driven convection and the standing accretion shock instability (SASI), can also emit GW. For this case, since the characteristic length is longer than PNS, the GW frequency tend to be lower. This appears as rather low GW signals compared to GWs from PNS, as s demonstrated (Murphy et al., 2009; Müller et al., 2013; Kuroda et al., 2016).

GW from Neutrinos

It is interesting that neutrino emission can be also a source for GW emission. The unique characteristic is the so-called memory effect (Christodoulou, 1991). There are several theoretical studies of GW memory due to CCSN and PNS cooling (Mukhopadhyay et al., 2021; Fu & Yamada, 2022). As the name suggests, the deformation of the metric due to GW memory does not go back to zero after the passage of the GW. Frequency of the GW memory is typically lower than GWs due to matter motion, and in principle, there is a mode with infinitesimally small frequency. Current GW detectors such as LIGO, Virgo, KAGRA are optimized for the detection of compact binary mergers (with GW frequency $\sim$ kHz), do not have good sensitivity in the low-frequency range. GW detectors with longer arm lengths are more suitable for the lower frequency GWs, such as the space-bourne detectors LISA and DECIGO.

1.5 Numerical Simulations of Core-collapse Supernovae

1.5.1 Brief History

Theoretical study of CCSNe has been mostly relied on numerical simulations due to its complicatedness. The first kind of CCSN simulation was performed in Colgate & White (1966), and the neutrino heating mechanism was recognized in Bethe & Wilson (1985). From the late 20th century to 2000s, spherically symmetric simulations have been extensively performed. The most sophisticated CCSN simulations using the Boltzmann radiation-hydrodynamics simulations in general relativity has been performed in 1D (Liebendörfer et al., 2001; Sumiyoshi et al., 2005), but explosion was not obtained. From late 2000s, multi-dimensional CCSN simulations become feasible thanks to the development of the computers. 2D and 3D CCSN simulations have been performed and the successful explosions are obtained by various simulations (Burrows & Vartanyan, 2021, and references therein). It was realized that the multi-dimensional effects, such as the convection and SASI are crucial for the successful shock revival. In 2020s, long-term 3D simulations has become feasible albeit there are still various approximations such as the neutrino transport.

1.5.2 Remaining Issues I. Reproducing Current Observations

Successful CCSN explosions are commonly reproduced by multi-dimensional simulations. The remaining task is to quantitatively reproduce the observational signals. Neutrinos and GWs would be very useful to probe CCSN core and the explosion mechanisms, but currently they are almost unavailable because the neutrino event number from the SN1987A is too few, and there is no GW observation from CCSNe. Currently available observational constraint comes from the explosion energy and the amount of produced ^{56}Ni. The simulations have been struggling with reproducing these values inferred from the observations; the theoretical estimate were a few orders of magnitude smaller than observed. Recently, some groups reported results that "reproduce" the observational values, and some people think that this issue is resolved. However, their results are still skeptical, as discussed in following paragraphs.

The group in the Max Planck Institute for Astrophysics recently reported a long-term CCSN simulation $\sim 7\,$s in Bollig et al. (2021). They reported that they reproduced the observational value of the explosion energy $\sim 10^{51}$ erg (see top panel of Fig.2 in Bollig et al. (2021)) and the ^{56}Ni mass (see Fig. 7 in Bollig et al. (2021)). However, they simplified the numerical method at $\sim 2\,$s, which seemingly caused artificial jump of these quantities, as shown in the figures. Therefore, the values are thought to be overestimated due to this artificial treatment. Furthermore, they employed a Ray-by-Ray+ approximation, which is known to sometimes artificially enhance the explosion.

The group in the Princeton university reported a series of CCSN simulations (Burrows & Vartanyan, 2021) and they claim that the explosion energy and the ejecta mass is well reproduced (see Fig. 6 in Burrows & Vartanyan (2021)). However, their numerical code FORNAX (Skinner et al., 2016) is known to be susceptive to explosion because the neutrino mean energy and the luminosity tends to be overestimated (as indicated by the comparison with other codes (see Fig. 4 in O'Connor et al. (2018))). It is worth mentioning that the deviation from other codes is not because they are correct and others are wrong; all of them are still approximate.

1.5.3 Remaining Issues II. Uncertainties of the Simulations

Although many CCSN simulations have been performed extensively, the simulation results still has lots of large uncertainties. It is not rare that the results by different research groups conflict each other. This confusion is attributed to the various approximations employed in the simulations. For example, current "state-of-the-art" CCSN simulations mostly employ approximate neutrino transport, and the results with the Boltzmann neutrino transport is only in Newtonian (Iwakami et al. (2020)

and references therein). Note that the result of the general relativistic simulation is presented in this thesis for the first time.

There are uncertainties due to our lack of knowledge about physics. One of the largest uncertainties on CCSN simulation is the nuclear matter equation of state (EOS). There are many approaches to constrain the EOS; laboratory experiments such as the neutron skin thickness (Abrahamyan et al., 2012; Horowitz et al., 2012; Adhikari et al., 2021), pulsar observation (Raaijmakers et al., 2021) and NS merger (Bauswein et al., 2017; Radice et al., 2018; Shibata et al., 2019). EOSs with extremal parameters have been excluded by the observations, but many different kinds EOSs are still possible. See Furusawa & Nagakura (2023) and Lattimer (2023) for the recent constraints and the comparison between different EOS models. In the first place, the experimental/observational constraints, which should be the reference, sometimes conflict each other. Naturally, EOS has large impact on the CCSN dynamics; for example, Harada et al. (2020) found out that the choice of the EOS determines the success or failure of the explosion. Another kind of physics that have large uncertainties is the collective neutrino oscillation. It is a unique phenomena that occurs in a dense neutrino media such as CCSNe, hence experiments are impossible to understand it. Further details of the collective neutrino oscillation is provided in chapter 7.

Chapter 2

Neutrino Transport

As mentioned earlier, neutrinos inside CCSNe has nontrivial momentum space distribution and its treatment is crucial for the neutrino transport. There are two branches of the most rigorous method[1]. One is the Boltzmann neutrino transport, which directly solves the Boltzmann equation with respect to the phase space distribution function. This thesis is devoted to this Boltzmann neutrino transport using the S_N method, which uses the finite difference. Note that there is an attempt to solve it with the spectral method (Peres et al., 2014). The basic idea is shown in section 2.1, and the details are shown in the following chapters. Second example of the rigorous transport method is the Monte Carlo (MC) neutrino transport. It tracks a finite number of particles as the representation of whole neutrino distribution. Comparison of S_N Boltzmann transport and MC transport has been performed in Richers et al. (2017).

Above two methods are computationally expensive, and approximate methods have been widely used in CCSN simulations and other astrophysical phenomena. Various approximations have been invented including the two-moment transport, (also called M1 method) (Thorne, 1981; Shibata et al., 2011; Cardall et al., 2013), the flux-limited diffusion (FLD) approximation (Arnett, 1977), the isotropic diffusion source approximation (IDSA) method (Liebendörfer et al., 2009). Comparison of the approximate neutrino transport have been performed in several studies (Janka, 1992) (MC and FLD), (Cabezón, Rubén M. et al., 2018) (IDSA and M1), (Just et al., 2018) (RbR+) and it has been shown that approximations can qualitatively change CCSN dynamics. In this thesis, the idea of two-moment neutrino transport is reviewed in section 2.2.

2.1 Boltzmann Neutrino Transport

Boltzmann Equation

Here, we will derive the Boltzmann equation using the differential form, following Lindquist (1966); Ehlers (1971); Sarbach & Zannias (2013, 2014a,b).

Tangent Bundle

First of all, the phase space can be considered as the momentum space embedded in the every position of the coordinate space. Hence it is useful to start from the tangent bundle, following Sarbach & Zannias (2013, 2014a,b). Suppose we have a n-dimensional manifold (M, g), and the tangential space associated with it: T_xM. The tangent bundle TM of the manifold M is defined as

$$TM \equiv \{(x, p) : x \in M,\, p \in T_xM\}\,. \tag{2.1}$$

[1] By the word "rigorous", I mean that it converges to the correct result as the mesh number is increased.

The detailed characteristics of TM is discussed in the references cited above.

Tangent vector on TM, i.e., $v \in T_{(x,p)}TM$ can be expanded as

$$v = X^\mu \frac{\partial}{\partial x^\mu}\bigg|_{x,p} + P^\mu \frac{\partial}{\partial p^\mu}\bigg|_{x,p}, \tag{2.2}$$

where

$$X^\mu \equiv dx^\mu_{(x,p)}(v), \quad P^\mu \equiv dp^\mu_{(x,p)}(v). \tag{2.3}$$

Decomposition of the Tangent Bundle

We want to decompose TM into two subspaces. By using the map $\pi : TM \to M$, we can define a projection map $\pi_{*(x,p)} : T_{(x,p)}(TM) \to T_xM$ through the push-forward of π defined as

$$\pi_{*(x,p)}(v)[h] \equiv v[h \circ \pi], \tag{2.4}$$

where h is a function $h : M \to \mathbb{R}$. The projection map π_* acts on a general vector on $T_{(x,p)}(TM)$ as

$$\pi_* \left(X^\mu \frac{\partial}{\partial x^\mu} + P^\mu \frac{\partial}{\partial p^\mu} \right) = X^\mu \frac{\partial}{\partial x^\mu}. \tag{2.5}$$

It only leaves the term with the basis $\frac{\partial}{\partial x^\mu}$. With π_*, we can define the vertical subspace as

$$V_{x,p} \equiv \ker \pi_*. \tag{2.6}$$

Frankly speaking, the vertical subspace corresponds to the "space without $\frac{\partial}{\partial x^\mu}$ component".

As a next step, complementary one, horizontal subspace is defined. Unlike the vertical subspace, it is inappropriate to define the horizontal subspace as the "vector space without $\frac{\partial}{\partial p^\mu}$ component". First, let us define a "connection" map $K_{(x,p)} : T_{(x,p)}TM \to T_xM$ as the push-forward of the projection map. We first consider a curve $\gamma(\lambda) = (x(\lambda), p(\lambda))$ in TM, parametrized by λ (see Fig. 1 in Sarbach & Zannias (2014b)). At $\lambda = 0$, it is specified as $\gamma(0) = (x, p)$ and $\dot{\gamma}(0) = v$, where the dot represent the derivative with respect to λ. The connection map is defined as

$$K_{(x,p)}(v) \equiv \nabla_{\dot{x}(0)} p = \left(\dot{p}^\mu(0) + \Gamma^\nu_{\alpha\beta} \dot{x}^\alpha(0) p^\beta \right) \frac{\partial}{\partial x^\mu}, \tag{2.7}$$

where ∇ is the Levi-Civita connection, and

$$\dot{x}^\mu(0) \equiv \frac{d}{d\lambda} x^\mu(\lambda)\bigg|_{\lambda=0}, \quad \dot{p}^\mu(0) \equiv \frac{d}{d\lambda} p^\mu(\lambda)\bigg|_{\lambda=0}, \tag{2.8}$$

and the expansion of v is

$$v = \dot{x}^\mu(0) \frac{\partial}{\partial x^\mu}\bigg|_{(x,p)} + \dot{p}^\mu(0) \frac{\partial}{\partial p^\mu}\bigg|_{(x,p)}. \tag{2.9}$$

By using the connection map K, the horizontal subspace is defined as

$$H_{x,p} \equiv \ker K_{(x,p)}. \tag{2.10}$$

In this horizontal subspace, following vector forms a basis

$$e_\mu \equiv \frac{\partial}{\partial x^\mu}\bigg|_{(x,p)} - \Gamma^\alpha_{\mu\beta} p^\beta \frac{\partial}{\partial p^\alpha}\bigg|_{x,p}. \tag{2.11}$$

The tangent bundle is decomposed into two subspaces defined above;

$$T_{(x,p)}TM = H_{(x,p)} \oplus V_{(x,p)}. \tag{2.12}$$

Naturally, any vector belong to $T_{(x,p)}TM$ can be decomposed into two components that belong to each subspace. Given that the basis vectors can be written as e_μ in the horizontal subspace and $\frac{\partial}{\partial p^\mu}|_{(x,p)}$ in the vertical subspace, the vector $v \in T_{(x,p)}TM$ can be written as

$$v = X^\mu e_\mu|_{(x,p)} + P^\mu \frac{\partial}{\partial p^\mu}\bigg|_{(x,p)}, \tag{2.13}$$

The dual basis belong to $T^*_{(x,p)}TM$ can be written as $\left\{dx^\mu_{(x,p)}, \theta^\mu_{(x,p)}\right\}$, where θ^μ is defined as

$$\theta^\mu_{(x,p)} \equiv dp^\mu_{(x,p)} + \Gamma^\mu_{\alpha\beta}(x) p^\beta dx^\alpha_{(x,p)}. \tag{2.14}$$

Hence the covectors X^μ, P^μ can be written as

$$X^\mu = dx^\mu_{(x,p)}(v), \quad P^\mu = \theta^\mu_{(x,p)}(v). \tag{2.15}$$

For later purposes, it is useful to define following maps

$$I^H_{(x,p)} \equiv \pi_{*(x,p)}|_{H_{x,p}} : H_{(x,p)} \to T_x M, \tag{2.16}$$

$$I^V_{(x,p)} \equiv K_{(x,p)}|_{V_{x,p}} : V_{(x,p)} \to T_x M, \tag{2.17}$$

which is the restriction of the push-forward (π_*) onto the horizontal subspace and the connection map (K) onto the vertical subspace. These maps have following characteristics;

$$I^H_{(x,p)}(X^\mu e_\mu|_{(x,p)}) = X^\mu \frac{\partial}{\partial x^\mu}\bigg|_x, \tag{2.18}$$

$$I^V_{(x,p)}\left(P^\mu \frac{\partial}{\partial p^\mu}\bigg|_{(x,p)}\right) = P^\mu \frac{\partial}{\partial p^\mu}\bigg|_x. \tag{2.19}$$

Let us define a natural metric. For given v_1 and v_2 in $T_{(x,p)}(TM)$,

$$\hat{g}_{(x,p)}(v_1, v_2) \equiv g(\pi_{(x,p)}(v_1), \pi_{(x,p)}(v_2)) + g(K_{(x,p)}(v_1), K_{(x,p)}(v_2)), \tag{2.20}$$

where g represents the Lorentzian metric on M. Above metric have following characteristics;

$$\hat{g}_{(x,p)}(e_\mu|_{(x,p)}, e_\nu|_{(x,p)}) = g\left(\frac{\partial}{\partial x^\mu}|_x, \frac{\partial}{\partial x^\nu}|_x\right) = g_{\mu\nu}, \tag{2.21}$$

$$\hat{g}_{(x,p)}\left(\frac{\partial}{\partial p^\mu}|_{(x,p)}, \frac{\partial}{\partial p^\nu}|_{(x,p)}\right) = g\left(\frac{\partial}{\partial x^\mu}|_x, \frac{\partial}{\partial x^\nu}|_x\right) = g_{\mu\nu}, \tag{2.22}$$

$$\hat{g}_{(x,p)}\left(e_\mu|_{(x,p)}, \frac{\partial}{\partial p^\nu}|_{(x,p)}\right) = 0. \tag{2.23}$$

In terms of the dual basis, the metric can be written as

$$\hat{g}_{(x,p)} = g_{\mu\nu} dx^\mu_{(x,p)} \otimes dx^\nu_{(x,p)} + g_{\mu\nu} \theta^\mu_{(x,p)} \otimes \theta^\nu_{(x,p)}. \tag{2.24}$$

Kinetic Theory

So far, we have defined the subspaces of the tangent bundle and defined useful maps. In the following, we define the quantity that can be interpreted as "invariant volume element", and consider how it can be used for introducing the neutrino distribution function. Let us first define a volume form η_{TM} as

$$\eta_{TM} \equiv -g\, dx^0 \wedge \cdots \wedge dx^n \wedge dp^0 \wedge \cdots \wedge dp^n. \tag{2.25}$$

The Liuville vector field is defined as

$$L_{(x,p)} \equiv \left(I^H_{(x,p)}\right)^{-1}(p). \tag{2.26}$$

As shown in Sarbach & Zannias (2014b), the Liuville vector field satisfies the geodesic equation

$$\nabla_L L = 0, \tag{2.27}$$

which makes it very useful to describe a particle motion. The Liuville vector can be explicitly written as

$$L_{(x,p)} = p^\mu e_\mu|_{(x,p)} = p^\mu \frac{\partial}{\partial x^\mu}\bigg|_{(x,p)} - \Gamma^\mu_{\alpha\beta} p^\alpha p^\beta \frac{\partial}{\partial p^\mu}\bigg|_{(x,p)}. \tag{2.28}$$

For our purpose, we can restrict the particle motion onto the mass shell defined as

$$\Gamma_m \equiv \left\{(x,p) \in TM :\, g(p,p) = -m^2\right\}, \tag{2.29}$$

and also

$$P_x \equiv \left\{p \in T_xM :\, g(p,p) = -m^2\right\}. \tag{2.30}$$

The induced metric on the mass shell can be defined as the pull-back of $\hat{g}$ with respect to the map $\iota :\, P_x \to TM$ as

$$\hat{h} \equiv \iota^* \hat{g}. \tag{2.31}$$

By calculating $\iota^*\theta$ and using equation 2.24, $\hat{h}$ can be written as

$$\hat{h} = g_{\mu\nu} dx^\mu dx^\nu + \left(g_{ij} - \frac{2}{p_0} g_{0(i} p_{j)} + \frac{1}{p_0^2} g_{00} p_i p_j\right) \theta^i \otimes \theta^j. \tag{2.32}$$

The volume form on the mass shell can be calculated as

$$\Omega \equiv \iota^*(i_N \eta_{TM}). \tag{2.33}$$

After rather lengthy calculation (e.g. determinant of the induced metric), it is given as

$$\Omega = (-1)^n \frac{g}{p_0} dx^0 \wedge dx^1 \wedge \cdots \wedge dx^n \wedge dp^1 \wedge dp^n. \tag{2.34}$$

The signature $(-1)^n$ comes from the interchange of dp^0 with dx^i's (see equation 2.25). Since the signature is not important for following discussion, it is simply dropped.

Let us now discuss the number of particles and the distribution function. First, define a hypersurface $\Sigma \subset \Gamma_m$ as

$$\Sigma \equiv \left\{(x,p) :\, x \in S, p \in P_x\right\}, \tag{2.35}$$

where S is the spacelike hypersurface in M. The number of particles intersecting the hypersurface Σ is denoted as $N[\Sigma]$ and its ensemble average is denoted as $\bar{N}[\Sigma]$. The volume element for the hypersurface is defined as

$$\omega \equiv L\Omega = \left(p^\mu \frac{\partial}{\partial x^\mu} - \Gamma^\mu_{\alpha\beta} p^\alpha p^\beta \frac{\partial}{\partial p^\mu}\right) \frac{g}{p_0} dx^0 \wedge dx^1 \wedge \cdots \wedge dx^n \wedge dp^1 \wedge \cdots \wedge dp^n. \tag{2.36}$$

It is useful because it is invariant with respect to the phase flow, i.e. $d\omega = 0$. It is argued in Ehlers (1971) that there exists a invariant distribution function f such that

$$\int_\Sigma f\omega = \bar{N}\left[\Sigma\right]. \tag{2.37}$$

Since $d\omega = 0$, following relationship holds

$$d(f\omega) = df \wedge \omega = df \wedge (L\Omega_s) = L(f)\Omega_s. \tag{2.38}$$

Let us consider a phase tube T and its spacelike slices Σ_1, Σ_2, and the domain D, between Σ_1 and Σ_2 (see Fig. 7 in Ehlers (1971)). The average number of collision can be related to the distribution function as

$$N\left[\partial D\right] = \int_{\partial D} f\omega = \int_D d(f\omega) = \int_D L(f)\Omega. \tag{2.39}$$

Hence the Boltzmann equation is derived;

$$L(f) = p^\mu \frac{\partial f}{\partial x^\mu} - \Gamma^\lambda_{\mu\nu} p^\mu p^\nu \frac{\partial f}{\partial p^\lambda} = \left[\frac{df}{dt}\right]_{\text{collision}}. \tag{2.40}$$

where the right hand side describe the change of distribution due to neutrino-matter interactions. The distribution function is the function of spacetime (four degrees of freedom) and the momentum space (three degrees of freedom), which makes the Boltzmann equation the seven-dimensional problem.

There are several previous studies of CCSNe based on the Boltzmann neutrino transport. In 1D, GR Boltzmann radiation hydrodynamics simulations have been performed in Liebendörfer et al. (2001); Sumiyoshi et al. (2005). In multi-dimension, only Newtonian simulations have been performed (Iwakami et al., 2020, and references therein).

2.2 Two-moment Neutrino Transport

In this section, the two-moment transport method is briefly reviewed, which is widely used in CCSN simulations. Instead of directly treating the neutrino distribution function in the phase space, angular moments are treated. As explained in the following, two-moment method only tracks the zeroth and first angular moments. It greatly drops most of the information in the momentum space, which helps to reduce the computational cost.

The moments equations was first formulated in Thorne (1981), and the truncated moment formalism and the equations in the conservative form are provided in Shibata et al. (2011). First, unprojected moments are defined as

$$M^{\alpha_1\alpha_2\cdots\alpha_k}_{(\nu)}(x^\beta) \equiv \int \frac{f(x^\beta, p'^\alpha)\delta(\nu - \nu')}{\nu'^{k-2}} p'^{\alpha_1} p'^{\alpha_2} \cdots p'^{\alpha_k} dV'_p, \tag{2.41}$$

where f is the distribution function, ν is the neutrino energy, and above integral is taken over momentum space with the measure dV'_p. Following Thorne (1981), the collection of superscripts $\alpha_1\alpha_2\cdots\alpha_k$ is represented as A_k hereafter. p^μ is the four-momentum, rewritten as

$$p^\alpha = \nu(u^\alpha + l^\alpha), \tag{2.42}$$

where u^α is the fluid velocity and l^α is the unit vector orthogonal to u^α. The moments can be also written as

$$M^{A_k}_{(\nu)} = \nu^3 \int f(\nu, \Omega_p, x^\mu)(u^{\alpha_1} + l^{\alpha_1}) \cdots (u^{\alpha_k} + l^{\alpha_k}) d\Omega_p, \tag{2.43}$$

where the integral is taken over the momentum space solid angle $d\Omega_p$. Following projection operator is defined for later convenience

$$h_{\alpha\beta} \equiv g_{\alpha\beta} + u_\alpha u_\beta. \tag{2.44}$$

Let us derive the moment equations. From equation 2.41,

$$\begin{aligned} & \frac{\partial}{\partial x^\beta} M^{A_k \beta}_{(\nu)} \\ = & \int \frac{p'^{\alpha_1} p'^{\alpha_2} \cdots p'^{\alpha_k} p^\beta}{\nu'^{k-2}} \delta(\nu - \nu') \frac{\partial f}{\partial x^\beta} dV'_p \\ + & \int \frac{p'^{\alpha_1} p'^{\alpha_2} \cdots p'^{\alpha_k} p^\beta}{\nu'^{k-2}} f(x^\beta, p'^\alpha) \frac{\partial}{\partial x^\beta} \delta(\nu - \nu') dV'_p. \end{aligned} \tag{2.45}$$

The first term describes the angle-moment of the collision terms, and hereafter rewritten as $S^{A_k}_{(\nu)}$. Above equation becomes

$$\begin{aligned} & \frac{\partial}{\partial x^\beta} M^{A_k \beta}_{(\nu)} \\ = & S^{A_k}_{(\nu)} + \int \frac{p'^{\alpha_1} p'^{\alpha_2} \cdots p'^{\alpha_k} p^\beta}{\nu'^{k-2}} f(x^\beta, p'^\alpha) \frac{\partial (p^\mu u_\mu)}{\partial x^\beta} \frac{\partial}{\partial (p^\mu u_\mu)} \delta(\nu + p^\mu u_\mu) dV'_p \\ = & S^{A_k}_{(\nu)} + \int \frac{p'^{\alpha_1} p'^{\alpha_2} \cdots p'^{\alpha_k} p^\beta}{\nu'^{k-2}} f(x^\beta, p'^\alpha) p^\gamma \partial_\beta u_\gamma \frac{\partial}{\partial \nu} \delta(\nu + p^\mu u_\mu) dV'_p \\ = & S^{A_k}_{(\nu)} + \frac{\partial}{\partial \nu} \left(\nu \int \frac{p'^{\alpha_1} p'^{\alpha_2} \cdots p'^{\alpha_k} p^\beta p^\gamma}{(-p^\mu u_\mu)^k} f(x^\beta, p'^\alpha) \delta(\nu + p^\mu u_\mu) dV'_p \right) \\ + & (k-1) \int \frac{p'^{\alpha_1} p'^{\alpha_2} \cdots p'^{\alpha_k} p^\beta p^\gamma}{\nu'^k} f(x^\beta, p'^\alpha) \partial_\beta u_\gamma \frac{\partial}{\partial \nu} \delta(\nu + p^\mu u_\mu) dV'_p, \end{aligned} \tag{2.46}$$

which results in an unprojected moment equation

$$\nabla_\beta M^{A_k \beta}_{(\nu)} - \frac{\partial}{\partial \nu} \left(\nu M^{A_k \beta \gamma}_{(\nu)} \nabla_\gamma u_\beta \right) - (k-1) M^{A_k \beta \gamma}_{(\nu)} \nabla_\gamma u_\beta = S^{A_k}_{(\nu)}. \tag{2.47}$$

Notice that the moment equation with respect to $M^{A_k \beta}$ is determined by $M^{A_k \beta \gamma}$, the moment one rank higher. This is an important properties of the moment formalism; all moments are related with the higher moments, which continues up to infinitely higher ranks. The truncated moment formalism truncate this endless relationship, and impose the closure relation for a certain rank moment.

Equation 2.47 is the unprojected, general form. For numerical simulations, however, projected quantities are more useful. Following quantities are defined:

$$E_{(\nu)} = M^{\alpha\beta}_{(\nu)} n_\alpha n_\beta, \quad F^i_{(\nu)} = -M^{\alpha\beta}_{(\nu)} n_\alpha \gamma^i_\beta, \quad P^{ij}_{(\nu)} = M^{\alpha\beta}_{(\nu)} \gamma^i_\alpha \gamma^j_\beta. \tag{2.48}$$

The equations with respect to above projected quantities can be obtained by projecting equation 2.47 in the same way.

$$\begin{aligned} \partial_t (\sqrt{\gamma} E_{(\nu)}) + & \partial_j \left[\sqrt{\gamma} (\alpha F^j_{(\nu)} - \beta^j E_{(\nu)}) \right] + \frac{\partial}{\partial \nu} \left(\nu \alpha \sqrt{\gamma} n_\alpha M^{\alpha\beta\gamma}_{(\nu)} \nabla_\gamma u_\beta \right) \\ = & \alpha \sqrt{\gamma} \left[P^{ij}_{(\nu)} K_{ij} - F^j_{(\nu)} \partial_j \ln \alpha - S^\alpha_{(\nu)} n_\alpha \right], \end{aligned} \tag{2.49}$$

$$\partial_t (\sqrt{\gamma} F_{(\nu)i}) + \partial_j \left[\sqrt{\gamma} (\alpha P^j_{(\nu)i} - \beta^j F_{(\nu)i}) \right] - \frac{\partial}{\partial \nu} \left(\nu \alpha \sqrt{\gamma} \gamma_{i\alpha} M^{\alpha\beta\gamma}_{(\nu)} \nabla_\gamma u_\beta \right) \tag{2.50}$$

$$= \sqrt{\gamma} \left[-E_{(\nu)} \partial_i \alpha + F_{(\nu)k} \partial_i \beta^k + \frac{\alpha}{2} P^{jk}_{(\nu)} \partial_i \gamma_{jk} + \alpha S^\alpha_{(\nu)} \gamma_{i\alpha} \right]. \tag{2.51}$$

Following energy-integrated version is often used instead to save the computational cost;

$$\partial_t(\sqrt{\gamma}E) + \partial_j\left[\sqrt{\gamma}(\alpha F^j - \beta^j E)\right] = \alpha\sqrt{\gamma}\left[P^{ij}K_{ij} - F^j\partial_j \ln\alpha - S^\alpha n_\alpha\right], \tag{2.52}$$

$$\partial_t(\sqrt{\gamma}F_i) + \partial_j\left[\sqrt{\gamma}(\alpha P^j_i - \beta^j F_i)\right] = \sqrt{\gamma}\left[-E\partial_i\alpha + F_k\partial_i\beta^k + \frac{\alpha}{2}P^{jk}\partial_i\gamma_{jk} + \alpha S^\alpha\gamma_{i\alpha}\right]. \tag{2.53}$$

Above equations can be solved in a similar way as the hydrodynamics equations. Further details, such as the evaluation of the characteristic speed, are written in Shibata et al. (2011).

The difference from the hydrodynamics equations is that the closure relation is required to truncate the moment equations. In the two-moment method, natural choice is to interpolate between two limits; isotropic distribution in the optically thick regime and the free-streaming distribution in the optically thin regime:

$$P^{ij}_{(\nu)} = \frac{3\chi - 1}{2}(P^{ij}_{(\nu)})_{\rm thin} + \frac{3(1-\chi)}{2}(P^{ij}_{(\nu)})_{\rm thick}. \tag{2.54}$$

Determination of χ is highly nontrivial and important, at the same time. One candidate is the Levermore closure (Levermore, 1984):

$$\chi = \frac{3 + 4\bar{F}^2}{5 + 2\sqrt{4 - 3\bar{F}^2}}, \tag{2.55}$$

where $\bar{F}$ is the flux factor. See Murchikova et al. (2017) for the comparison between different closures. In appendix C, the results with Boltzmann transport and the closure relation is compared.

Two-moment neutrino transport simulation is widely used in the research groups worldwide. Since the computational cost is orders of magnitude cheaper than the Boltzmann transport, systematic study using long term (second scale) 3D simulations have been performed (Burrows et al., 2023b).

2.3 Neutrino-matter Interactions

The interaction of neutrinos with surrounding matter is crucial for CCSN dynamics and the observational signals. There are various neutrino-matter interactions that should be taken into account for understanding CCSN theory.

2.3.1 Minimum Set

There is a so-called "standard set" (Bruenn, 1985), which is commonly referenced. Here, I only show what kinds of reactions are included, and the derivations of the reaction rates are provided in the original paper.

For the emission and absorption reactions, following reactions are included: electron capture on proton

$$e^- + p \longleftrightarrow \nu_e + n, \tag{2.56}$$

positron capture on neutron

$$e^+ + n \longleftrightarrow \bar{\nu}_e + p, \tag{2.57}$$

electron capture on nuclei

$$e^- + A \longleftrightarrow \nu_e + A'. \tag{2.58}$$

Following scattering process are considered. Scattering by nucleon

$$\nu + N \longleftrightarrow \nu + N, \tag{2.59}$$

scattering by nucleus

$$\nu + A \longleftrightarrow \nu + A, \tag{2.60}$$

scattering by electron

$$\nu + e \longleftrightarrow \nu + e. \tag{2.61}$$

Note that in the standard set, scattering processes are assumed to be elastic scattering i.e. the neutrino and the target particle does not lose nor gain any energy/momentum.

Neutrinos can also experience pair creation/annihilation by electron pair

$$e^- + e^+ \longleftrightarrow \nu + \bar{\nu}. \tag{2.62}$$

Although it was not included in Bruenn (1985), neutrino/antineutrino pair reaction by the Nucleon Bremsstrahlung is thought to be also important and commonly implemented in modern CCSN simulations;

$$N + N \longleftrightarrow N + N + \nu + \bar{\nu}.. \tag{2.63}$$

2.3.2 Extensions

The above set is roughly recognized as the "minimum set" for CCSN simulation. However, many approximations are used to derive the reactions, and there are many possible extensions which may affect the result dramatically. I briefly review two examples; neutrino scattering by nucleon, and muon interactions.

Neutrino Scattering by Nucleon

Among various kinds of neutrino-matter interactions, neutrino-nucleon scattering has a large room for improvement. As explained earlier, the scattering process is usually treated as elastic scattering. However the "recoil" of the nucleon should be taken into account, and it can lead to additional channel of energy exchange between neutrinos and the matter. In addition, weak magnetism effect, which originates from the fact that nucleon is not a single particle but it comprises of three quarks, may also play a role. It makes the reaction rates different between ν_e and $\bar{\nu}_e$. Approximate formulae for inclusion of these effects have been proposed in Horowitz (2002) and have been applied to CCSN simulation in Burrows et al. (2006). However, their method still employ crude approximations, and further improvements are needed.

Muon Interactions

The existence of muons is usually ignored in CCSN simulations. This assumption stems on the fact that the mass of the muon is 105.66 MeV, which is much higher than the typical matter temperature realized in CCSNe. However, this is not well justified because the temperature can reach ~ 30 MeV, which creates a non-negligible amount of electrons beyond ~ 100 MeV, which will be converted into muons. It is pointed out in Bollig et al. (2017) that the muons can make the EOS softer, and may facilitate CCSN explosion. Furthermore, the charged-lepton interactions related to muons can also affect μ-type neutrinos (Sugiura et al., 2022).

Chapter 3

Boltzmann Radiation Hydrodynamics Code

This thesis focus on the numerical simulation performed with the Boltzmann radiation-hydrodynamics code. This chapter gives the basic equations and the numerical method; section 3.1 for the Boltzmann neutrino transport, and section 3.3 for the hydrodynamics solver.

3.1 Boltzmann Equation

In this thesis, spherical polar coordinate system is used both for the configuration space and momentum space. Fig. 3.1 shows the schematic picture of the coordinate system employed. With this choice, directional cosines in momentum space $l_{(i)}$ are expressed as

$$l_{(1)} = \cos\theta_\nu, \quad l_{(2)} = \sin\theta_\nu\cos\phi_\nu, \quad l_{(3)} = \sin\theta_\nu\sin\phi_\nu. \tag{3.1}$$

As derived in section 2.1, the Boltzmann equation can be written as

$$p^\mu \frac{\partial f}{\partial x^\mu} - \Gamma^i_{\mu\nu} p^\mu p^\nu \frac{\partial f}{\partial p^i} = -p^\mu u_\mu S_{\rm rad}, \tag{3.2}$$

where the right-hand side represent the collision terms. In the numerical computations, however, it is more useful to rewrite the equation into the conservative form, which is provided in Shibata et al. (2014);

$$\begin{aligned} &\frac{1}{\sqrt{-g}} \frac{\partial}{\partial x^\mu}\bigg|_{q_i} \left[\left(e^\mu_{(0)} + \sum_{i=1}^{3} l_i e^\mu_{(i)} \right) \sqrt{-g} f \right] \\ &- \frac{1}{\epsilon^2} \frac{\partial}{\partial \epsilon} \left(\epsilon^3 f \omega_{(0)} \right) + \frac{1}{\sin\theta_\nu} \frac{\partial}{\partial \theta_\nu} \left(\sin\theta_\nu f \omega_{(\theta_\nu)} \right) - \frac{1}{\sin^2\theta_\nu} \frac{\partial}{\partial \phi_\nu} \left(f \omega_{(\phi_\nu)} \right) = S_{\rm rad}, \end{aligned} \tag{3.3}$$

where the neutrino energy is $\epsilon = -p_\mu e^\mu_{(0)}$, tetrad basis is specified by $e^\alpha_{(\mu)}$. In this study, neutrinos are assumed to be massless with their minuscule masses being neglected. The factors ω_0, $\omega_{(\theta_\nu)}$, and $\omega_{(\phi_\nu)}$

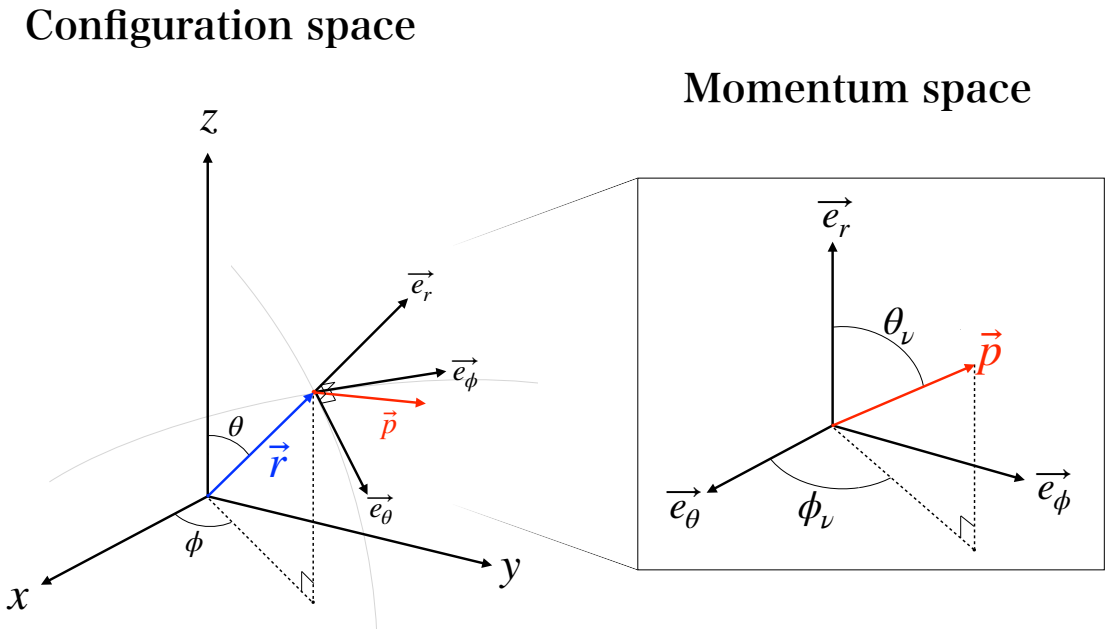

Figure 3.1: Schematic picture of the phase space coordinates employed in this thesis.

are defined as

$$\begin{aligned}
\omega_{(0)} &\equiv \epsilon^{-2} p^\mu p_\nu \nabla_\mu e^\mu_{(0)}, \\
\omega_{(\theta_\nu)} &\equiv \sum_{i=1}^{3} \omega_{(i)} \frac{\partial l_{(i)}}{\partial \theta_\nu}, \\
\omega_{(\phi_\nu)} &\equiv \sum_{i=2}^{3} \omega_{(i)} \frac{\partial l_{(i)}}{\partial \phi_\nu}, \\
\omega_i &\equiv \epsilon^{-2} p^\mu p_\nu \nabla_\mu e^\nu_{(i)}.
\end{aligned}$$

A natural choice of the tetrad basis may be given by the Gram-Schmidt normalization as

$$\begin{aligned}
e^\mu_{(0)} &= n^\mu, \\
e^\mu_{(1)} &= \gamma_{rr}^{-1/2} \left(\frac{\partial}{\partial r} \right)^\mu, \\
e^\mu_{(2)} &= -\frac{\gamma_{r\theta}}{\sqrt{\gamma_{rr}(\gamma_{rr}\gamma_{\theta\theta} - \gamma_{r\theta}^2)}} \left(\frac{\partial}{\partial r} \right)^\mu + \sqrt{\frac{\gamma_{rr}}{\gamma_{rr}\gamma_{\theta\theta} - \gamma_{r\theta}^2}} \left(\frac{\partial}{\partial \theta} \right)^\mu, \\
e^\mu_{(3)} &= \frac{\gamma^{r\phi}}{\sqrt{\gamma^{\phi\phi}}} \left(\frac{\partial}{\partial r} \right)^\mu + \frac{\gamma^{r\theta}}{\sqrt{\gamma^{\phi\phi}}} \left(\frac{\partial}{\partial \theta} \right)^\mu + \sqrt{\gamma^{\phi\phi}} \left(\frac{\partial}{\partial \phi} \right)^\mu .
\end{aligned} \tag{3.4}$$

Above expression can be applied to arbitrary spacetime metric. The choice of metric is described in each simulation.

In this thesis, S_N method is used to solve equation 3.3, which requires to discretize the equations for each coordinate variables. The discretization should be performed with care, otherwise it can lead to numerical instability. For example, the above equation is written in the conservative form, and the derivative of the prefactors (e.g. $\sqrt{-g}$ in the spatial advection terms) appears irrespective of the value of the distribution function. This is to be cancelled with the derivative of the prefactors of the other advection terms, such as the angular advection. Unfortunately, in finite difference, such cancellation may not be satisfied because the Leibniz rule is not exact in the finite difference. This may cause the unphysical appearance of neutrinos. I have chosen the discretization method that minimizes such effect, which is explained in appendix A. The code verification tests of the GR version are performed in appendix C.

Note that special case is also taken to take into account the effect of fluid velocity. Many CCSN simulations only take into account finite order of "v/c" (e.g. Hubeny & Burrows (2007)), assuming that the fluid velocity is not so large compared to the speed of light. On the other hand, our code treats the fluid velocity effect up to infinite order, in principle. The advection term is calculated in the laboratory frame, and the collision terms are calculated in the fluid-rest frame, and the conversion between two frames are performed with Lorentz transformation. The conversion itself is also taken with care so that the neutrino number is conserved. See Nagakura et al. (2014) for details.

3.2 Neutrino-matter interactions

In this thesis, the neutrino-matter interactions employ the the standard set (Bruenn, 1985) with a few modifications. As mentioned earlier, the standard set includes following seven neutrino-matter interactions; the electron capture on proton (ecp), positron capture on neutron (aecp), electron capture on nuclei (eca), scattering by nucleon (nsc), scattering by nucleus (csc), scattering by electron (esc) neutrino pair creation/annihilation by electron pair (pap). In addition to this, the neutrino pair creation/annihilation by nucleon-nucleon Bremsstrahlung (nbr) is incorporated based on Friman & Maxwell (1979). Furthermore, the treatment of electron capture on heavy-nuclei is updated based on Juodagalvis et al. (2010); Langanke & Martínez-Pinedo (2000); Langanke et al. (2003).

The collision integral, which is necessary to calculate the collision terms is estimated as follows. As for the emission/absorption reactions,

$$\left[\frac{\delta f}{\delta(ct)}\right]_{\rm emis-abs} = -R_{\rm abs}(\epsilon,\Omega)f(\epsilon,\Omega) + R_{\rm emis}(\epsilon,\Omega)(1-f(\epsilon,\Omega)), \tag{3.5}$$

where the emission and absorption rates are related each other as

$$R_{\rm emis}(\epsilon,\Omega) = R_{\rm abs}(\epsilon,\Omega)e^{-\beta(\epsilon-\mu)}, \tag{3.6}$$

to ensure the detailed balance, and β is the inverse temperature, μ is the neutrino chemical potential.

As for the scattering reactions, it is given as

$$\begin{aligned}\left[\frac{\delta f}{\delta(ct)}\right]_{\rm scat} = & -\int \frac{\epsilon'^2 d\epsilon'}{(2\pi)^3}\int d\Omega' R_{\rm scat}(\epsilon,\Omega;\epsilon',\Omega')f(\epsilon,\Omega)(1-f(\epsilon',\Omega')), \\ & +\int \frac{\epsilon'^2 d\epsilon'}{(2\pi)^3}\int d\Omega' R_{\rm scat}(\epsilon',\Omega';\epsilon,\Omega)f(\epsilon',\Omega')(1-f(\epsilon,\Omega)).\end{aligned} \tag{3.7}$$

As for the pair creation/annihilation processes, it is given as

$$\left[\frac{\delta f}{\delta(ct)}\right]_{\rm pair} = -\int \frac{\epsilon'^2 d\epsilon'}{(2\pi)^3}\int d\Omega' R_{\rm pair-anni}(\epsilon,\Omega;\epsilon',\Omega')f(\epsilon,\Omega)\bar{f}(\epsilon',\Omega'), + \int \frac{\epsilon'^2 d\epsilon'}{(2\pi)^3}\int d\Omega' R_{\rm pair-emis}(\epsilon,\Omega;\epsilon',\Omega')(1-f(\epsilon,\Omega))(1-\bar{f}(\epsilon',\Omega')). \quad (3.8)$$

where $\bar{f}$ denotes the anti-neutrino distribution function. The reaction rates are related as

$$R_{\rm pair-anni}(\epsilon,\Omega;\epsilon',\Omega') = R_{\rm pair-emis}(\epsilon,\Omega;\epsilon',\Omega')e^{\beta(\epsilon+\epsilon')}. \quad (3.9)$$

3.3 Hydrodynamics

In this thesis, the hydrodynamics equations formulated in Shibata (2015) are used. Necessary equations for the hydrodynamics is following three kinds of equations. First equation is the baryon number conservation

$$(\rho_0 u^\nu)_{;u} = 0. \quad (3.10)$$

Second equation is the conservation of the energy-momentum tensor

$$T^{\mu\nu}_{;\nu} = -G^\mu, \quad (3.11)$$

where G^μ denote the feedback from neutrinos. Third equation is the conservation of lepton-number

$$N^\nu_{;\nu} = -\Gamma, \quad (3.12)$$

where Γ denote the lepton number change due to charged-current interactions. The symbols ρ, P, u^μ, h, represent the density, the pressure, the four velocity, and the specific enthalpy, respectively.

For later convenience, following auxillary variables are defined;

$$v^j \equiv \frac{u^j}{u^t}, \quad \rho_* \equiv \alpha\sqrt{\gamma}\rho_0 u^t = \sqrt{\gamma}\rho_0\omega, \quad S_j \equiv \rho_* h u_j c, \quad (3.13)$$

$$S_0 \equiv \sqrt{\gamma}(\rho h w^2 - P), \quad w \equiv \alpha u^t, \quad S_{ij} \equiv \rho h u_i u_j + P\gamma_{ij}. \quad (3.14)$$

The feedback of neutrinos, in equation 3.11 can be written as

$$G^\mu \equiv \sum_i \int p^\mu_i S_{{\rm rad}\,i} dV_p, \quad (3.15)$$

where the summation over i is taken for all flavors. The feedback in equation 3.12 is give as

$$\Gamma \equiv \int (S_{{\rm rad}\,\nu_e} - S_{{\rm rad}\,\bar{\nu}_e}) dV_p. \quad (3.16)$$

In the same way as the Boltzmann equation, conservative forms are more useful for the numerical simulations. The above equations 3.11, 3.12 is rewritten as follows (Shibata, 2015);

$$\partial_t \rho_* + \partial_j(\rho_* v^j) = 0, \quad (3.17)$$

$$\partial_t(\rho_* Y_e) + \partial_j(\rho_* v^j Y_e) = -\Gamma, \quad (3.18)$$

The energy-momentum conservation equation are separated into two; spatial part and the timelike part. By projecting the equation 3.11 onto the spacelike hypersurface and the timelike normal vector respectively, following equations can be obtained

$$\partial_t S_i + \partial_j(S_i v^j + \alpha\sqrt{\gamma}Pc^2\delta_i{}^j) - S_0 c^2\partial_i\alpha + S_j c\partial_i\beta^j - \frac{1}{2}\alpha c^2\sqrt{\gamma}S_{jk}\partial_i\gamma^{jk} - \alpha\sqrt{\gamma}\gamma_i{}^\mu G_\mu, \quad (3.19)$$

$$\partial_t(S_0 - \rho_* c^2) + \partial_k((S_0 - \rho_* c^2)v^k + \sqrt{\gamma}P(v^k + c\beta^k))\alpha\sqrt{\gamma}S^{ij}K_{ij} - S_i D^i\alpha + \alpha\sqrt{\gamma}n^\mu G_\mu. \tag{3.20}$$

The numerical fluxes are evaluated with Harten Lax–van Leer (HLL) scheme (Harten et al., 1983).

In the similar way as the Boltzmann solver, a special care should be taken to discretize the equations. The discretization method is provided in appendix B. The code verification tests are performed in appendix D. In addition to above hydrodynamics equations, the equation of state (EOS) should be employed to determine the pressure. The choice of the EOS is described in each simulation.

Chapter 4

Simulation of Early Postbounce Phase of CCSN

In this chapter, we will present the simulation of early postbounce phase of CCSN performed with the GR Boltzmann radiation hydrodynamics code in 2D. The results are compared with the results performed in Newtonian gravity.

Let me first briefly review the treatment of gravity in the previous studies. In 1D simulations such as Liebendörfer et al. (2001); Sumiyoshi et al. (2005), GR simulations have been extensively performed. Performing GR simulation in 1D is not actually difficult because the metric equations reduce to the ordinary differential equations (ODEs). However, in multidimensional simulations, many recent studies employ the Newtonian gravity or effective GR potential (O'Connor & Couch, 2018; Iwakami et al., 2020; Bollig et al., 2021; Nakamura et al., 2022; Burrows et al., 2023a, and references therein), with several full GR simulations (Shibagaki et al., 2023, and references therein).

Effect of GR on CCSN dynamics is studied in several studies (Kuroda et al., 2012; O'Connor & Couch, 2018). It was pointed out that GR makes the central PNS to get more compact and hotter than Newtonian case, and this leads to higher neutrino luminosity and facilitate the explosion. Currently, simulations with GR effects all employ approximate neutrino transport and the simulation with the Boltzmann neutrino transport is limited to Newtonian. In this chapter, we investigate GR effect on CCSN dynamics using the newly developed GR Boltzmann radiation hydrodynamics code.

4.1 Setup

4.1.1 Numerical Setup

The simulation is performed with the code described in chapter 3. The spacetime metric is specified in section 4.1.2. The mesh configuration is same as the existing Newtonian simulation, whose result is compared. The radial mesh covers the range $r \in [0, 5000]$ km with 384 grid points, where the mesh width is varied so that the resolution around the steep density gradient (e.g. PNS surface) is appropriately captured. The zenith angle θ mesh covers the range $\theta \in [0, \pi]$ with 128 grid points. In the momentum space, the zenith angle θ_ν covers the range $\theta_\nu \in [0, \pi]$ with 10 grid points, and the azimuth angle ϕ_ν covers the range $\phi_\nu \in [0, 2\pi]$ with 6 grid points. The boundary conditions are imposed as follows: the reflective condition at the center $r = 0$ and on the poles $\theta = 0$, π, and the free-streaming condition at the outer boundary located at $r = 50\,\mathrm{km}$, and the periodic condition for $\phi_\nu = 0$, 2π. Furusawa-Togashi EOS (Furusawa et al., 2017), which is based on the variational method, is used for the nuclear matter.

4.1.2 Spacetime Metric

In principle, self-consistent derivation of the spacetime metric is to solve numerical relativity equations. However, it is technically difficult to implement. In this simulation, the spacetime metric is assumed to be spherically symmetric, which is actually a valid assumption because the gravitational source can be approximated to spherical symmetry. When we assume spherical symmetry, it is useful to impose the so-called "radial gauge polar-slicing condition" to the metric. It assumes the metric only with diagonal components and the values for two components are assumed $g_{\theta\theta} = r^2$, $g_{\phi\phi} = r^2 \sin\theta$. By introducing two functions $\Phi(t,r)$ and $m(t,r)$, spacetime metric is assumed to be as follows

$$g_{\mu\nu} = \begin{pmatrix} -e^{2\Phi(t,r)} & 1 & 0 & 0 \\ 0 & \left(1 - \frac{2m(t,r)}{r}\right)^{-1} & 1 & 0 \\ 0 & 0 & r^2 & 0 \\ 0 & 0 & 0 & r^2 \sin^2\theta \end{pmatrix}. \tag{4.1}$$

The equations for calculating $\Phi(t,r)$ and $m(t,r)$ are provided below.

The equation with respect to $m(t,r)$ can be obtained from the Hamiltonian constraint equation. In the above choice of metric, the Ricci tensor becomes

$$R_{\mu\nu} = \begin{pmatrix} \frac{2(r\partial_r m(t,r) - m(t,r))}{r^2(r-2m(t,r))} & 0 & 0 \\ 0 & \partial_r m(t,r) + \frac{m(t,r)}{r} & 0 \\ 0 & 0 & \left(\partial_r m(t,r) + \frac{m(t,r)}{r}\right) \sin^2\theta \end{pmatrix}, \tag{4.2}$$

and the nonvanishing component of the extrinsic curvature is the rr-component;

$$K_{rr} = -\frac{r e^{-\Phi(t,r)} \partial_t m(t,r)}{(r - 2m(t,r))^2}. \tag{4.3}$$

Hence the Hamiltonian constraint equation becomes

$$\begin{aligned} 0 &= R + K^2 - K_{ij}K^{ij} - 16\pi\rho \\ &= \frac{4}{r^2}\frac{\partial m}{\partial r} - 16\pi(\rho h W^2 - P), \end{aligned} \tag{4.4}$$

where the ideal fluid is assumed and the energy-momentum tensor is given as $T^{\mu\nu} = \rho u^\mu u^\mu + P g^{\mu\nu}$. Above equation leads to an ODE with respect to $m(t,r)$

$$\frac{\partial m}{\partial r} = 4\pi r^2(\rho h W^2 - P). \tag{4.5}$$

The equation with respect to $\Phi(t,r)$ can be obtained from the relation that $\partial_t K_{\theta\theta} = 0$.

$$0 = \frac{\partial K_{\theta\theta}}{\partial t} \quad = \quad \alpha(R_{ij} - 2K_{ik}K^k K_j + K K_{ij}), \tag{4.6}$$

which leads to an ODE with respect to $\Phi(t,r)$

$$\frac{\partial \Phi}{\partial r} = \left(1 - \frac{2m(t,r)}{r}\right)^{-1} \left(\frac{m(t,r)}{r^2} + 4\pi r(\rho h v^2 + P)\right). \tag{4.7}$$

Naturally, if we impose the fluid velocity to be zero, and the neutrinos are absent, above equations coincide the metric equations of the TOV equations. If the background hydrodynamic variables are provided, spacetime metric can be obtained by solving equations 4.5 and 4.7 with the Runge-Kutta method. In this simulation, angle-averaged hydrodynamical variables are used to calculate the metric.

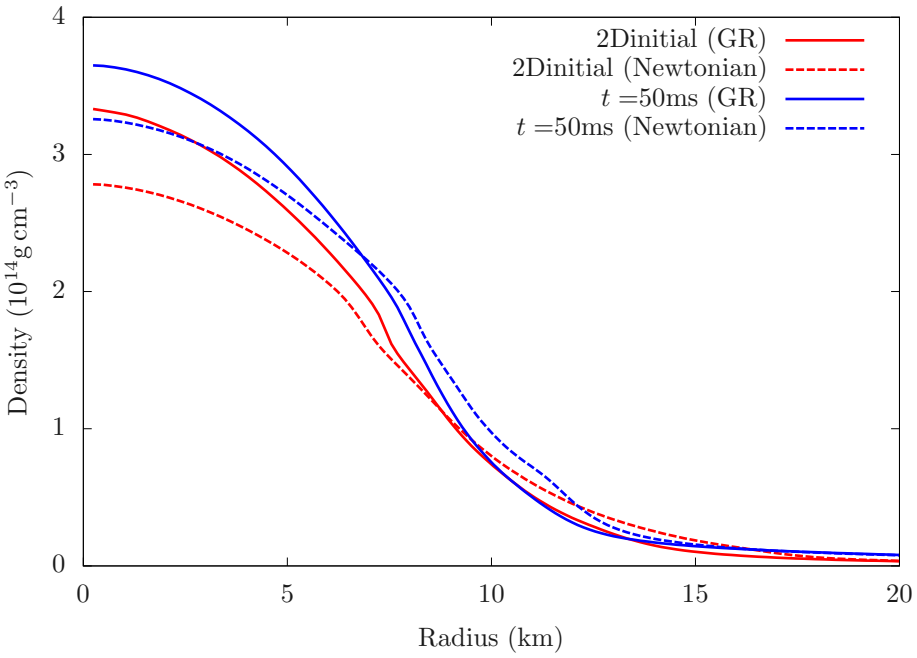

Figure 4.1: Radial profiles of the angle-averaged density for `2Dinitial` (red) and t = 50ms (blue). The solid and dashed lines correspond to GR and Newtonian, respectively.

4.1.3 Initial Model and Collapse Simulation

The procedure explained below is the same as the Newtonian counterpart. The initial progenitor mass is chosen as the $11.2M_\odot$ in Woosley et al. (2002). The collapse phase is followed in 1D, considering that multidimensional effect is small. About $\sim$ 1 ms after the bounce [1], negative entropy gradient appears right behind the shock wave. Since it is a signature that the state starts to become convectively unstable, 2D simulation is started from this point. Hereafter, this snapshot is called `2Dinitial`. In order to induce the convection, the radial velocity is randomly perturbed by 0.1% in the radial region of $30 < r < 50$km.

4.2 Results

Figs. 4.1 4.2 compares the density and the temperature between GR and Newtonian gravity. As can be clearly seen, the density and the temperature at the center is higher in GR than in Newtonian gravity. This result is consistent with previous studies that PNS gets more compact and the temperature gets higher in GR.

Let us see the CCSN dynamics. Fig. 4.3 shows the time evolution of the shock radius. The time evolution shows fluctuation, but the shock wave gradually propagate outward. GR and Newtonian results do not show large difference, but the evolution of the average value indicate that the the shock wave is slightly smaller in GR.

Figures 4.5 and 4.6 show the neutrino luminosity and the mean energies. In the same way as the shock wave evolution, the explosion morphology is stochastic and there are temporal variations between GR and Newtonian gravity. Apart from the temporal variations, there is no systematic

[1] Bounce is defined at the time when the maximum central density is reached

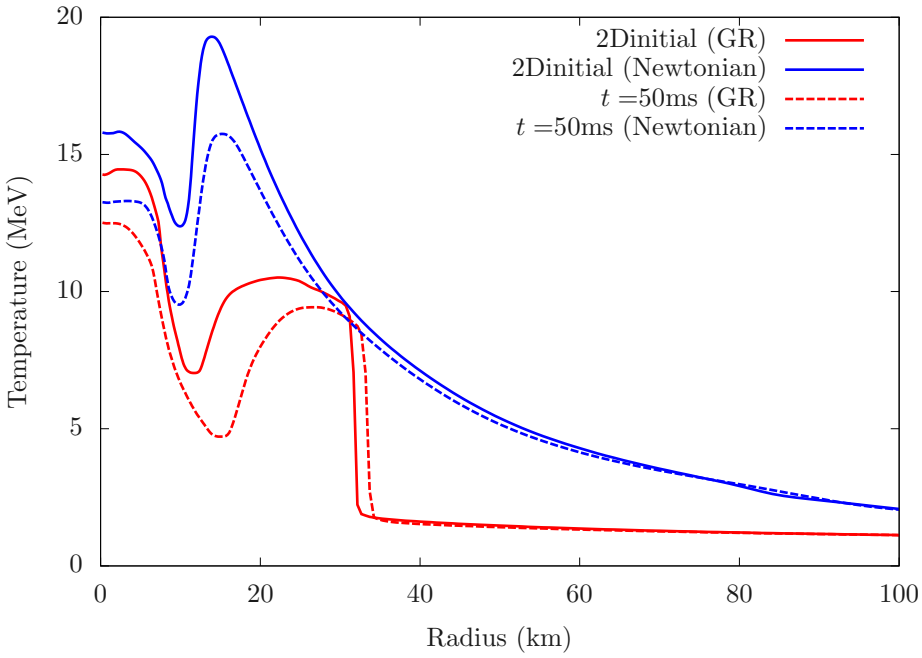

Figure 4.2: Radial profiles of the angle-averaged temperature for `2Dinitial` (red) and $t = 50$ms (blue). The solid and dashed lines correspond to GR and Newtonian, respectively.

difference between GR and Newtonian. This makes the neutrino heating rate almost the same, and the stronger gravity in GR makes the shock propagation slower.

At a first glance, this result is in disagreement with previous simulations, where the compact PNS would make the luminosity higher and aid the explosion. However, it is not necessarily an inconsistency as discussed below. The reason for the non-difference of the neutrino luminosity can be understood as follows. Let me first define the neutrino sphere. It is the position where the optical depth becomes $\tau = 2/3$, which can be roughly regarded as the position where the neutrinos are emitted. For the estimation of the optical depth, both emission/absorption reactions and scattering reactions are taken into account. Following Rybicki & Lightman (1986), effective optical thickness is calculated as

$$\tau \equiv \sqrt{\tau_a(\tau_a + \tau_s)}, \tag{4.8}$$

where τ_a and τ_s represent the optical depth only by taking into account the emission/absorption reactions, and the scattering reactions, respectively. Fig. 4.7 shows the time evolution of the temperature at the neutrino sphere for different neutrino energies. The difference between GR and Newtonian case is small, and the largest difference is seen for the low-energy neutrinos but at most $\sim$ 5%. This small difference can be understood by looking at the correspondence between the temperature and the density, as shown in Fig. 4.8. The central high-density region indeed show higher temperature for GR case, but the temperature near the neutrino sphere (density of $10^{10} \lesssim \epsilon \lesssim 10^{12}\,\mathrm{g\,cm^{-3}}$) show very little difference between GR and Newtonian.

This situation may be changed if the high temperature matter is dredged up by the PNS convection. Unfortunately, the duration of the current simulation is not enough so that strong PNS convection has not yet started. By continuing the simulation, GR effect may play positive role for the explosion.

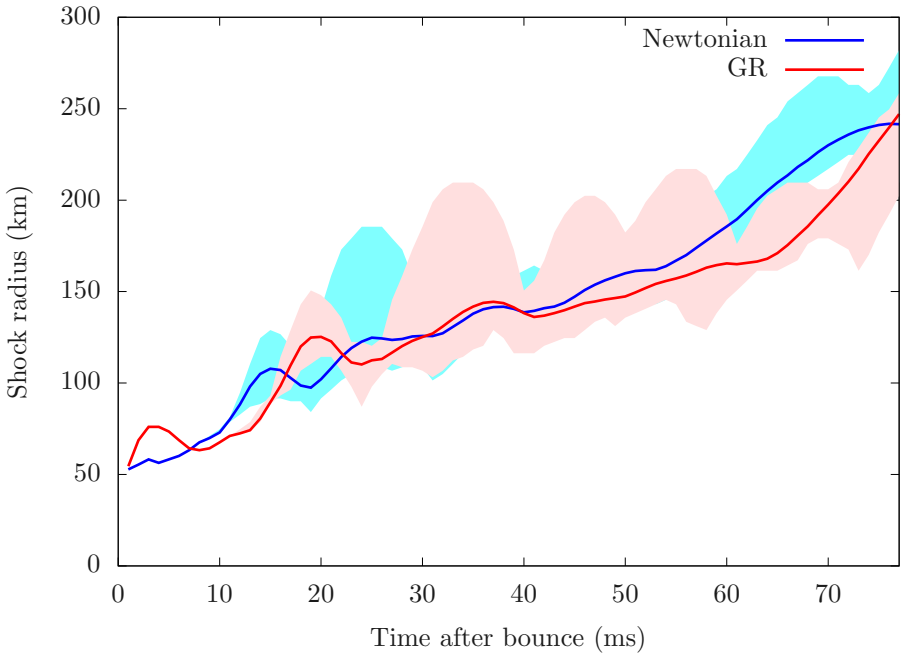

Figure 4.3: Time evolution of the shock radius for general relativity (red) and in Newtonian gravity (blue). The solid line shows the average shock radius and the reddish and bluish regions shows the range between the minimum and maximum shock radius.

4.3 Summary of Chapter 4

In this chapter, 2D CCSN simulation results with general relativistic Boltzmann radiation hydrodynamics code is presented. The density and the temperature is clearly higher in GR than Newtonian case, which is because the stronger gravity in GR makes the central PNS to get more compact. This feature is consistent with the previous studies. However, the neutrino luminosity and the mean neutrino energy does not show large difference between GR and Newtonian, because the temperature at the neutrino sphere has little difference. Stronger gravity in GR only has negative effect on the shock propagation, and the shock radius tend to be smaller than newtonian case.

If the PNS convection occurs after $\gtrsim 100\,\mathrm{ms}$, high temperature matter at the center will be likely to be dredged up and it is expected that neutrino luminosity would get higher. The simulated time $\sim 70\mathrm{ms}$ is way too short to judge the explodability, and we will continue the simulation further.

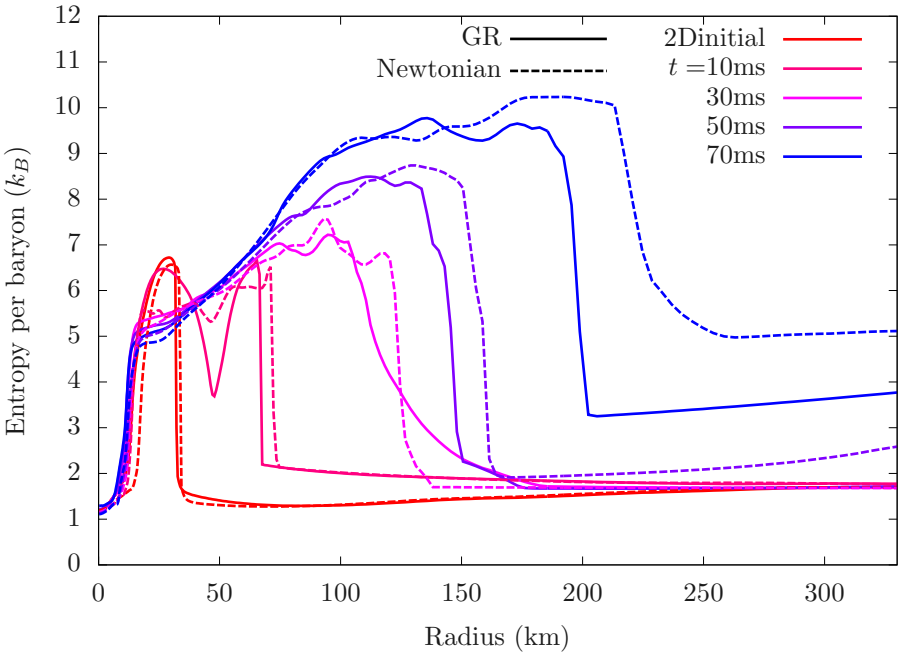

Figure 4.4: Radial profile of the entropy per baryon for different snapshots.

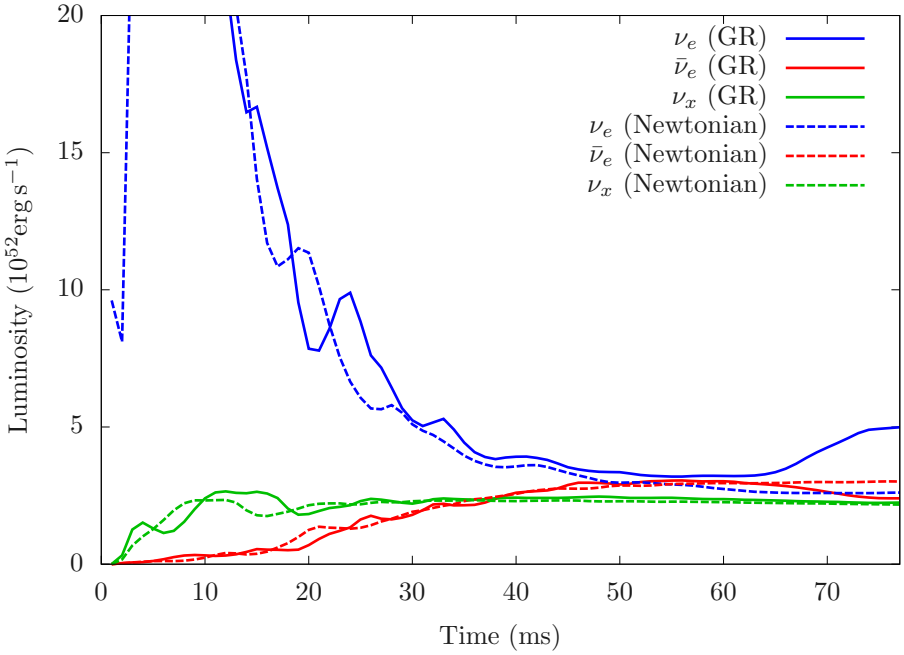

Figure 4.5: Time evolution of the energy luminosity for ν_e (blue), $\bar{\nu}_e$ (red) and ν_x (green). The solid and dashed lines show the GR result, and the Newtonian gravity, respectively.

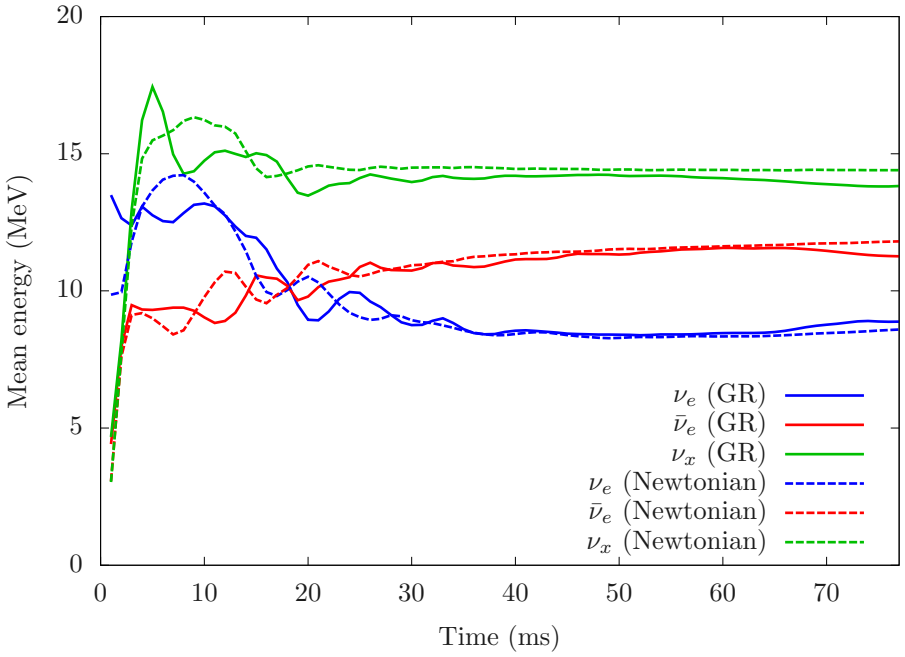

Figure 4.6: Time evolution of the mean neutrino energy for ν_e (blue), $\bar{\nu}_e$ (red) and ν_x (green). The solid and dashed lines show the GR result, and the Newtonian gravity, respectively.

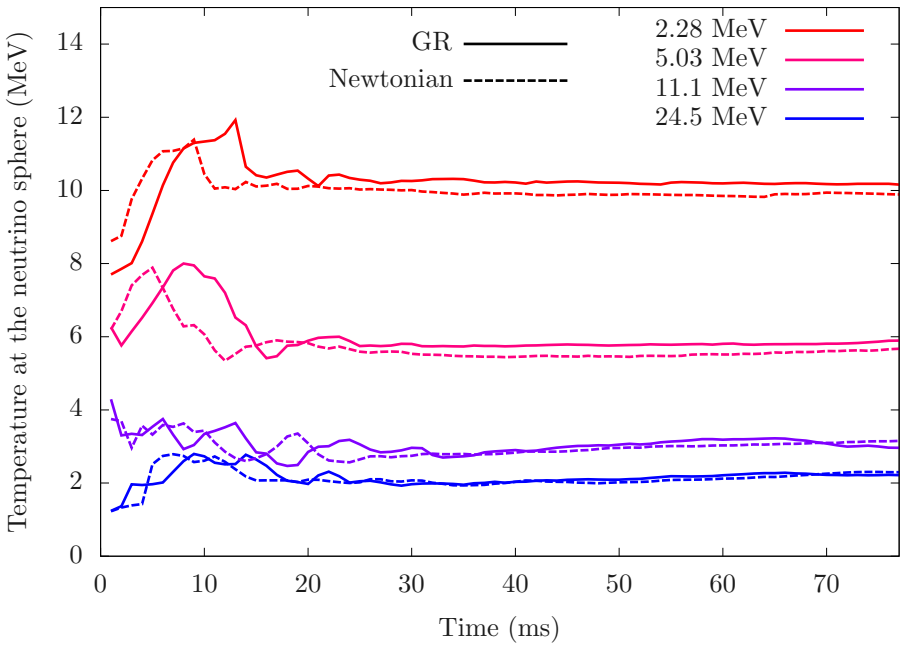

Figure 4.7: Time evolution of the temperature at the neutrino sphere for different neutrino energies.

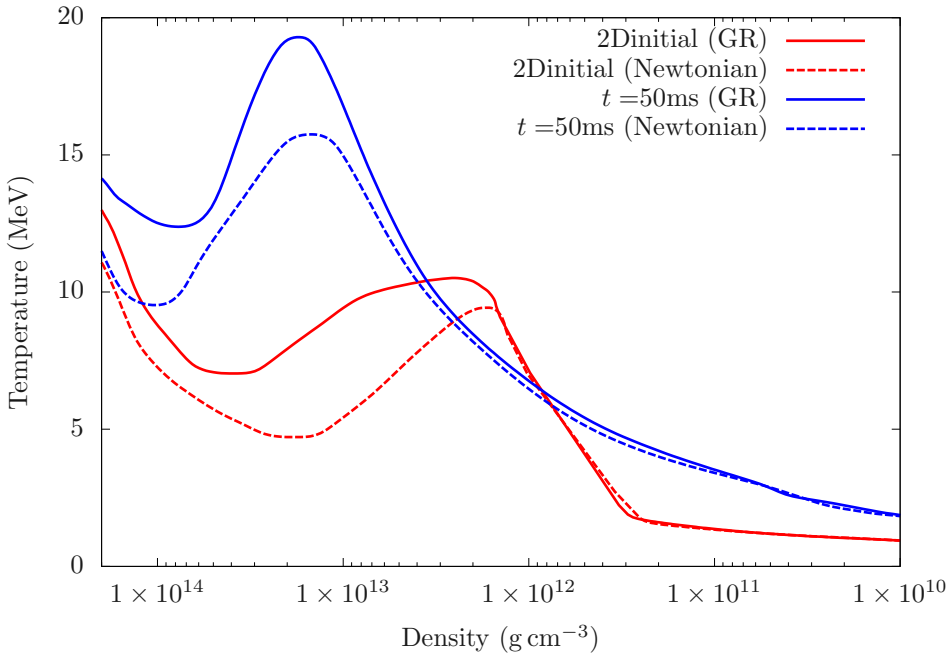

Figure 4.8: Same as figure 4.2, but the horizontal axis is the density.

Chapter 5

Late-time Evolution of Protoneutron Star I. Effect of Convection

For a long time, postbounce explosion phase of CCSNe has been extensively investigated to understand the explosion mechanism. Recently, the subsequent phase, i.e., the protoneutron star (PNS) cooling, is also getting attention. For galactic CCSNe, a large amount of neutrinos will be observed for ~ 100 seconds by the current and future detectors (Li et al., 2021). Unlike the explosion phase, PNS cooling is less chaotic, and may also be useful for tightly constraining the nuclear EOS (Pons et al., 2001a,b; Roberts et al., 2012; Nakazato & Suzuki, 2020; Nagakura & Vartanyan, 2022; Nakazato et al., 2022). The difficulty of simulating the PNS cooling phase is that it lasts for a long time ($\sim 10 \sim 100\,\mathrm{s}$). This makes it almost impossible to perform multi-dimensional simulation with sophisticated neutrino transport for the entire phase.

In fact, the long-term ($\gtrsim 10\,\mathrm{s}$) PNS cooling calculations have been performed only in 1D (Roberts & Reddy, 2017; Nakazato & Suzuki, 2019) However, the multi-dimensional effect may also play important role for the PNS evolution. The most prominent multi-dimensional feature is the convection, which is actually crucial in the explosion phase. In the previous 1D simulations, it was either simply ignored (Nakazato et al., 2013; Nakazato & Suzuki, 2019), or the mixing-length treatment was employed to model the matter mixing (Roberts et al., 2012). It has been pointed out that luminosity and the energy is enhanced by the convection (Keil et al., 1996; Roberts et al., 2012; Pascal et al., 2022). In addition, there are also other multidimensional features such as rotation, NS kick, and asymmetric accretion, whose effects may systematically change the result.

Behavior of the PNS convection has been investigated only in the early phase (∼several seconds) (Dessart et al., 2006; Nagakura et al., 2020, 2021). For example, Keil et al. (1996) studied the PNS convection up to $\sim$ 1s after core bounce in 2D under axisymmetry with the radial, gray (energy independent) neutrino transport taken into account. The initial condition is constructed by extracting a central portion ($1.1M_\odot$) of the supernova core at 25 ms post bounce in their 2D simulation for a $15M_\odot$ progenitor. They showed that a lepton-driven convection occurs inside PNS, and the convective zone is extended inward with time as the positive entropy gradient gets weaker. They also found that the neutrino luminosity and the mean energy are both enhanced by the convection. Mezzacappa et al. (1998), employing the 1D multi-group flux-limited diffusion (MGFLD) transport coupled with 2D hydrodynamics, reported that the PNS convection is suppressed by the neutrino transport in their simulations up to $\sim 100\,\mathrm{ms}$ after bounce. This may be an artifact of the angle-averaged 1D neutrino transport, though, in which the lateral transfer will be overestimated. In fact, the simulations with the 2D neutrino transport performed by Buras et al. (2006) and Dessart et al. (2006) observed a

convection, which enhances the neutrino luminosities. Note that these studies are all limited to the very early phase up to a few 100 ms after bounce, since their main focus is the explosion mechanism. To our knowledge, the paper by Nagakura et al. (2020) is the only one that is devoted to the study of the PNS convection in 3D. It is based on their 3D supernova simulations, which obtained shock revival. They demonstrated that the convection enhances the luminosity of ν_x, but not of ν_e and $\bar{\nu}_e$. There are even longer simulations in 2D (Burrows & Vartanyan, 2021) and 3D (Bollig et al., 2021) up to several seconds post bounce with the two-moment approximation employed for neutrino transfer. Unfortunately, the PNS convection was not discussed there. Hence there has been no detailed multi-dimensional numerical investigation on the PNS convection after ~ 1 s. That is what we want to do in this chapter.

Although there are aforementioned studies, all of them employed approximate neutrino transport. Since the PNS convection is induced by the deleptonization of the PNS, the treatment of the neutrinos around the semi-transparent regime is crucial. In this study, we perform GR Boltzmann radiation hydrodynamics simulation of PNS convection and discuss its effect on the PNS evolution.

5.1 Setup

5.1.1 Numerical Setup

As same as in the previous simulation in chapter 4, the general relativistic Boltzmann radiation-hydrodynamics code is used for the simulations. The radial mesh covers the range $r \in [0:50]$km with 384 grid points. The mesh configurations for θ and the momentum space variables are completely same as the simulation in chapter 4. In order to see the resolution dependence, simulations with different resolutions are also performed; we also run a simulation with a higher spatial resolution: $N_r = 512$, $N_\theta = 192$ (referred to as model `HR-S`) and another with a higher angular resolution in momentum space: $N_{\theta_\nu} = 14$, $N_{\phi_\nu} = 10$ (model `HR-M`).

5.1.2 Initial Model

As the initial model, PNS model is chosen to be the 2.3s after bounce calculated in Nakazato & Suzuki (2019). In their paper, the collapse of a $15\,M_\odot$ progenitor (Woosley & Weaver, 1995) was followed with the Lagrangian radiation hydrodynamics code by Sumiyoshi et al. (2005) up to 300 ms. Since this is in 1D, the shock revival does not occur. In order to mimic the successful explosion case, the central PNS is extracted to avoid further matter accretion. The resulting PNS is tracked for ~ 2 s by another code for the quasi-static PNS cooling developed by the same authors. This cooling computation was done under the assumption of spherical symmetry, and Togashi EOS (Togashi et al., 2017) was employed.

The initial model was constructed based on the FLD neutrino transport, which is different from this simulation. The numerical method is also different; the initial model was based on the Lagrangian hydrodynamics code where current simulation is based on Eulerian. In order to minimize the effect of this discontinuity, 1D relaxation simulation is first performed with the Boltzmann radiation hydrodynamics code. If the state reaches the quasi-steady state, it is mapped to 2D.

When the result is mapped to 2D, following perturbation is added to the four-velocity in order to invoke convection.

$$\begin{aligned} \delta u_r &= V\cos\left(m\pi\frac{r-r_{\rm min}}{r_{\rm max}-r_{\rm min}}\right)\cos(n\theta), \\ \delta u_\theta &= Vr\sin\left(m\pi\frac{r-r_{\rm min}}{r_{\rm max}-r_{\rm min}}\right)\sin(n\theta), \end{aligned} \tag{5.1}$$

where $V \equiv 1 \times 10^{-4} \times c$, $r_{\rm min} \equiv 3$km, $r_{\rm max} \equiv 13$km, $m \equiv 10$ and $n \equiv 10$. In this study, we employ the Furusawa-Togashi EOS (Furusawa et al., 2017). Although it is slightly inconsistent with the PNS model constructed with Togashi EOS, the only difference is the treatment of nuclei, and it is minor. The implemented neutrino-matter interactions are same as the previous simulation in chapter 4.

5.2 Results

5.2.1 Overview

First, result for the 1D relaxation calculation is shown below. Figure-5.1 compares the radial profiles of some hydrodynamical variables at 50 ms with those at the initial time. Note that the computational range in this calculation is extended from the original one because the original calculation in Nakazato & Suzuki (2019) did not cover low density region below $\sim 10^{11}\,{\rm g\,cm^{-3}}$. Therefore, the matter background is extended smoothly, in the region $17 \lesssim r < 50\,{\rm km}$. Since the density is low there, it does not dramatically change the result.

The density and the temperature distributions are almost the same as the original ones with the deviations being at most several %. As for the electron fraction, the dip gets a bit shallower from the initial data at $r \sim 15\,{\rm km}$. Further out a continuous rise of Y_e is observed toward the outer boundary. This is because the absorption of ν_e is dominant over that of $\bar{\nu}_e$ while the emissions of these neutrinos are much smaller in this optically thin region. As explained above, the initial Y_e distribution at $r \gtrsim 17\,{\rm km}$ is set by the extrapolation and the large discrepancy found there is just as expected. Since the density in this region is low and the region with negative lepton gradients inside are little affected by the initial transients, we think it is rather unlikely that the convection of our interest is severely modified by the presence of the extended layer. The overall agreement between the data before and after the relaxation with no anomalous behavior is an indirect indication that our code is working properly and can treat PNS correctly in general relativity. In the similar manner as chapter 4, the initial profile is called `2Dinitial` hereafter. From the snapshot at 50ms, which we refer to as `2Dinitial` hereafter, we start the 2D calculation. For comparison we continue the 1D calculation also. Fig. 5.1 compares the background profiles between the original 1D data and the profile after the relaxation calculations.

Fig. 5.2 shows the hydrodynamic profiles for some snapshots. The temperature distribution and the Y_e distributions are extended to larger radii in 2D. The dredge up of matter by the convection dredge up matter to the larger radii. The noteworthy difference is the entropy profile. Negative entropy gradient exists in the 1D model, where it disappears in 2D.

Figure 5.2 compares the angle-averaged radial profiles of the temperature, the electron fraction, and the entropy per baryon between `2Dinitial` and some snapshots from the 2D simulation at later times. For all quantities, the radial distributions get smoothed out with time due to the matter mixing driven by the convection. The most notable difference appears in the entropy per baryon: the peak and dip feature is gone and the gradient is positive at all radii in the 2D case.

In order to see the vigor of convection, we show the time evolution of the kinetic energy in figure 5.3. The perturbation given in equation 5.1 instigates violent convective motions in several milliseconds. The tangential kinetic energy accounts for the large portion of the total kinetic energy. The kinetic energy decreases until 30 ms and settles gradually down to a fluctuation around a constant value thereafter. The initial violent turbulence is an artifact produced by the transition from 1D to 2D. After $\sim 100\,{\rm ms}$, however, the transient is subsided and the convection has reached a (quasi) steady state, in which the angle-averaged matter profiles change much more slowly on the secular time scale. Regarding this state as representative of the PNS convection around this time of the cooling phase, we analyze it further in the following.

Fig. 5.3 shows the time evolution of the kinetic energy. The initial rise of the kinetic energy is the artifact due to suddenly switching from 1D to 2D. On the other hand, the persistent convection seen

in the later phase can ne thought to represent the PNS convection occurring in reality.

Fig. 5.4 shows the meridian map of the kinetic energy density for different snapshot times. We first look at where the PNS convection occurs. Figure 5.4 is the meridian maps of the kinetic energy for some time snapshots. The velocity field inside the PNS is superimposed. Note that the PNS is defined as the region where the density is higher than $10^{11}\,\mathrm{g\,cm^{-3}}$. The kinetic energy and velocity distributions are non-spherical from the center up to $r \sim 17\,\mathrm{km}$, with the lateral motions dominant over the radial ones (see also figure 5.3). This seems to be consistent with the convection that Nagakura et al. (2020) investigated. It indicates that convection commonly occurs in the wide range of PNS. As we saw in the figure 5.2, the entropy gradient is positive for all region and the Y_e gradient is negative up to $\sim 17\,\mathrm{km}$. As can be seen in figure 5.4, the kinetic energy and the velocity are large for inside ($\lesssim 17\,\mathrm{km}$), and small for outer convectively stable region. This is in contrast to other earlier works, though, in which either almost no convection was found (Lattimer & Mazurek, 1981; Mezzacappa & Bruenn, 1993) or it was observed in a rather limited region (Dessart et al., 2006; Nagakura & Johns, 2021a). This discrepancy may be attributed to the differences in the treatment of neutrino transfer as well as to the difference in the phase we focus to. As we saw in figure 5.2, the entropy gradient is positive in the entire region while the Y_e-gradient remains negative in the convective region at this rather late time of $t \sim$ 2s. Although our simulation is not fully self-consistent as the initial matter profile is taken from the 1D PNS cooling calculation (Nakazato & Suzuki, 2019), in which convection was ignored, the entropy and Y_e distributions are self-adjusted and sustained once the (quasi) steady state is established, and hence the results obtained in this study will have some generality.

In order to see the convectively unstable region more quantitatively, we evaluate the relativistic Brunt-Väisälä frequency

$$N^2 = \frac{\partial \alpha}{\partial r}\frac{\alpha}{\rho h \gamma_{rr}}\left(\frac{1}{c_s^2}\frac{\partial P}{\partial r} - \frac{\partial \rho(1+\epsilon)}{\partial r}\right), \tag{5.2}$$

where $N^2 < 0$ indicates the linear convective instability. We adopted this formula from Müller et al. (2013), in which the conformal flatness is assumed, by simply replacing the conformal factor with γ_{rr}. It is conventional (Gossan et al., 2020) to define the following quantity:

$$f_{\rm BV} = \mathrm{sign}(N^2)\sqrt{|N^2|}. \tag{5.3}$$

Figure 5.5 shows the meridian maps of $f_{\rm BV}$ for some time snapshots. The leftmost panel presents the result for the initial time. We can see clear boundaries between the (linearly) unstable region with bluish colors and the stable regions with reddish colors. It is found that the inner region $r < 9\,\mathrm{km}$ is linearly stable although it has negative Y_e-gradients (see figure 5.2). The convection occurs in this linearly unstable region initially indeed. As it grows with time and becomes nonlinear, the convective region is extended inward by overshooting and the inner stable region is extinct eventually. At the same time, the value of $f_{\rm BV}$ gets smaller inside the convective region as can be observed in other panels to the right. This happens because the convection mixes the matter up until its profiles become marginally stable, since the neutrino emissions still work in the opposite way to produce unstable Y_e-profiles. As a result, the convection is sustained even if the Brunt-Väisälä frequency is marginally positive.

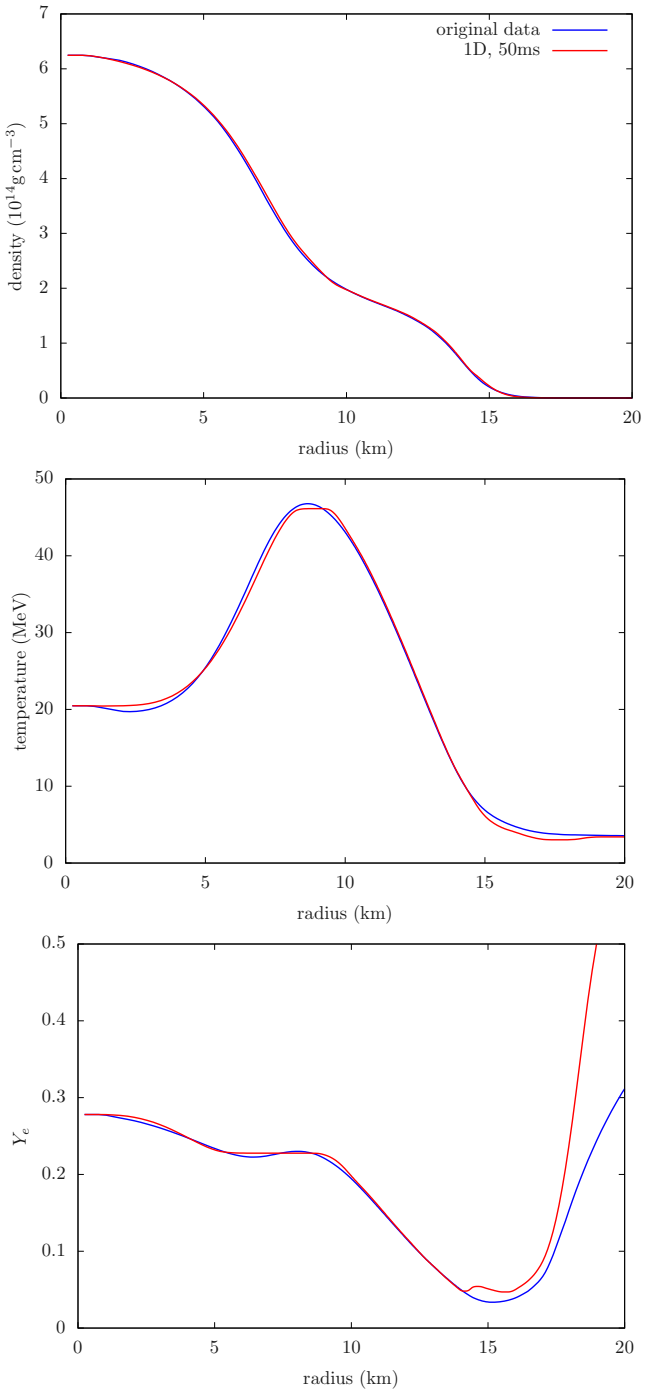

Figure 5.1: Radial profiles of the density (top), the temperature (middle), and the electron fraction (bottom) are shown with red lines. The original data (provided by another code) is shown with blue lines.

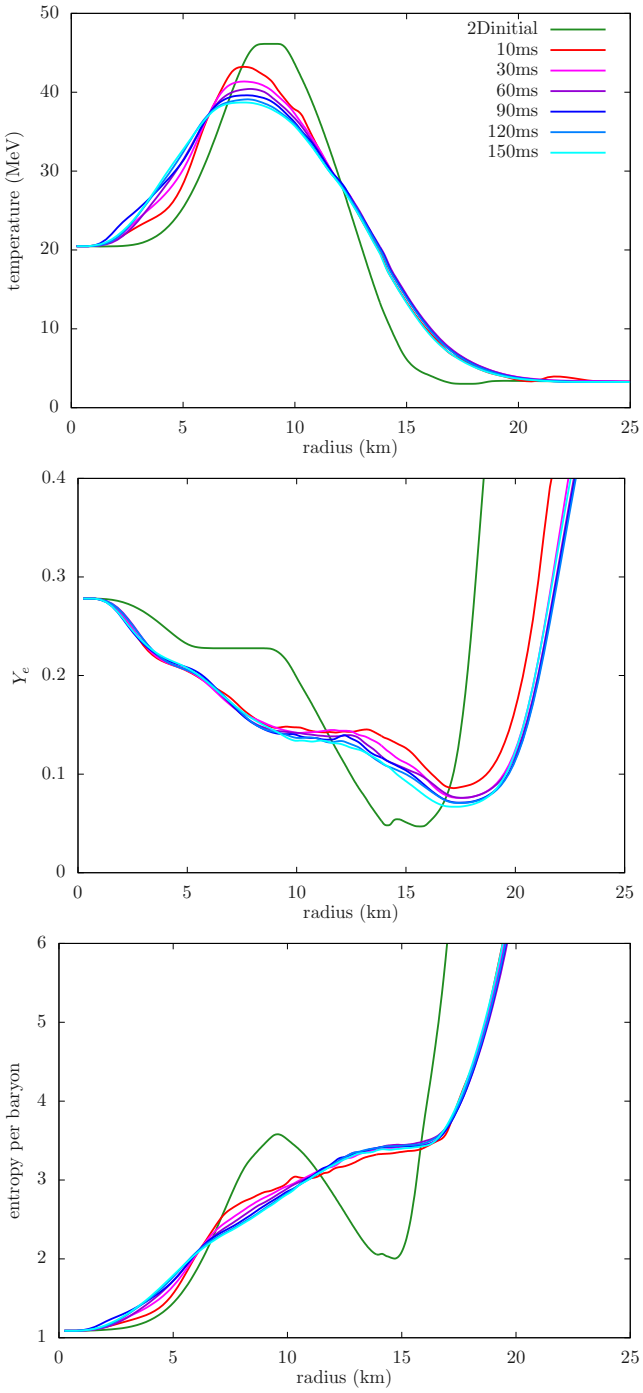

Figure 5.2: Radial profiles of temperature (top), the electron fraction (middle), and the entropy per baryon (bottom). Green line denote `2Dinitial`, and the rest denote 2D data for time snapshots 10, 30, 60, 90, 120, and 150ms, respectively. Note that θ-averaged quantities are shown for 2D data.

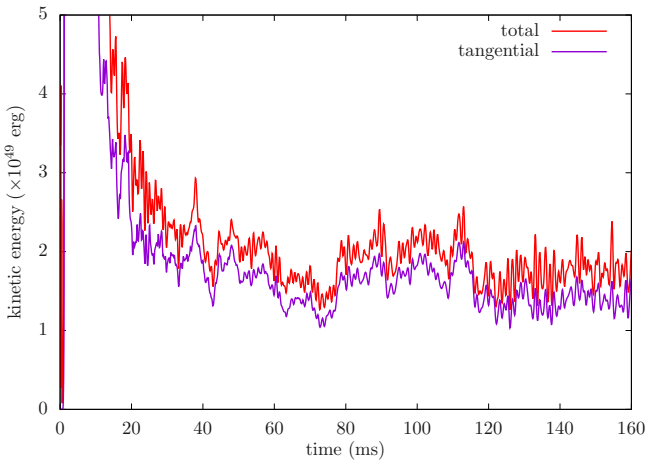

Figure 5.3: Time evolution of the kinetic energy. The red and purple lines denote total and tangential ones, respectively.

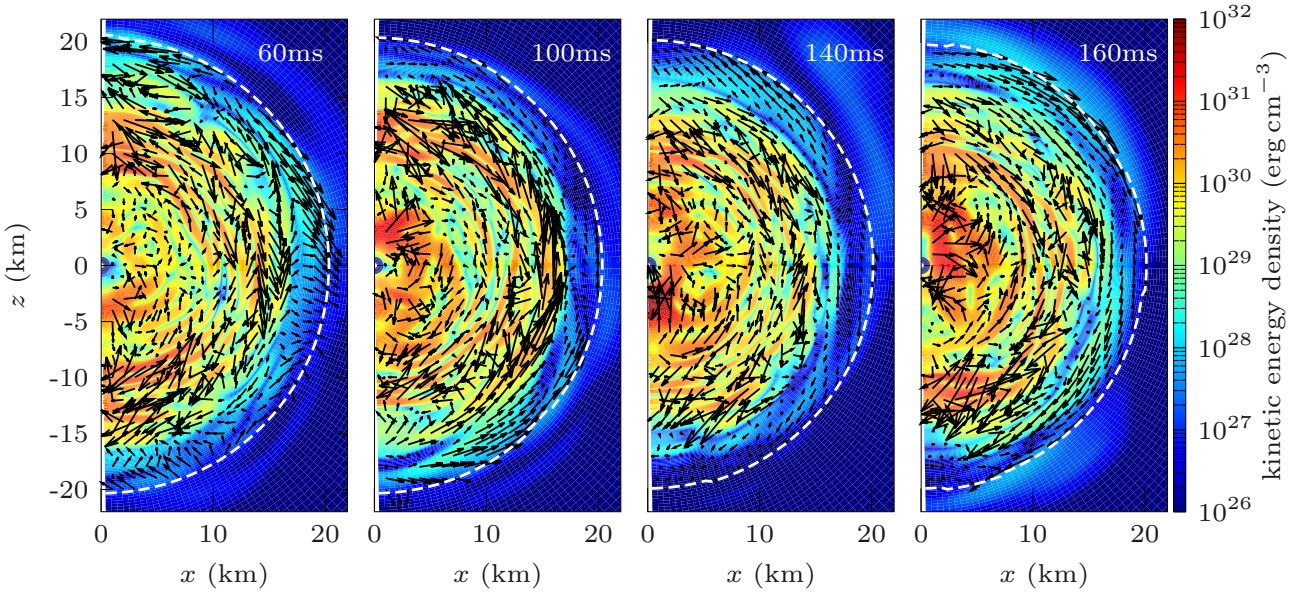

Figure 5.4: Kinetic energy density (total) on the meridian slice for some time snapshots; from left to right, 60ms, 100ms, 140ms and 160ms. Matter velocity field inside the PNS is also plotted as black arrows. The white broken line denote the PNS surface.

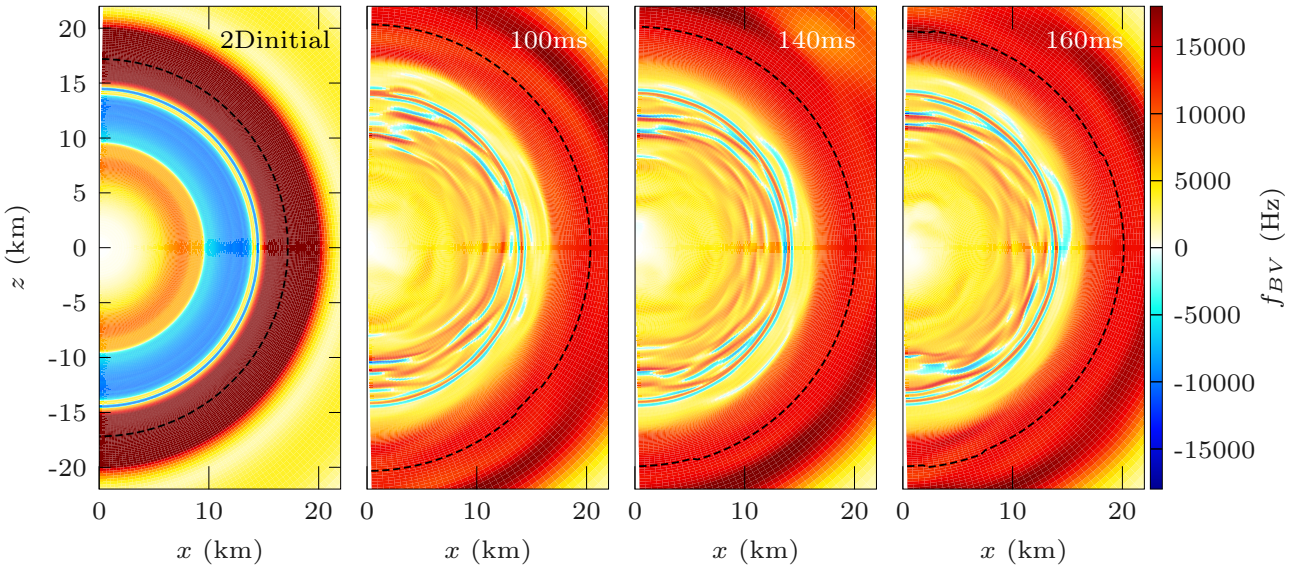

Figure 5.5: Brunt-Väisälä frequency on the meridian slice for `2Dinitial` and rest for 2D (100, 140, and 160ms). The black broken lines denote the PNS surface.

5.2.2 Neutrino Emission Characteristics

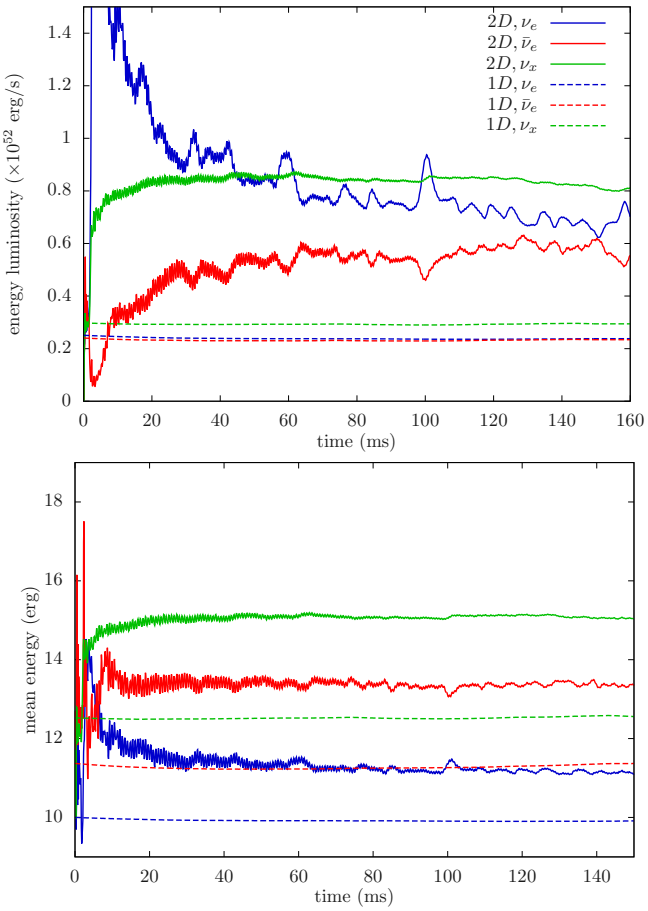

Figure 5.6: Time evolution of the energy luminosity (left) and mean neutrino energy (right). The solid lines correspond to 2D, and the broken line correspond to 1D. Blue, red, and green lines denote ν_e, $\bar{\nu}_e$, and ν_x, respectively.

Next, we discuss the properties of neutrino emissions from the PNS. Figure 5.6 shows the time evolution of the luminosity and mean energy of neutrinos. Similarly to the kinetic energy, we found a sudden increase of the ν_e luminosity right after the start of the simulation, which is followed by a gradual decline as the initial transient subsides, and is settled to a roughly constant value in ~ 70 ms. The rise of the $\bar{\nu}_e$ luminosity is turned to a decline very quickly, followed by a gradual increase to a constant value over several tens milliseconds. It is interesting that the time variations are anti-correlated with those of ν_e. The ν_x luminosity, on the other hand, increases monotonically and approaches an asymptotic value a bit more quickly than other neutrinos without producing a pronounced peak. These different behaviors reflect the difference in their decoupling with matter. This early time evolution is an artifact, though, caused by the switch from 1D to 2D. We hence focus on the asymptotic phase after the (quasi) steady convection is established. The luminosity and the mean energy in 2D are both higher than those in 1D (compare the solid lines with the dashed lines). Such an enhancement was also observed in the previous studies on the earlier phase (Keil et al., 1996; Buras et al., 2006; Dessart et al., 2006; Roberts et al., 2012; Pascal et al., 2022).

Fig. 5.6 shows the time evolution of the energy luminosity and the average neutrino energy.

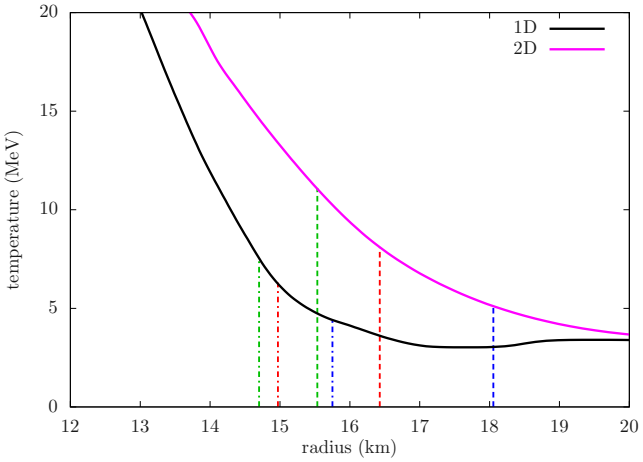

Figure 5.7: Temperature profiles near the neutrino sphere of the neutrinos with the energy of 12.8 MeV. The black and magenta lines denote the result for 1D and 2D, respectively. We pick up the snapshot $t = 150\,\mathrm{ms}$. The vertical lines denote the positions of the neutrino sphere for each flavor; ν_e (blue), $\bar{\nu}_e$ (red), and ν_x (green), and the chain lines denote 1D, and the broken lines for 2D. Note that angle-averaged quantities are shown for the 2D result.

Similarly as the time evolution of the kinetic energy, the initial rise is due to the sudden mapping from 1D to 2D. The time evolution can be compared with the result in 1D, which is shows with dashed lines. The luminosity and the mean energy are clearly larger in 2D than in 1D.

The enhancement of the mean energy in 2D can be understood from the angle-averaged radial profiles of temperature near the neutrino sphere shown in figure 5.7. The neutrino sphere is estimated in the same way as chapter 4. The vertical lines indicate the positions of the neutrino sphere for individual neutrino species at the energy of 12.8 MeV. The dash-dotted and dashed lines indicate the positions of the neutrino sphere for 1D and 2D, respectively. Since we focus on the neutrino emission, the absorption reactions are only taken into account to calculate the mean free path here. It is evident that the temperature is higher in 2D than in 1D. This is due to the dredge-up by convection of the hotter matter located originally deeper inside. If the location of the neutrino sphere were unchanged, the mean energy would be even higher. As should be also apparent in figure 5.7, the neutrino spheres are all shifted outwards to lower temperatures. This is due to the density rise at $r \gtrsim 15\,\mathrm{km}$ (see figure 5.8) associated with the expansion of PNS, which is in turn driven by the convection. For all flavors, the temperatures at the neutrino spheres are higher, which naturally leads to their greater mean energies as well as luminosities as observed in figure 6.7. In addition, the smaller neutrino sphere in 1D means that it is located deeper in the gravitational well, and the neutrinos emitted from it experience a greater gravitational redshift. This effect further lowers the luminosity and the mean energy for all flavors of neutrinos in 1D.

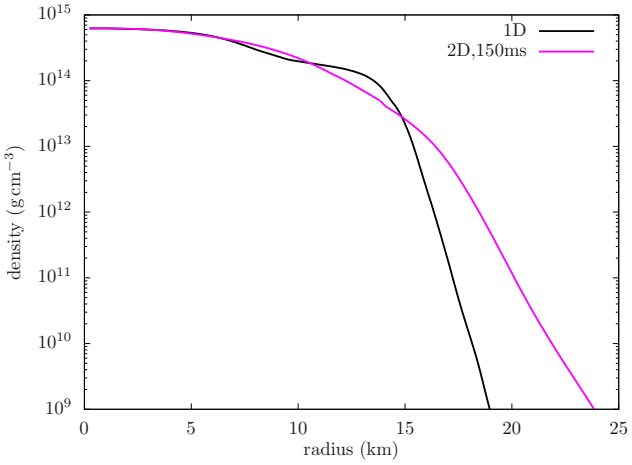

Figure 5.8: Comparison of density between 1D and 2D.

5.2.3 Anisotropy of PNS and Neutrino Emission

In this subsection, we discuss the asymmetry caused by the convection and its effect on the neutrino emission. Since we assume axisymmetry in this study, the results are inevitably affected by the artifacts unique to 2D. Nevertheless, the results will be useful as the reference for the 3D study in the future.

Figures 5.9 and 5.10 show the angle-dependence of density, temperature, and electron fraction at different times. The density variation is rather small except for the outer low-density layer at $r \gtrsim 20\,\mathrm{km}$, which we do not consider. The temperature distribution shows remarkable variations at $r \lesssim 13\,\mathrm{km}$ due to the convection, whereas it is almost symmetric at larger radii. The temperature profiles are especially bumpy at the north ($\theta = 0$) and the south ($\theta = \pi$) poles, suggesting that the convective motion is more violent there. The Y_e profile is also highly asymmetric in a more extended region, in which the maximum deviation from the average, $\Delta Y_e \gtrsim 0.05$, occurs around $r = 10\,\mathrm{km}$. In addition, Y_e tends to be lower on the poles than on the equator. This again indicates that the convection is stronger near the poles than around the equator.

In order to see the convective pattern more clearly, we plot the time-averaged electron fraction and velocity in figure 5.11. One can see three large vortices: one near the north pole, another centered at an intermediate latitude in the northern hemisphere and the other covering most of the southern hemisphere. Note that we do not impose the equatorial symmetry. They are extended radially from $\sim 7\,\mathrm{km}$ to $\sim 16\,\mathrm{km}$. Near the both poles matter is moving downwards, causing lower values of Y_e to prevail at $r \lesssim 15\,\mathrm{km}$. At the same time, the central region with higher values ($\gtrsim 0.15$) of Y_e becomes a bit oblate. This is why we observed Y_e tends to be lower near the poles in figures 5.9 and 5.10. The converging flows observed at the poles are mostly due to the artifact well-known in the axisymmetric simulation. However, a similar Y_e anisotropy was observed by Keil et al. (1996) (Fig. 3), in their 2D simulation, in which the poles were avoided by choosing a 45°-wedge region centered at the equator as their computational zone. They found that the zone at $15 \lesssim r \lesssim 20\,\mathrm{km}$ is divided into two, large vortices with lepton-rich matter rising and deleptonized matter sinking. We hence think that such configurations are rather generic and expect that the downdraft of low-Y_e matter and the updraft of high-Y_e matter will occur also in 3D at several points. Moreover, if the PNS is rotating rapidly, there may occur converging flows at the poles indeed. We have to wait for 3D studies, however.

Bearing this possible caveat in mind, we discuss the directional dependence of the neutrino emission caused by the asymmetric matter distribution derived above. Figure 5.12 shows a comparison of the luminosities at several angles in space. Both ν_e and $\bar{\nu}_e$ show large angular variations, where the maximum value becomes twice as large as the minimum value. The temporal changes at different angles for $\bar{\nu}_e$ are inversely correlated with that of ν_e. The ν_e luminosities near the south pole ($\theta = 5\pi/6$, π) tends to be lower than other angles. This is because the low-Y_e environment there (figures 5.9, 5.10) is preferable for the absorption of ν_e and emission of $\bar{\nu}_e$. Although ν_e luminosities near the north pole ($\theta = 0$, $\pi/6$) are higher than those near the south pole at early times, they become similar later as the transient subsides and the convection becomes quasi-steady. It is important that there is $\sim 30\%$ of anisotropy existent even if these pole regions are excluded. The ν_x luminosity, on the other hand, shows much smaller angular variations ($\lesssim 10\%$) compared to those of ν_e and $\bar{\nu}_e$ $\lesssim 10\%$ in the late phase. This is because the ν_x emission is barely affected by the anisotropy of Y_e and the temperature variations are smaller.

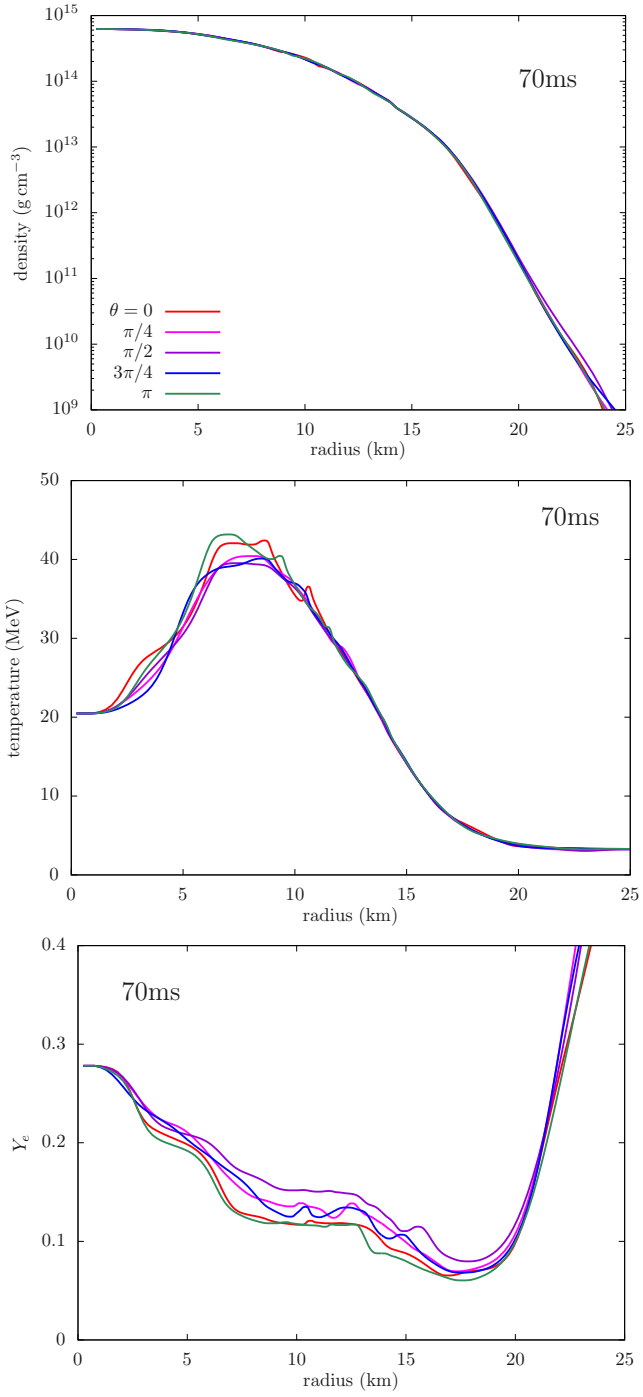

Figure 5.9: Comparison of the density (top), and the electron fraction (middle), and the temperature (bottom) for different angles at a time snapshot 70ms. The red, magenta, purple, blue, and green lines correspond to $\theta = 0$, $\pi/4$, $\pi/2$, $3\pi/4$, and π, respectively.

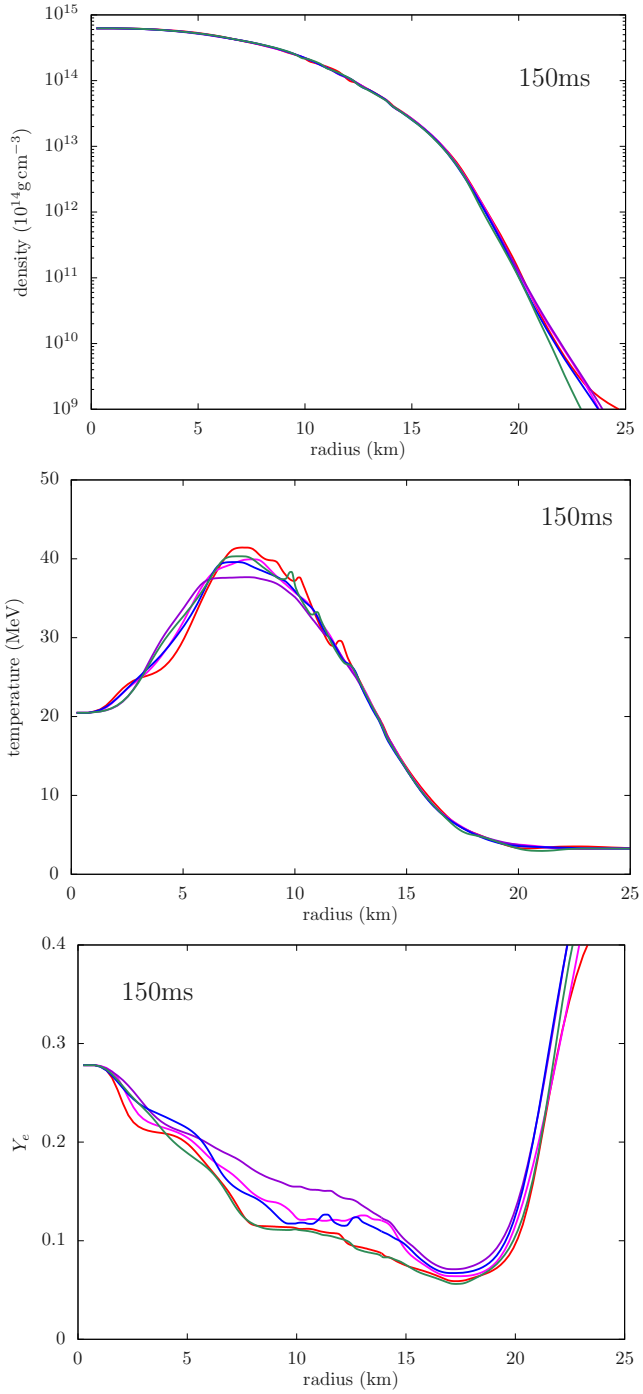

Figure 5.10: Same as figure 5.9, but for the time snapshot 150ms.

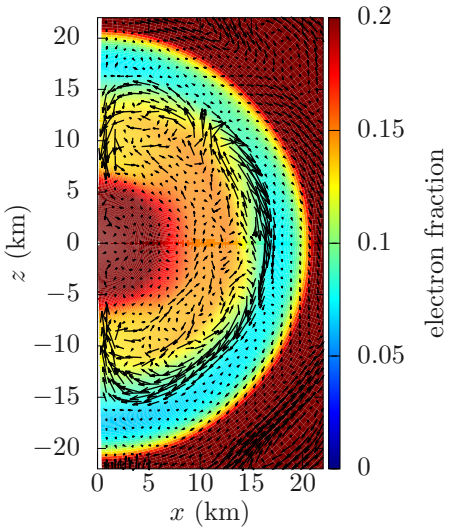

Figure 5.11: Time-averaged electron fraction and the velocity field on the meridian slice. The average is taken for the time period of $t \in [20, 40]$ ms.

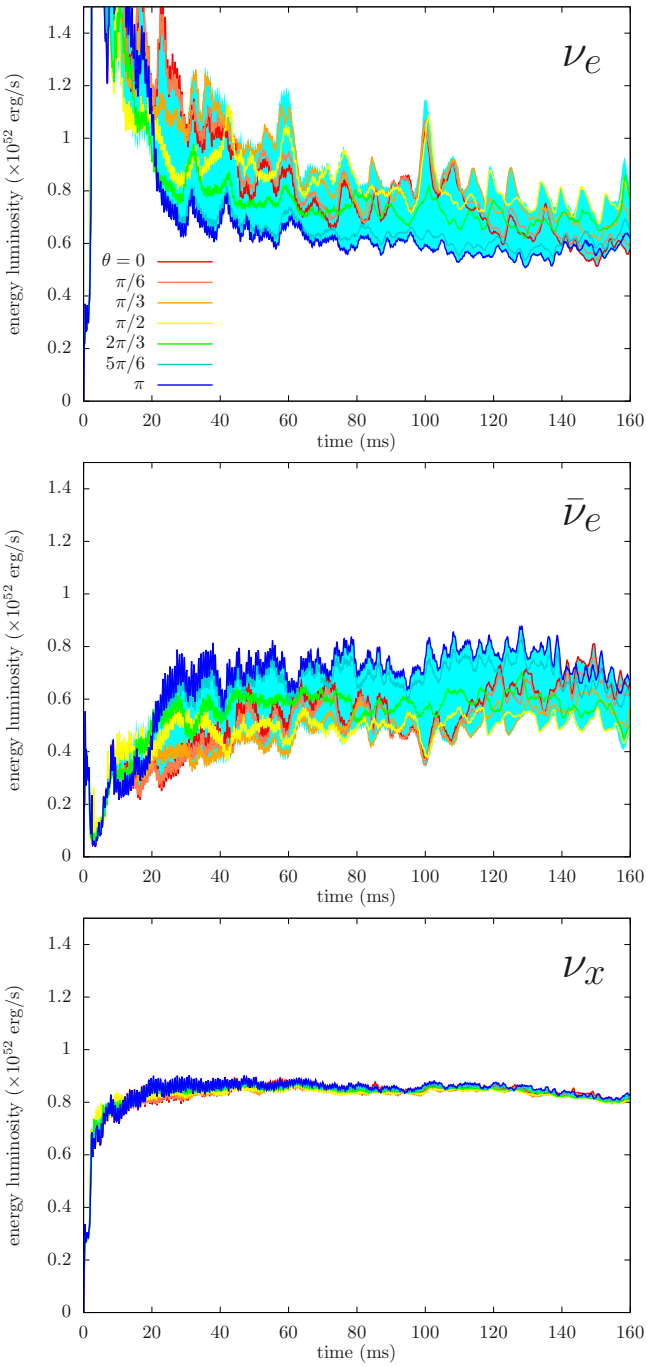

Figure 5.12: Comparison of the energy luminosity for different directions. Three panels correspond to different flavors; ν_e (top), $\bar{\nu}_e$ (middle), and ν_x (bottom). The red, orange, and the blue lines denote the luminosity for the north pole, the equator, and the south pole, respectively. The region shaded with light-blue represent the value between the maximum and the minimum luminosity.

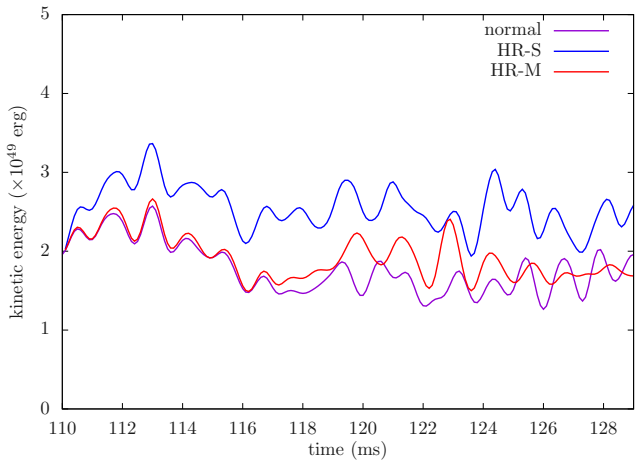

Figure 5.13: Time evolution of the matter kinetic energy for the normal resolution (purple), `HR-S` (blue), and `HR-M` (red).

5.2.4 Resolution Dependence

Here we investigate the numerical resolution in our 2D simulation. As mentioned earlier, we run the additional simulations either with a higher spatial resolution (model `HR-S`) or with a higher angular resolution in momentum space (model `HR-M`). Since we are interested in the (quasi) steady convection, we start these runs from the normal-resolution result at 110ms.

Figure 5.13 shows the time evolutions of the kinetic energy for the three runs. Since the convection is stochastic, the time variations are a bit different from model to model but they show the same trend. It is apparent that model `HR-S` has larger values of kinetic energy than the other two by $\sim 20\%$ for most of the time. The enhancement of turbulence due to higher spatial resolution is already reported in the context of CCSN simulation (Nagakura et al., 2019). Model `HR-M` also tends to have higher values than the normal-resolution model but the difference is much smaller and it may be a temporary trend. The period of the oscillation ~ 1 ms, is the same for different resolution models.

Figure 5.14 shows the resolution dependence of the neutrino luminosity. The ν_e luminosity for model `HR-S` is slightly higher than that for the normal resolution whereas the $\bar{\nu}_e$ luminosity shows opposite behavior. The ν_x luminosity gets greater for the higher spatial resolution but the difference is even smaller. The luminosities in model `HR-M` are almost the same as those in the normal-resolution model. Figure 5.15 shows the comparison of the (angle-averaged) mean neutrino energy among the three runs. For all flavors, the resolution dependence is very minor. We can say that although the turbulence induced by the convection is under-resolved spatially by a few tens percent in our 2D simulation, the enhancement in the neutrino luminosities and mean energies is much less affected by the resolution.

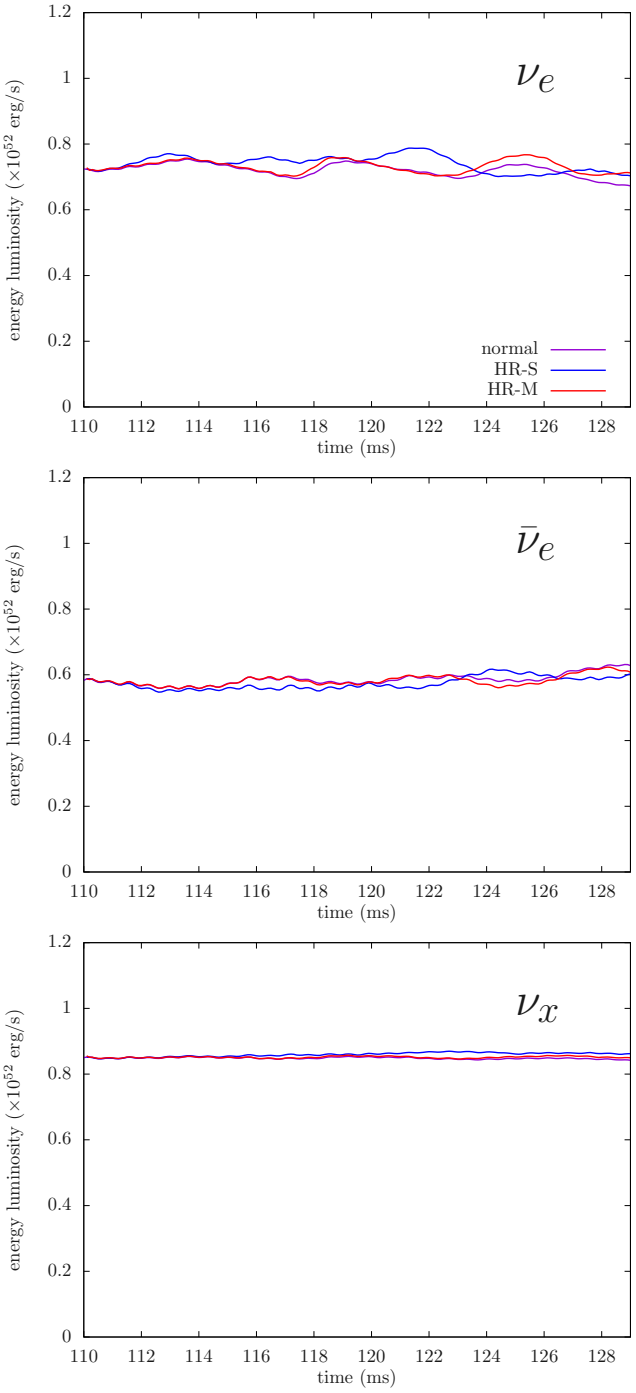

Figure 5.14: Time evolution of the energy luminosity for three different flavors; ν_e (top), $\bar{\nu}_e$ (middle), and ν_x (bottom). Different colors denote the different resolution; normal resolution (purple), `HR-S` (blue), and `HR-M` (red).

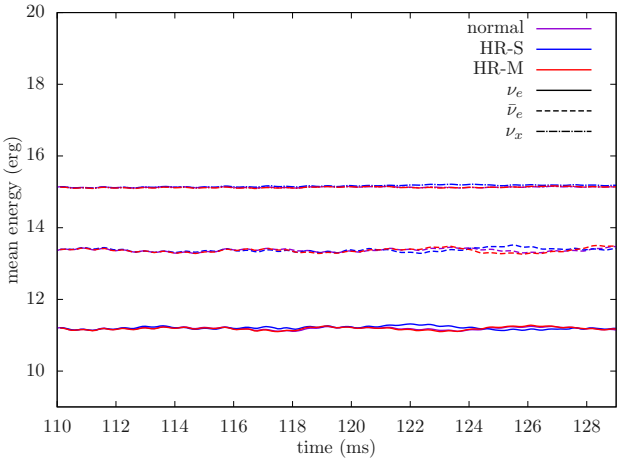

Figure 5.15: Time evolution of the mean neutrino energy for the normal resolution (purple), `HR-S` (blue), and `HR-M` (red).

5.3 Summary of Chapter 5

We investigated the PNS convection in 2D under axisymmetry, using our newly developed general relativistic Boltzmann neutrino radiation-hydrodynamics code. This is meant to be a pilot study for more comprehensive explorations of the PNS cooling in multi-dimensions. To our knowledge, it has not been conducted yet in the literature for a couple of reasons. In fact, most of the previous works on the PNS were done either in 1D (Roberts et al., 2012; Roberts, 2012; Nakazato & Suzuki, 2019; Nakazato & Suzuki, 2020; Li et al., 2021; Nakazato et al., 2022; Pascal et al., 2022) or in the early phase ($\lesssim 1$ s) of core-collapse supernova explosion (Mezzacappa et al., 1998; Dessart et al., 2006; Buras et al., 2006; Nagakura et al., 2020) (but also see recent advancements (Bollig et al., 2021; Burrows et al., 2023b)). For the purpose of this study, we extracted from a conventional 1D PNS-cooling calculation in spherical symmetry by Nakazato & Suzuki (2019) a snapshot of PNS at 2.3 s post bounce, mapped it onto a 2D grid and ran our code, adding some perturbations initially, to see the subsequent convective activity.

The Brunt-Väisälä frequency calculated at each grid point shows that this model has indeed a radially extended zone inside the PNS, that is linearly unstable against convection. We observed that the PNS convection is actually instigated in that region. The convective motion is particularly violent in the first $\sim$ 100 ms, extending itself inward by overshooting and rendering the entropy gradient positive there. We also saw a rapid rise of the neutrino luminosities and mean energies. These are all transients, though, which are induced by the switch from 1D to 2D and the subsequent growth of the convective motions. They subside gradually in $\sim$ 100 ms. Then the convection enters a quasi-steady phase sustained up to the end of the simulation at $\sim$ 160 ms by the negative radial gradient of Y_e, which remains thanks to the lasting neutrino emissions from the PNS surface. The PNS, on the other hand, is settled to a new expanded configuration, emitting neutrinos at higher luminosities and mean energies. The density, temperature and Y_e as well as the neutrino luminosities and spectra change much more slowly on the secular time scale thereafter. The sustained convection with the extension of the convective zone inward is consistent with Keil et al. (1996) but is at odds with Mezzacappa et al. (1998). The latter is due probably to their approximation in the neutrino transport as well as to the difference in the phase focused. The higher neutrino luminosities and mean energies in 2D than in 1D were also observed by other earlier works done for the core-collapse supernova simulations (Dessart et al., 2006).

Supposing that the self-sustained state above is representative of the PNS around this time in its cooling, we investigated it further. Note that the difference between the original matter profile obtained in the 1D PNS cooling calculation, and the self-sustained state in our 2D simulation indicates clearly that the multi-dimensional PNS calculation should be done from much earlier on, possibly from right after a successful launch of the shock wave from the supernova core.

We analyzed angular variations in the matter distributions that are produced by the convective motions. We found that the temperature and Y_e showed larger deviations from spherical symmetry than the density. In particular, Y_e tends to be lower near the poles and higher around the equator. This asymmetry in the Y_e distribution in turn gives rise to anisotropic emissions of ν_e and $\bar{\nu}_e$. The time-averaged convective pattern revealed that this Y_e distribution is generated by the subduction of low-Y_e matter and the dredge-up of high-Y_e matter by the convective motion. In our 2D simulation with axisymmetry imposed, the former occurs predominantly in the polar region and is most likely to be exaggerated. On the other hand, the downdraft of low-Y_e matter and the updraft of high-Y_e matter were also observed in other's simulations (Keil et al., 1996) that avoided the polar artifact. Hence we think it is a rather generic feature and expect that a similar asymmetry will occur also in 3D.

As repeatedly mentioned, convection in 2D under axisymmetry is different from that in 3D qualitatively (Lentz et al., 2015) and the converging flows in the polar regions are most likely due to the 2D artifact. As argued above, however, the convective pattern with low-Y_e matter sinking and high-Y_e matter rising will be rather generic and likely to occur also in 3D. In the rapidly rotating PNS, the converging flows may be realized indeed.

Chapter 6

Late-time Evolution of Protoneutron Star II. Effect of Fallback Accretion

This chapter focus on the fallback accretion (FBA) onto PNS and its effect on the neutrino emission. Fallback accretion is normally ignored in the late-time evolution of PNS. However, even after the successful explosion, a certain amount of FBA matter is expected. In following paragraphs, FBA in CCSNe is reviewed.

Even after the shock wave begins its runaway expansion, a certain amount of post-shock matter is bound by the gravity of the PNS, and it eventually returns back to the PNS. Such FBA in CCSNe has been studied in the literature from the early 1970s. The importance of FBA was first pointed out by Colgate (1971). They suggested that FBA is necessary to explain the consistent amount of nucleosynthetic yields. From the observational point of view, some previous studies suggested that FBA has an influence on both electromagnetic- (Dexter & Kasen, 2013) and neutrino emission (Fryer, 2009) in the late phase. We also note that FBA potentially accounts for some peculiar energetic (Moriya et al., 2018, 2019) and weak CCSN explosions (Moriya et al., 2010). If FBA leads to an oversupply of mass onto the PNS, it may trigger a black hole formation (Zhang et al., 2008; Chan et al., 2018). If the core is rapidly rotating, gamma-ray burst would occur following the collapsar scenario (MacFadyen & Woosley, 1999; MacFadyen et al., 2001; Perna et al., 2014). FBA can also affect the PNS spin (Barrère et al., 2022; Ronchi et al., 2022; Coleman & Burrows, 2022) and its spin-kick alignment indicated by some pulsar observations (Johnston et al., 2005, 2007; Ng & Romani, 2007; Janka et al., 2022).

FBA in CCSNe can be categorized into several phases (Chevalier, 1989). In the early post shock revival phase, it would be chaotic due to the turbulent accretion flows originated from multi-D fluid instabilities in the post-shock region. It should also be mentioned that asymmetric shock revival can lead to large FBA from the angular region where the shock expansion is weaker (Nagakura & Johns, 2021a; Bollig et al., 2021). In the very later phase, which is referred to as the uniform expansion phase $\gtrsim 10^3$ s, the accretion rate simply scales as $\dot{M} \propto t^{-5/3}$ (Chevalier, 1989). This scaling is verified by various numerical studies (Zhang et al., 2008; Dexter & Kasen, 2013; Janka et al., 2022). Note that the accretion rate on this free-expansion phase may be significantly enhanced by the arrival of the reverse shock onto PNS. It has also been suggested that strong FBA can be formed by the deceleration of the shock at the CO/He-core or He/H interfaces (Janka et al., 2022) (see also Fig. 2 of Zhang et al. (2008), in which the enhancement of FBA is clearly visible).

Most previous studies have a priori assumed that FBA has no influence on the neutrino signal. One thing we do notice here is, however, that large amounts of FBA have been observed rather commonly

in recent multi-dimensional (multi-D) CCSN simulations (see, e.g., Burrows & Vartanyan, 2021; Bollig et al., 2021; Nagakura & Johns, 2021a). More interestingly, they may last a very long time ($\gg$ 10s) (see, e.g., Fig.2 in Janka et al., 2022) due to the shock deceleration or reverse shock that occurs after the shock wave passes the CO/He-core interface (Fryxell et al., 1991) and He/H interface (Chevalier, 1989). This suggests that the neutrino emission from FBA potentially overwhelms those radiated from PNS.

The impact of FBA in the late time neutrino emission was investigated by the pioneering work of Fryer (2009). This study showed that FBA has a large influence on the neutrino luminosity and their average energy. It should be noted, however, that there are potential systematic uncertainties in their models; for instances, the inner boundary of the computational domain in the simulations is located much outside the neutrino sphere (which will be shown later and see also Table 2 in Fryer (2009)), and the neutrino transport was handled with a gray flux-limited diffusion approximation (Herant et al., 1994). These simplifications prevented them from studying detailed features of neutrinos from FBA, and they may discard some important properties inherent in FBA.

Although the FBA is a priori multi-D, the accretion energy converts to thermal energy in the vicinity of PNS, and eventually spreads all over the PNS surface. This suggests that the asymmetry of neutrino emission becomes milder than that of FBA, and numerical simulations also support this assumption (Vartanyan et al., 2019). Whether large asymmetries of neutrino emission can be created by non-radial FBA is an interesting question which we defer to future work. We also note that the spherically symmetric conditions artificially suppress the PNS convection. One may wonder if this may cause to underestimate the diffusion component of the neutrino luminosity. According to recent multi-D simulations, however, the PNS convection subsides by $\sim$ 5s after bounce (Nagakura & Johns, 2021a), suggesting that it does not affect FBA neutrinos in the late phase ($t \gtrsim$ 10s).

In this study, we pay attention to the phase of $\gtrsim$ 10 s after core bounce. In this phase, the PNS temperature at the surface becomes less than $\sim$ 3 MeV (Roberts, 2012; Nakazato et al., 2013), and the neutrino emission gradually subsides in the Kelvin-Helmholtz timescale. This suggests that the neutrino emission can be dominated by FBA, inferred from the previous works (Fryer, 2009; Nagakura et al., 2020; Nagakura & Johns, 2021a; Bollig et al., 2021).

It should also be noted that we develop a general discussion of FBA neutrino emission without specifying any late phases in this study, since our approach can be applied to different situations. Nevertheless, the increase of FBA by a reverse shock created at the CO/He-core or He/H interfaces is an intriguing phase, since a large FBA may happen at a very late phase of CCSNe ($\gtrsim 10^3$ s) (Zhang et al., 2008).

6.1 Setup

6.1.1 Numerical Setup

We perform GR Boltzmann radiation-hydrodynamics simulation in 1D, employing the code described in chapter 3. We employ 512 radial grid points covering the range $r \in [0:100]$ km. We note that the resolution is high around the PNS surface (where the minimum mesh width is $\sim$ 30 m). Such a high spatial resolution is mandatory in studying FBA, since the scale heights of matter- and neutrino-radiation field around the PNS are very small. The mesh configurations for θ_ν and the energy are completely same as the previous 2D simulations in chapters 4 and 5. Since the spherical symmetry is assumed, the dependence on ϕ_ν can be dropped unlike previous 2D simulations.

We employ the Furusawa-Togashi EOS (Furusawa et al., 2017) with some extension. It should be mentioned that, in the case with low mass accretion rate, the thermodynamical quantities can be outside of the range covered by the EOS table. To deal with this issue, we extended the EOS table in a pragmatic way; it is smoothly connected to the gamma-law EOS as the pressure given as $P = (\Gamma - 1)\rho\epsilon$, where ρ and ϵ denote the density and the specific internal energy, respectively. The

gamma law index Γ is obtained from the edge of the EOS table. We found that Γ is almost 4/3 for various input parameters. We note, however, that our prescription is rather pragmatic, and it does not have the ability to capture the realistic matter evolution; in particular for shock dynamics. For this reason, we stop the calculation if the shock wave reaches the position where thermodynamical quantities are out of the range of the Furusawa-Togashi EOS. On the other hand, these prescriptions do not compromise the present result, since neutrino emission occurs in high density regions, which are always covered by the Furusawa-Togashi EOS.

6.1.2 PNS Model and the Fallback Matter

The accurate determination of the neutrino emission from FBA requires resolving the PNS surface where the accretion energy is converted to thermal energy. We also note that the neutrino opacity hinges on the energy, and the low energy neutrinos can escape from the very high density region ($> 10^{14}$g/cm^3), exhibiting that the PNS structure needs to be determined to quantify the neutrino energy spectrum. Hence, we construct the PNS structure by assuming steady state, before running FBA simulations.

We assume an isotropic temperature of $T = 2\,\mathrm{MeV}$ and the electron fraction of $Y_e = 0.05$ inside the PNS as a reference model, which represents the matter state of the PNS in the cooling phase. For the sake of completeness, the temperature dependence in the neutrino signal is also checked in this study (section 6.2.5). Given T and Y_e, we prepare two different PNS structures by solving TOV equations, by varying the central baryon mass density. The first one has the central density of $\rho_c = 8.5\times10^{14}\,\mathrm{g\cdot cm^{-3}}$, leading to the total mass $M_{\rm PNS} = 1.41 M_\odot$. For the second one, we set $\rho_c = 1.2\times10^{15}\,\mathrm{g\cdot cm^{-3}}$, that leads to $M_{\rm PNS} = 1.98 M_\odot$. The spacetime metric obtained from solving the TOV equations is used for the radiation-hydrodynamic simulations, and kept fixed in time.

Below, we describe our FBA model. One thing to note here is that the self-consistent treatment of FBA requires successful CCSN explosion models. It should be noted, however, that detailed features of FBA such as the mass accretion rate, the thermodynamical states, and their time evolution strongly depend on the progenitor, the timing of the shock revival, and the ejecta morphology. In this study, we are not interested in such details of the neutrino signal, but rather in generic features that can be applied to any types of FBA. To this end, we treat FBA in a simple manner capturing the essential features. In our models, we assume a mass inflow from the outer boundary of the computational domain. The accretion rate is one of the control parameters, and we study four cases: $\dot{M} = 10^{-2}, 5\times10^{-3}, 2\times10^{-3}$, and $10^{-3}\,M_\odot\cdot\mathrm{s}^{-1}$.

The choice of mass accretion rate is motivated by previous studies of FBA by (Chan et al., 2018; Moriya et al., 2019; Janka et al., 2022);. According to their results, strong FBA ($10^{-3}M_\odot/s$) can occur in the late phase (> 10s) for some progenitors. In this study, we increase the mass accretion rate to see its dependence on the neutrino luminosity. We note that it is necessary to check this dependence by decreasing the mass accretion rate for the sake of completeness, but these simulations are currently not available due to some technical problems associated to EOS tables. Addressing this issue is postponed to a future work. The matter temperature is set as $T = 0.5\,\mathrm{MeV}$. We note that this setup (cold FBA) leads to a conservative estimation of the neutrino signal by FBA. Y_e is set to be 0.5. We run each model until the system reaches a quasi-steady state.

For computational reasons, the temperature inside 8 km is fixed in time. It is well inside the PNS; in fact the matter density is $\rho > 1.5\times10^{14}$g/cm^3 and its temperature is also low (~ 2MeV), indicating that the boundary condition does not affect the neutrino emission. This is to avoid over-cooling of PNS. If the evolution is fully solved, the PNS temperature will get persistently lowered due to the neutrino emission. This is undesirable because the EOS table employed in this study has a lower limit. Furthermore, low temperature makes the system numerically difficult to treat.

6.2 Results

6.2.1 Matter distributions

We first focus on the matter distributions of FBA after the system has settled to a quasi-steady state. The time it took to reach the steady state varies for different models, in the range of $50 \lesssim t \lesssim 120\,\mathrm{ms}$. It took longer for lower accretion rate models.

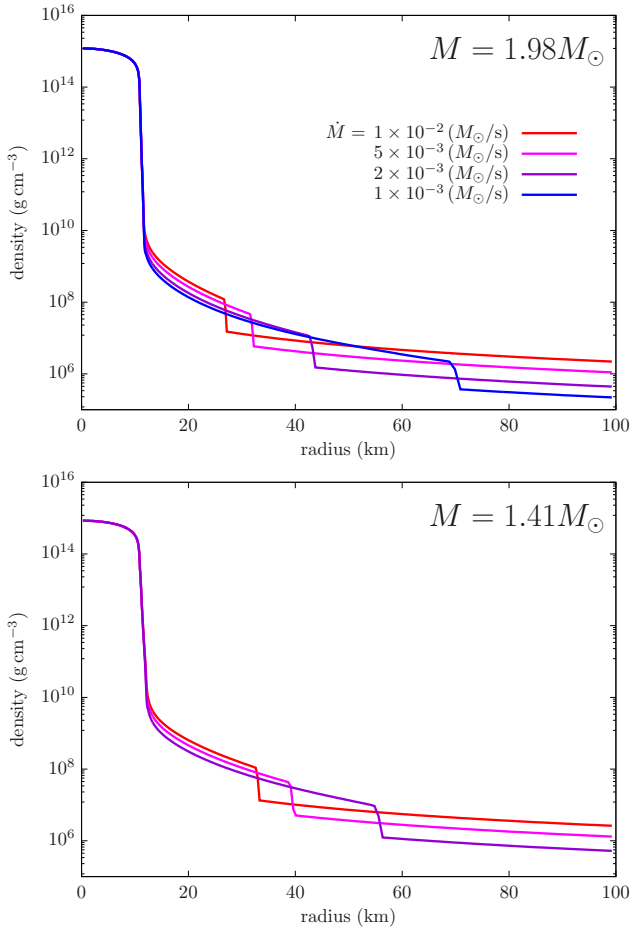

Figure 6.1: Radial profiles of the density for the $1.98M_\odot$ model (top) and the $1.41M_\odot$ (bottom). The different colors indicate different accretion rates.

Figures 6.1, 6.2, and 6.3 show the density, temperature, and four-velocity of the fluid. In these figures, color distinguishes models with different mass accretion rates $\dot{M}$ and PNS masses $M_{\rm PNS}$: four models ($\dot{M} = 1 \times 10^{-2}$ to $1 \times 10^{-3}\,M_\odot \cdot \mathrm{s}^{-1}$) for $M_{\rm PNS} = 1.98M_\odot$, and three models ($\dot{M} = 1 \times 10^{-2}$ to $2 \times 10^{-3}\,M_\odot \cdot \mathrm{s}^{-1}$) for $M_{\rm PNS} = 1.41M_\odot$.

As can be seen in these figures, an accretion shock wave is formed due to FBA. We note that similar phenomena are observed in recent multi-D CCSN simulations (see, e.g., Fig. 9 in Nagakura & Johns (2021a)). According to these CCSN models, FBA tends to be cold or lower entropy (otherwise the thermal pressure hampers accretion), and the downflow onto the PNS becomes supersonic. At the surface of the PNS, the fluid needs to be subsonic, implying that a shock wave is inevitably formed. As displayed in these figures, the shock position is larger for the lower accretion rate and the lower

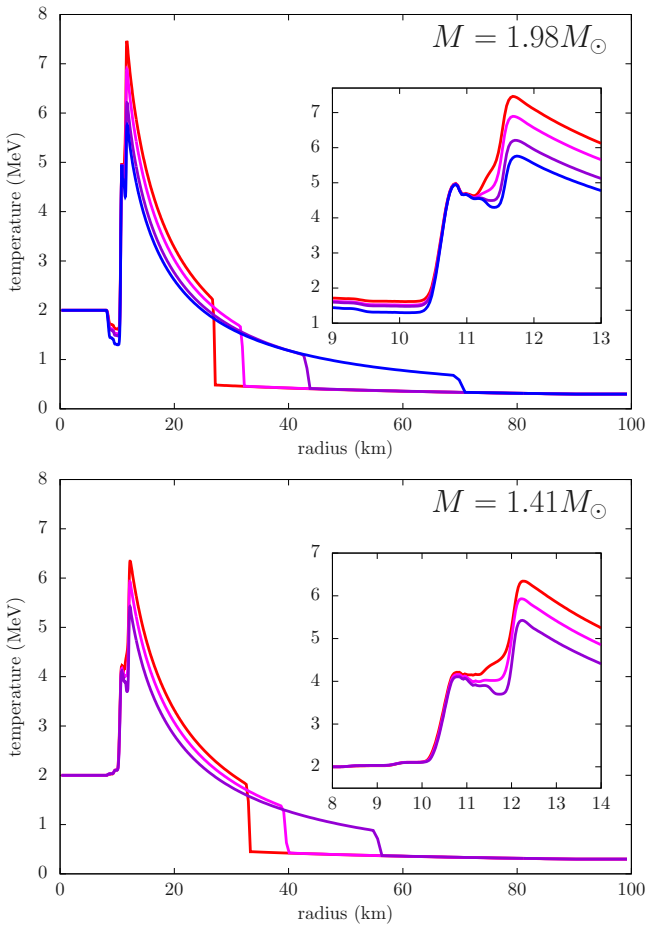

Figure 6.2: Same as figure 6.1, but for the temperature.

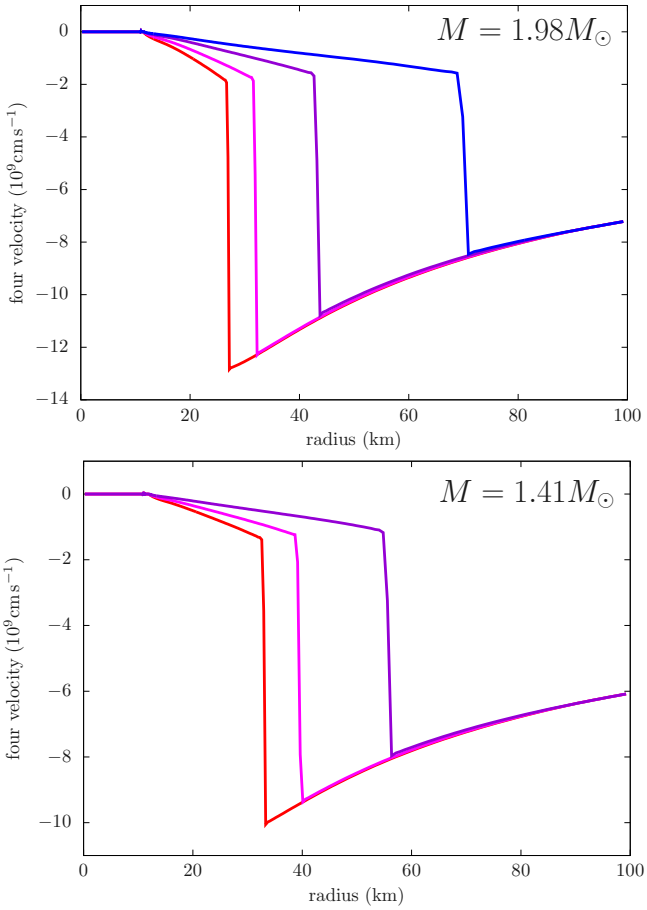

Figure 6.3: Same as figure 6.1, but for the four-velocity.

PNS mass. This is attributed to the lower ram pressure in the preshock region.

Another notable feature displayed in Fig. 6.2 is that sharp peak profiles in the temperature distribution emerge in the vicinity of the PNS. To see the profile clearly, we magnify the corresponding region (10km $\leq r \leq$ 13km), which is displayed in the same panel. The sharp increase of temperature is due to the hard wall of the PNS surface, in which the matter density changes by four orders of magnitude over a width $\lesssim 1$ km. We stress that this is not the artifact caused by the inner boundary at 8 km. The temperature distribution at $8 < r \lesssim 11$ km remains rather flat distribution (see the magnified figures), and it suggests that flat temperature distribution is a reasonable assumption. In this region, the kinetic energy of FBA can be efficiently converted into thermal energy, and therefore the temperature of FBA also increases rapidly with decreasing radius. We also note that the thermal energy of matter is proportional to $\dot{M}{v_{\rm ff}}^2$, where $v_{\rm ff}$ denotes the free-fall velocity where the kinetic energy is dissipated. Since the dissipation region is less sensitive to the PNS mass, $v_{\rm ff}$ is proportional to $M_{\rm PNS}^{0.5}$. This is the rationale behind the higher peak temperature for the higher mass accretion rate and the higher PNS mass (see Fig. 6.2).

It is worth mentioning that a smaller PNS radius means that a larger gravitational energy is converted into thermal energy. Since our focus is the late phase, the PNS radius is thought to have shrunk to a small radius due to cooling (in our setting, ~ 11 km). This situation is actually advantageous for creating a high temperature peak and leads to a larger amount of neutrino emission. If different EOS with smaller NS radius is employed, the peak temperature would be higher.

Contrary to the trend which we have discussed so far, the temperature decreases rapidly with decreasing radius at $\lesssim$ 11.5km and $\lesssim$ 12km for $M_{\rm PNS} = 1.98 M_\odot$ and $1.41 M_\odot$, respectively (see the magnified figure of Fig. 6.2). This exhibits that neutrino cooling gives feedback on the matter distribution. On the other hand, the temperature profile is very complicated in the transition layer between the cold PNS envelope and the inner edge of FBA. As we shall show below, weak processes are responsible for the complex radial profile in the temperature distribution. It is also interesting to note that the matter profile in the region 10km $\lesssim r \lesssim$ 11km does not depend on the mass accretion rate. Although we postpone the detailed investigation to future work, this may be due to a self-regulation mechanism around the PNS surface. Since the matter pressure needs to be connected smoothly across the layer, the fluid element at the PNS surface undergoes shrinking. This implies that the gravitational energy is converted into thermal energy, which also accounts for the increase of neutrino luminosity, in particular for heavy-leptonic neutrinos (ν_x).

6.2.2 Neutrino distributions

Before going into details, let us first provide the information on species-dependent neutrino spheres. As a reference, we show them in the case of $\dot{M} = 10^{-3}\,M_\odot \cdot \mathrm{s}^{-1}$ and the PNS mass $1.98M_\odot$. The neutrino spheres for the energy of 23.4 MeV, roughly corresponding to the average energy of neutrinos, are 11.2 km 10.7 km, 3.66 km for ν_e, $\bar{\nu}_e$, and ν_x, respectively. The density at each neutrino sphere is $2.55 \times 10^{12}\,\mathrm{g} \cdot \mathrm{cm}^{-3}$, $1.88 \times 10^{14}\,\mathrm{g} \cdot \mathrm{cm}^{-3}$ and $1.11 \times 10^{15}\,\mathrm{g} \cdot \mathrm{cm}^{-3}$, respectively. This exhibits that the neutrino sphere is located at higher matter density than in the early post-bounce phase (a few hundreds of milliseconds after core bounce); for instance, the neutrino sphere of ν_e is located at $\sim 10^{11}\mathrm{g/cm}^3$ in the early post-bounce phase. This difference can be understood as follows. The density gradient becomes so steep in the late phase, indicating that the scale height in this region becomes small. Since the neutrino optical depth is determined not only by the local reaction rate but also by the scale height, the optical depth tends to be smaller in the late phase for the region with the same matter density. It is also worthy to note that these neutrino spheres are located much deeper than the inner boundary adopted in the simulations of Fryer (2009).

To delve into the neutrino feedback on matter, we portray the radial profiles of the energy flux (F_ν) of each species of neutrinos in the case of the PNS mass $1.98M_\odot$ and the accretion rate $\dot{M} = 10^{-3}\,M_\odot \cdot \mathrm{s}^{-1}$ (see Fig 6.4.). In the figure, neutrino fluxes are multiplied by a factor r^2. We note that $F_\nu r^2$ is approximately constant in space, if there are no neutrino emission and absorption[1]. This indicates that the information on neutrino cooling (or heating) is imprinted in the radial profile of $F_\nu r^2$. As shown in the top panel of Fig 6.4, neutrino fluxes for ν_e and $\bar{\nu}_e$ increase with radius in the region $11\mathrm{km} \leq r \leq 11.5\mathrm{km}$, indicating that these neutrinos are substantially produced there. The fact that ν_x is approximately constant in space indicates that ν_x is not produced in this region. It is also worthy to note that ν_e absorption dominates over emission in the narrow region at ~ 10.9km (see blue line). A similar profile is also observed for $\bar{\nu}_e$ at smaller radius (see the red line). It is also informative to see the temperature profile as a function of the matter density, which is displayed in the bottom panel of Fig 6.4. For ν_e ($\bar{\nu}_e$), strong neutrino production occurs at very high density $5 \times 10^{13}\mathrm{g/cm}^3 \lesssim \rho \lesssim 2 \times 10^{14}\mathrm{g/cm}^3$ ($10^{14}\mathrm{g/cm}^3 \lesssim \rho \lesssim 2 \times 10^{14}\mathrm{g/cm}^3$). When these neutrinos propagate outwards in the lower density environment, neutrino absorption becomes dominant in the region $10^{13}\mathrm{g/cm}^3 \lesssim \rho \lesssim 5 \times 10^{13}\mathrm{g/cm}^3$ ($5 \times 10^{13}\mathrm{g/cm}^3 \lesssim \rho \lesssim 10^{14}\mathrm{g/cm}^3$), but neutrino emission again dominates over absorption until $\rho \sim 10^9\mathrm{g/cm}^3$. These non-monotonic profiles of ν_e and $\bar{\nu}_e$ fluxes are clearly associated with the matter temperature profile, which shall be discussed later. Our result also suggests that there is a substantial amount of diffusion component for both ν_e and $\bar{\nu}_e$ in their energy fluxes, which are missing components in the simulations of Fryer (2009). We also find that ν_x profile is much simpler than others; ν_x is mainly produced at $5 \times 10^{13}\mathrm{g/cm}^3 \lesssim \rho \lesssim 2 \times 10^{14}\mathrm{g/cm}^3$ and then they freely escape from the system. This suggests that ν_x production mainly occurs in such a high density region. It is, hence, mandatory to cover the high density region in numerical simulations to quantify the neutrino signal from FBA.

To see what weak process accounts for the neutrino emission and absorption, we display the radial profile of inverse mean free path of each weak process in Figs. 6.5 and 6.6, for the accretion rate of $\dot{M} = 10^{-3}\,M_\odot \cdot \mathrm{s}^{-1}$ and the PNS mass $1.98M_\odot$ model. These figures show the inverse mean free path as a function of the radius and the matter density, respectively. Except for the high density region ($\sim 5 \times 10^{13}\mathrm{g/cm}^3$ for ν_e and $\sim 2 \times 10^{14}\mathrm{g/cm}^3$ for $\bar{\nu}_e$), electron-capture on free proton and positron-capture on free neutron dominate the ν_e and $\bar{\nu}_e$ emission, respectively. We also find that nucleon–nucleon bremsstrahlung becomes dominant in the high density regions, leading to a non-monotonic radial profile of neutrino opacity. This is responsible for the non-monotonic profile for both neutrino fluxes in ν_e and $\bar{\nu}$. This leads to the complex radial profile of matter temperature. Indeed, the inverse mean free path peaks at $11 \lesssim r \lesssim 12\,\mathrm{km}$ for ν_e and $10 \lesssim r \lesssim 11\,\mathrm{km}$ for $\bar{\nu}_e$, and these spatial positions are

[1]Strictly speaking, $F_\nu r^2$ is not constant in curved spacetime. However, the deviation due to general relativistic (GR) effects is minor and not important for the argument; hence we multiply by a factor r^2 without any GR corrections just for simplicity.

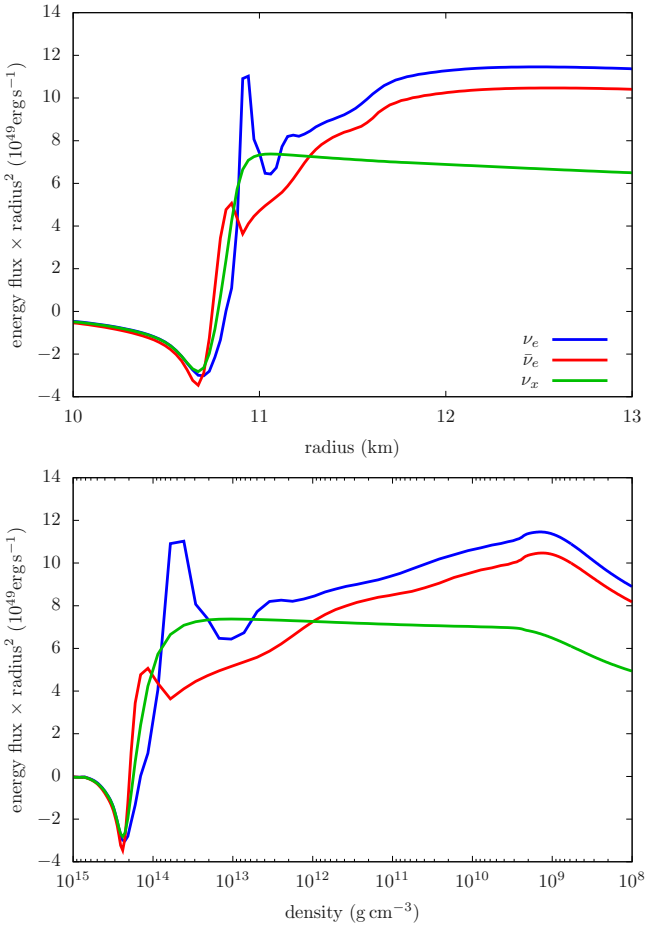

Figure 6.4: Energy flux times the square of radius for the PNS mass $1.98M_\odot$ and the accretion rate $\dot{M} = 10^{-3}\,M_\odot \cdot \mathrm{s}^{-1}$. The horizontal axis are the radius and density, for top and bottom panels, respectively.

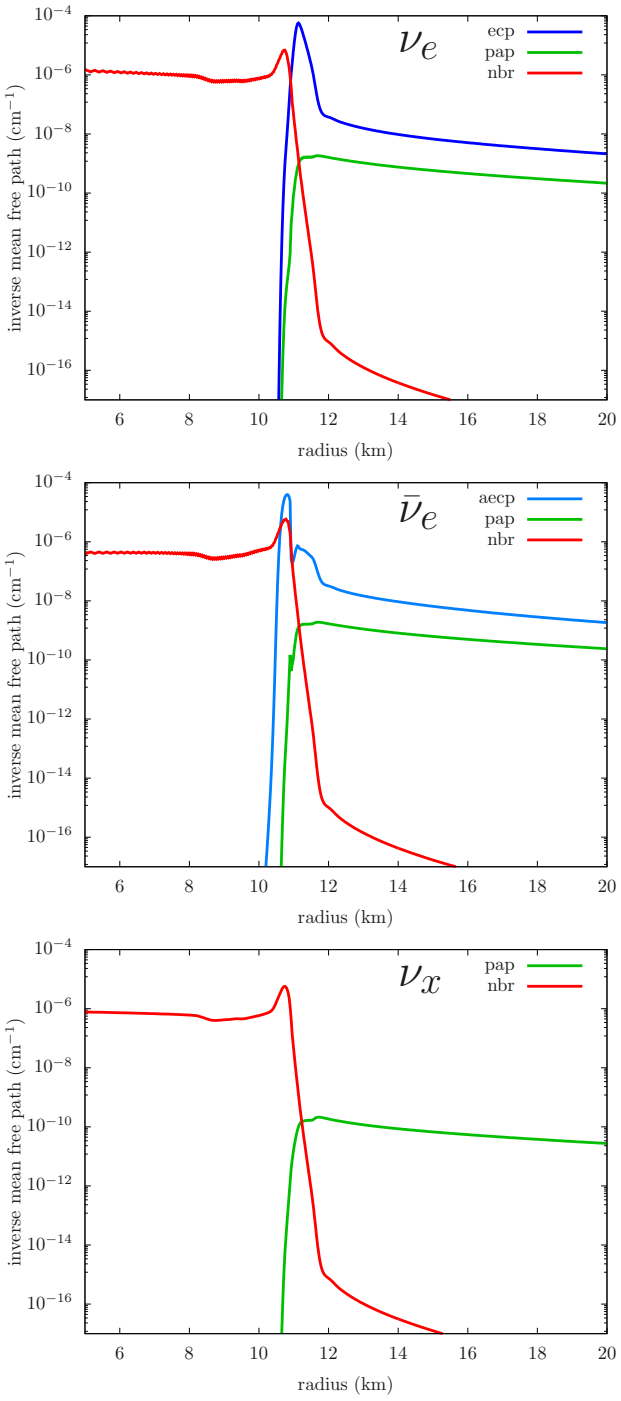

Figure 6.5: Radial profile of the inverse mean free path for ν_e (top), $\bar{\nu}_e$ (middle) and ν_x (bottom) with the energy of 23.4 MeV, for the model with the accretion rate $\dot{M} = 10^{-3}\, M_\odot \cdot \mathrm{s}^{-1}$ and the PNS mass $1.98 M_\odot$. The abbreviation of the neutrino reactions are as follows: the electron-capture on nucleon (ecp), the positron capture (aecp), the electron–positron process (pap) and the nucleon–nucleon bremsstrahlung (nbr).

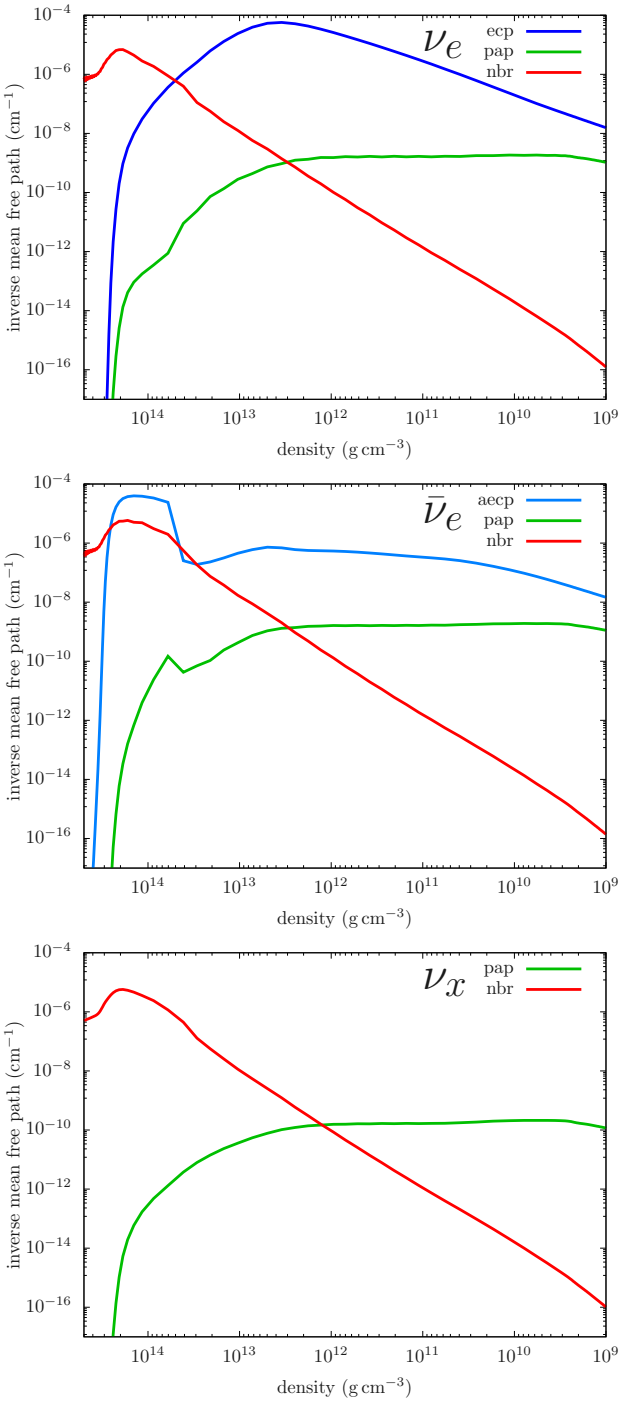

Figure 6.6: Same as figure 6.5, but the horizontal axis is the density.

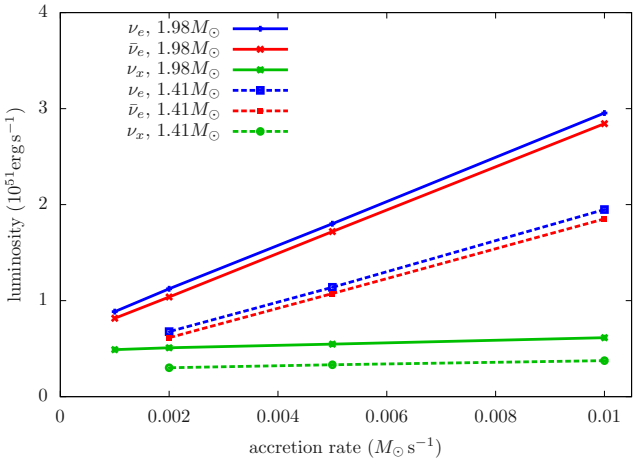

Figure 6.7: Energy luminosity versus the accretion rate. Different colors show the different flavors, and the solid lines correspond to the $1.98M_\odot$ model and the broken lines for the $1.41M_\odot$ model.

roughly the same as those at the temperature dips. This exhibits that temperature dips are caused by the neutrino cooling by ν_e and $\bar{\nu}_e$. For ν_x, on the other hand, the neutrino opacity is dominated by nucleon–nucleon bremsstrahlung at the emission region ($5 \times 10^{13}\mathrm{g/cm^3} \lesssim \rho \lesssim 2 \times 10^{14}\mathrm{g/cm^3}$). Although the electron-positron pair production becomes dominant at $\rho \lesssim 10^{12}\mathrm{g/cm^3}$, the emissivity is very small. In fact, the radial profile of $F_\nu r^2$ for ν_x is almost constant in space over the low density region (see Fig 6.4).

6.2.3 Neutrino Luminosity and Mean Energy

Figure 6.7 summarizes the energy luminosity for all simulated models. As shown in the figure, larger accretion rates and larger PNS masses leads to higher luminosities. The energy luminosity for ν_e and $\bar{\nu}_e$ are of the order of $o(10^{51})\,\mathrm{erg \cdot s^{-1}}$, and ν_x luminosities are below $10^{51}\,\mathrm{erg \cdot s^{-1}}$. One thing we do notice here is that neutrino luminosities obtained in our simulations are systematically higher than those reported in Fryer (2009). This is again due to the fact that the simulations of Fryer (2009) did not cover the high density region, which results in underestimating neutrino luminosities. Our result suggests that it is mandatory to include the high density region in theoretical models to quantify the neutrino signal from FBA and to extract physical information from the neutrino signal in real observation (see Sec. 6.2.4 for more details). Luminosities for ν_x hardly depend on the accretion rates. This is because ν_x are mainly emitted from the inner PNS, as we saw in the radial profiles of the flux. The luminosities of ν_e and $\bar{\nu}_e$ are also not proportional to the accretion rates and shifted to higher values, due to the same reason.

In Fig. 6.8, we provide mean energies of the emitted neutrinos. The mean energy of ν_e is $\epsilon \sim 13\,\mathrm{MeV}$ for the highest accretion case ($\dot{M} = 10^{-2}\,M_\odot \cdot \mathrm{s^{-1}}$), and it is still $\epsilon \gtrsim 10\,\mathrm{MeV}$ for other cases with lower mass accretion rate. The mean energy of $\bar{\nu}_e$ is always higher than that of ν_e, and reaches a maximum of $\epsilon \sim 17\,\mathrm{MeV}$. We also find that, similar to the luminosity, larger accretion rates and PNS masses lead to higher neutrino mean energies. This is due to the higher matter temperature in the neutrino emission region (see Fig. 6.2).

It is worthy to note that ν_x has the lowest mean energy among three flavors, which is $\epsilon \sim 10\,\mathrm{MeV}$. This tendency is clearly different from the canonical hierarchy of neutrino mean energy in CCSNe. In general, the mean energy of ν_x is the highest among all flavors of neutrinos in early post-bounce phase, and then the mean energy of all flavors becomes almost identical in the late phase. This exhibits

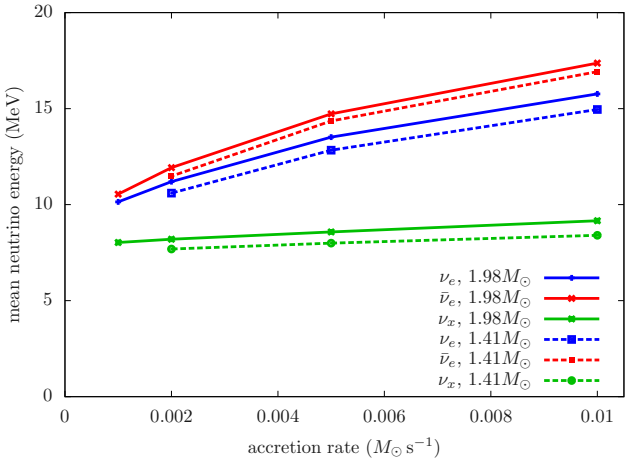

Figure 6.8: Same as 6.7, but for the mean energy of emitted neutrinos.

that FBA leads to a qualitatively different neutrino emission from PNS cooling, and that the neutrino detection rate should depend on the neutrino oscillation model. The low luminosity and low mean energy of ν_x are attributed to the temperature distribution in the ν_x emission region. As shown in Fig. 6.4, most of the ν_x are produced in the region of $5 \times 10^{13}\mathrm{g/cm^3} \lesssim \rho \lesssim 2 \times 10^{14}\mathrm{g/cm^3}$. This region corresponds to the transition layer between the PNS surface and the inner edge of FBA. Although the matter temperature sharply increases with radius, it is still very low ($\lesssim$ 4MeV). As a result, both the luminosity and the mean energy of ν_x become much lower than those associated to ν_e and $\bar{\nu}_e$. We note that the radius of the emission region for ν_x is smaller than for other flavors. This causes a lower neutrino luminosity, although this effect is minor since the difference of emission region among all flavors of neutrinos is only $\lesssim$ 1km.

We remind the readers that our current focus is the late phase ($t \gtrsim 10\,\mathrm{s}$), where the typical mean energy of the diffusive neutrino component from PNS is $\epsilon \lesssim 10\,\mathrm{MeV}$ (Suwa et al., 2019). This is much smaller than neutrinos from FBA. As discussed in Sec. 6.2.4, higher luminosities and mean energies of neutrinos are more favorable for neutrino detection. Our results support the claim in Fryer (2009) that FBA can substantially increase the neutrino event rate, which is quantified in the next section.

6.2.4 Detectability of FBA Neutrinos

We evaluate the detectability of the FBA neutrinos by two representative terrestrial neutrino detectors, Super-Kamiokande (Hereafter Super-K) and Deep Underground Neutrino Experiment (DUNE). In this estimation, we employ the neutrino cross section data taken from the SNOwGLoBES (Scholberg et al., 2021). We ignore any smearing effects caused by the detector response and various noises just for simplicity.

Super-K is a water-Cherenkov detector using pure water (Fukuda et al., 2003) with gadolinium compound loaded recently (Abe et al., 2022). The main detection channel of Super-K is the inverse-beta interaction

$$\bar{\nu}_e + p \rightarrow e^+ + n. \tag{6.1}$$

We assume the fiducial volume of 32.5 kton for the estimation of the event rate. Its update version, Hyper-Kamiokande is also under construction (Hyper-Kamiokande Proto-Collaboration et al., 2018). Its fiducial volume will be 220 kton, and the detection rate can be easily scaled from the result of Super-K. We assume pure water for the evaluation of the event rates. It should be mentioned that the gadolinium-loading in SK plays an important role to decouple the FBA neutrino signal from the

background (Li et al., 2022; Simpson et al., 2019). Unlike the strong neutrino burst in the early post-bounce phase, the luminosity is lower and the timescale is longer for FBA neutrinos, indicating that the reduction of the background is very important to identify the signal.

DUNE is a future-planned neutrino detector. It will use liquid argon as the neutrino detector medium. The main detection channel of DUNE is the neutrino-argon charged-current interaction

$$\nu_e + {}^{40}\mathrm{Ar} \rightarrow e^- + {}^{40}\mathrm{K}^*. \tag{6.2}$$

We assume a full volume of 40 kton for the estimation of the event rate. For the estimation of the neutrino flux arriving on the earth, we take into account the neutrino oscillation effect in the same way as Dighe & Smirnov (2000); Nagakura & Johns (2021a). Neutrino flavors are assumed to convert adiabatically by the Mikheyev–Smirnov–Wolfenstein (MSW) effect. Although it is a simple oscillation model, this provides an essential feature of how detectability of FBA neutrinos depends on flavor conversions.

Following Nagakura & Johns (2021a), the neutrino fluxes arriving on earth F_e, $\bar{F}_e$, F_x, $\bar{F}_x$ (corresponds to ν_e, $\bar{\nu}_e$, ν_x, $\bar{\nu}_x$, respectively) are calculated from the values of the fluxes without neutrino oscillation (F_e^0, $\bar{F}_e^0$, F_x^0, $\bar{F}_x^0$) as:

$$\begin{aligned}
F_e &= pF_e^0 + (1-p)F_x^0, && (6.3)\\
\bar{F}_e &= \bar{p}\bar{F}_e^0 + (1-\bar{p})\bar{F}_x^0, && (6.4)\\
F_x &= \frac{1}{2}(1-p)F_e^0 + \frac{1}{2}(1+p)F_x^0, && (6.5)\\
\bar{F}_x &= \frac{1}{2}(1-\bar{p})\bar{F}_e^0 + \frac{1}{2}(1+\bar{p})\bar{F}_x^0, && (6.6)\\
& && (6.7)
\end{aligned}$$

where p, $\bar{p}$ are survival probabilities. In the normal-mass hierarchy case, they are defined as

$$\begin{aligned}
p &= \sin^2\theta_{13}, && (6.8)\\
\bar{p} &= \cos^2\theta_{12}\cos^2\theta_{13}. && (6.9)
\end{aligned}$$

On the other hand, in the inverted-mass hierarchy case, they are defined as

$$\begin{aligned}
p &= \sin^2\theta_{12}\cos^2\theta_{13}, && (6.10)\\
\bar{p} &= \sin^2\theta_{13}. && (6.11)
\end{aligned}$$

The values of the neutrino mixing angles θ_{12}, θ_{13} are assumed to be $\sin^2\theta_{12} = 2.97 \times 10^{-1}$ and $\sin^2\theta_{13} = 2.15 \times 10^{-2}$, adopted from Capozzi et al. (2017). We assume $F_x^0 = \bar{F}_x^0$ in this study.

Figure 6.9 shows the neutrino event rates per unit time, in which we integrate over energy, while the energy-dependent feature is discussed later. The distance is assumed to be 10 kpc. The event rate is inversely proportional to the square of distance, so the reader can easily estimate the event rate for desired distance. As shown in Fig. 6.9, the event rate clearly depends on the mass hierarchy, where the difference is more than double. In the case with the normal(inverted)-mass hierarchy, p ($\bar{p}$) becomes small, indicating that neutrinos (anti-neutrinos) undergo large flavor conversions. As shown in Sec. 6.2.3, both the energy luminosities and the average energies of ν_e and $\bar{\nu}_e$ are higher than those of ν_x at the source, indicating that the large flavor conversion results in reducing the ν_e and $\bar{\nu}_e$ number flux. As a result, the number of event rate at Super-K and DUNE becomes lower in the case of inverted-mass hierarchy and normal one, respectively. Hence, simultaneous observation of FBA neutrinos with Super-K and DUNE will provide a strong constraint on neutrino mass hierarchy.

The estimated event rate is found to be $o(10)\,\mathrm{s}^{-1}$ for the accretion rate of $\dot{M} \sim 10^{-3}\,M_\odot \cdot \mathrm{s}^{-1}$. This result also suggests that if we detect a large number of neutrinos in the very late phase, the detection will be an evidence for the occurrence of FBA neutrinos. It is also worthy to note that similar accretion

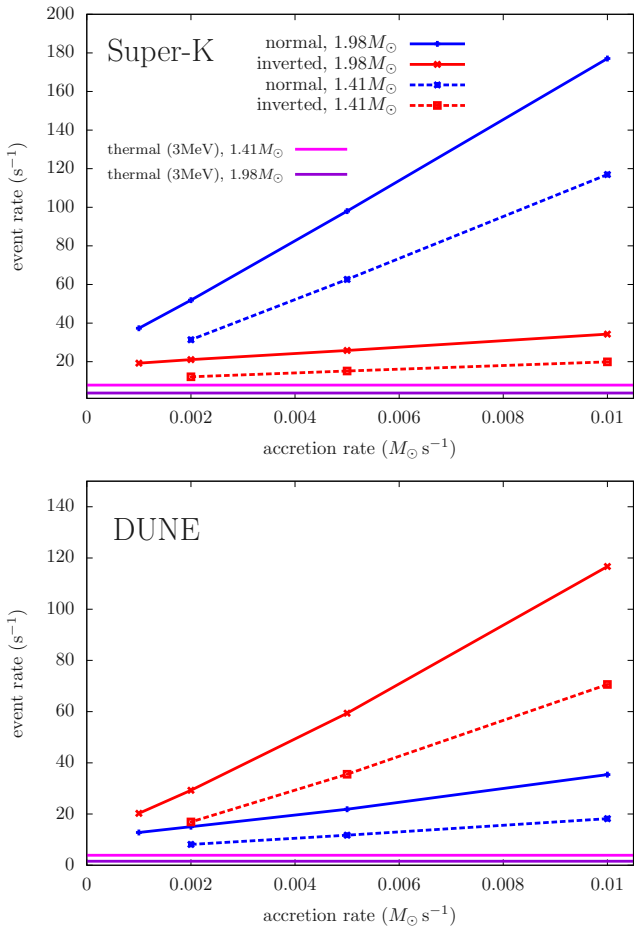

Figure 6.9: The event rate of neutrinos for the Super-K (top) and DUNE (bottom), assuming the distance of 10 kpc. The horizontal lines denote the event rates assuming thermal emission.

rates were found in previous studies Chan et al. (2018); Moriya et al. (2019); Janka et al. (2022) in the late phase.

We also find that the dependence of the event rate on the mass accretion rate hinges on the neutrino oscillation model. In the case of normal (inverted) mass hierarchy, the detection rate at Super-K (DUNE) becomes remarkably higher for higher mass accretion rates, whereas it is less sensitive to the accretion rate in the case of inverted (normal) one. This trend can also be understood through the species-dependent feature of neutrino emission at the CCSN source. As shown in Figs. 6.7 and 6.8, both the luminosity and the average energy of ν_x weakly depend on the mass accretion rate, and therefore the large flavor conversion makes the detection count at each detector less sensitive to the mass accretion rate. Nevertheless, the number of event count at each detector is remarkably higher than that emitted from the PNS. As a reference, we show the case for the neutrino signal without FBA but only with isothermal PNS of $T = 3$MeV in Fig. 6.9 (see below for the details). This figure illustrates that the detection rate of neutrinos from FBA is remarkably higher than in the case with thermal neutrinos from the PNS. It is also worthy to note that flavor dependent features would be resolved by using other reaction channels or joint analysis with other detectors (see, e.g. Beacom et al., 2002; Dasgupta & Beacom, 2011; Nagakura & Johns, 2021b), that would provide a key information to distinguish the neutrinos powered by FBA from those radiated only from the inner region of the PNS.

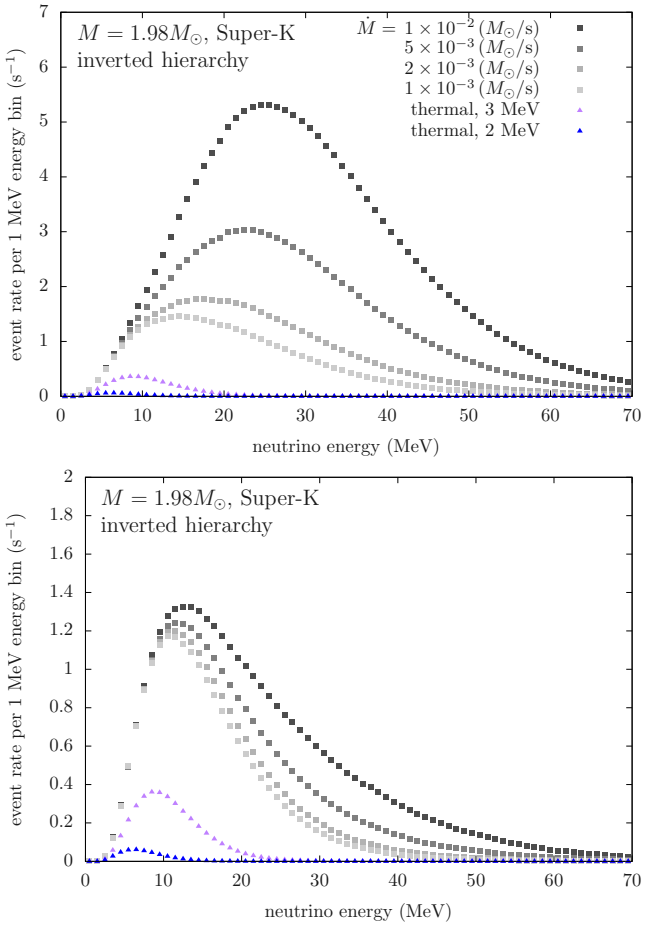

Figure 6.10: The event rate per 1 MeV energy bin for $M_{\rm PNS} = 1.98 M_\odot$ model, assuming the distance of 10 kpc. The top and bottom panel corresponds to normal and inverted mass hierarchy, respectively. The left panels are for Super-K and right panels are for DUNE. The gray plots corresponds to the numerical results, and the purple and blue plots corresponds to thermal values.

In order to see the energy spectrum of the detection, event rate per 1 MeV energy bin is shown in Figs. 6.10 and 6.11. As references, event rates for the the purely thermal emission (Fermi-Dirac distribution with zero chemical potential) with a PNS temperature of 2 and 3MeV are shown. The emission radius is assumed to be 11 km, and the gravitational redshift is taken into account for this estimation. For all simulated models, the event rates are orders of magnitude larger than the background event rates (see the latest experimental data of Super-K in Harada et al. (2023b). These figures illustrate that a large neutrino emission can be expected in the case of higher mass accretion rate. Another notable feature found in these figures is the high energy tail in each spectrum. Even in the case with the low mass accretion rate ($\dot{M} = 10^{-3}\,M_\odot \cdot \mathrm{s}^{-1}$), neutrinos with $\gtrsim$ 30MeV may be observed. It should be noted that these high energy neutrinos cannot be detected in the late phase ($t \gg 10$s) by thermal emission of PNS, unless the source is extremely close (Nakazato et al., 2022). If we detect them in real observations in the late phase, these neutrinos would be generated by FBA. We note that Figs. 6.10 and 6.11 show the energy event rate per second, indicating that the actual event count may be a factor of > 10 larger than this value (since we are currently considering in the phase

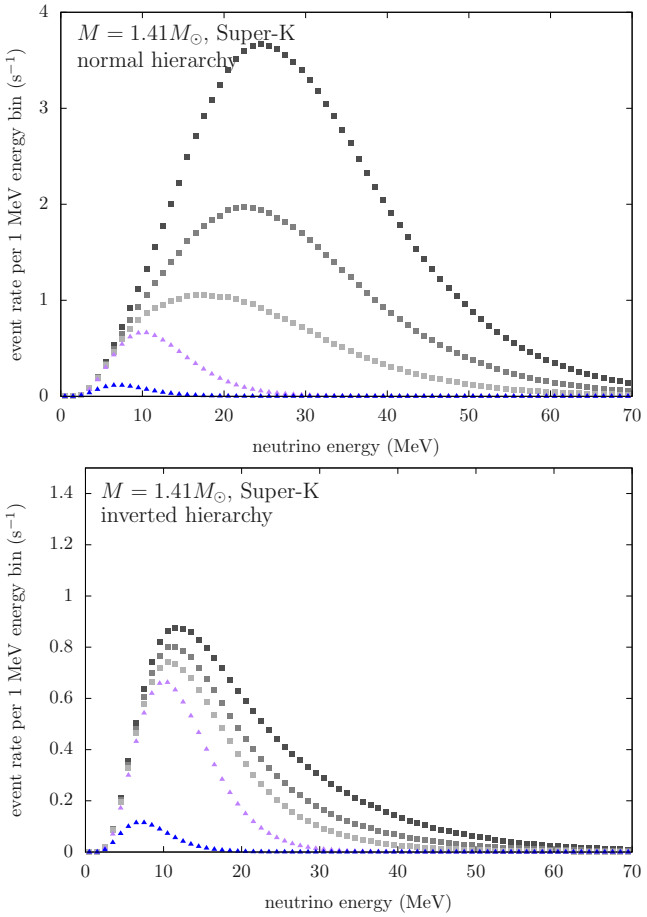

Figure 6.11: Same as figure 6.10, but for PNS mass $1.41M_\odot$ model.

of $>$ 10s after core bounce).

6.2.5 PNS Temperature Dependence

It is interesting to see how the neutrino signal from FBA depends on the PNS temperature. The increase of the PNS temperature would lead to higher neutrino emission inside the PNS, which potentially alters the neutrino signal. In this test, we employ the same numerical setup as that used in our model with the PNS mass of $1.98M_\odot$ and the accretion rate of $\dot{M} = 10^{-3}\,M_\odot \cdot \mathrm{s}^{-1}$ except for the PNS temperature. We consider two cases: 3 MeV and 4 MeV. We note that $T = 4$ MeV is too hot for PNS in the late phase which we consider in this study (> 10s after core bounce), but the result is still informative.

In Fig. 6.12, we show the energy spectrum of the neutrino event rate at Super-K and DUNE in the case of normal- and inverted mass hierarchy, respectively. We note that each oscillation model corresponds to the case having the lower number of event rate than the other mass hierarchy. As shown in these figures, even in these pessimistic cases, the PNS temperature does not affect the neutrino event rate. This result supports the claim that neutrinos from FBA overwhelm the thermal neutrinos from the PNS, unless they are extremely hot ($T \gg 4$ MeV).

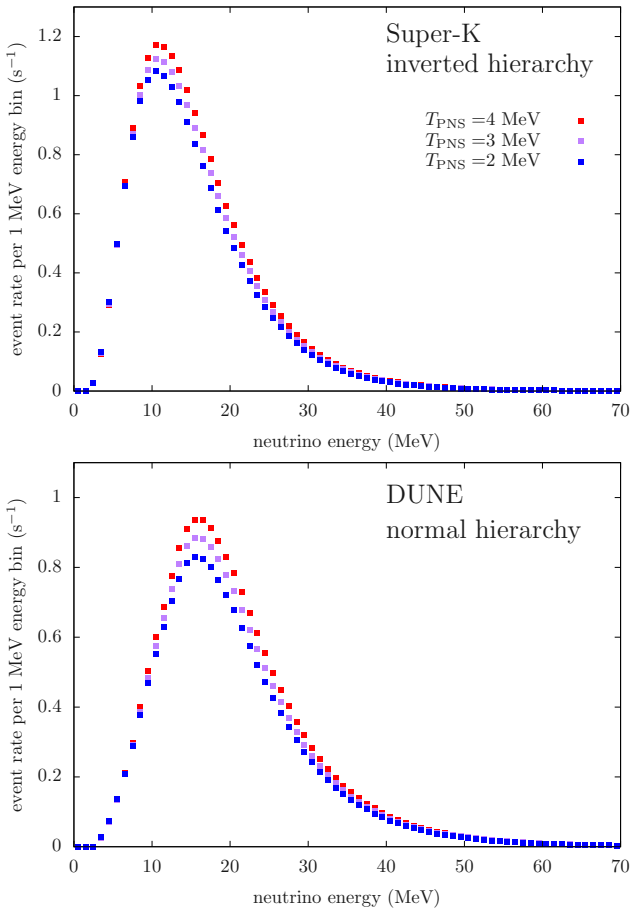

Figure 6.12: The event rate per 1 MeV energy bin for different PNS temperatures; 2 MeV (blue), 3 MeV (purple) and 4 MeV (red), assuming the distance of 10 kpc. Top panel is for Super-K and bottom panel for DUNE. Mass hierarchy is inverted (top) and normal (bottom). PNS mass is $M_{\rm PNS} = 1.98M_\odot$ and the accretion rate is $\dot{M} = 10^{-3}\,M_\odot \cdot \mathrm{s}^{-1}$.

6.3 Summary of Chapter 6

In this chapter we investigated neutrino emission from fallback mass accretion (FBA) onto PNS in the late phase of CCSN (> 10s) by using general relativistic neutrino radiation-hydrodynamic simulations with full Boltzmann neutrino transport. In our numerical simulations, we covered the very high density region ($> 10^{14}$g/cm^3) where we set a quasi-steady PNS structure as initial conditions. We changed the mass accretion rate in a parametric manner, and ran each simulation until the system settled to a quasi-steady state.

We found that a higher accretion rate and a higher PNS mass leads to a higher temperature in the transition layer from the PNS surface to the inner edge of FBA, where most of the neutrinos are radiated. As a result, both luminosities and mean energies of neutrinos tend to be higher with increasing mass accretion rates. On the other hand, the sensitivity of neutrino emission to the mass accretion rate hinge on neutrino species. Although ν_e and $\bar{\nu}_e$ emission strongly vary with the mass accretion rate, ν_x is less sensitive. This is due to the fact that ν_x is produced in the highest density region ($\rho \gtrsim 5 \times 10^{13}$g/cm^3), indicating that the impact of FBA on the temperature distribution tends to be weak. Nevertheless, both the luminosity and the mean energy of ν_x are remarkably higher than those estimated by standard PNS cooling models.

The present study supports the claim by Fryer (2009) that FBA can substantially change the neutrino emission in the late phase of CCSN. On the other hand, we also find that most of the neutrinos by FBA are produced in the high density region which the simulations of Fryer (2009) did not cover. As a result, the neutrino luminosities in his estimation are underestimated by a factor of $\gtrsim 5$, and this systematic error has a non-negligible effect to extract physical information from neutrino signal in real observations. We also find that the dominant weak processes for neutrino emission depends on species: electron-capture by free proton, positron-capture by free neutron, and nucleon–nucleon bremsstrahlung for ν_e, $\bar{\nu}_e$, and ν_x, respectively. Although the electron-positron pair can be a dominant emission process for ν_x in the low density region, the emissivity is too low to change the neutrino flux.

Based on the numerical results, we estimate the expected event rate for Super-K and DUNE with the adiabatic MSW oscillation model. One thing we need to stress is that neutrino emission from FBA has a rich flavor-dependent structure, indicating that the neutrino observation should depend on the neutrino oscillation model. Indeed, the difference of event rate between normal- and inverted mass hierarchy at each detector becomes more than double. In short, the detection rate tends to be smaller if the flavor conversion is strong. This is attributed to the fact that ν_x luminosity and mean energy are systematically lower than those of other species. Nevertheless, the event rate is the order of $o(100)\,\mathrm{s}^{-1}$ for the optical case with the highest accretion rate in both detectors, and still $o(10)\,\mathrm{s}^{-1}$ for the least optimal setting, which is much larger than the canonical PNS cooling model. We also provide energy-dependent features in the neutrino signal. We find that the peak energy of neutrino detection is remarkably higher than the thermal emission of PNS with ≤ 3MeV. Our result suggests that high energy neutrinos ($\gtrsim 30$MeV) may be observed in the late phase, which will be evidence that neutrinos are emitted by FBA.

As a final remark, we point out a couple of limitations in our study. First, we assumed spherical symmetry. In the multi-D case, the accretion shock wave may be unstable to non-radial perturbations (Blondin et al., 2003; Yamasaki & Yamada, 2005, 2006, 2007; Foglizzo et al., 2007), and FBA is usually accompanied by turbulence (Vartanyan et al., 2022), which potentially leads to temporal variations in the neutrino signal. On the other hand, it would be hard to resolve the temporal variation by the current- and even future-planned neutrino detectors, unless the CCSN source is very close (see, e.g., Nagakura et al., 2021). This is because the neutrino luminosity is very low in the late phase, and the temporal variation would be smeared out by noise. It should be mentioned, however, that the thermodynamical properties in the post-shock flow may be influenced by the shock instability, which may change the neutrino signal. We postpone this detailed study to future work. Second, the number of models simulated in this study is limited due to the computational cost. It should be stressed that high spatial resolution is required to resolve both matter and neutrino distributions around the surface

of the PNS, implying that the time step is severely limited by the Courant condition. To prepare for future observations, however, we need a systematic study by covering wider ranges of PNS masses and mass accretion rates than those studied in this study . The EOS dependence is also worthy of investigation.

Numerical simulations are not suitable to carry out such a systematic study, and therefore we are planning to take a semi-analytic approach to address this issue. If we cover full parameter space, we may be able to infer the EOS parameters or accretion rates from the future neutrino detection. An analysis pipeline based on a Bayesian approach has been already developed for thermal neutrino detection (Harada et al., 2023a). The results with similar approach will be reported elsewhere.

Chapter 7

Collective Neutrino Oscillation inside CCSN

In the theoretical modelling of CCSNe, neutrino oscillation is usually neglected because it was expected that the dense matter is likely to suppress it (details are explained later). However, inside CCSN core, neutrino number density is typically larger than the electron number density, which makes the neutrino oscillation due to neutrino self-interaction to take place without hindered by the matter potential. This is called "collective neutrino oscillation", and recently getting great attention. In this chapter, the occurrence of collective neutrino oscillation inside CCSN is discussed. Section 7.1 reviews the basics of the neutrino oscillation. Section 7.2 explains the method of the linear stability analysis (LSA) used for this study. Section 7.3 shows the results of the LSA performed for 2D CCSN simulation.

7.1 Introduction to Neutrino Oscillation

Before going into the collective neutrino oscillation, let us first review the basics of neutrino oscillation in this section. Neutrino oscillation occurs due to the fact that the neutrino mass eigenstates and the flavor eigenstates are different. Derivations presented below follows Sasaki (2019); Morinaga (2021).

7.1.1 Vacuum Neutrino Oscillation

General Expression

We start with the vacuum neutrino oscillation. Since it is the simplest, it is instructive to understand the basics of the neutrino oscillation. The starting point is the Schrödinger equation

$$i\frac{d}{dt}\left|\psi(t)\right\rangle = \hat{H}\left|\psi(t)\right\rangle, \tag{7.1}$$

where $|\psi(t)\rangle$, $\hat{H}$ denote the quantum state at time t and the Hamiltonian, respectively. In order to discuss neutrino oscillation, it is useful to introduce Liuville-von Neumann equation with respect to the density operator $\hat{\rho}(t) \equiv |\psi(t)\rangle \langle\psi(t)|$;

$$i\frac{d}{dt}\hat{\rho}(t) = \left[\hat{H}, \hat{\rho}(t)\right], \tag{7.2}$$

The vacuum Hamiltonian for free neutrino can be written as

$$\hat{H}_0 = \int \frac{d^3p}{(2\pi)^3}\sqrt{p^2 + m_i^2}\hat{a}_i^\dagger(p)\hat{a}_i(p), \tag{7.3}$$

where $\hat{a}_i^\dagger(p)$ and $\hat{a}_i(p)$ are the creation and annihilation operators. The subscript i denote the mass eigenstate. They satisfies the anti-commutation relationship

$$\left\{\hat{a}_i(q), \hat{a}_i^\dagger(p)\right\} = (2\pi)^3\delta^3(p-q)\delta_{ij}. \tag{7.4}$$

Since the neutrinos can be considered as the ultrarelativistic particles, the square-root part inside the Hamiltonian can be decomposed, leading to following representation;

$$\hat{H}_0 \sim \int \frac{d^3p}{(2\pi)^3} p\hat{a}_i^\dagger(p)\hat{a}_i(p) + \int \frac{d^3p}{(2\pi)^3}\frac{m_i^2}{2p}\hat{a}_i^\dagger(p)\hat{a}_i(p). \tag{7.5}$$

The first term does not have effect on the neutrino oscillation, and dropped in the following discussions.

The operators for the flavor eigenstates $\hat{a}_\alpha(p)$, $\hat{a}_\alpha^\dagger(p)$ are introduced, where the relationship with the mass eigenstates is given by following equations;

$$\hat{a}_i(p) = U_{\alpha i}^*\hat{a}_\alpha(p), \tag{7.6}$$

$$\hat{a}_i^\dagger(p) = U_{\alpha i}\hat{a}_\alpha^\dagger(p). \tag{7.7}$$

The vacuum Hamiltonian can be written with respect to the

$$\hat{H}_0 = \hat{\Omega} \equiv \int \frac{d^3p}{(2\pi)^3}\hat{a}_\alpha(p)\Omega_{\alpha\beta}\hat{a}_\beta^\dagger(p), \tag{7.8}$$

where

$$\Omega_{\alpha\beta} \equiv U_{\alpha i}\frac{m_i^2}{2p}U_{\beta i}^*. \tag{7.9}$$

Note that if the same indices appear in the same term, the sum is taken. For the discussion of the neutrino oscillation, one-body neutrino density matrix $\rho_{\alpha\beta}(t,p)$ is introduced, which is defined as follows;

$$\langle\hat{a}_\beta^\dagger(q)\hat{a}_\alpha(p)\rangle = \mathrm{tr}\left[\hat{a}_\beta^\dagger(q)\hat{a}_\alpha(p)\hat{\rho}(t)\right] = (2\pi)^3\delta^3(p-q)\rho_{\alpha\beta}(t,p) \tag{7.10}$$

Note that the diagonal component of $\rho_{\alpha\beta}$ can be considered to be related to the neutrino number density n_{ν_α} as

$$n_{\nu_\alpha}(t) = \int \frac{d^3p}{(2\pi)^3}\rho_{\alpha\alpha}(t,p) \tag{7.11}$$

By using the Liouville-von Neumann equation, the time evolution of the one-body density matrix can be given as follows

$$i\frac{d}{dt}\langle\hat{a}_\beta^\dagger(q)\hat{a}_\alpha(p)\rangle = \Omega_{\alpha k}(p)\langle\hat{a}_\beta^\dagger(q)\hat{a}_k(p)\rangle - \langle\hat{a}_k^\dagger(q)\hat{a}_\alpha(p)\rangle\Omega_{k\beta}(p). \tag{7.12}$$

Hence

$$i\frac{d}{dt}\rho_{\alpha\beta}(t,p) = \left[\Omega(p), \rho(t,p)\right]_{\alpha\beta}. \tag{7.13}$$

Two-flavor Example

As mentioned earlier, two-flavor framework is used; μ-type and τ-type neutrinos are treated as ν_x. By explicitly writing down the conversion matrix by introducing the mixing angle θ_{12}, the mass and flavor eigenstates are related as

$$\begin{pmatrix}\nu_e\\ \nu_x\end{pmatrix}\begin{pmatrix}\cos\theta_{12} & \sin\theta_{12}\\ -\sin\theta_{12} & \cos\theta_{12}\end{pmatrix}\begin{pmatrix}\nu_1\\ \nu_2\end{pmatrix} \tag{7.14}$$

By using above relationship, the vacuum Hamiltonian can be explicitly written down as

$$\Omega = \frac{m_1^2 + m_2^2}{4E}\begin{pmatrix}1 & 0\\ 0 & 1\end{pmatrix} + \frac{\Delta m^2}{4E}\begin{pmatrix}-\cos 2\theta_{12} & \sin 2\theta_{12}\\ \sin 2\theta_{12} & \cos 2\theta_{12}\end{pmatrix}, \tag{7.15}$$

where $\Delta m^2 \equiv m_2^2 - m_1^2$. The second term has off-diagonal components, and it leads to the neutrino oscillation. From the Liuville-con Neumann equation, the time dependence of the density matrix is given as

$$\rho(t, E) = e^{-i\Omega(E)t}\rho(0, E)e^{i\Omega(E)t}. \tag{7.16}$$

As a result, the neutrino density matrix "oscillate", because it can be written as the trigonometric function with respect to time. Above simple example would give the basic idea of neutrino oscillation.

7.1.2 Matter Effect

In a presence of surrounding matter, neutrino scatterings by the charged leptons change the effective mass of neutrinos, and can change the behavior of the neutrino oscillation. This is called the Mikheyev–Smirnov–Wolfenstein (MSW) effect. This effect can be taken into account by adding a additional "matter potential" to the Scrödinger equation. If the existence of muon and tauon are ignored, the matter potential can be written with the number density of electron as (Sasaki, 2019; Morinaga, 2021);

$$H_{\rm mat} = \sqrt{2}G_F n_e \begin{pmatrix}1 & 0 & 0\\ 0 & 0 & 0\\ 0 & 0 & 0\end{pmatrix}. \tag{7.17}$$

Since the neutrino oscillation is associated with the off-diagonal components, large matter potential has negative impact on the occurrence of neutrino oscillation. However, if the value of the matter potential coincides with the vacuum term, the diagonal component vanishes and the neutrino oscillation is facilitated. This is called the MSW resonance, and induces the neutrino oscillation as well.

7.2 Collective Neutrino Oscillation and the Linear Stability Analysis

As repeatedly mentioned, the focus of this study is the collective neutrino oscillation, induced by neutrino self-interaction. Especially, the linear stability analysis (LSA) is performed for CCSN simulation result, which is to analyze whether the given state is unstable to flavor conversion. It also provides the linear growth rate, which gives us the idea how fast the flavor conversion evolves. The advantage is that it is easy to implement, and computationally cheap. The drawback is that it does not provide the asymptotic state after the flavor conversion, which requires to follow the nonlinear evolution by directly solving the quantum kinetic equation (QKE), as performed by several studies (Johns & Xiong, 2022; Padilla-Gay et al., 2022; Zaizen & Nagakura, 2022; Hansen et al., 2022; Kato et al., 2023).

7.2.1 Linearizing the QKE

The starting point is the QKE

$$iv^\mu \partial_\mu \rho = [H, \rho] + iC, \tag{7.18}$$

where H and C denote the Hamiltonian and the collision terms, respectively. The components of the density matrix is defined as

$$\rho \equiv \begin{pmatrix}f_{\nu_e} & S_{ex}\\ S_{xe} & f_{\nu_x}\end{pmatrix}. \tag{7.19}$$

The interacting Hamiltonian can be expressed as the sum of vacuum, matter, and neutrino self-interaction terms as follows;

$$H_{\rm vac} = \frac{M^2}{2E}, \tag{7.20}$$

$$H_{\rm mat} = \sqrt{2}G_F v_\mu {\rm diag}(j_e^\mu(x), j_x^\mu(x)), \tag{7.21}$$

$$H_\nu = \sqrt{2}G_F v^\mu \int dP' \rho(x,P') v'_\mu, \tag{7.22}$$

where M^2, $j_\alpha^\mu(x)$ and G_F are the neutrino mass-squared matrix, the lepton number four-currents, and the Fermi constant, respectively. The integral over momentum space is expressed as

$$\int dP \equiv \int_{-\infty}^{\infty} \frac{E^2 dE}{2\pi^2} \int \frac{d\Omega_p}{4\pi}, \tag{7.23}$$

where E and Ω_p are the energy and solid angle in momentum space, respectively. Following the common practice, the negative energy corresponds to antineutrinos.

By assuming the relaxation approximation (Johns, 2023), the collision terms can be expressed as

$$C(x,P) = \frac{1}{2}\{{\rm diag}(\Gamma_{\nu_e}(x,P), \Gamma_{\nu_x}(x,P)), \rho_{\rm eq} - \rho\}, \tag{7.24}$$

where $\Gamma_{\nu_\alpha}(x,P)$ and $\rho_{\rm eq}$ stand for the collision rates and the density matrix for the equilibrium state, respectively.

By assuming that the off-diagonal components of the density matrix are initially smaller than the diagonal components, as $S_{ex} \ll f$, the QKE can be linearized. Off-diagonal component becomes

$$\begin{aligned} v^\mu(i\partial_\mu - \Lambda_{0e\mu} + \Lambda_{0x\mu})S_{ex} &+ \frac{1}{2E}\sum_{z=e,x}(M^2_{ez}S_{zx} - S_{ez}M^2_{zx}) \\ &+ (f_{\nu_e} - f_{\nu_x})\sqrt{2}G_F \int dP' v^\mu v'_\mu S_{ex}(x,P') + i\Gamma_{ex}S_{ex} = 0, \end{aligned} \tag{7.25}$$

where $\Lambda_{0\alpha}$ is defined as

$$\Lambda^\mu_{0\alpha} \equiv \sqrt{2}G_F[j^\mu_\alpha(x) + \int {\rm d}P f_{\nu_\alpha}(x,P)v^\mu]. \tag{7.26}$$

and

$$\Gamma_{ex}(E) \equiv [\Gamma_e(E) + \Gamma_x(E)]/2. \tag{7.27}$$

For the stability analysis, plane-wave ansatz is assumed for the off-diagonal component as

$$S_{ex}(x,P) = \tilde{S}_{ex}(x,k)e^{ik^\mu x_\mu}, \tag{7.28}$$

where $k \equiv (\omega, \vec{k})$ is the four-wave vector. Furthermore, the vacuum and the matter Hamiltonian are ignored in this study because they can be considered to be small in the regime where the collective flavor instability takes place.

The linearized equation can be simplified in the following form

$$\Pi^{\mu\nu}_{ex}(k)a_\nu(k) = 0, \tag{7.29}$$

by introducing a matrix Π_{ex} and a vector $a(k)$ as follows,

$$\Pi^{\mu\nu}_{ex}(k) \equiv \eta^{\mu\nu} + \sqrt{2}G_F \int dP \frac{(f_{\nu_e} - f_{\nu_x})v^\mu v^\nu}{v^\lambda(k_\lambda - \Lambda_{0e\lambda} + \Lambda_{0x\lambda}) + i\Gamma_{ex}}, \tag{7.30}$$

$$a^\mu(k) \equiv \sqrt{2} G_F \int \mathrm{d}P \tilde{S}_{ex}(k, P) v^\mu. \tag{7.31}$$

The nontrivial solution exists if and only if the following relation is satisfied:

$$\det \Pi_{ex}(k) = 0. \tag{7.32}$$

By solving the equation 7.32 with respect to ω, it is possible to know whether the state is unstable to flavor conversion or not; if the resultant ω has a negative imaginary part, the $S_{ex}(x, P)$ will grow exponentially and otherwise it decays.

In this thesis, we intend to perform systematic study of flavor instabilities for the entire computational domain and every time step of CCSN simulation. For this purpose, finding the root using equation 7.32 is still computationally expensive. We will separate flavor instability into two kinds, namely fast flavor instability (FFI), and the collisional flavor instability (CFI). The former is induced by the angular crossing in the momentum space, and the latter is induced by the collision terms. The procedures of LSA for FFI and CFI are discussed in the following subsections.

7.2.2 Fast Flavor Instability

The existence of FFI was first recognized in Sawyer (2005), and many theoretical studies have been performed (Tamborra & Shalgar, 2021). As proven in Morinaga (2021), the occurrence of FFI is known to be equivalent with the existence of neutrino flavor lepton number (NFLN) crossing, which is defined as follows. The difference between the NFLN angular distribution for ν_α and ν_β is defined as

$$G_{\alpha\beta} \equiv \int_\infty^\infty \frac{E^2 dE}{2\pi^2} (f_{\nu_\alpha} - f_{\nu_\beta}). \tag{7.33}$$

The NFLN crossing is that G have positive and negative values. Since the three-species assumption is imposed, the existence of NFLN crossing is equivalent to that of the electron lepton number (ELN) crossing.

For the LSA, we would like to derive a formula for estimating the linear growth rates. The rigorous formulae for a general neutrino distribution is impossible, hence we consider a simple example. We first consider a so-called two-beam model, where two collimated beams of ν_e and $\bar{\nu}_e$ cross. In this case, the ELN angular distribution with respect to the velocity v is given as

$$G(v) = 4\pi(\mathscr{G}_{\nu_e} \delta(v - v_{\nu_e}) + \mathscr{G}_{\bar{\nu}_e} \delta(v - v_{\bar{\nu}_e})), \tag{7.34}$$

where $\mathscr{G}_{\nu_e}$ and $\mathscr{G}_{\bar{\nu}_e}$ are coefficients and the neutrino flowing direction is v_{ν_e} and $v_{\bar{\nu}_e}$, respectively. In this case, the growth rate is given as

$$\sigma = (1 - v_{\nu_e \mu} v^\mu_{\bar{\nu}_e}) \mathrm{Re} \sqrt{-\mathscr{G}_{\nu_e} \mathscr{G}_{\bar{\nu}_e}}. \tag{7.35}$$

The factor $v_{\nu_e \mu} v^\mu_{\bar{\nu}_e}$ makes the growth rate depends on the crossing angle; it is maximized in the head-on case and becomes zero in the parallel case. The important part is the square-root part, which determines the order of the growth rate.

Above example naturally suggests that in general case, the growth rate can be roughly estimated as

$$\sigma \equiv \sqrt{-\left(\int_{\Delta G > 0} \frac{d\Omega}{4\pi} \Delta G\right) \left(\int_{\Delta G < 0} \frac{d\Omega}{4\pi} \Delta G\right)}, \tag{7.36}$$

where

$$\Delta G = \frac{\sqrt{2} G_F}{2\pi^2} \int (f_{\nu_e} - f_{\bar{\nu}_e}) \nu^2 d\nu. \tag{7.37}$$

The performance of the equation 7.36 is verified in Morinaga et al. (2020) and turned out that it is not bad.

7.2.3 Collisional Flavor Instability

Collisional flavor instability (CFI) is induced by the collision terms. The analytical formulae for LSA of CFI was derived in Liu et al. (2023), and the overview is showed below. The matrix $\Pi^{\mu\nu}$ given in equation 7.30 is recalled by explicitly rewriting the tensor $v^\mu v^\nu$;

$$\begin{aligned}\Pi^{\mu\nu}_{ex}(k) &= \eta^{\mu\nu} + \sqrt{2}G_F \int_{-\infty}^{\infty} \frac{E^2 dE}{2\pi^2} \int \frac{d\Omega_p}{4\pi} \frac{f_{\nu_e}(E,v) - f_{\nu_x}(E,v)}{\omega - v^\mu k_\mu + \mathrm{i}\Gamma_{ex}(E)} \\ &\times \begin{pmatrix} 1 & \cos\theta_\nu & \sin\theta_\nu\cos\phi_\nu & \sin\theta_\nu\sin\phi_\nu \\ \cos\theta_\nu & \cos^2\theta_\nu & \sin\theta_\nu\cos\theta_\nu\cos\phi_\nu & \sin\theta_\nu\cos\theta_\nu\sin\phi_\nu \\ \sin\theta_\nu\cos\phi_\nu & \sin\theta_\nu\cos\theta_\nu\cos\phi_\nu & \sin^2\theta_\nu\cos^2\phi_\nu & \sin^2\theta_\nu\cos\phi_\nu\cos\phi_\nu \\ \sin\theta_\nu\sin\phi_\nu & \sin\theta_\nu\cos\theta_\nu\sin\phi_\nu & \sin^2\theta_\nu\sin\phi_\nu\cos\phi_\nu & \sin^2\theta_\nu\sin^2\phi_\nu \end{pmatrix}. \end{aligned} \tag{7.38}$$

In order to simplify the equation and derive the analytical formulae to evaluate the CFI growth rate, angular distribution is assumed to be isotropic. Under this assumption, the only angular-dependent part is the tensor $v^\mu v^\nu$. As shown above, it is a collection of trigonometric functions, and the angular integration can be performed and only the diagonal components remain.

As a result, equation 7.32 is simplified as

$$I = \sqrt{2}G_F \int_{-\infty}^{\infty} \frac{E^2 \mathrm{d}E}{2\pi^2} \frac{f_{\nu_e}(E) - f_{\nu_x}(E)}{\omega + \mathrm{i}\Gamma_{ex}(E)} = -1, 3. \tag{7.39}$$

Note that $I = -1$ corresponds to the time components and $I = 3$ corresponds to three spatial components that are degenerate. Above equation is further simplified by assuming the energy distribution. By assuming the monochromatic distribution

$$f_{\nu_e}(E) - f_{\nu_x}(E) = \frac{2\pi^2}{\sqrt{2}G_F E^2}[\mathfrak{g}\delta(E-\epsilon) - \bar{\mathfrak{g}}\delta(E+\bar{\epsilon})], \tag{7.40}$$

where $\mathfrak{g}$, $\bar{\mathfrak{g}}$ are defined as

$$\mathfrak{g} \equiv n_{\nu_e} - n_{\nu_x},\ \bar{\mathfrak{g}} \equiv n_{\bar{\nu}_e} - n_{\bar{\nu}_x}. \tag{7.41}$$

With this assumption, the above equation becomes

$$\frac{\mathfrak{g}}{\omega + \mathrm{i}\Gamma} - \frac{\bar{\mathfrak{g}}}{\omega + \mathrm{i}\bar{\Gamma}} = -1, 3, \tag{7.42}$$

The solution for $I = -1$, called the isotropy-preserving branch, is given as

$$\omega^{\mathrm{pres}}_{\pm} = -A - i\gamma \pm \sqrt{A^2 - \alpha^2 + 2iG\alpha}, \tag{7.43}$$

and the solution for $I = 3$, called the isotropy-breaking branch, is given as

$$\omega^{\mathrm{break}}_{\pm} = -\frac{A}{3} - i\gamma \pm \sqrt{\left(\frac{A}{3}\right)^2 - \alpha^2 - \frac{2}{3}iG\alpha}. \tag{7.44}$$

Symbols G, A, γ, α are defined as

$$G \equiv \frac{\mathfrak{g} + \bar{\mathfrak{g}}}{2},\ A \equiv \frac{\mathfrak{g} - \bar{\mathfrak{g}}}{2},\ \gamma \equiv \frac{\Gamma + \bar{\Gamma}}{2},\ \alpha \equiv \frac{\Gamma - \bar{\Gamma}}{2}, \tag{7.45}$$

where the collision rates Γ, $\bar{\Gamma}$ are given as

$$\Gamma \equiv \frac{\Gamma_e + \Gamma_x}{2},\ \bar{\Gamma} \equiv \frac{\bar{\Gamma}_e + \bar{\Gamma}_x}{2}, \tag{7.46}$$

and n_{ν_i} and Γ_i are the number densities, and the energy-integrated collision rates, respectively. They are expressed as follows:

$$n_i = \sqrt{2} G_F \int \frac{E^2 dE}{2\pi^2} f(E), \tag{7.47}$$

$$\Gamma_i \equiv \sqrt{2} G_F \int \frac{E^2 dE}{2\pi^2} \Gamma(E) f_i(E), \tag{7.48}$$

with $\Gamma(E)$ being the energy-dependent emission/absorption rates.

CFI occurs when the imaginary part of ω is positive. Eqs. 7.43 and 7.44 are obtained under the assumption that the neutrino distribution is isotropic and monochromatic. In Liu et al. (2023), it was found that they are reasonable approximations if the average energies of neutrino and anti-neutrino are plugged in ϵ and $\bar{\epsilon}$, respectively, as long as there is no NFLN crossing.

In this study, we define the CFI growth rate as

$$\sigma_{\rm CFI} \equiv \max\left(\mathrm{Im}(\omega_\pm^{\rm pres}), \mathrm{Im}(\omega_\pm^{\rm break})\right). \tag{7.49}$$

The growth rate can be calculated by using the number densities (Eq. 7.47) and the energy-integrated collision rates Eq. 7.48), which are provided by the CCSN model.

It is useful to consider the following limits:

$$\max\left(\mathrm{Im}\,\omega_\pm^{\rm pres}\right) = \begin{cases} -\gamma + \frac{|G\alpha|}{|A|}, & (A^2 \gg |G\alpha|), \\ -\gamma + \sqrt{|G\alpha|}, & (A^2 \ll |G\alpha|), \end{cases} \tag{7.50}$$

for the isotropy-preserving branch and

$$\max\left(\mathrm{Im}\,\omega_\pm^{\rm break}\right) = \begin{cases} -\gamma + \frac{|G\alpha|}{|A|}, & (A^2 \gg |G\alpha|), \\ -\gamma + \frac{\sqrt{|G\alpha|}}{\sqrt{3}}, & (A^2 \ll |G\alpha|), \end{cases} \tag{7.51}$$

for the isotropy-breaking branch.

In the typical CCSN situation, $A^2 \gg |G\alpha|$ is satisfied because $A \sim G \gg \alpha$ (Liu et al., 2023). However, if n_{ν_e} and $n_{\bar{\nu}_e}$ are very close to each other, A becomes small and the lower case ($A^2 \ll |G\alpha|$) applies. Then the growth rate is $\sim \sqrt{G\alpha}$, which is larger than the ordinary CFI growth rate of $\sim G|\alpha|/A$. This is called the resonance-like CFI (Lin & Duan, 2023; Liu et al., 2023; Xiong et al., 2023a). In contrast, we will refer to the CFI in the regime of $A^2 \gg |G\alpha|$ as the "non-resonance" CFI hereafter.

7.3 Analysis of FFI and CFI

We perform post-process analysis of CFI and FFI for 2D CCSN simulation performed with the Boltzmann neutrino transport. The model setup is provided in section 7.3.1. The overall properties are shown in section 7.3.2, and the origin of CFI and FFI are independently discussed in sections 7.3.3, 7.3.4. Section 7.3.5 shows the comparison between CFI and FFI.

7.3.1 CCSN Model

We give here only basic information on the CCSN model we employ in this study. It is a result of the 2D CCSN simulation under axisymmetry for the progenitor with the zero-age main sequence mass of $11.2 M_\odot$ (Woosley et al., 2002). The Boltzmann equations are faithfully solved for three neutrino species (ν_e, $\bar{\nu}_e$ and ν_x) by discretizing the entire phase space, i.e., by the S_N method. Newtonian hydrodynamics equations are solved simultaneously with the feedback from/to neutrinos fully taken

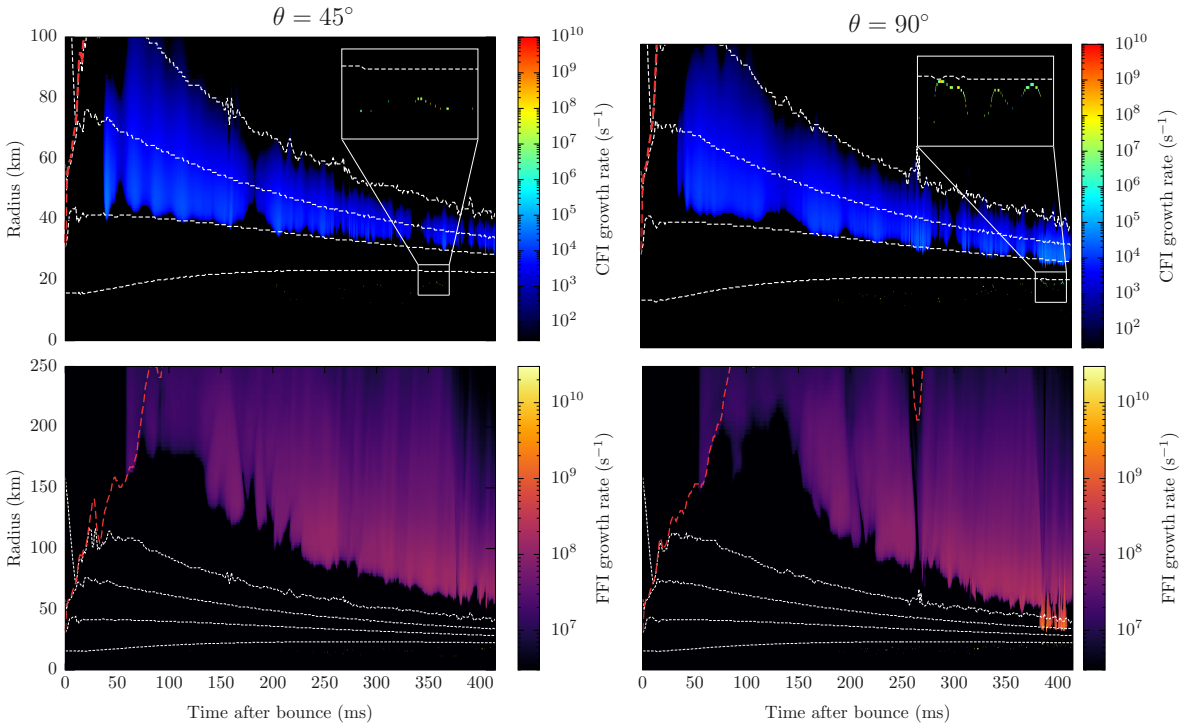

Figure 7.1: Time-radius map of the growth rate of CFI (top) and FFI (bottom) for the angle $\theta = 45°$ and 90°. White broken lines, from top to bottom, denote the radius for the density 10^{10}, 10^{11}, 10^{12} and $10^{13}\,\mathrm{g\,cm^{-3}}$, respectively. Red broken line denote the shock radius.

into account. The radial range of $[0 : 5000]\,\mathrm{km}$ is divided into 384 grid points, and the zenith angle $\theta \in [0 : \pi]$ is divided into 128 grid points. The energy range of $[0 : 300]\,\mathrm{MeV}$ is divided into 20 logarithmically spaced grid points. The zenith angle in momentum space $\theta_\nu \in [0 : \pi]$ and the azimuth angle $\phi_\nu \in [0 : 2\pi]$ are divided into 10, and 6 grid points, respectively. The neutrino-matter interactions are based on the so-called standard set (Bruenn, 1985) with a few modifications; the inelastic scattering off electrons and the nucleon–nucleon bremsstrahlung (Friman & Maxwell, 1979) are implemented. Note that the emission/absorption rates in Eq. 7.48 for the CFI growth rates are the same as those employed in the simulation. The details of the numerical code are described in the series of papers Nagakura et al. (2014, 2017, 2019). In this simulation, Lattimer-Swesty equation of state (Lattimer & Swesty, 1991) with the incompressibility parameter $K = 220\mathrm{MeV}$ is employed. The simulation was conducted up to $\sim 400\,\mathrm{ms}$ after bounce when we observed a successful explosion with the maximum shock radius reaching 1000 km in $t \sim 400\,\mathrm{ms}$ after bounce. See Harada et al. (2020) for the details of this simulation.

7.3.2 Overall Properties

Top panels of Fig. 7.1 shows the time-radius maps of CFI growth rate at $\theta = 45°$ and 90°. CFI is expected to occur in the region with a bright color. In fact, the black regions in the plots have growth rates smaller than $10^{-9}\,\mathrm{cm^{-1}}$, and we do not think CFI is important there. It is clear at both angles (and actually at all angles as shown in Fig. 7.2) that a CFI region appears at $t \sim 50\,\mathrm{ms}$ for the first time and continues to exist later on. This unstable region moves to smaller radii as the PNS contracts. It roughly corresponds to the region with $10^{10} \lesssim \rho \lesssim 10^{12}\,\mathrm{g\,cm^{-3}}$, similar density range as reported

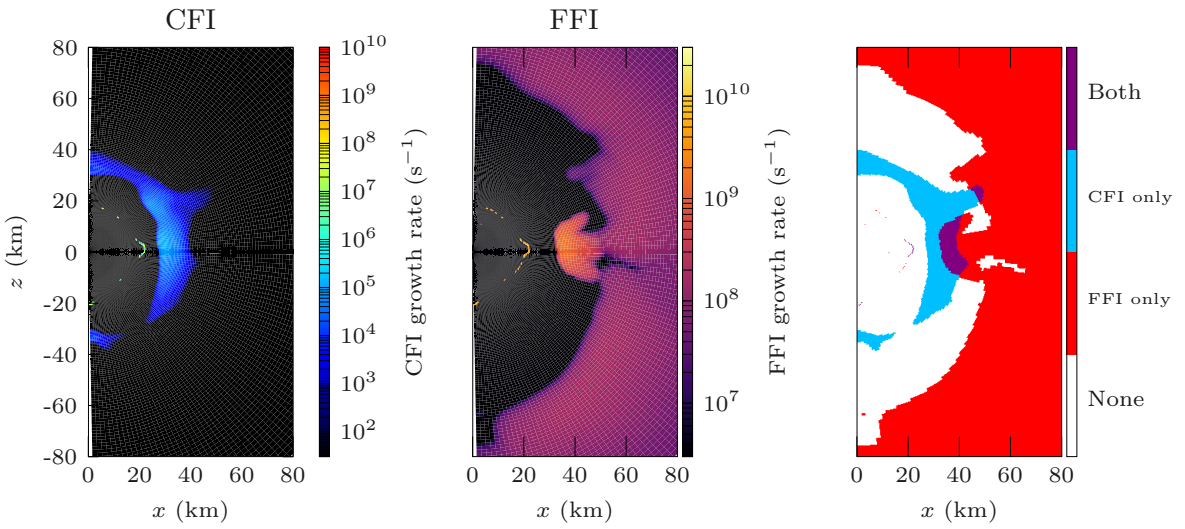

Figure 7.2: Meridian map of CFI growth rate (left), FFI growth rate (middle), and the dominant instability (right) at $t = 404$ms after bounce.

in a 1D study (Liu et al., 2023). In the 2D case, however, the radial extent of the region changes rather rapidly in time whereas such time variations were absent in the 1D model. This is due to the turbulence that occurs commonly on the multi-dimensional models.

A closer inspection of the plots reveals another CFI region deeper inside, $r \sim 20\,\mathrm{km}$, at later times, $t \gtrsim 200\,\mathrm{ms}$, (see the magnified figures). It is very narrow but has greater growth rates than the region mentioned above and was not found in the 1D model. In fact, this corresponds to the resonance-like CFI, a feature unique to multi-dimensional models, as we discuss later.

For comparison we present the time-radius maps of the FFI growth rate in the bottom panels of Fig. 7.1. The reddish region is unstable to FFI this time. Note that the radial range and the color scale are different between top and bottom panels. The four dashed lines that show the locations of $\rho = 10^{10}$, 10^{11}, 10^{12}, $10^{13}\,\mathrm{g\,cm^{-3}}$ will help the correspondence between the plots. There is a wide FFI region with located at larger radii much outside than the CFI region in general. In the late phase, $t \gtrsim 400\,\mathrm{ms}$ however, the two regions are partially overlapped with each other at $\theta = 90°$. Note that we analyze CFI and FFI independently, assuming that the latter is absent in the analysis of the former.

The spatial extents of the CFI and FFI regions in the meridian section are shown in Fig. 7.2 at $t = 404\,\mathrm{ms}$ after bounce. The resonance-like CFI occurs sporadically at $r \sim 20\,\mathrm{km}$ whereas the non-resonance CFI regions prevail at $30 \lesssim r \lesssim 40\,\mathrm{km}$. The FFI region is extended at even larger radii, $r \gtrsim 50\,\mathrm{km}$, but also appears at almost the same positions as the resonance-like CFI. Although the non-resonance CFI region is mostly separated from the FFI region, there are some overlaps (see the rightmost panel of Fig. 7.2). It is apparent that it occurs in a convective eddy. The growth rates of CFI and FFI tend to be higher around the equator than near the poles. This comes from the stronger $\bar{\nu}_e$ emission in the lower latitudes, induced by the large-scale fluid motion. The morphology of fluid motion is known to be qualitatively different between 2D and 3D (Couch, 2013), and the degree of asymmetry may be exaggerated in this study. However, the qualitative trend will be unchanged in 3D.

In the following subsections 7.3.3 and 7.3.4, we look into CFI and FFI individually. The growth rates of CFI and FFI are compared in subsection 7.3.5.

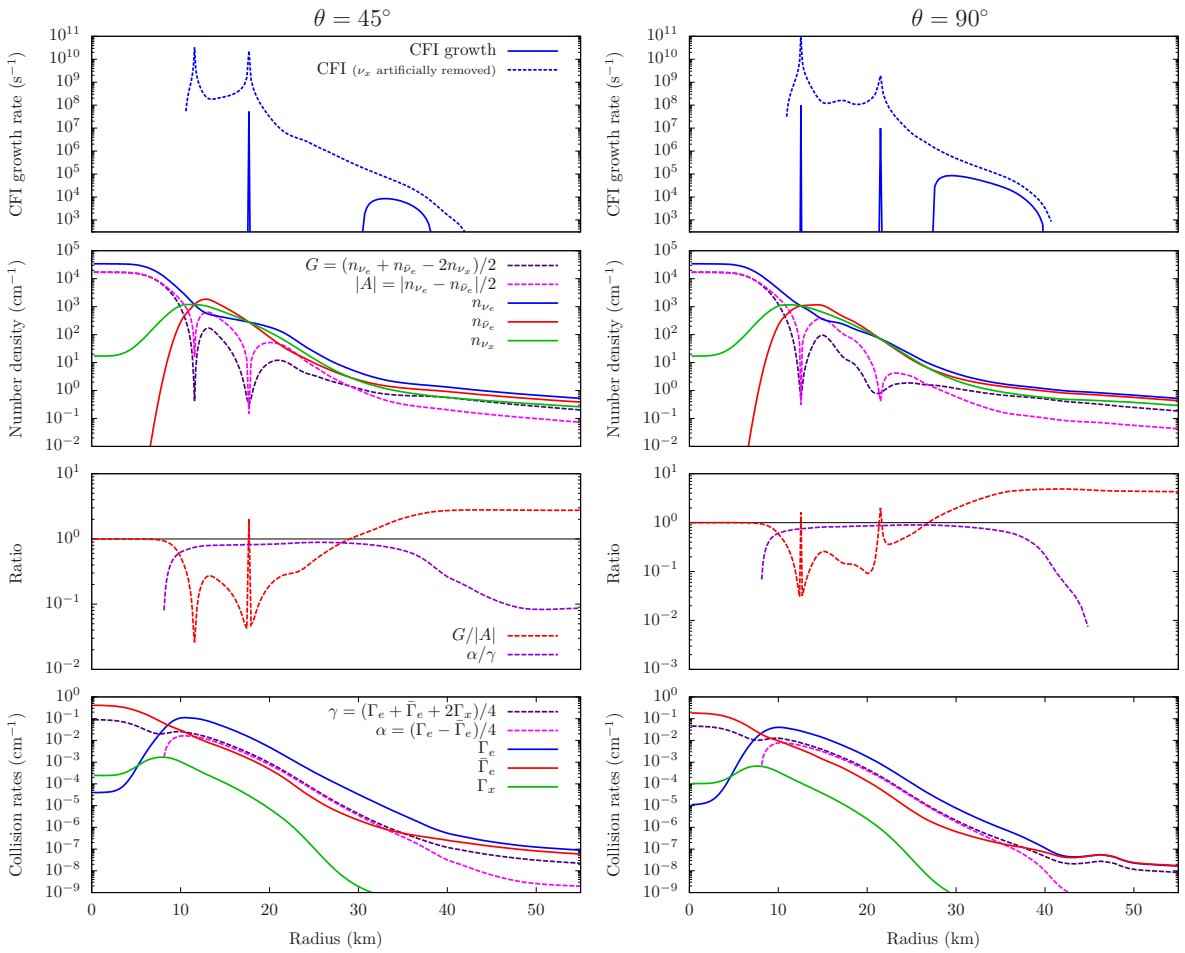

Figure 7.3: From top to bottom, radial profiles of (1) the growth rates of CFI and FFI, (2) ratios G/A and α/γ, (3) number densities and G, $|A|$, and (4) collision rates for each species of neutrinos and γ, α. Left and right panels are for the angle $\theta = 45°$ and $\theta = 90°$, respectively. The snapshot is at $t = 404\,\mathrm{ms}$ after bounce.

7.3.3 CFI

The CFI growth rates are shown as solid lines in the top panels of Fig. 7.3, for $\theta = 45°$ and $90°$ at $t = 404\,\mathrm{ms}$. Both the resonance-like CFI (sharp peaks) and the non-resonance CFI ($30 \lesssim r \lesssim 40\,\mathrm{km}$) are observed in both plots. The maximum growth rate of $\sim 10^{-3}\,\mathrm{cm}^{-1}$ is reached by the resonance-like CFI whereas the non-resonance CFI has a typical growth rate of $\sim 10^{-6}\,\mathrm{cm}^{-1}$.

In the same plots we present the CFI growth rate when we artificially set the number density ν_x to zero. In this case the CFI region is much extended, with the non-resonance CFI region merged with the resonance-like CFI region. Moreover, the growth rate becomes higher by orders with the maximum growth rate reaching $\sim 1\,\mathrm{cm}^{-1}$ for the resonance-like CFI. This experiment clearly demonstrates that the existence of ν_x suppress CFI. This is in sharp contrast with FFI, on which ν_x has no effect as long as ν_x and $\bar{\nu}_x$ do not have angular crossing.

In the following we look into the resonance-like CFI and non-resonance CFI's more closely in turn.

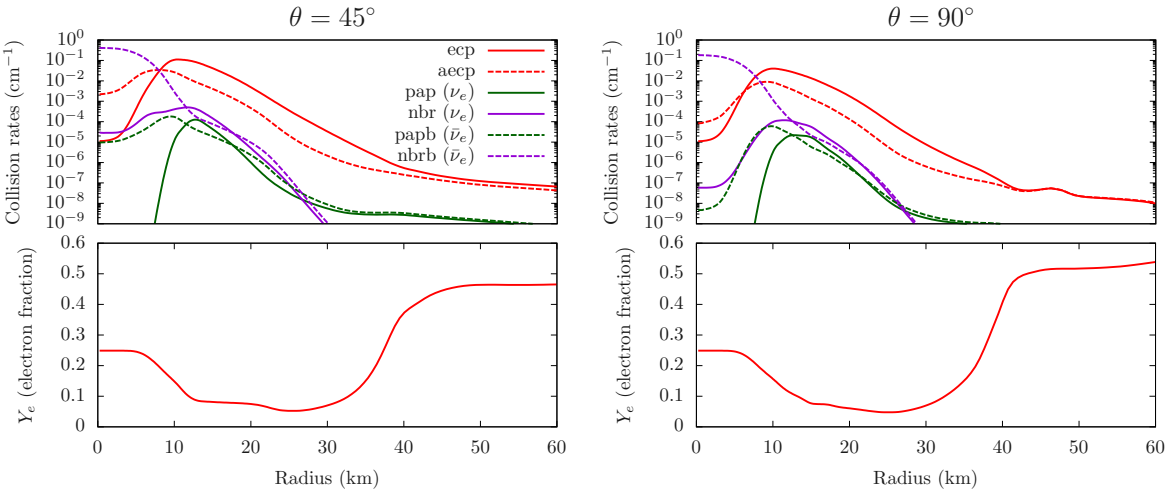

Figure 7.4: Radial profiles of collision rates for individual neutrino interactions (top) and Y_e (bottom). The angles and the time snapshot is same as Fig. 7.3. The abbreviations of neutrino interactions are as follows: electron capture (ecp), anti-electron capture (aecp), neutrino pair production (pap) and the nucleon bremsstrahlung (nbr).

Resonance-like CFI

The resonance-like CFI occurs when the situation $A \approx 0$ is realized (Liu et al., 2023; Liu et al., 2023). This is vindicated in the panels in the second row of Fig. 7.3, where we plot the radial profiles of the number densities of all neutrinos as well as $G = (n_{\nu_e} + n_{\bar{\nu}_e} - 2n_{\nu_x})/2$ and $|A| = |n_{\nu_e} - n_{\bar{\nu}_e}|/2$ (see Eq. 7.45). The very sharp dips in A correspond to the peaks in the growth rate (see the top panels) indeed. It is also found that G has dips at the same positions, but so as deep as A. By definition, the situation $A \approx 0$ occurs when the number densities of ν_e and $\bar{\nu}_e$ become close to each other. On the other hand, G becomes zero if $n_{\nu_e} + n_{\bar{\nu}_e} = 2n_{\nu_x}$, which is not completely the case at $A = 0$. As a result, $G/|A|$ gets very large at the points, creating the resonance-like CFI as observed in the plots on the third row of Fig. 7.3. Note that we assume $n_{\nu_x} = n_{\bar{\nu}_x}$. If this assumption is not valid due to muonization, it may prevent A to become zero at the point where $n_{\nu_e} = n_{\bar{\nu}_e}$, and might hinder the resonance-like CFI. We will investigate it in the future.

Here we comment on the possible artifact of the low radial resolution. With a finite number of grid points, it is impossible to have $A = 0$ on one of the grid points. As a result, the CFI growth rate is underestimated in the vicinity of the resonance-like CFI. The insufficient resolution also explains the absence of the resonance-like CFI at $r \sim 10\,\mathrm{km}$ for $\theta = 45°$ in spite of $n_{\nu_e} \sim n_{\bar{\nu}_e}$. As a matter of fact, matter is more compressed and the scale height at this angle is shorter than at $\theta = 90°$.

The non-detection of the resonance-like CFI in the 1D study (Liu et al., 2023) is not an artifact by the low resolution, on the other hand. As already mentioned, the abundance of $\bar{\nu}_e$ tends to be underestimated in 1D due to the lack of convection. As a result, $A = 0$, which is equivalent to resonance-like CFI, is unlikely to be realized. This clearly indicates the importance of multi-dimensionality for CFI.

Non-resonance CFI

We now move on to the non-resonance CFI. The inner edge of the CFI region ($r \sim 30\,\mathrm{km}$) corresponds to the position where $n_{\bar{\nu}_e}$ exceeds n_{ν_x}. Then $G > |A|$ holds above this radius. Since $\gamma \approx \alpha$ is satisfied, it leads to the occurrence of the ordinary non-resonance CFI there. At larger radii ($r \gtrsim 40\,\mathrm{km}$), however, the CFI ceases to exist despite $G > |A|$ is sustained. This is because the ratio

α/γ gets smaller as shown in the panels on the third row of Fig. 7.3. The two ratios G/A and γ/α dictate the emergence/extinction of the CFI region: the growth rate becomes positive (and hence the CFI occurs) only when they are comparable or larger than unity.

The behavior of γ and α can be understood from the panels in the fourth row of Fig. 7.3, where the collision rates (Eq. 7.48) are plotted together with α and γ. It is found that Γ_e is dominant over $\bar{\Gamma}_e$ and Γ_x at $10 \lesssim r \lesssim 30\,\mathrm{km}$, which results in $\gamma \sim \alpha$ there. At larger radii $r \gtrsim 40\,\mathrm{km}$, on the other hand, $\bar{\Gamma}_e$ becomes comparable to Γ_e. As a result, α gets smaller than γ.

In order to understand the behavior of Γ_e and $\bar{\Gamma}_e$ further, we plot the contributions of individual neutrino-matter interactions in Fig. 7.4. As can be seen, the electron capture on proton (ecp) and the anti-electron capture on neutron (aecp) dominate other interactions at $r \gtrsim 10\,\mathrm{km}$, which means that they mainly drive Γ_e and $\bar{\Gamma}_e$, respectively.

It is interesting to compare Γ's with the Y_e distribution shown in the bottom panels of Fig. 7.4. At $10 \lesssim r \lesssim 30\,\mathrm{km}$, Y_e is low ~ 0.1. This corresponds to the region where ν_e opacity dominates over $\bar{\nu}_e$, i.e., $\Gamma_e > \bar{\Gamma}_e$. On the other hand, at $r \gtrsim 40\,\mathrm{km}$, Y_e is ~ 0.5. In this region, ecp and aecp have similar collision rates, which yields $\Gamma_e \sim \bar{\Gamma}_e$. This analyses is in line with the 1D result that CFI was observed only for rather low-Y_e region.

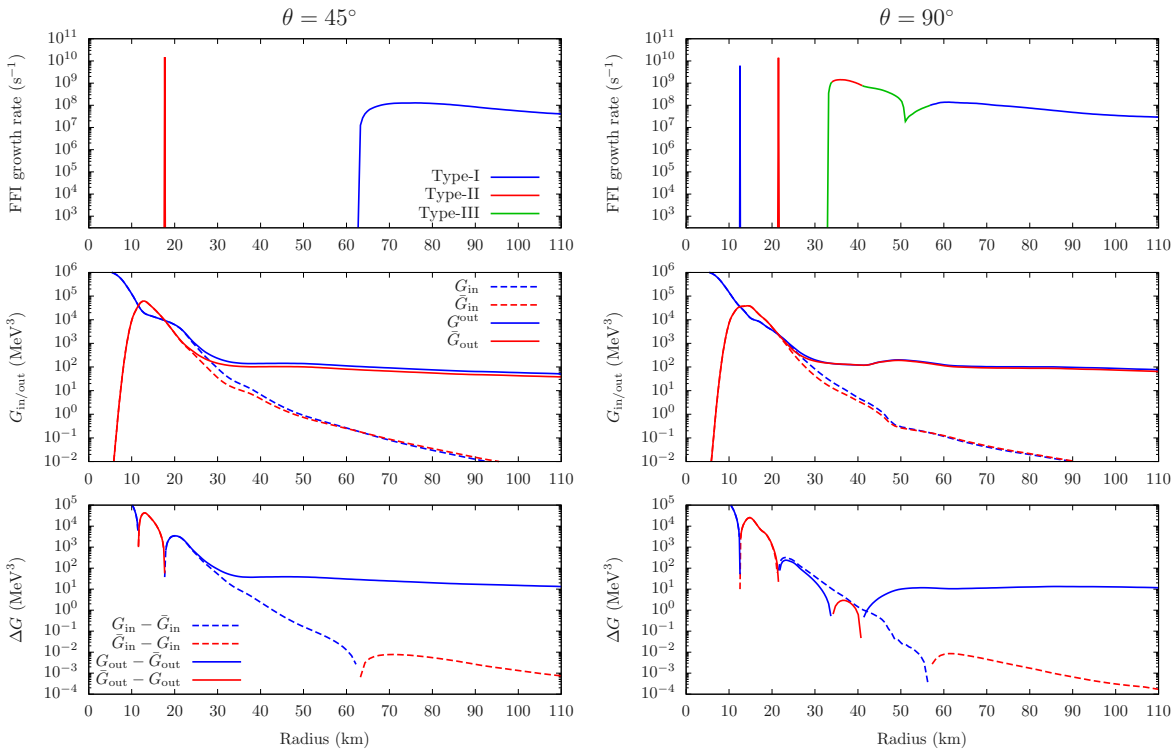

Figure 7.5: Radial profiles of the FFI growth rate (top) and $G_{\rm in/out}$, $\bar{G}_{\rm in/out}$ (middle) and the differences between $G_{\rm in/out}$ and $\bar{G}_{\rm in/out}$ (bottom) at $t = 404\,$ms after bounce.

7.3.4 FFI

We turn our attention to the FFI region found in our model. Top panels of Fig. 7.5 shows the growth rates of FFI for $\theta = 45$ and $90°$. Different colors distinguish the types of angular crossing. Here, we use the terminology of Nagakura & Johns (2021b); type-I crossing means ν_e is dominant over $\bar{\nu}_e$ in the outgoing direction ($\mu_\nu = 1$) whereas $\bar{\nu}_e$ is dominant over ν_e in the incoming direction ($\mu_\nu = -1$). Type-II crossing means the opposite. Note that it is possible that FFI exists but the type cannot be categorized into either of them. We call this case type-III hereafter. There are two possible reasons; (1) the number of crossing is even, or (2) shallow crossing appears for some energy or ϕ_ν, but the integration smear it out. Note that we judge the crossing type by the energy-integrated and ϕ_ν-averaged distribution function. It should be pointed out that the detection scheme proposed previously for results obtained with the truncated moment method (Nagakura & Johns, 2021b) assumed an odd number of crossings. The FFI region with even number of crossings may have been overlooked with such a scheme.

In the middle panels of Fig. 7.5, we exhibit the energy-integrated and ϕ_ν-averaged distribution functions defined as

$$G_{\rm in} \equiv \int E^2 dE \int \frac{d\phi_\nu}{2\pi} f_{\nu_e}(\mu_\nu = -1) \quad \text{(incoming)}, \tag{7.52}$$

$$G_{\rm out} \equiv \int E^2 dE \int \frac{d\phi_\nu}{2\pi} f_{\nu_e}(\mu_\nu = 1) \quad \text{(outgoing)}, \tag{7.53}$$

and $\bar{G}_{\rm in/out}$ for $\bar{\nu}_e$. The bottom panels give the difference of $G_{\rm in/out}$ between ν_e and $\bar{\nu}_e$. Since it is a logarithmic plot, a line is shown only if the value is positive. Note that the colors distinguish

the signatures. The combination of blue solid line and red dashed line means type-I crossing exists there, whereas the pair of blue dashed line and red solid line corresponds to type-II crossing. Other combinations indicate either no crossing or type-III crossing. There are several types and reasons of FFI in the semi-transparent and optically-thin region. The angular distributions for three representative radii are shown in Fig. 7.6. Type-I crossing is observed at $r \gtrsim 60\,\mathrm{km}$ for both angles (see Fig. 7.5 and the top panel of Fig. 7.6). As already pointed out in Nagakura & Johns (2021b), this is produced by the back-scattering of $\bar{\nu}_e$. Since $\bar{\nu}_e$'s tend to have higher energies than ν_e's as they come from deeper inside, the nucleon scattering occurs more frequently for $\bar{\nu}_e$ than for ν_e. It produces a larger population of the former in the inward direction. It is mentioned that type-I crossing produced this way was observed only for the exploding models in Nagakura & Johns (2021b).

We find a type-II crossing at $r \sim 40\,\mathrm{km}$ only for $\theta = 90°$ (also see the middle panel of Fig. 7.6). It actually corresponds to the mushroom-shaped FFI region in Fig. 7.2, which is produced by convective motions. As may be inferred from the $G_{\mathrm{in/out}}$ distributions in Fig. 7.5 , it is located in the neutrino decoupling region. Because $\bar{\nu}_e$ decouples from matter deeper inside than ν_e, its angular distribution in momentum space is more forward-peaked. As a result, $\bar{\nu}_e$ is more abundant than ν_e for the outgoing direction while the opposite is true for the incoming direction. The generation of type-II crossing by this mechanism was already discussed in previous studies (Nagakura & Johns, 2021b; Harada & Nagakura, 2022; Akaho et al., 2023). It did not happen in other angles including $\theta = 45°$, because ν_e is clearly dominant over $\bar{\nu}_e$ there.

Type-III crossings are found at $\theta = 90°$. They are actually separated into two regions; (1) the very narrow strip at the inner boundary of type-II crossing, and (2) the domain between type-I and type-II crossing regions. The former corresponds to the shallow crossing mentioned earlier. On the other hand, the latter domain has two crossings instead of one. The typical angular distribution is presented in the bottom panel of Fig. 7.6. In fact, We find that $\bar{\nu}_e$ is dominant over ν_e at both $\mu_\nu = -1$, 1 but opposite for $\mu_\nu \sim 0$. Since this domain is sandwiched by the type-II crossing region at smaller radii and the type-I crossing region at larger radii, both mechanisms operate in this region, creating the two crossings. As mentioned earlier, the detection of FFI based on moments assuming that the number of crossings is odd (Nagakura & Johns, 2021b) will fail to find this region. In this respect, the Boltzmann neutrino transfer is certainly advantageous.

We find very narrow spikes in the FFI growth rate at both $\theta = 45°$ and $90°$. They are located at the same position as the resonance-like CFI, as we will see later. This is natural because the condition $n_{\bar{\nu}_e}/n_{\nu_e} \sim 1$ is favorable not only for the resonance-like CFI but also for the FFI, as already reported previously (Glas et al., 2020; Delfan Azari et al., 2020). The absence of the inner peak for $\theta = 45°$ is due to the low radial resolution, just as for the resonance-like CFI. The type of crossing at this point is rather meaningless because both ν_e and $\bar{\nu}_e$ have almost isotropic distributions at these points.

7.3.5 Comparison between CFI and FFI

Finally, we compare the growth rates of CFI and FFI in Fig. 7.7. It is clear that the growth rate of FFI is higher than CFI by many orders if both of them exist. This is as expected because the dependence of the growth rate on the neutrino number density n is different between the two modes; $\sigma_{\mathrm{FFI}} \propto n$, and $\sigma_{\mathrm{CFI}} \propto \sqrt{n}$. However, it is worth mentioning that the relation $\sigma_{\mathrm{FFI}} \gg \sigma_{\mathrm{CFI}}$ is not the universal relationship and may be opposite if the angular crossing is shallow or the collision rates are large.

The above comparison indicates that CFI is subdominant in the linear evolution even the resonance-like CFI occurs. However, it does not mean that CFI is unimportant. As long as the growth rate is shorter than the typical time scale of the background evolution, the flavor conversion will reach the nonlinear phase anyway. The subsequent evolution and possible saturation are currently under extensive investigations (Padilla-Gay et al., 2022; Johns & Xiong, 2022; Lin & Duan, 2023; Xiong et al., 2023b,a). For example, the Monte Carlo simulations in Kato et al. (2023) found that the resonance-like CFI induces the flavor swap rather than the settlement to the flavor equilibrium. It will be eventually

needed to somehow incorporate these results in the supernova simulations and see their effects on the fluid dynamics, neutrino signals, and nucleosynthesis in CCSNe.

7.4 Summary of Chapter 7

We conducted the post-process analyses of one of our 2D CCSN simulations performed with the Boltzmann neutrino radiation hydrodynamics code to search for the regions where the collisional and/or fast flavor instabilities will possibly happen. We employed the criterion for these flavor instabilities that were derived in the previous studies (Morinaga et al., 2020; Liu et al., 2023) based on the linear analysis.

We found that the non-resonance CFI would occur in the region with the density of $10^{10} \lesssim \rho \lesssim 10^{12}\,\mathrm{g\,cm^{-3}}$, which is consistent with the previous findings in the 1D study Liu et al. (2023). In the multi-dimensional model, however, the radial extent of the CFI region changes in time on the dynamical timescale, which was absent in the 1D model. This is due to the turbulence in the supernova core. Non-resonance CFI region is likely to be separated from FFI region most of the time, but they can be overlapped with each other at some angles depending on the asymmetry of fluid motions. The non-resonance CFI region is characterized as follows; the inner boundary corresponds to the points where the number density of $\bar{\nu}_e$ becomes equal to that of ν_x i.e., $G = |A|$. On the other hand, the outer boundary corresponds to the positions where $\bar{\nu}_e$ opacity becomes comparable to that of ν_e. It is also noted that the outer edge roughly corresponds to $Y_e \approx 0.5$.

We found that the resonance-like CFI occurs when the value of A is close to zero, which happens in turn if the number densities of different species of neutrinos almost coincide with one another. This is in contrast with the previous 1D study Liu et al. (2023). As mentioned earlier, abundance of $\bar{\nu}_e$ tend to be artificially suppressed in 1D, which makes it hard to realize $A \approx 0$. Our result clearly indicate the importance of multi-dimensional effect for CFI.

The overall properties of the appearance of FFI regions we observed in this study are consistent with those of the previous study in Nagakura & Johns (2021b); (1) in the optically thick region, the FFI occurs if $n_{\nu_e}/n_{\bar{\nu}_e} \sim 1$, (2) in the decoupling region, type-II crossing occurs if $\bar{\nu}_e$ emission is strong, and (3) in the optically thin region, type-I crossing is produced due to nucleon scattering. However, we found that multiple angular crossing can be realized in the domain between the regions with type-I and type-II crossings. Note that this detection was made possible by the exploitation of the results of Boltzmann neutrino transport, where the full information on the angular distribution in momentum space is available.

The linear growth rate of CFI is always lower than that of FFI by many orders. This is true of the resonance-like CFI also but its growth rate is larger than that of the non-resonance counterpart by orders. It should be pointed out that whether CFI or FFI have larger linear growth rates may not be so important. As a matter of fact, as long as they are shorter than the typical timescale of background evolutions and the neutrino crossing time over the background scale height, the flavor conversions reach the nonlinear stage anyway. The eventual outcomes should then be explored with different approaches (Johns & Xiong, 2022; Padilla-Gay et al., 2022; Zaizen & Nagakura, 2022; Hansen et al., 2022; Kato et al., 2023).

This chapter is wrapped up by noting the limitations of this study and giving some future prospects. First, as we have just mentioned, this study is based on the linear analysis, which can address only the trigger of flavor conversions. The subsequent evolution and the asymptotic state should be investigated, for example, by directly solving the QKE. Second, flavor conversions at a certain spatial position propagate in space, leading to a qualitative change of global neutrino radiation field in CCSNe (Nagakura & Vartanyan (2022); Shalgar & Tamborra (2023); Nagakura (2023); Nagakura & Zaizen (2023)). However, our post-process analysis does not have the ability to incorporate the feedback of global neutrino advection, which should be kept in mind as a caveat. We are updating our Boltzmann radiation-hydrodynamics code to incorporate the possible outcomes of FFI and CFI and the results

will be reported in the future.

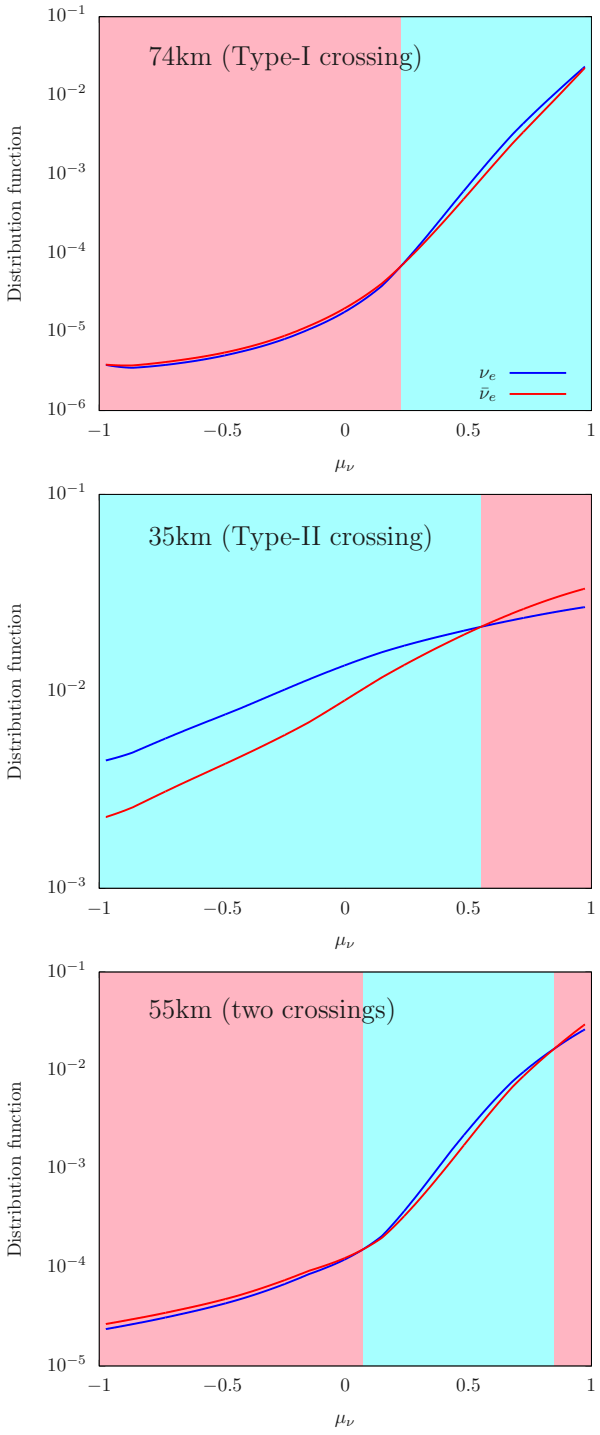

Figure 7.6: Angular distribution of the distribution function of 16.5MeV neutrinos at 74 km (top), 35 km (middle), 55 km (bottom). The angle is $\theta = 90°$ and the snapshot time is $t = 404$ ms after bounce.

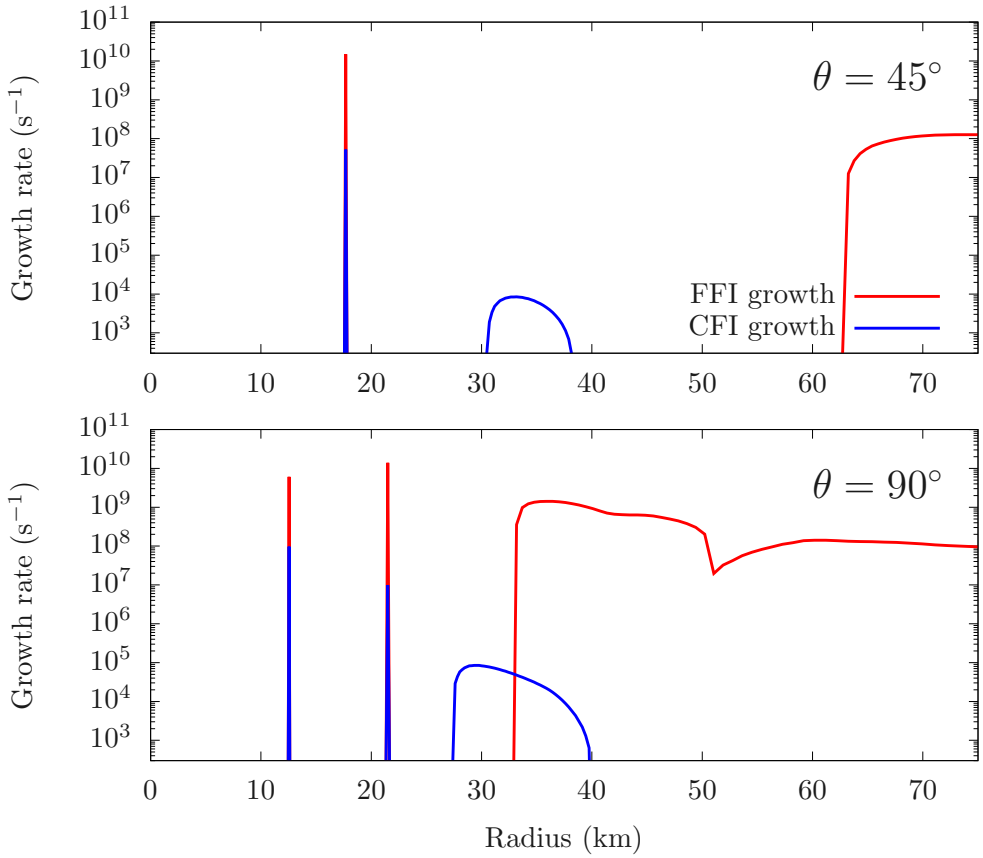

Figure 7.7: Radial profiles of the CFI and FFI growth rates for $\theta = 45°$ (top) and $\theta = 90°$ (bottom) at $t = 404\,\mathrm{ms}$ after bounce.

Chapter 8

Summary and Future Prospects

I performed theoretical investigation of CCSNe using Boltzmann neutrino radiation-hydrodynamics simulations. First of all, I developed GR version of the code and performed three kinds of simulations of which results are presented in chapters 4 5, 6. In chapter 4, I performed 2D CCSN simulation and investigated the GR effect on the postbounce explosion phase of CCSN. It was confirmed that the central density and the temperature are clearly higher in GR, due to the stronger gravity. However, the neutrino luminosity did not show large difference, because the high temperature matter was contained at the center. Second and third parts focus on the late time evolution of the protoneutron star (PNS), which is the remnant of CCSNe. Chapter 5 considered how the convection can affect the PNS evolution. It was found that the negative lepton gradient causes the convection and dredge-up of the hot matter raises the temperature at the neutrino sphere. As a result, the neutrino luminosity and the mean energy were found to be clearly higher than 1D. Chapter 6 considered how the fallback accretion onto PNS affects the neutrino emission. It was found that the accreted matter creates a temperature peak and the neutrino mean energy due to fallback is clearly higher than the thermal emission from PNS. It was also found that the event rates can be high enough for the galactic events for realistic accretion rates. Chapter 7 considered the collective neutrino oscillation which is induced by the neutrino self-interaction in CCSNe. Post-process analyses of the fast flavor instability (FFI) and the collisional flavor instability (CFI) were performed for 2D CCSN simulation. It was found that both FFI and CFI occur in CCSNe, and the criteria for their occurrence is discussed. By comparing the linear growth rates, it was found that FFI would be dominant over CFI.

I conclude this thesis by addressing some future prospects.

1. In the simulation of chapter 4, the computational time was too short to determine the explodability. I will extend the simulation time and investigate the effect of GR on the CCSN dynamics and the neutrino signals.

2. The studies in chapters 5 and 6 clearly showed the importance of convection and the fallback accretion, which are not very taken into account in previous studies. I will address this issue further, by collaborating with other research groups, implement these effect on long term PNS cooling simulations and predict future observational signals.

3. The post-process analysis in chapter 7 clearly indicates that collective neutrino oscillation can commonly occur in CCSNe, and the growth rates are faster than the typical timescale of the weak interaction for some region. I will extend the code to take into account the effect of flavor conversion to the Boltzmann radiation hydrodynamics simulation.

Appendix A

Discretization of the Boltzmann Equation

In this appendix, we describe how the advection terms are evaluated in our finite difference scheme. As mentioned in the main text, the evaluation of the advection terms in the discretized form is tricky when they are written in the conservative form. This may be understood if one considers a constant f in the phase space. Then all advections should be vanishing. This is apparent in the Boltzmann equation written as in equation 3.2, since all the derivatives of f are zero. This is not so obvious, however, if the Boltzmann equation is cast into the conservative form, as in equation 3.3. In fact, the advection terms are not simply vanishing but are cancelled among them in nontrivial ways. Analytically these cancellations are with no problem; it is difficult to enforce in the finite-difference, however. If one treats them carelessly, neutrinos may appear from nowhere. The formulation described in Sumiyoshi & Yamada (2012) ensures the perfect cancellation of those terms for the flat spacetime. In the general relativistic case with an arbitrary metric, the formulation for the flat spacetime is not applicable, though. In this study, we do not stick to the perfect cancellation and evaluate the advection terms are evaluated in a rather straightforward way as described below. As shown in the advection tests in sections C.1.2 and C.2.2, however, we found no problem in the general relativistic cases even if the cancellation is not exactly enforced. We will investigate this issue further and, if necessary, revise the general relativistic formulation in future works.

Throughout this chapter, variables with the lowercase subscript n (such as r_n) are defined at the cell centers whereas those with the uppercase subscript N (such as r_N) are defined at the cell interfaces. This is because there are some delicate cancellations among the terms that are a part of different advection terms.

A.1 Mesh Configuration

The cell interface variables of the radial mesh is varied depending on the situation; the resolution is high where the density gradient is steep. The cell-center values of the radial grid points are calculated from the interface values as follows

$$r_i = \left[\frac{r_{I-1}^3 + r_I^3}{2}\right]. \tag{A.1}$$

The zenith angle in the configuration space θ and the momentum space are constructed in the same way, as follows. When the zenith angle is treated, $\mu = \cos\theta$ is the basic variable. μ grid points are given by the Gaussian quadrature as

$$\mu_J = \mu_{J-1} + d\mu_j, \tag{A.2}$$

where $d\mu_j$ denote the mesh width. The angle factor $\sin^2\theta$ and $\sin\theta$ appear in some advection terms. They are directly evaluated as

$$(1-\mu^2)_I = (1-\mu^2)_(I-1) - 2\mu_i d\mu_i, \tag{A.3}$$

$$(1-\mu^2)_I^{\frac{1}{2}} = (1-\mu^2)_{I-1}^{\frac{1}{2}} - \frac{\mu_i}{(1-\mu_i^2)^{\frac{1}{2}}} d\mu_i. \tag{A.4}$$

The azimuth angles for the configuration space ϕ and for the momentum space ϕ_ν are also determined by the Gaussian quadrature points

$$\phi_I = \phi_{I-1} + d\phi_i, \tag{A.5}$$

where $d\phi_i$ denote the mesh width. The angle factor for some advection term are evaluated as follows;

$$(\sin\phi)_I = (\sin\phi)_{I-1} + \cos\phi_i. \tag{A.6}$$

As for the energy grid points, the interface values can be analyzed arbitrarily; it is logarithmically distributed in the simulations presented in the main text. The cell center values are calculated as

$$\epsilon_i = (\epsilon_I \epsilon_{I-1})^{\frac{1}{2}}. \tag{A.7}$$

A.2 Finite Difference Representation

The spatial advection terms (r, θ and ϕ) are finite-differenced as

$$\begin{aligned} & \frac{1}{\sqrt{-g}} \frac{\partial}{\partial x^i} \left[L^i \sqrt{-g} f \right] \\ \longrightarrow \quad & \frac{1}{\sqrt{-g_n} dx_n^i} \left[\sqrt{-g_N} L_N^i f_N - \sqrt{-g_{N-1}} L_{N-1}^i f_{N-1} \right], \end{aligned} \tag{A.8}$$

where dx_n^i is the width of the n-th cell, and we defined $L^\mu \equiv e^\mu_{(0)} + \sum_{i=1}^3 l_i e_i^\mu$ for notational simplicity. In the flat or the Schwarzschild case, for example, $L^1 = \cos\theta_\nu$, $L^2 = \sin\theta_\nu \cos\phi_\nu$, $L^3 = \sin\theta_\nu \sin\phi_\nu$. The value of $L_N f_N$ on the N-th cell interface ($L_N^i f_N$) is evaluated as

$$L_N^i f_N = \frac{L_n^i - |L_n^i|}{2}[(1-\beta_N) f_n + \beta_N f_{n+1}] + \frac{L_{n+1}^i + |L_{n+1}^i|}{2}[\beta_N f_n + (1-\beta_N) f_{n+1}], \tag{A.9}$$

where β_N is introduced to smoothly switch from the upwind differencing in the free streaming limit ($\beta_N = 1$) to the central differencing in the diffusion limit ($\beta_N = 1/2$). We use the following expression of β_N based on Mezzacappa & Bruenn (1993):

$$\beta_N = 1 - \frac{1}{2} \frac{\alpha_p dr_N \lambda_N}{1 + \alpha_p dr_N \lambda_N}. \tag{A.10}$$

where the mean free path on the cell interface is calculated as $\lambda_N = (\lambda_{n+1} + \lambda_n)/2$. The adjustable parameter α_p is set to be 100, following Sumiyoshi & Yamada (2012). In the free streaming case $\beta_N = 1$, the upwind direction is accounted for by the signature of L^i.

The energy advection term is expressed as follows:

$$\begin{aligned} & -\frac{\partial}{\partial(\epsilon^3/3)} \left(\epsilon^3 f \omega_{(0)} \right) \\ \longrightarrow \quad & -\frac{3}{\epsilon_N^3 - \epsilon_{N-1}^3} \left[\epsilon_N^3 \omega_{(0)N} f_N - \epsilon_{N-1}^3 \omega_{(0)N-1} f_{N-1} \right], \end{aligned} \tag{A.11}$$

with

$$\omega_{(0)N} f_N = \frac{\omega_{(0)N} + |\omega_{(0)N}|}{2} f_{n+1} + \frac{\omega_{(0)N} - |\omega_{(0)N}|}{2} f_n, \tag{A.12}$$

Here the one-sided differencing is employed and its direction is dictated by the signature of $\omega_{(0)n}$: the forward finite-differencing is adopted for $\omega_{(0)n} > 0$, i.e., in the case for redshift whereas the backward differencing is employed for the blueshift case.

The angular advection terms are finite-differenced just in a similar way, by switching the direction of one-sided differencing according to the signatures of $\omega_{(*)}$: employing $\mu_\nu = \cos\theta_\nu$, we write the θ_ν advection term as

$$\begin{aligned} & -\frac{\partial}{\partial \mu_\nu}(\sin\theta_\nu f \omega_{(\theta_\nu)}) \\ \longrightarrow \quad & -\frac{1}{(d\mu_\nu)_n}\left[\sin(\theta_\nu)_N \omega_{(\theta_\nu)N} f_N - \sin(\theta_\nu)_{N-1}\omega_{(\theta_\nu)N-1} f_{N-1}\right], \end{aligned} \tag{A.13}$$

with

$$\omega_{(\theta_\nu)N} f_N = \frac{\omega_{(\theta_\nu)N} + |\omega_{(\theta_\nu)N}|}{2} f_{n+1} + \frac{\omega_{(\theta_\nu)N} - |\omega_{(\theta_\nu)N}|}{2} f_n, \tag{A.14}$$

The ϕ_ν advection term is finite-differenced as

$$\begin{aligned} & \frac{1}{\sin^2\theta_\nu}\frac{\partial}{\partial \phi_\nu}(f \omega_{(\phi_\nu)}) \\ \longrightarrow \quad & \frac{1}{\sin^2(\theta_\nu)_{n_{\theta_\nu}}}\frac{1}{(d\phi_\nu)_{n_{\phi_\nu}}}\left[\omega_{(\phi_\nu)N_{\phi_\nu}} f_{N_{\phi_\nu}} - \omega_{(\phi_\nu)N_{\phi_\nu}-1} f_{N_{\phi_\nu}-1}\right], \end{aligned} \tag{A.15}$$

with

$$\omega_{(\phi_\nu)N} f_N = \frac{\omega_{(\phi_\nu)N} - |\omega_{(\phi_\nu)N}|}{2} f_{n+1} + \frac{\omega_{(\phi_\nu)N} + |\omega_{(\phi_\nu)N}|}{2} f_n. \tag{A.16}$$

Appendix B

Discretization of the Hydrodynamics Equations

In this appendix, we describe the formulation of the hydrodynamics equations solver. It is a general relativistic extension of the Newtonian counterpart employed in the previous papers (Nagakura et al., 2014, 2017, 2019). In the code, the mesh configuration is same as the Boltzmann solver, as described in the previous chapter. By following Kawaguchi et al. (2021), we first decompose the variables as follows:

$$\Lambda^{r}_{(r)} \equiv 1,\ \Lambda^{\theta}_{(\theta)} \equiv \frac{1}{r},\ \Lambda^{\phi}_{(\phi)} \equiv \frac{1}{r\sin\theta},\ \Lambda^{j}_{(i)} \equiv 0\,(i \neq j), \tag{B.1}$$

$$\Lambda^{(r)}_{r} \equiv 1,\ \Lambda^{(\theta)}_{\theta} \equiv r,\ \Lambda^{(\phi)}_{\phi} \equiv r\sin\theta,\ \Lambda^{(i)}_{j} \equiv 0\,(i \neq j), \tag{B.2}$$

$$\tilde{\gamma}_{(i)(j)} \equiv \Lambda^{k}_{(i)}\Lambda^{\ell}_{(j)}\gamma_{k\ell}, \tag{B.3}$$

$$\tilde{K}_{(i)(j)} \equiv \Lambda^{k}_{(i)}\Lambda^{\ell}_{(j)}K_{k\ell}, \tag{B.4}$$

$$\sqrt{\tilde{\gamma}} \equiv \frac{1}{r^2\sin\theta}\sqrt{\gamma}, \tag{B.5}$$

$$\tilde{\rho_*} \equiv \frac{1}{r^2\sin\theta}\rho_*, \tag{B.6}$$

$$v^{(i)} \equiv \Lambda^{(i)}_{j}v^{j}, \tag{B.7}$$

$$\beta^{(i)} \equiv \Lambda^{(i)}_{j}\beta^{j}, \tag{B.8}$$

$$\tilde{S}_{(i)} \equiv \frac{1}{r^2\sin\theta}\Lambda^{j}_{(i)}S_{j}, \tag{B.9}$$

$$\tilde{S}_{(i)(j)} \equiv \Lambda^{k}_{(i)}\Lambda^{\ell}_{(j)}S_{k\ell}. \tag{B.10}$$

Note that if the spacetime is flat, the parenthesis indices ((r), (θ), and (ϕ)) means the orthonormal components of the flat spacetime. Therefore, similarly to the philosophy of Baumgarte et al. (2013), we factor out the trivial coordinate dependence from the coordinate components of the tensors. This decomposition gives better accuracy of the interface value reconstruction.

With the variables defined above, we discretized the equations (3.17–3.11) into the following form:

$$\begin{aligned}
\partial_t(\rho_{*i}) &= -\frac{r_i^2}{r_I^3/3 - r_{I-1}^3/3}\Delta_r(r_I^2 \sin\theta_j \tilde{\rho}_{*I} v_I^{(r)}) && \text{(B.11)}\\
&+ \frac{\sin\theta_j}{\mu_J - \mu_{J-1}}\Delta_\theta(r_i \sin\theta_J \tilde{\rho}_{*J} v_J^{(\theta)}) && \text{(B.12)}\\
&- \frac{1}{\phi_K - \phi_{K-1}}\Delta_\phi(r_i \tilde{\rho}_{*K} v_K^{(\phi)}) = 0, && \text{(B.13)}
\end{aligned}$$

$$\begin{aligned}
\partial_t(S_{r,i}) &= -\frac{r_i^2}{r_I^3/3 - r_{I-1}^3/3}\Delta_r(r_I^2 \sin\theta_j(\tilde{S}_{(r),I} v_I^{(r)} + P_I \alpha_I \sqrt{\tilde{\gamma}}_I)) && \text{(B.14)}\\
&+ \frac{\sin\theta_j}{\mu_J - \mu_{J-1}}\Delta_\theta(r_i \sin\theta_J \tilde{S}_{(r),J} v_J^{(\theta)}) && \text{(B.15)}\\
&- \frac{1}{\phi_K - \phi_{K-1}}\Delta_\phi(r_i \tilde{S}_{(r),K} v_K^{(\phi)}) && \text{(B.16)}\\
&- S_{0,i}(\partial_r \alpha)_i + \Lambda^\ell_{(m)} S_{\ell,i}(\partial_r \beta^{(m)})_i - \frac{1}{2}\alpha_i \sqrt{\gamma}_i \Lambda^j_{(\ell)} \Lambda^k_{(m)} S_{jk,i}(\partial_r \tilde{\gamma}^{(\ell)(m)})_i && \text{(B.17)}\\
&+ \frac{r_I^2 - r_{I-1}^2}{r_I^3/3 - r_{I-1}^3/3}(\alpha_i \sqrt{\gamma}_i P_i + \frac{1}{2}(S_{\theta,i} v_i^\theta + S_{\phi,i} v_i^\phi)) && \text{(B.18)}\\
&- \alpha_i \sqrt{\gamma}_i G_{r,i}, && \text{(B.19)}
\end{aligned}$$

$$\begin{aligned}
\partial_t(S_{\theta,i}) &= -\frac{r_i^2}{r_I^3/3 - r_{I-1}^3/3}\Delta_r(r_I^3 \sin\theta_j \tilde{S}_{(\theta),I} v_I^{(r)}) && \text{(B.20)}\\
&+ \frac{\sin\theta_j}{\mu_J - \mu_{J-1}}\Delta_\theta(r_i^2 \sin\theta_J(\tilde{S}_{(\theta),J} v_J^{(\theta)} + P_J \alpha_J \sqrt{\tilde{\gamma}}_J)) && \text{(B.21)}\\
&- \frac{1}{\phi_K - \phi_{K-1}}\Delta_\phi(r_i^2 \tilde{S}_{(\theta),K} v_K^{(\phi)}) && \text{(B.22)}\\
&- S_{0,j}(\partial_\theta \alpha)_j + \Lambda^\ell_{(m)} S_{\ell,j}(\partial_\theta \beta^{(m)})_j - \frac{1}{2}\alpha_j \sqrt{\gamma}_j \Lambda^j_{(\ell)} \Lambda^k_{(m)} S_{jk,j}(\partial_\theta \tilde{\gamma}^{(\ell)(m)})_j && \text{(B.23)}\\
&+ \frac{\sin\theta_{J-1} - \sin\theta_J}{\mu_J - \mu_{J-1}}(\alpha_j \sqrt{\gamma}_j P_j + S_{\phi,j} v_j^\phi) && \text{(B.24)}\\
&- \alpha_j \sqrt{\gamma}_j G_{\theta,j}, && \text{(B.25)}
\end{aligned}$$

$$\begin{aligned}
\partial_t(S_{\phi,i}) &= -\frac{r_i^2}{r_I^3/3 - r_{I-1}^3/3}\Delta_r(r_I^3 \sin^2\theta_j \tilde{S}_{(\phi),I} v_I^{(r)}) && \text{(B.26)}\\
&+ \frac{\sin\theta_j}{\mu_J - \mu_{J-1}}\Delta_\theta(r_i^2 \sin^2\theta_J \tilde{S}_{(\phi),J} v_J^{(\theta)}) && \text{(B.27)}\\
&- \frac{1}{\phi_K - \phi_{K-1}}\Delta_\phi(r_i^2 \sin\theta_j(\tilde{S}_{(\phi),K} v_K^{(\phi)} + P_K \alpha_K \sqrt{\tilde{\gamma}}_K)) && \text{(B.28)}\\
&- S_{0,k}(\partial_\phi \alpha)_k + \Lambda^\ell_{(m)} S_{\ell,k}(\partial_\phi \beta^{(m)})_k - \frac{1}{2}\alpha_k \sqrt{\gamma}_k \Lambda^j_{(\ell)} \Lambda^k_{(m)} S_{jk,k}(\partial_\phi \tilde{\gamma}^{(\ell)(m)})_k && \text{(B.29)}\\
&- \alpha_k \sqrt{\gamma}_k G_{\phi,k}, && \text{(B.30)}
\end{aligned}$$

$$\partial_t(S_{0,i} - \rho_{*i}) = -\frac{r_i^2}{r_I^3/3 - r_{I-1}^3/3}\Delta_r(r_I^2 \sin\theta_j((\tilde{S}_{0,I} - \tilde{\rho_*})_I)v_I^{(r)} + \sqrt{\tilde{\gamma}}_I P_I(v_I^{(r)} + \beta_I^{(r)})) \quad \text{(B.31)}$$

$$+ \frac{\sin\theta_j}{\mu_J - \mu_{J-1}}\Delta_\theta(r_i \sin\theta_J((\tilde{S}_{0,J} - \tilde{\rho_*})_J)v_J^{(\theta)} + \sqrt{\tilde{\gamma}}_J P_J(v_J^{(\theta)} + \beta_J^{(\theta)})) \quad \text{(B.32)}$$

$$- \frac{1}{\phi_K - \phi_{K-1}}\Delta_\phi(r_i((\tilde{S}_{0,K} - \tilde{\rho_*})_K)v_K^{(\phi)} + \sqrt{\tilde{\gamma}}_K P_K(v_K^{(\phi)} + \beta_K^{(\phi)})) \quad \text{(B.33)}$$

$$+ \alpha_i\sqrt{\gamma}_i S_i^{\ell m} K_{\ell m,i} - \gamma_i^{\ell m} S_{\ell,i}(\partial_m \alpha)_i \quad \text{(B.34)}$$

$$+ \alpha_i\sqrt{\gamma}_i(n^\mu G_\mu)_i, \quad \text{(B.35)}$$

where $\mu \equiv \cos\theta$; lower (e.g., i) and upper (e.g., I) case subscripts denote the cell center and interface values, respectively; i, j, and k indicates the grid ID numbers of the radial (r), zenith (μ), and azimuthal (ϕ) coordinates, respectively; the symbols Δ_r, Δ_θ, and Δ_ϕ means the difference between the interface values along the indicated coordinates, e.g., $\Delta_r(f_j g_I) \equiv f_j g_I - f_j g_{I-1}$ for any functions f and g. The interface values of the decomposed hydrodynamic variables (rest mass density ρ_0, temperature T or pressure P, electron fraction Y_e, and the spatial components of four-velocity $u^{(i)} \equiv u^t v^{(i)}$) are evaluated by the piecewise parabolic method (PPM, Colella & Woodward, 1984) with minmod flux limiter; the interface values of the decomposed metric variables (lapse α, shift $\beta^{(i)}$, and spatial metric $\tilde{\gamma}_{(i)(j)}$) are evaluated by the third order Lagrange interpolation; the coordinate values r_I, θ_J, and ϕ_K is exactly evaluated. The numerical flux is evaluated by the Harten-Lax-van Leer (HLL) method (Harten et al., 1983) and the time evolution is solved by the fourth order Runge-Kutta scheme. By evaluating the curvature terms such as $\alpha\sqrt{\gamma}P/r$ and so on in these ways, the steady state of uniform matter in flat spacetime is guaranteed.

Appendix C

Code Tests of the Boltzmann Solver

Here, we provide the results of the code tests of the Boltzmann solver. First, energy and angular advection tests are performed in spherical symmetry in Sec. C.1. Second, the multi-dimensional test is performed in Sec. C.2.

C.1 Spherically Symmetric Tests

We present the results of advection tests under the assumption of spherical symmetry in the neutrino distribution function, i.e., it depends only on r, ϵ, and θ_ν. Although our code is multi-dimensional, we suppress the angular degrees of freedom in space intentionally and treat the radial advection alone in space (plus the advections in momentum space) for the tests in C.1. In the following, we separately discuss the energy advection and the angular advection in momentum space in sections C.1.1 and C.1.2, respectively.

C.1.1 Energy Advection Tests

In the gravitational field, neutrinos change their energy as they move. In the computation of neutrino transport it is important to take such effects into account because the neutrino interactions strongly depend on the neutrino energy.

In order to study the capability of our code to treat those energy changes, we conduct the following test. We fix the neutrino distribution function to $f = 1$ on a single energy bin at a certain radius, which serves as a monochromatic and spherical neutrino source. We set $f = 0$ elsewhere initially. Then neutrinos will flow out of this source and fill the space, the evolution of which we will compute with our new code. As for the initial angular distribution in momentum space, we assume that the neutrinos move in a single direction with the zenith angle $\theta_\nu = 0$ (outward) or π (inward). We can test redshift in the former and blueshift in the latter. Note, however, that it is difficult in our code to set the single-angle distributions given above strictly. We hence set $f = 1$ either on the first or on the last angular bin and $f = 0$ on other bins in the numerical test. In order to focus on the energy advection, we switch off angular advection in this test. One prominent difference in general relativity is that the neutrinos can experience gravitational redshift or blueshift. I checked the performance of the code whether it can treat energy advection. The results are compared with the analytical formula for the neutrino energy $\epsilon_{\rm ana}$ as a function of radius:

$$\epsilon_{\rm ana}(r) = \left(1 - \frac{2GM}{c^2 r_{\rm source}}\right)\left(1 - \frac{2GM}{c^2 r}\right)^{-1} \epsilon_{\rm source}, \tag{C.1}$$

where $\epsilon_{\rm source}$ and $r_{\rm source}$ are the energy and radius of the source, respectively.

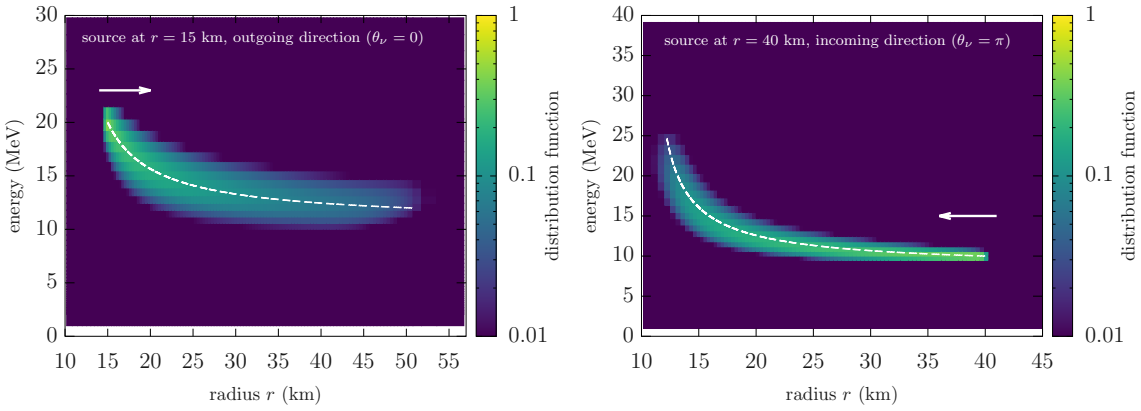

Figure C.1: The neutrino distributions in energy space as a function of radius for the energy advection tests. The left and right panels show the results for the redshift and blueshift tests, respectively. The arrows indicate the directions of the neutrino motions, and the white dashed curves show the trajectory of the massless particles emitted from the source, truncated at the radius where the massless particles reach at the time of the snapshot $t = 2 \times 10^{-4}$ s.

It should be stressed that for mesh-based codes like ours this is a very challenging problem, with sharp edges existing both in the energy and angular distributions. As will be witnessed later, rather large numerical diffusions occur inevitably. We choose this test, though, since this enables us to see most clearly if the code can reproduce the redshift/blueshift of neutrino energy as it moves in the gravitational well; the resolution dependence also manifests itself.

Throughout this test, we deploy the radial mesh with $N_r = 128$ grid points that covers the range $r \in [0, 100]$ km. It is finer in the region $r \in [10, 50]$ km. The number of angular mesh points in momentum space is $N_{\theta_\nu} = 20$. The energy mesh has logarithmically spaced grid points and covers the range $\epsilon \in [0, 50]$ MeV. We vary the number of energy mesh points as $N_\epsilon = 20$, 30, 40, and 60 to study the resolution dependence of the result.

Figure C.1 shows the energy distributions as a function of radius at a certain time for $N_\epsilon = 60$. The white dashed curves depict the analytical solutions. The left panel presents the result of the gravitational redshift test at the coordinate time $t = 2 \times 10^{-4}$ s. In this calculation, the neutrino source is located at $r = 15$ km and emits monochromatic neutrinos with $\epsilon = 20$ MeV outward. The energy distributions obtained numerically trace the analytical curve although they are somewhat broadened due to numerical diffusions arising from the finite energy resolution in the simulation. We stress again that this is actually a very challenging problem for finite difference methods like ours. In fact, the single energy bin has a finite width and cannot express the monochromatic energy distribution very well in the first place. The same trend is found for the blueshift test as exhibited in the right panel. The neutrino source is located at $r = 40$ km and emits neutrinos with $\epsilon = 10$ MeV inward in this test. The energy of neutrinos increases indeed as they propagate radially inward. It is also observed that the numerical diffusion is weaker at large radii as the advection is rather small there. In both panels, the analytic curves are drawn from the source positions to the points that the massless neutrino reaches at the given time. It is obvious that the terminal points are well reproduced by the numerical computations. In order to see the resolution dependence of the numerical diffusion quantitatively, we repeat the redshift tests with different numbers of energy bins. We quantify the numerical diffusion by defining the following error function:

$$E_\epsilon(r) \equiv \frac{\sum_{n=1}^{N_\epsilon} f(r, \epsilon_n)(\epsilon_n - \epsilon_{\rm ana}(r))^2 d\epsilon_n}{(\epsilon_{\rm ana}(r))^2 \sum_{n=1}^{N_\epsilon} f(r, \epsilon_n) d\epsilon_n}, \tag{C.2}$$

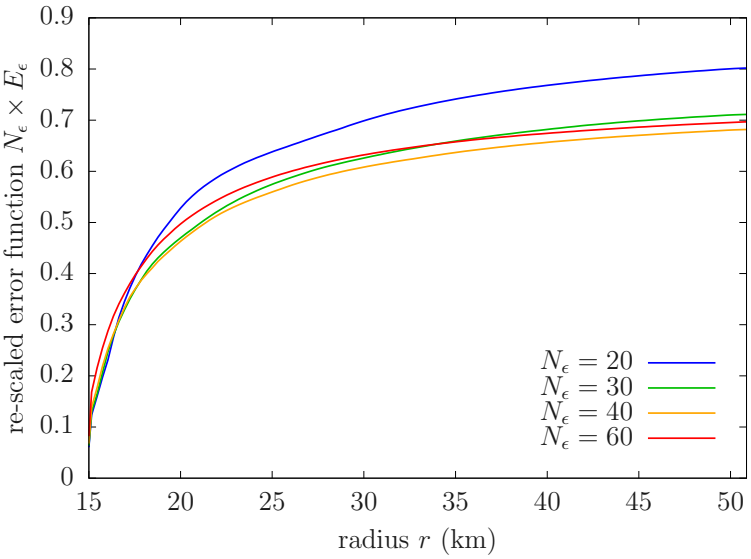

Figure C.2: Radial profiles of the re-scaled error function defined in the text. Different colors indicate the numbers of energy mesh points: blue, green, yellow, and red curves are for $N_\epsilon = 20$, 30, 40, and 60, respectively.

where ϵ_n and $d\epsilon_n$ are the value of energy at the n-th cell center and the width of the same cell, respectively. In figure C.2, we show the radial profiles of the error function re-scaled by the number of energy mesh points N_ϵ. It is seen that the re-scaled error functions for the different energy resolutions almost coincide with one another except for $N_\epsilon = 20$. This indicates that the error function is inversely proportional to N_ϵ, roughly implying the first-order convergence. This is expected, since the energy advection term is evaluated with a first-order finite difference scheme as described in appendix A.

C.1.2 Angular Advection Tests

The greatest advantage of directly solving the Boltzmann equation is that we are able to obtain information not only on energy but also on the angular distribution in momentum space. The direction of the neutrino momentum is specified by the zenith and azimuth angles, (θ_ν, ϕ_ν) (see figure 3.1). Note that the distribution function depends on θ_ν alone in the spherical symmetry assumed in this section. As a neutrino moves non-radially, the zenith angle θ_ν, which is measured from the local radial direction, changes even in the flat space time. This angular advection is shown schematically in Fig. C.3. The blue curve is one of geodesic curves, along which the free neutrino moves in the Schwarzschild spacetime. Note that it is no longer a straight line due to gravity. In this example the neutrino moves outward and the zenith angle approaches $\theta_\nu = 0$, i.e., the outward radial direction, with the increasing radius r. Since the geodesic curve is bent inward by gravity, the approach is slower for the Schwarzschild spacetime than in the flat spacetime. In this subsection, we test the capability of our code to reproduce this angular advection.

The numerical setting is essentially the same as in the previous test for the energy advection: we put the monochromatic neutrino source uniformly on a sphere with a certain radius by setting $f = 1$ on an single energy bin there and $f = 0$ otherwise. The difference is that we choose $\theta_\nu = \pi/2$, which corresponds to direction of $p^r = 0$, at the source. Note that we actually set $f = 1$ on a single angular bin nearest to $\theta_\nu = \pi/2$ for numerical convenience. We vary the source radius to investigate the angular advections both inside and outside the photon sphere, i.e., the circular orbit. The neutrinos emitted outside the photon sphere with $p^r = 0$ propagate outward with θ_ν decreasing monotonically to zero whereas those emitted inside the photon sphere go inward with θ_ν increasing as they propagate. In this test, we switch off the energy advection, which should occur simultaneously in reality. This is to avoid numerical diffusions both in angle and energy at the same time. The results are compared with those for the flat spacetime as well as with the reference solution obtained.

The geodesic curves in the Schwarzschild spacetime is calculated as follows. In the Schwarzschild (exterior) spacetime, the geodesic motion on the equatorial plane satisfies the following equation (see §25.6 in Misner (1973), for example):

$$\left(\frac{dr}{d\phi}\right)^2 = r^2\left(\frac{r^2}{b^2} + \frac{2GM}{c^2 r} - 1\right), \tag{C.3}$$

where r and ϕ are the coordinate variables, and b is the impact parameter. When the trajectory is on the meridional plane, one may replace the azimuth angle ϕ with the zenith angle θ. The impact parameter b can be expressed in terms of the radius r_0 and the zenith angle $(\theta_\nu)_0$ of a reference point on the geodesic curve as

$$b = \frac{r_0 \sin(\theta_\nu)_0}{1 - 2GM/(c^2 r_0)}, \tag{C.4}$$

For numerical calculations, it is more useful to rewrite the above equation (C.3) as

$$\frac{d^2u}{d\phi^2} = \frac{3GMu^2}{c^2} - u, \tag{C.5}$$

where the new variable is introduced as $u = 1/r$. The second derivative of u changes signature at the radius $r = 3GM/c^2$, which corresponds to the radius of the photon sphere. In this work, equation (C.5) is solved with the fourth-order explicit Runge-Kutta method by dividing it into the following two equations:

$$\frac{du}{d\phi} = v, \quad \frac{dv}{d\phi} = \frac{3GMu^2}{c^2} - u. \tag{C.6}$$

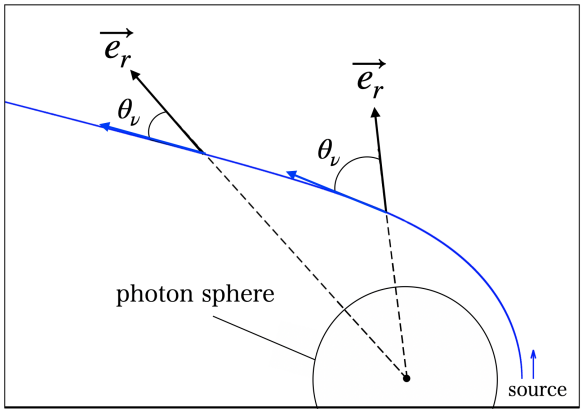

Figure C.3: Schematic picture of the angular advection in momentum space angle θ_ν for Schwarzschild spacetime. The blue curve indicates the trajectory of a massless particle emitted from the source located outside the photon sphere. The blue arrows are the tangent vectors of the trajectory; the black arrows are the radial vectors with the dashed lines indicating the radial ray from the coordinate center. The angle θ_ν is the angle between these two vectors.

For the angular advection tests, the zenith angle θ_ν in momentum space along the geodesic, which is given in equation (13) in Shibata et al. (2014):

$$\theta_\nu = \tan^{-1}\left(\frac{p_{(2)}}{p_{(1)}}\right) = \tan^{-1}\left(r\sqrt{1-\frac{2GM}{c^2 r}}\frac{p^\theta}{p^r}\right), \tag{C.7}$$

where $p_{(i)}$ is the momentum components for the tetrad basis and given as $p_{(i)} = p_\mu e^\mu_{(i)}$.

We employ the same radial mesh with $N_r = 128$ as in the previous tests. As for the mesh in momentum space, we vary the number of grid points as $N_{\theta_\nu} = 20$, 30 and 40 to see the resolution dependence. We set $N_{\phi_\nu} = 2$ for numerical convenience although the distribution does not depend on ϕ_ν in the present case.

Figure C.4 shows the angular distributions of neutrinos in momentum space as a function of the radius r for the angular advection tests with $N_{\theta_\nu} = 40$. The white dashed curves depict the reference geodesic curves, truncated at the radius that the massless particles reach at the time of the snapshot. The left panel shows the result for the flat spacetime at $t = 1 \times 10^{-4}$ s, with the source placed at $r = 20$ km. As mentioned earlier, there is a nontrivial angular advection even in the flat spacetime, since we deploy the polar coordinates in space. Neutrinos emitted with $p_r = 0$ always move outward in the flat spacetime and the zenith angle monotonically converges to $\theta_\nu = 0$ as they go outward. The middle panel presents the result at $t = 2.5 \times 10^{-4}$ s for the Schwarzschild spacetime. Note that the neutrino source is located outside the the photon sphere, the radius of which is 16 km in the present test. The neutrinos emitted from this source with $p_r = 0$ move outward. The outward radial propagation of neutrinos is slower in this case than in the flat case because of the geodesic deflection and the gravitational time delay. As a result, the radius-angle curve for the Schwarzschild spacetime is less steep than that for the flat spacetime. The right panel is the result at $t = 2 \times 10^{-4}$ s with the neutrino source located at $r = 15$ km, i.e., inside the photon sphere in the Schwarzschild spacetime. This time, the trajectory is directed radially inward and, as a result, θ_ν approaches $\theta_\nu = \pi$, instead of 0. The distributions are consistent with the reference curves although there are some numerical diffusions.

Just as in the energy advection tests in section C.1.1, we quantify the numerical diffusion as follows:

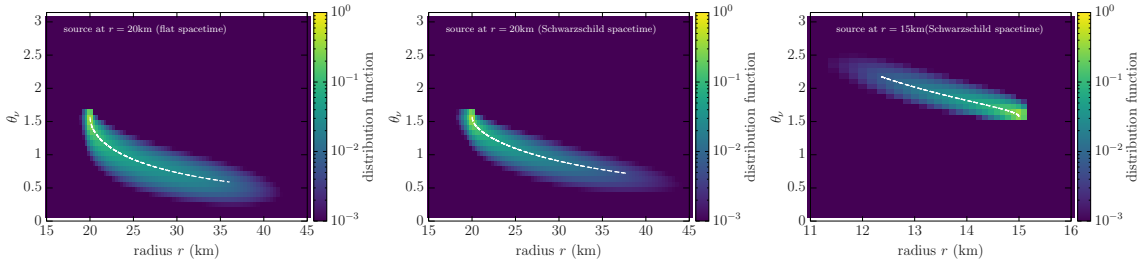

Figure C.4: Angular distributions in momentum space as a function of the radius r. The white dashed curves show the reference geodesic curves, drawn from the source to the radius that the massless particles reach at the time of the snapshot. The left panel is the result for the flat spacetime at $t = 1 \times 10^{-4}$ s, with the source placed at $r = 20\,\mathrm{km}$. The middle and right panels are the results in the Schwarzschild spacetime at $t = 2.5 \times 10^{-4}\,\mathrm{s}$ and $t = 2 \times 10^{-4}\,\mathrm{s}$ with the sources located at $r = 20\,\mathrm{km}$ (outside the photon sphere) and $r = 15\,\mathrm{km}$ (inside the photon sphere), respectively.

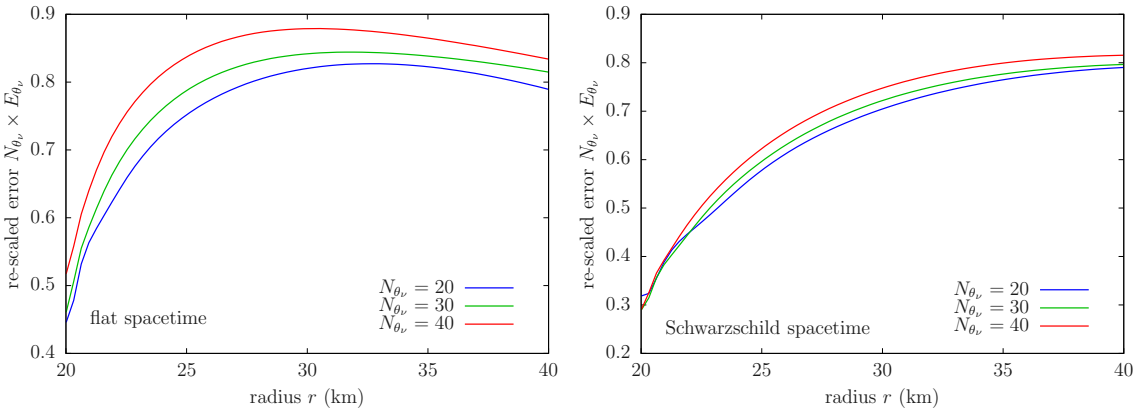

Figure C.5: Radial profiles of the re-scaled error function defined in the text. The left and right panels are for the flat and Schwarzschild spacetimes, respectively. The blue, green, and red lines correspond to the different angular resolutions in momentum space: $N_{\theta_\nu} = 20$, 30, and 40.

we define the error function as

$$E_{\theta_\nu}(r) \equiv \frac{\sum_{n=1}^{N_{\theta_\nu}} f(r, (\theta_\nu)_n)((\theta_\nu)_n - (\theta_\nu)_{\mathrm{ref}})^2 (d\theta_\nu)_n}{\sum_{n=1}^{N_{\theta_\nu}} f(r, (\theta_\nu)_n) d\theta_\nu}, \tag{C.8}$$

where $(\theta_\nu)_n$ and $(d\theta_\nu)_n$ are the value of θ_ν at the n-th cell center and the width of the same cell, respectively; $(\theta_\nu)_{\mathrm{ref}}$ is the zenith angle for the reference geodesic curve. We evaluate this function both for the flat and Schwarzschild spacetimes.

Figure C.5 shows the radial profiles of the re-scaled error function, i.e., the error function multiplied by the number of angular mesh points N_{θ_ν}. The left and right panels show the results for the flat and Schwarzschild spacetimes, respectively. For both cases, the re-scaled errors for the different numbers of mesh points are close to each other, implying that our code is of first order in the angular advection. This is just as expected, since we adopt the first-order finite difference scheme for the angular advection terms.

It is also checked whether the above result is changed by the existence of the energy advection. Firstly, we re-do the same test as in section C.1.2 with the energy advection turned on. We deploy

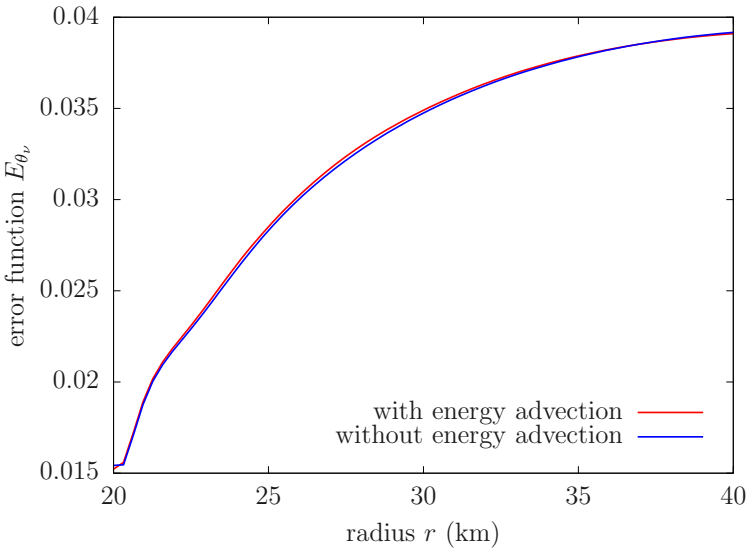

Figure C.6: Radial profiles of the error function for angular advection. The red curve indicates the result with both angular and energy advection taken into account, and the blue curve is the one only with angular advection, same as C.1.2.

the same mesh with $N_r = 128$, $N_\epsilon = 20$ and $N_{\theta_\nu} = 20$ and place neutrino steady source at $r = 20\,\mathrm{km}$ that emits neutrinos in a single angular bin closest to $\theta_\nu = \pi/2$ and a single energy bin at $\epsilon = 20\,\mathrm{MeV}$. The angular advection error E_{θ_ν} is calculated for the energy-integrated distribution function, and compared with the previous result without energy advection (see section C.1.2). Figure C.6 shows E_{θ_ν} as a function of radius for both cases. The results are very close to each other, implying that the inclusion of the energy advection does not affect the angular advection.

C.1.3 Tests with Continuous Distribution

Some readers may be concerned by the numerical diffusion seen in the previous tests. In fact, the grid-based code like this is not good at treating such discrete distribution. This is unlikely to be problematic, because the distribution in simulations are usually much continuous. Here, we consider a neutrino source that has smooth, extended energy and angular distributions in order to demonstrate that the numerical diffusion behavior is reduced for smoother distributions. We set the following distribution at the source:

$$f(x) = \begin{cases} \frac{1}{1+e^{(\epsilon-\mu)/kT}} \frac{1+\cos 2\theta_\nu}{2} & (\theta_\nu \leq \frac{\pi}{2}) \\ 0 & (\theta_\nu > \frac{\pi}{2}) \end{cases}, \tag{C.9}$$

where we choose the parameters as $\mu = 20\,\mathrm{MeV}$ and $kT = 10\,\mathrm{MeV}$. We place this steady source at $r = 20\,\mathrm{km}$. We employ the same radial mesh with $N_r = 128$ as in the previous tests whereas we vary the number of grid points in the energy mesh that covers the range $\epsilon \in [0, 300]\,\mathrm{MeV}$ as $N_\epsilon = 10$ and 20; the cell number in the angular mesh is chosen to be either $N_{\theta_\nu} = 20$ or 40.

Neutrino emitter is placed at $r = 20\,\mathrm{km}$, and the Figure C.7 shows the angular-integrated energy distribution (top left panel), and angular distribution for the neutrino energy of $\epsilon = 5\,\mathrm{MeV}$ (top right panel) at $r = 40\,\mathrm{km}$. The dashed lines are the distributions at the source position while the solid lines give the analytic solutions (green) and the numerical results (blue for the lower resolution and red for the higher resolution). The bottom panels present the absolute values of errors. As can be seen, the energy spectrum is well reproduced already with 10 energy-grid points, which is actually smaller than

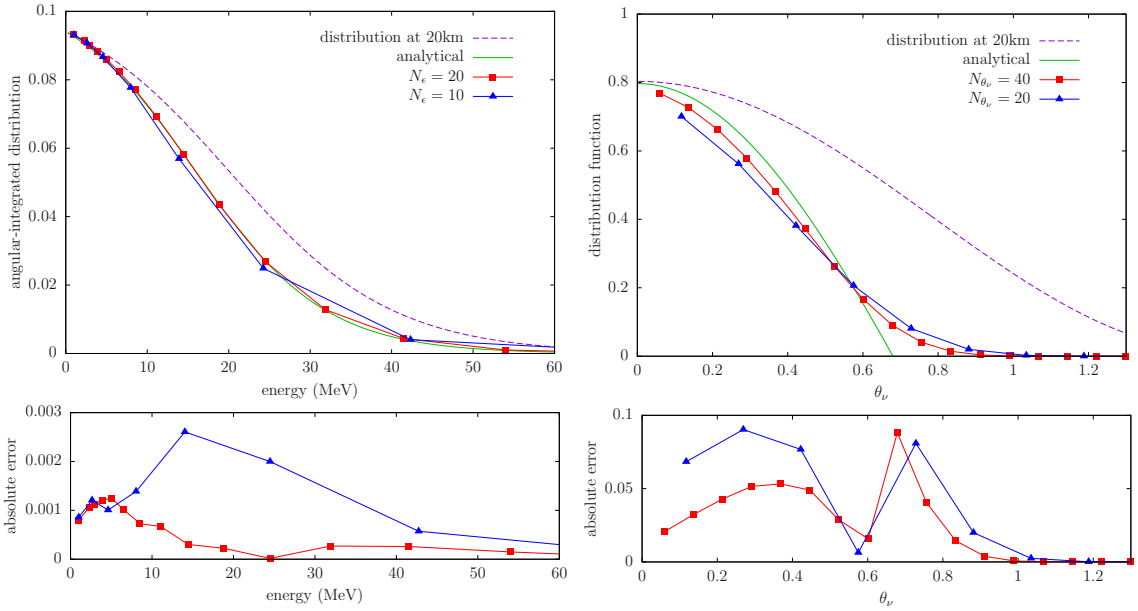

Figure C.7: The neutrino distributions in energy and momentum angle at 40 km. The top left panel shows the energy distribution of angular-integrated distribution function, and the top right panel shows the angular distribution of neutrinos with energy $\epsilon = 5$ MeV. The green curves indicates analytical values, where blue and red curves indicate the numerical results for low and high resolution, respectively. The distribution at 20 km (source position) are shown with purple dotted curves for comparison. The bottom panels show the absolute errors for energy and angular distribution.

the standard number employed in our recent CCSN simulations, and the numerical result gets even closer to the analytic solution with 20 energy-grid points. Such a converging feature is also seen for the angular distributions. The results of the above test for the smooth distribution suggest that 20 energy bins employed in our CCSN simulations are large enough whereas 10 angular bins in momentum space are not sufficient at large radii, where the angular distribution becomes forward-peaked as assumed in this test. This is actually a well-known problem and is consistent with the previous investigation by Richers et al. (2017). We note, however, that the number of these mesh points can be increased by a factor of 2 or more (depending on which number is increased) when the latest Japanese flagship supercomputer Fugaku is available soon, which is roughly ~ 40 times faster than K supercomputer which we used for the SN simulations so far.

C.2 Multi-dimensional Advection Tests

Our code is multi-dimensional in space. Here we test our code's capability to deal with the angular advection in space by calculating again the non-radial streaming of neutrinos in the Schwarzschild spacetime with this θ-advection explicitly taken into account.

C.2.1 2D Tests in the Schwarzschild Spacetime

We hence run the code in 2D under axisymmetry in this section. We compute the distribution function of neutrino on the ϕ-constant meridional plane. The initial condition is as follows: we set $f = 1$ for a single cell at $r = 30$ km and $\theta = \pi/2$ with $\theta_\nu = \pi/2$ and $\phi_\nu = \pi$ (i.e., moving in the

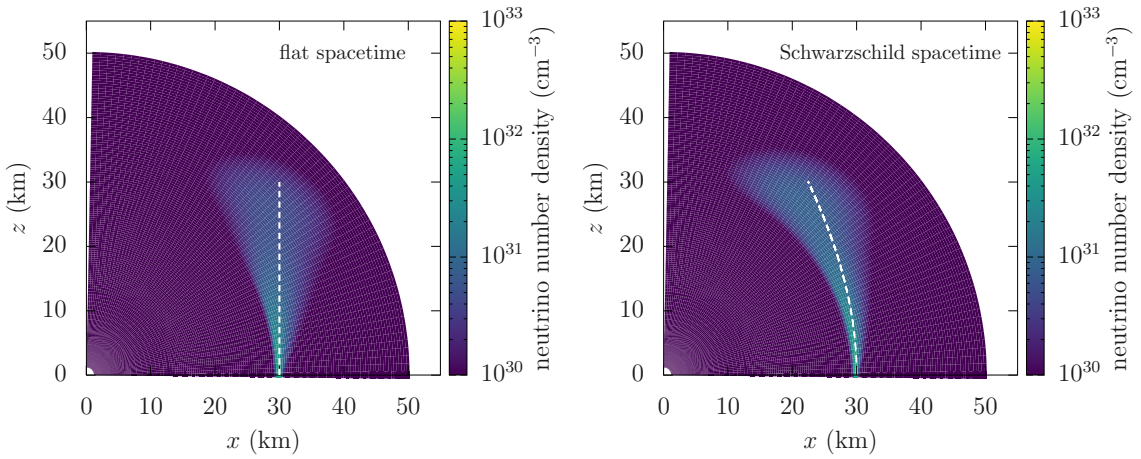

Figure C.8: Neutrino number densities on the meridional plane. The horizontal and vertical axes are $x = r\sin\theta$ and $y = r\cos\theta$, respectively.)

The white dashed lines depict the geodesic curves drawn from the source to the position that the massless particles reach at the time of the snapshot. The left panel shows the result for the flat spacetime at time $t = 1 \times 10^{-5}$ s, and the right panel is for the Schwarzschild spacetime at time $t = 1.3 \times 10^{-5}$ s.

positive z direction) in momentum space. Note that the neutrinos move along a geodesic curve also in this case that is essentially the same as the one in the previous test. We again switch off the energy advection in this test. Also, the ϕ_ν advection is switched off, since neutrinos following the geodesic do not advect in that direction, in the current setting.

The radial mesh is the same as in section C.1, with $N_r = 128$. In addition to this, we deploy the θ-mesh that has $N_\theta = 128$ bins, covering the range $\theta \in [0, \pi]$. As for the angular mesh in momentum space, we adopt $N_{\theta_\nu} = 10$, 20, and 40 to see the resolution dependence; the number of ϕ_ν-mesh points fixed to $N_{\phi_\nu} = 10$.

Figure C.8 shows the neutrino number density, i.e., the distribution function integrated over the momentum space, on the meridional plane for $N_{\theta_\nu} = 40$. The white dashed curve depicts the geodesic curve drawn from the source to the point that the massless particles reach at the time of the snapshot. The left panel is the result for the flat spacetime at the coordinate time $t = 1 \times 10^{-4}$ s, where the geodesic is the straight line parallel to the z axis. The right panel is for the Schwarzschild spacetime at $t = 1.3 \times 10^{-4}$ s. It is apparent that the geodesic is deflected by gravity in this case. In both cases, the numerically obtained distributions are consistent with the analytical curves. On the other hand, the broadening of the beam is also evident. Just as in the previous tests, this is partly because the the beam has a finite width from the beginning and partly because there are numerical diffusions. We now quantify the numerical diffusion. This time we look at the neutrino propagation speed, which should be the speed of light but the diffusion will affect it. For this purpose we first evaluate the number densities on the geodesic as a function of θ by linearly interpolating the values on the neighboring radial cells as follows:

$$N_{\rm int}(\theta) = \frac{(r_n - r(\theta))N_{n-1}(\theta) + (r(\theta) - r_{n-1})N_n(\theta)}{r_n - r_{n-1}}, \tag{C.10}$$

where $N_n(\theta)$ is the neutrino number density on the n-th radial mesh point for the given θ, and $r(\theta)$ is the radial coordinate of the geodesic curve at the same angle θ. We parametrize the geodesic not with

θ but with the "light-traveling distance" defined as

$$\int \sqrt{g_{00}^{-1}(g_{11}dr^2 + g_{22}d\theta^2)}, \tag{C.11}$$

where $g_{\mu\nu}$ is the spacetime metric and the integration runs from the source to a point on the geodesic curve. This quantity has a simple physical interpretation: the light speed times the coordinate time it takes a massless particle to reach the point.

Figure C.9 shows the number density profile for different time steps along the geodesic obtained with equation C.10 and parametrized with the light-traveling distance in equation C.11. The upper and lower panels show the results for the flat and Schwarzschild spacetimes, respectively. The dashed lines indicate the exact results. Although the number density is not constant owing to the beam broadening and there are some superluminal diffusions, the distribution declines rapidly ahead of the exact position and we may hence say that the propagation velocity is roughly consistent with the speed of light. We finally study the resolution dependence, defining the following error function to quantitatively estimate the numerical diffusion:

$$E_{r\theta}(\theta) \equiv \frac{\sum_{m=1}^{N_r} N_n(\theta)(r_n - r(\theta))^2 dr_n}{(r(\theta))^2 \sum_{n=1}^{N_r} N(r_n, \theta) dr_n}, \tag{C.12}$$

where r_n and dr_n are the radial coordinate at the center and the width of the n-th radial cell, respectively, and $r(\theta)$ is the radius of the point on the geodesic curve at θ.

Figure C.10 shows the re-scaled error function, which is defined as the error function in equation (C.12) multiplied by N_{θ_ν}; although the equation (C.12) is a function of θ, we employ the light-traveling distance to parametrize the geodesic in this figure. The left and right panels again present the results for the flat and Schwarzschild spacetimes, respectively. It is recognized that both cases roughly show the first-order convergence.

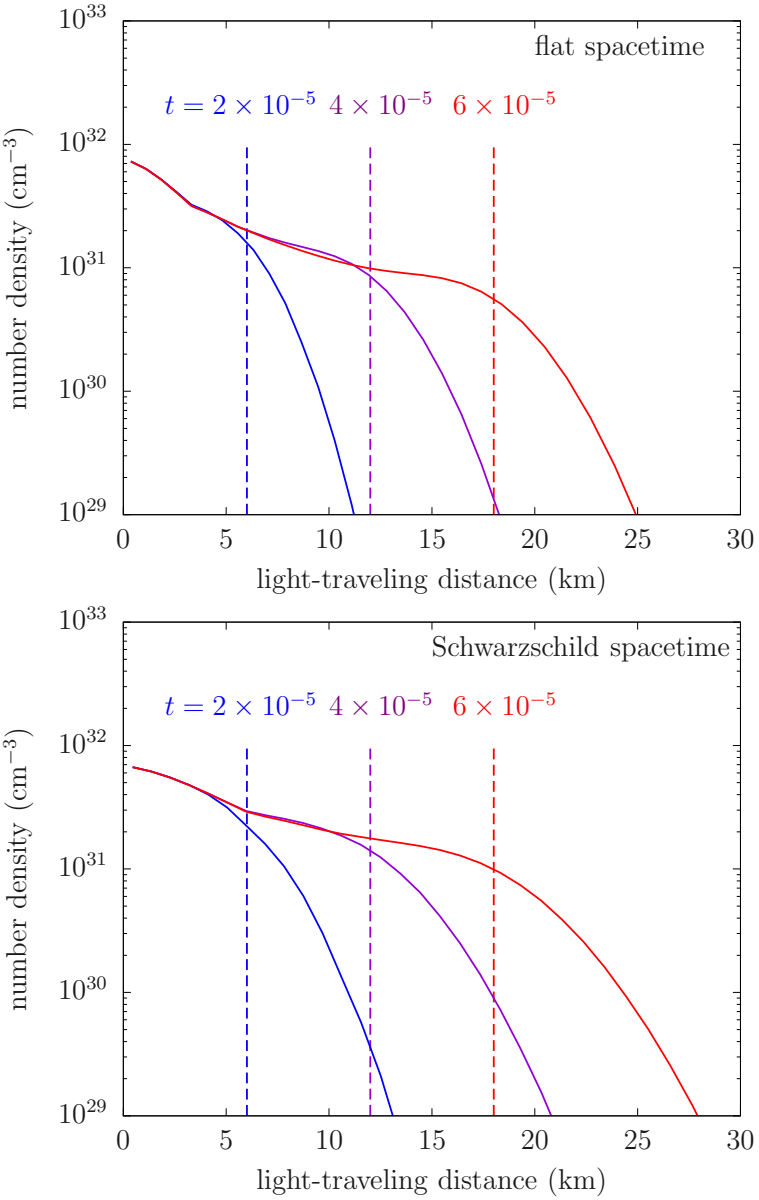

Figure C.9: The profiles of the neutrino number density along the geodesic curve at different coordinate times. The upper and lower panels show the results for the flat and Schwarzschild spacetimes, respectively. The colors denote the times: the blue, purple, and red correspond to $t = 2 \times 10^{-5}$, 4×10^{-5}, and 6×10^{-5} s, respectively; the dashed lines indicate the exact positions of the front edge of the geodesic curves at these times.

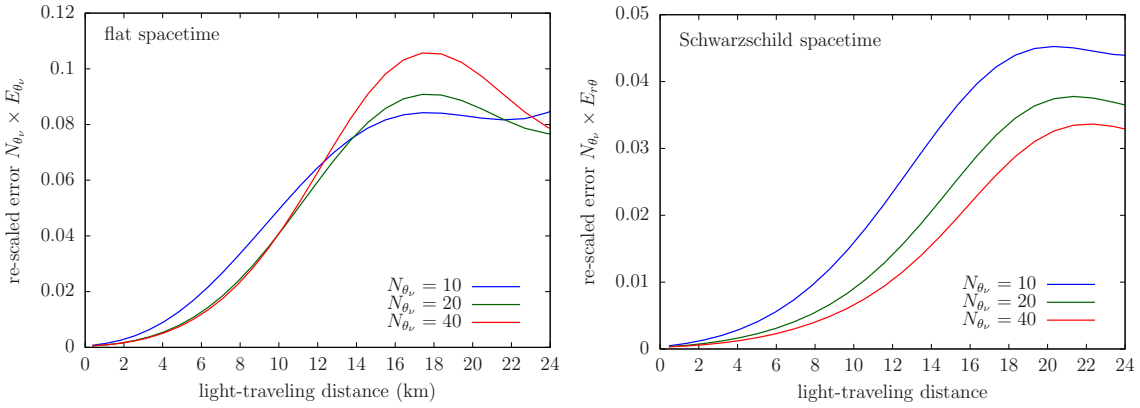

Figure C.10: The error function in equation (C.12) re-scaled with the number of angular mesh points N_{θ_ν}. The left and right panels show the results for the flat and Schwarzschild spacetimes, respectively. The blue, green, and red curves correspond to the errors for the $N_{\theta_\nu} = 10$, 20, and 40, respectively.

C.2.2 Tests in the Kerr Spacetime

We now move on to the advection tests in the Kerr spacetime. They are intended to demonstrate the applicability of our code to rotating BH spacetimes. We ignore all neutrino reactions again in this section.

We employ the Kerr-Schild coordinates:

$$\begin{aligned} ds^2 &= -\left(1-\frac{2GMr}{c^2\Sigma}\right)c^2dt^2+\frac{4GMr}{c^2\Sigma}\left[\frac{\Sigma}{r^2+a^2}dr-a\sin^2\theta d\phi\right]cdt \\ &+ \left(\frac{\Sigma}{r^2+a^2}+\frac{2GMr\Sigma}{c^2(r^2+a^2)^2}\right)dr^2+\Sigma d\theta^2+\frac{\Xi}{\Sigma}\sin^2\theta d\phi^2-\frac{4GMra}{c^2(r^2+a^2)}\sin^2\theta dr d\phi, \end{aligned} \tag{C.13}$$

where a is the BH spin parameter, and

$$\begin{aligned} \Sigma &= r^2+a^2\cos^2\theta, \\ \Xi &= (r^2+a^2)\Sigma+2GMa^2r\sin^2\theta/c^2. \end{aligned} \tag{C.14}$$

Note that there is no (apparent) singularity at the event horizon in these coordinates. Throughout this section, we choose $M=5M_\odot$ and $a=0.5GM/c^2$. The tetrad in equation (3.4) is explicitly given as follows:

$$\begin{aligned} e^\mu_{(0)} &= \frac{1}{\alpha}\left[\left(\frac{\partial}{\partial t}\right)^\mu-\beta^r\left(\frac{\partial}{\partial r}\right)^\mu-\beta^\phi\left(\frac{\partial}{\partial\phi}\right)^\mu\right], \\ e^\mu_{(1)} &= \frac{1}{\sqrt{\gamma_{rr}}}\left(\frac{\partial}{\partial r}\right)^\mu, \\ e^\mu_{(2)} &= \frac{1}{\sqrt{\Sigma}}\left(\frac{\partial}{\partial\theta}\right)^\mu, \\ e^\mu_{(3)} &= \frac{\gamma^{r\phi}}{\sqrt{\gamma^{\phi\phi}}}\left(\frac{\partial}{\partial r}\right)^\mu+\frac{1}{\sqrt{\gamma^{\phi\phi}}}\left(\frac{\partial}{\partial\phi}\right)^\mu, \end{aligned} \tag{C.15}$$

where the lapse function, shift vector, and inverse of the spatial metric are written as

$$\begin{aligned} \alpha &= \sqrt{\frac{c^2\Sigma}{c^2\Sigma+2GMr}}, \\ \beta^r &= \frac{2GMr}{c^2\Sigma+2GMr}, \\ \beta^\phi &= -\frac{2GMar}{(c^2\Sigma+2GMr)(r^2+a^2)}, \\ \gamma^{rr} &= \frac{c^2\Xi}{\Sigma(c^2\Sigma+2GMr)}, \\ \gamma^{r\phi} &= \frac{2GMar}{(c^2\Sigma+2GMr)(r^2+a^2)}, \\ \gamma^{\phi\phi} &= \frac{\Sigma(r^2+2GMr/c^2+a^2)}{(r^2+a^2)^2(\Sigma+2GMr/c^2)\sin^2\theta}, \end{aligned} \tag{C.16}$$

respectively. As mentioned in Shibata et al. (2014), there is no coordinate singularity if we use this tetrad in the Kerr-Schild coordinates.

For the Kerr spacetime, there is no simple differential equation to describe the geodesic curve unlike for the Schwarzschild spacetime. We hence solve the geodesic equation

$$\frac{d^2x^\mu}{d\lambda^2} = -\Gamma^\mu_{\alpha\beta}\frac{dx^\alpha}{d\lambda}\frac{dx^\beta}{d\lambda}, \tag{C.17}$$

where λ is the affine parameter. Since we consider the geodesic curves only on the equatorial plane, we solve the equations only for t, r, and ϕ. We employ the fourth order explicit Runge-Kutta for the following forms of equations:

$$\begin{aligned}
\frac{dt}{d\lambda} &= p^t, & \frac{dp^t}{d\lambda} &= -\Gamma^t_{\alpha\beta}p^\alpha p^\beta,\\
\frac{dr}{d\lambda} &= p^r, & \frac{dp^r}{d\lambda} &= -\Gamma^r_{\alpha\beta}p^\alpha p^\beta,\\
\frac{d\phi}{d\lambda} &= p^\phi, & \frac{dp^\phi}{d\lambda} &= -\Gamma^\phi_{\alpha\beta}p^\alpha p^\beta.
\end{aligned} \tag{C.18}$$

Here p^μ is the 4-momentum.

In the Kerr spacetime, the photon sphere for the prograde orbits with respect to the BH spin is given as

$$r_{\rm prog} = \frac{2GM}{c^2}\left\{1+\cos\left[\frac{2}{3}\cos^{-1}\left(\frac{c^2|a|}{GM}\right)\right]\right\}, \tag{C.19}$$

whereas for the retrograde orbits it is given as

$$r_{\rm ret} = \frac{2GM}{c^2}\left\{1+\cos\left[\frac{2}{3}\cos^{-1}\left(-\frac{c^2|a|}{GM}\right)\right]\right\}. \tag{C.20}$$

For the metric parameters, we employ the same values as the advection tests in section C.2.2; with $M = 5M_\odot$ and $a = 0.5GM/c^2$.

Figure C.11 shows some geodesic curves on the equatorial plane. The left panel exhibits four prograde geodesic curves with $p^r = 0$ at $r = 16$, 17, 18 and 19 km. The first two radii are smaller than that of the photon sphere, which is $r = 17.33$ km in the present case whereas the last two are larger. The photon sphere is indicated with the black circle in the figure. The right panel, on the other hand, presents some retrograde geodesic curves with $p^r = 0$ at $r = 25$, 26, 27, and 28 km. The photon sphere has the radius of $r = 26.07$ km in this case. It is found in both panels that the geodesic curves are confined either inside or outside the photon sphere.

As in section C.1.2, we perform the advection test by placing a point source in the Kerr spacetime. We treat the neutrino propagation only on the equatorial plane ($\theta = \pi/2$) as our main concern here is the dragging of inertial frame. We fix $f = 1$ for a single angular bin at the position of the point source and set $f = 0$ otherwise initially. The energy advection is turned off again in this case. We set the initial direction of neutrino momentum to $\phi_\nu = 3\pi/2$, i.e., the retrograde direction with respect to the BH spin, to maximize the frame-dragging effect. We further assume $p^r = 0$ to distinguish the geodesic curves outside the photon sphere from those inside clearly. There appears a bit complication then, because this does not correspond to $\theta_\nu = \pi/2$ for our choice of tetrad in the Kerr spacetime. That happens because the coordinate basis is not orthogonal. We need to find the value of θ_ν by solving the following equation:

$$p^r = \epsilon(e^1_{(0)} + e^1_{(1)}\cos\theta_\nu - e^1_{(3)}\sin\theta_\nu) = 0. \tag{C.21}$$

This yields, for example, $\theta_\nu = 0.9668$ for $r = 28$ km and $\theta_\nu = 0.7695$ for $r = 22$ km.

Throughout this test, the radial mesh is the same as in the previous tests, deploying $N_r = 128$ grid points. We vary the number of angular mesh points as $N_{\theta_\nu} = 30$, 40, and 60 to see the resolution dependence.

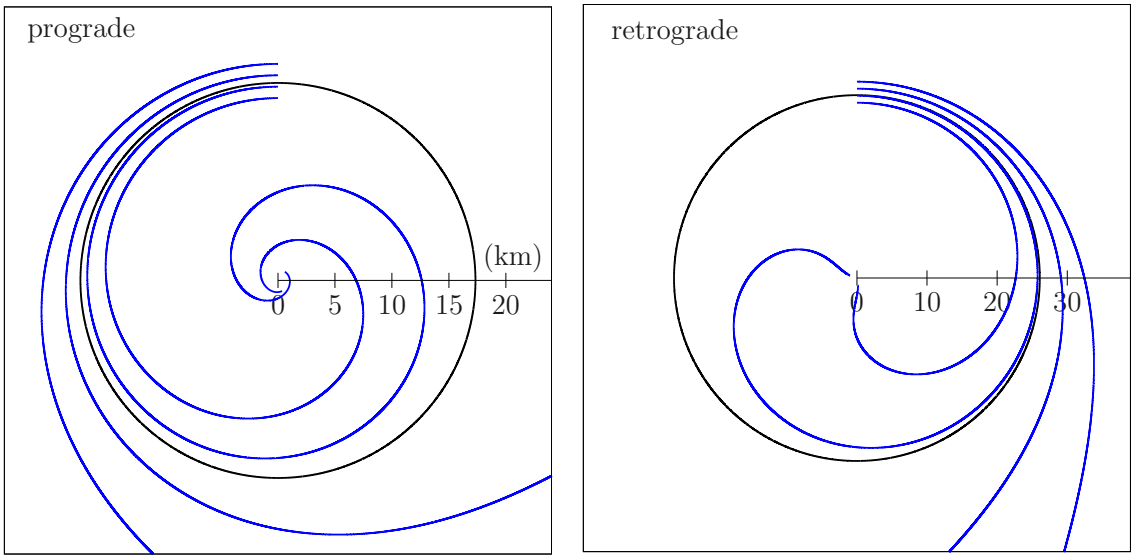

Figure C.11: Some geodesic curves on the equatorial plane in the Kerr spacetime. The mass and spin of BH are set to $M = 5M_\odot$ and $a = 0.5GM/c^2$, respectively. Left: prograde geodesic curves with $p^r = 0$ at $r = 16, 17, 18, 19\,\mathrm{km}$. Right: retrograde geodesic curves with $p^r = 0$ at $r = 25, 26, 27, 28\,\mathrm{km}$. The photon spheres are indicated as the black circles, the radius of which is 17.33 km and 26.07 km for the prograde and retrograde orbits, respectively.

Figure C.12 shows the angular distribution in momentum space as a function of the radius r for $N_{\theta_\nu} = 60$. The white dashed curve is the reference geodesic curve calculated in appendix C.2.2, drawn from the source to the radius that the massless particles reach at the time of the snapshot. The left panel shows the result at the coordinate time $t = 4 \times 10^{-4}\,\mathrm{s}$ with the source located at $r = 28\,\mathrm{km}$. In this case, the source is sitting outside the photon sphere ($r = 26\,\mathrm{km}$) and the neutrinos propagate radially outward. The right panel shows the result at $t = 1.5 \times 10^{-4}\,\mathrm{s}$ with the source located at $r = 22\,\mathrm{km}$, i.e., inside the photon sphere, and the geodesic goes radially inward. The broadening of the beam is again apparent, which is inevitable as the mesh size is finite, and in the latter case, in particular, there are a fraction of neutrinos going radially outward due to the numerical diffusion. Nevertheless, most of neutrinos propagate consistently with the geodesic curves in both cases. We may hence claim that our code can handle the advection also in the rotating spacetime.

We look at the neutrino propagation speed. Since our computation does not take the ϕ advection into account directly thanks to the axisymmetry, we inspect the radial propagation. The geodesic is again parametrized by the light-traveling distance defined in the current case as

$$\int (g_{00})^{-1}[-(g_{01}dr + g_{03}d\phi) \\ -\sqrt{(g_{01}dr + g_{03}d\phi)^2 - g_{00}(g_{11}dr^2 + g_{33}d\phi^2 + 2g_{13}drd\phi)}\,]. \tag{C.22}$$

It has the same physical interpretation as in the Schwarzschild spacetime (equation (C.11)). Figure C.13 shows the profiles of the number density along the geodesic as a function of the light-traveling distance. Although the the results are consistent with the propagation at the speed of light, the numerical diffusion is more remarkable than in the flat or Schwarzschild spacetime. This is due to the slower radial propagation of neutrinos in the current case, which is in turn caused by the frame-dragging in the rotating spacetime. Recall that we are considering the retrograde advection here.

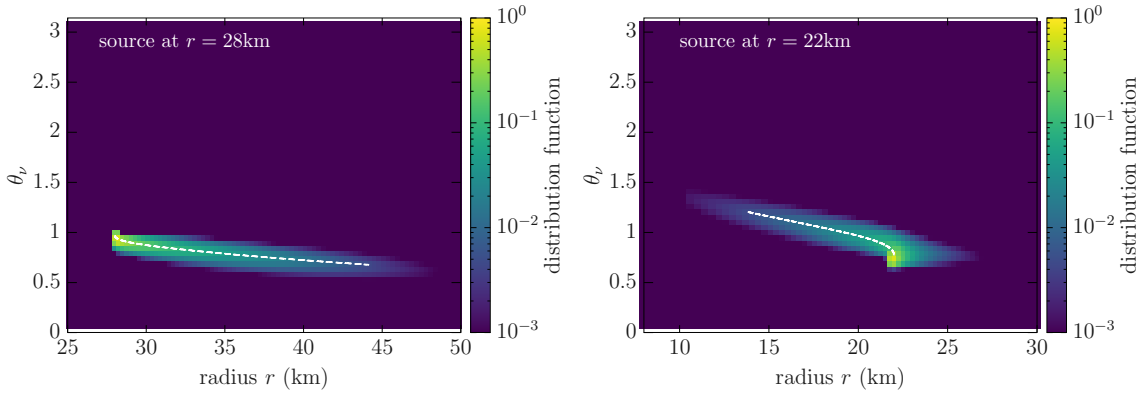

Figure C.12: Angular neutrino distributions along the geodesic curve on the equatorial plane as a function of the radius r in the Kerr spacetime. The left panel is the result at time $t = 4 \times 10^{-4}$ s, with the source located at $r = 28$ km outside the photon sphere. The right panel is the result at time $t = 1.5 \times 10^{-4}$ s, with the source located at $r = 22$ km inside the photon sphere. The white dashed curves are the reference geodesic curves, drawn from the source to the radius that the massless particles reach at the time of the snapshot.

Using the error function given in equation (C.8), we show in figure C.14 the re-scaled error function for the advection test in the Kerr spacetime. It is apparent that the error scales linearly with the number of angular mesh points just as in the previous tests in the flat or Schwarzschild spacetime.

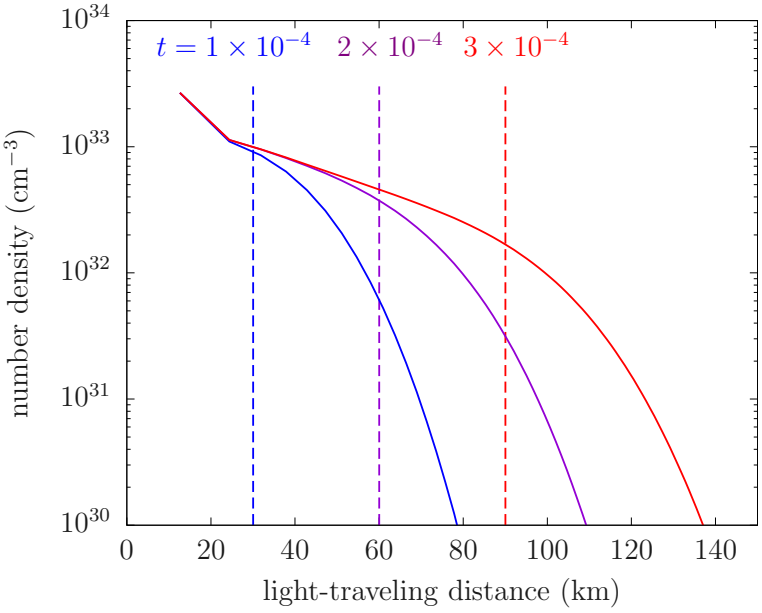

Figure C.13: The profiles of neutrino number density along a geodesic curve in the Kerr metric at three different coordinate times: the blue, purple, and red colors correspond to $t = 1 \times 10^{-4}$, 2×10^{-4} and 3×10^{-4} s, respectively. The dashed lines show the exact positions that the massless particles reach at these times.

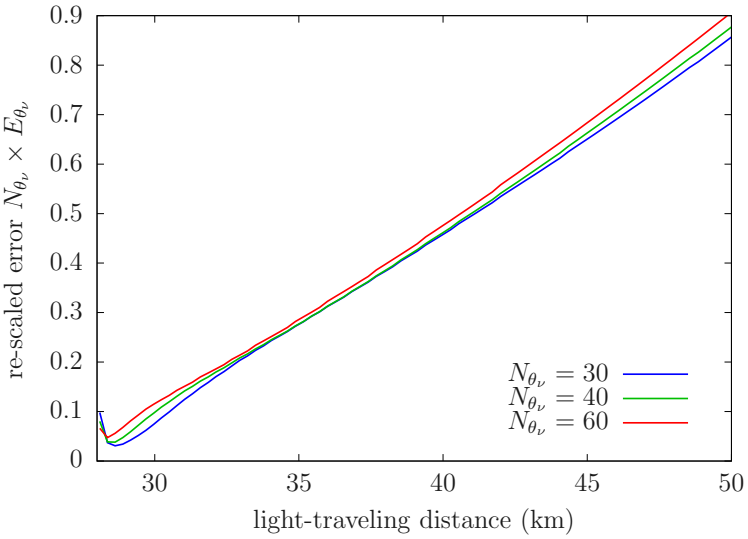

Figure C.14: Radial profiles of the error function re-scaled with the number of angular mesh points N_{θ_ν}. The blue, green, and red colors are the results for the different mesh numbers $N_{\theta_\nu} = 30$, 40, and 60, respectively.

C.3 Tests Including Collision Terms

We have so far conducted various verification tests in the free-streaming limit alone. This is because the computation of advection is the most challenging numerically for mesh-based codes like ours. In the actual astrophysical simulations, collision terms of the Boltzmann equation are also important. In this section, we perform a test that takes into account interactions of neutrinos with matter.

We fix the background matter distribution and compute with our new code the neutrino distribution that approaches a steady state. Since the collision terms are the focus of this test, we assume spherical symmetry again. As a reference, we employ the results obtained with another spherically symmetric, general relativistic Boltzmann solver (hereafter 1D GR code) developed by Sumiyoshi et al. (2005). We run these two Boltzmann solvers for the same (fixed) matter distribution until the steady states are achieved. As for the matter distribution, we pick up a snapshot at 100 ms after bounce in the CCSN simulation by Sumiyoshi et al. (2005) with the $15\,M_\odot$ model of Woosley & Weaver (1995). It allows us to test the neutrino propagation in a wide range of mean free path. The major neutrino-matter reactions are the same for both simulations, the rates of which are based on Bruenn (1985). The explicit expressions of the collision terms are identical to those described in Sumiyoshi & Yamada (2012). The chemical potential profile is also common because it affects the reaction rates: it is calculated from Shen equation of state (Shen et al., 1998). In the 1D GR code, the hydrodynamics variables as well as the spacetime metric are the functions of the enclosed mass as it is a Lagrangian code. However, the fluid velocity is fixed to zero. They are transformed into the functions of the radius when they are implemented in the new code.

The numbers of the radial mesh points are the same for the two codes: the radial mesh has $N_r = 256$ grid points, which covers the range $r \in [0, 10^4]\,\mathrm{km}$. As for the momentum space, we adopt $N_{\theta_\nu} = 6$ and $N_\epsilon = 14$. The latter mesh covers $\epsilon \in [0, 300]\,\mathrm{MeV}$. The reader may be worried that the resolution employed here are relatively lower compared to the advection tests in sections C.1.2 and C.2.2, or recent core collapse simulations. This is no problem, since our purpose is the regression test, i.e. to confirm that the collision terms work properly.

Figure C.15 shows the radial profiles of the electron-type neutrino number density for our new code and the 1D GR code (upper panel), as well as the relative difference with respect to the latter result (lower panel). The shock wave is located at $r = 174\,\mathrm{km}$, at which a small bump can be seen. It is apparent that they are in a reasonable agreement with the overall relative error of $\sim 10\%$ ($\sim 14\%$ at the maximum). It is particularly small $\sim 1\%$ near the center ($r \lesssim 10\,\mathrm{km}$), where the neutrino distribution is close to that of thermal equilibrium.

It should be noted that the above comparison does not tell which code is more accurate. To get some hints, we compare them with the equilibrium number densities, which are obtained by the energy integration of the Fermi–Dirac distribution. Figure C.16 shows the relative deviation of the neutrino number density obtained with each of the two codes from the equilibrium density. As is clear, the difference is much smaller for the new code in the very optically thick regime. It is thought to come from the different way of evaluating the equilibrium distribution for the calculation of the reaction kernels. The 1D GR code simply calculates the equilibrium distribution by the value of energy at the center of the cell, whereas the new code derives the equilibrium value as the average over a energy bin, by dividing it into subgrid. Incidentally, neither result is very accurate at large radii because of the rather coarse angular resolutions employed.

Finally, we give some results of the comparison with the M1 closure. Although the basics was explained in section 2.2, the basics is repeated here. In the neutrino transport with the M1 closure, second angular moment P^{ij} of the distribution function in momentum space is given as the interpolation of the optically thin and thick limits:

$$P^{ij}(\epsilon) = \frac{3\chi - 1}{2} P^{ij}_{\mathrm{thin}}(\epsilon) + \frac{3(1-\chi)}{2} P^{ij}_{\mathrm{thick}}(\epsilon), \tag{C.23}$$

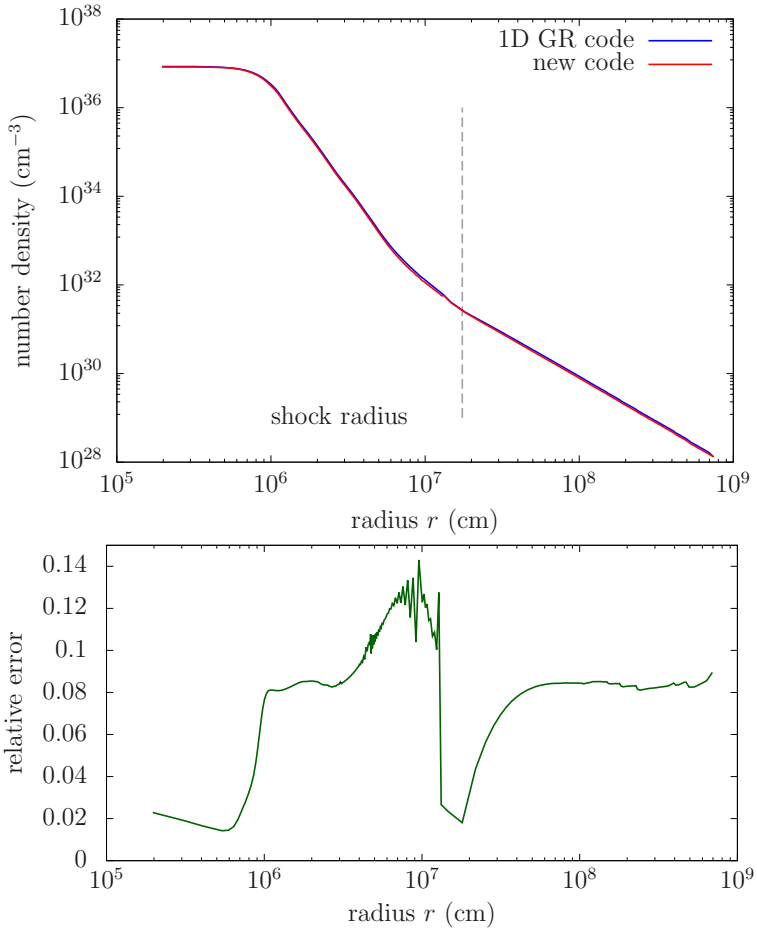

Figure C.15: Radial profiles of the electron-type neutrino number density for the 1D code and the new code (upper panel) and their relative errors (lower panel). The blue and red curves in the upper panel represent the results for the 1D GR and new codes, respectively.

where the optically thin and thick limits are given as

$$P^{ij}_{\rm thin}(\epsilon) = E(\epsilon)\frac{F^i(\epsilon)F^j(\epsilon)}{\gamma_{kl}F^k(\epsilon)F^l(\epsilon)}, \quad P^{ij}_{\rm thick}(\epsilon) = \frac{\delta^{ij}}{3}, \tag{C.24}$$

respectively, where $E(\epsilon)$ and $F^i(\epsilon)$ are the energy density and flux, respectively. Note that we only treat the case where fluid velocity is zero throughout this discussion. The Eddington factor χ is given, for example, as (Levermore, 1984)

$$\chi = \frac{3+4\bar{F}^2}{5+2\sqrt{4-3\bar{F}^2}}, \tag{C.25}$$

where the flux factor $\bar{F}$ may be calculated as (Shibata et al., 2011)

$$\bar{F} = \frac{\sqrt{\gamma_{ij}F^i(\epsilon)F^j(\epsilon)}}{E(\epsilon)}. \tag{C.26}$$

In the Boltzmann transport, the second moment can be directly calculated from the distribution function, and in spherical symmetry, the Eddington factor is $\chi = k^{rr}$, where $k^{ij}(\epsilon) = P^{ij}(\epsilon)/E(\epsilon)$ is the Eddington tensor.

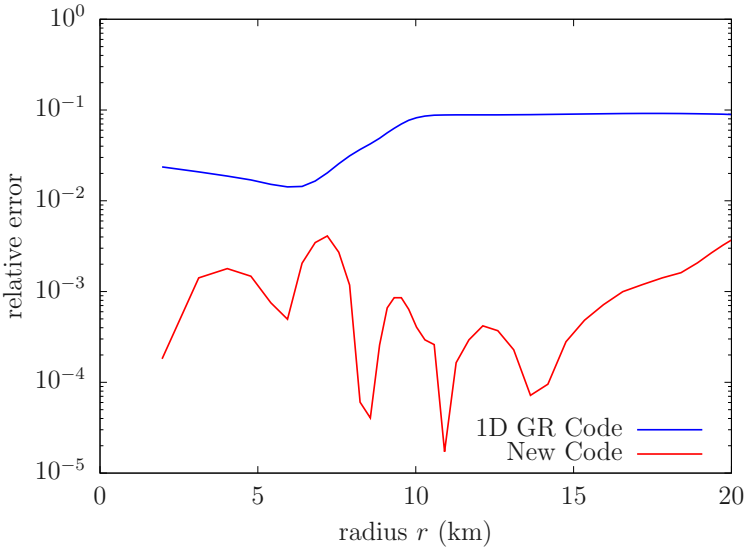

Figure C.16: Relative deviations of the simulated neutrino number densities from the equilibrium values. The blue and red curves represent the results for the 1D GR and new codes, respectively.

Figure C.17 shows the radial profiles of the Eddington factors obtained directly by the Boltzmann solver (solid lines) and approximately with the M1 closure relation (dashed lines). It is observed that the M1 closure tends to give larger values than the Boltzmann solver; the latter with lower angular resolutions tends to underestimate the Eddington factor particularly at large radii where the neutrino angular distribution becomes forward-peaked; the M1 closure fails, on the other hand, in the semi-transparent region $\sim 140\,\mathrm{km}$. All these results are quantitatively consistent with those found in our previous studies in the Minkowski spacetime (Harada et al., 2019). It is worth mentioning that, however, that this is not a true comparison between the Boltzmann transport and the two-moment transport with the M1 closure. In this analysis of the M1 closure approximation, the Eddington factor is calculated from the energy density and the flux obtained by the Boltzmann solver. In actual two-moment transport, they should be computed on their own and errors may be accumulated with time and could be larger than suggested in figure C.17. In the mean time, 10 grid points in θ_ν is not sufficient in our Boltzmann solver and should be doubled or more, which has actually come in sight.)

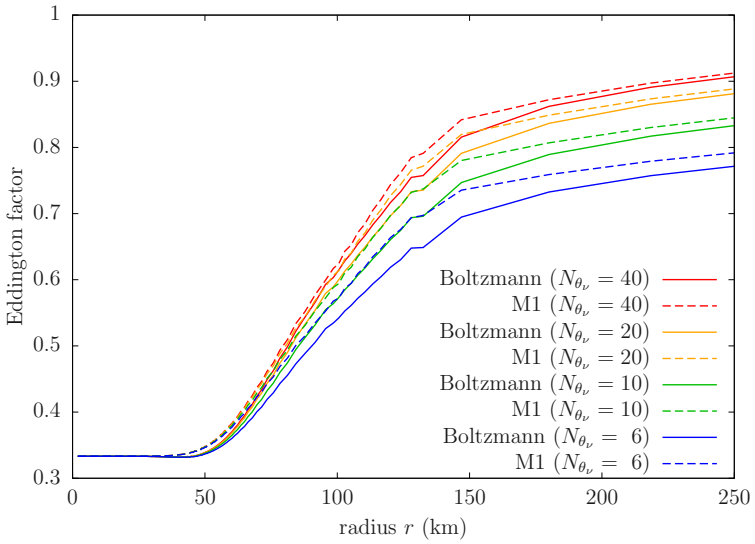

Figure C.17: Radial profiles of the Eddington factor. The solid curves and dotted curves correspond to Boltzmann and M1, respectively. Different colors indicate the numbers of angular mesh points: blue, green, orange and red curves are for $N_{\theta_\nu} = 6$, 10, 40, respectively.

Appendix D

Code Tests of the Hydrodynamics Solver

In this chapter, we provide the code tests for the GR hydrodynamics solver. In the extension, two important points appear matter motion close to the speed of light, and the matter motion under strong gravitational field.

D.1 Special Relativistic Shock Tube Tests

Since our previous code was for Newtonian hydrodynamics, the matter with relativistic motion could not be treated properly. Here, we perform the special relativistic shock tube tests. As the initial state, we employ the first case in Nagakura et al. (2011). The initial left state is $(\rho, v, p) = (10, 0, 13.3)$, and the right state is $(\rho, v, p) = (1, 0, 10^{-6})$. Since those values are for the geometrical unit, the input hydrodynamics quantities should be re-scaled for our code written in cgs unit. If the length conversion factor is defined as L, the conversion are like: $\rho_{\rm cgs} = \rho \times c^2/G \times L^2$, $p_{\rm cgs} = p \times c^4/G \times L^2$, $v_{\rm cgs} = v \times c$ and $t = L/c$. We choose the value $L = 1 \times 10^6$ cm. We employ the gamma-law EOS with the adiabatic index $\Gamma = 5/3$. Analytical solution can be exactly calculated by (Pons et al., 2000).

Since our code employs the polar coordinates, in principle, we cannot perform this test meant for the Cartesian coordinates. Similarly to Yamada et al. (1999), we simulate in a very thin shell where the curvature can be ignored. The initial discontinuity is placed at the radius $r = 10^5$ km, and the width of the computational domain is 10 km, which is four-orders of magnitude smaller than the distance from the origin. In order to check the resolution dependence, we test three mesh; 100, 200, and 400 grid points. The computational region is equally divided.

Figure D.1 shows the hydrodynamic quantities at the time snapshot $t = 1.5 \times 10^{-5}$ s. The analytical solution is well reproduced for all resolutions. In addition, raising the resolution improves the result, which indicates the resolution convergence of our code.

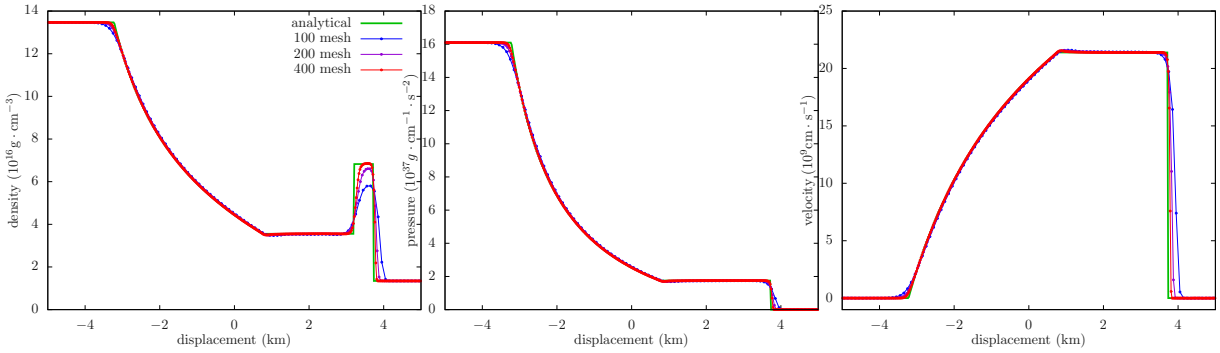

Figure D.1: Radial distributions of the density (left), the pressure (middle), and the velocity (right). The red, purple, and the blue lines denote the results for 400 mesh, 200 mesh, and 100 mesh, respectively.

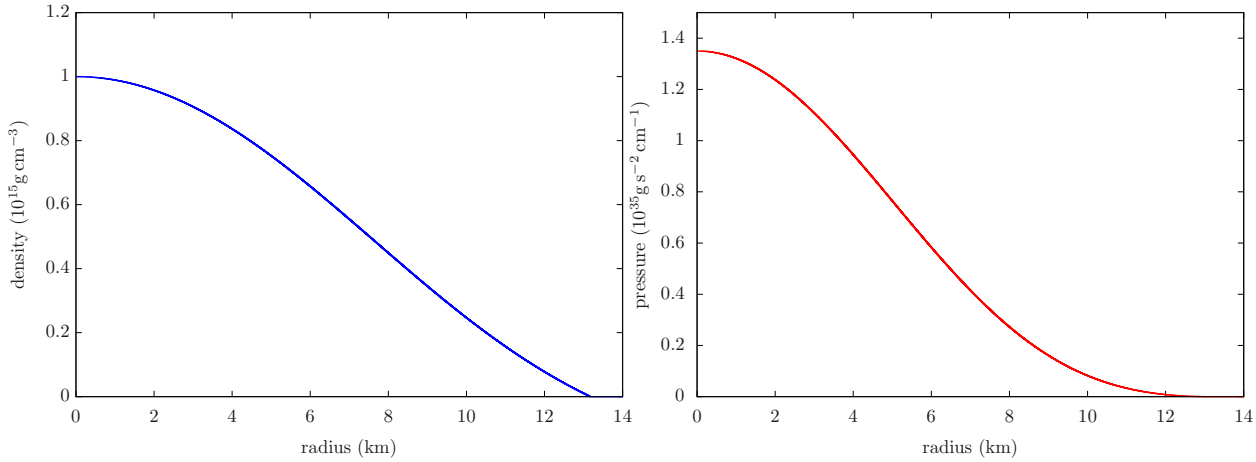

Figure D.2: Radial profile of density (left) and the pressure (right) for the initial model.

D.2 Stability test of Neutron Star

We check the code's ability to test matter under a strong gravitational field. By starting from the stable neutron star model as the initial condition, we check that the initial state is maintained by time evolution.

We constructed a neutron star model with a central density of 1×10^{15} g cm^{-3} and the central pressure of $p = 1.35 \times 10^{35}$ g cm^{-1} s^{-2}. We employ the gamma-law EOS with the adiabatic index of $\Gamma = 2$. We solve the TOV equations by using the fourth-order explicit Runge-Kutta method. This results in the neutron star with mass $1.42 M_\odot$ and the radius 13.2 km. The density and the pressure distributions are shown in figure D.2. In order to check the resolution dependence, we test three mesh cases; $N_r = 128$, 256, and 384 grid points. The computational region is $r \in [0 : 15]$ km, and it is equally divided. TOV equation is solved to construct the neutron star.

Figure B.3 shows the time evolution of the relative error of density for different radii. The error for $N_r = 128$ increases with time. On the other hand, the error for $N_r = 256$ and 384 shows the oscillation around the initial data. The amplitude of the oscillation is smaller for the highest resolution case. Hence we can conclude that resolution convergence is obtained for this test.

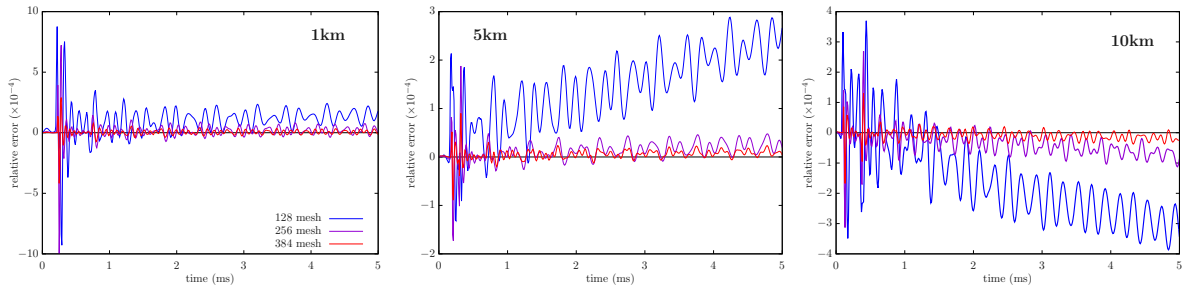

Figure D.3: Relative error of density for different spatial positions; 1km (left), 5km (middle), and 10km (right). Red, purple and blue lines denote the results for 384 mesh, 256 mesh, and 128 mesh, respectively.

D.3 Stability Test of Black Hole Accretion

In this test, we test code's ability to treat matter with relativistic speed under a strong gravitational field. We will perform tests for the matter accreting onto a Kerr BH. Similarly to the previous test in section D.2, we start from a stable state and check that the initial state is maintained with time evolution.

We constructed the reference model in the following way. If we assume steady state and limit the motion only on the equatorial plane ($\theta = \pi/2$), the matter equations around a Kerr BH reduce to the ordinary differential equations with respect to radius (Nagakura & Yamada, 2009):

$$\partial_r \left(r^2 \rho u^r\right) = 0, \tag{D.1}$$

$$\partial_r p + \rho_0 u^r \partial_r (h u_r) = \frac{1}{2}\rho_0 h \left\{\partial_r g_{rr} (u^r)^2 + \partial_r g_{\phi\phi} (u^\phi)^2 + \partial_r g_{tt} (u^t)^2 + 2\partial_r g_{t\phi} u^t u^\phi\right\}, \tag{D.2}$$

$$\partial_r (h u_t) = 0, \tag{D.3}$$

$$\partial_r (h u_\phi) = 0. \tag{D.4}$$

Note that Boyer–Lindquist coordinates are used for the Kerr metric.

By explicitly expanding the specific enthalpy by the pressure, the equation D.2 can be rewritten as the equation with a single pressure derivative term as following:

$$\frac{dp}{dr} = \frac{\rho h u^r u_r/2 - \rho h (u^r)^2 g_{rr,r} + 2u^r h g_{rr} S_r/r^3}{1 + u^r u_r - u^r h g_r r S_r/(r^2 \Gamma p)}, \tag{D.5}$$

where $S_r \equiv r^2 \rho u^r$. We solve the equation D.5 using the fourth-order explicit Runge-Kutta method. The other equations D.1, D.3 and D.4 are used to calculate the four-velocity from the pressure.

In this test, we employ a BH with mass $M_{\rm BH} = 5M_\odot$ with dimensionless spin parameter 0.5. With these parameters, horizon is located at 13.8 km. We do not solve hydrodynamic equations inside the horizon, where the metric is singular. We employ the gamma-law EOS with $\Gamma = 4/3$ in this test.

The parameters for the hydrodynamics variables are as follows. We assume that the matter with the density $\rho = 1 \times 10^7\,{\rm g\,cm^{-3}}$ is constantly injected from the radius $r = 300\,{\rm km}$ with supersonic velocity $u^r = -1.2 c_s$ where c_s is the speed of sound $c_s \equiv \sqrt{\Gamma p/\rho}$. As for the specific angular momentum $\lambda = u_\phi/u_t$, we test three cases; $\lambda = 0$ (no rotation), $GM_{\rm BH}/c^2$ (prograde) and $GM_{\rm BH}/c^2$ (retrograde). Figure D.3 shows the initial hydrodynamics profiles for three cases. In the hydrodynamics calculation,

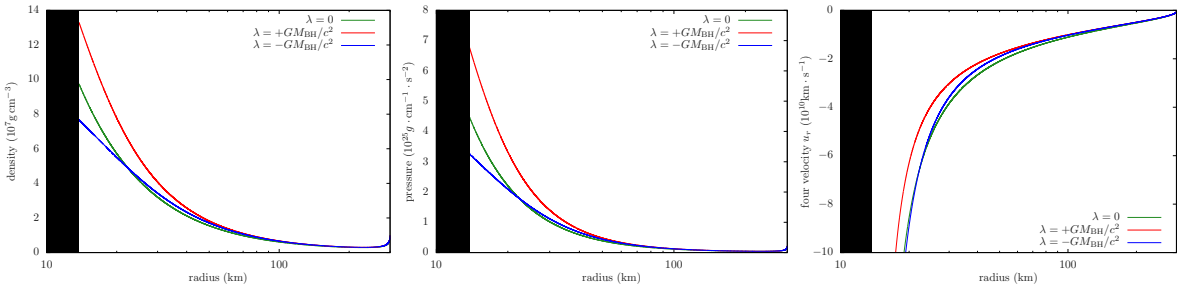

Figure D.4: Radial profiles of density (left), pressure (middle), and the r-component of the four velocity (right). The green, red, and blue lines denote the profiles for $\lambda = 0$, $\lambda = GM_{\rm BH}/c^2$ and $\lambda = -GM_{\rm BH}/c^2$, respectively. The black-shaded region shows the horizon of the central BH.

the outermost meshes are fixed to constantly inject the matter. As same as previous tests, we test three resolutions; $N_r = 128$, 256, and 384 grid points. The computational region is $r \in [0 : 300]\,{\rm km}$, and the mesh width is varied exponentially so that the resolution gets finer for smaller radius.

Fig. D.3 shows the time evolution of the relative error of density. The error at 20km is the order of $o(10^{-3})$, and the error at 50km is the order of $o(10^{-4})$. All calculations show reasonable agreement. In addition, the highest resolution case $N_r = 384$ gives the most accurate result, which indicates the resolution convergence.

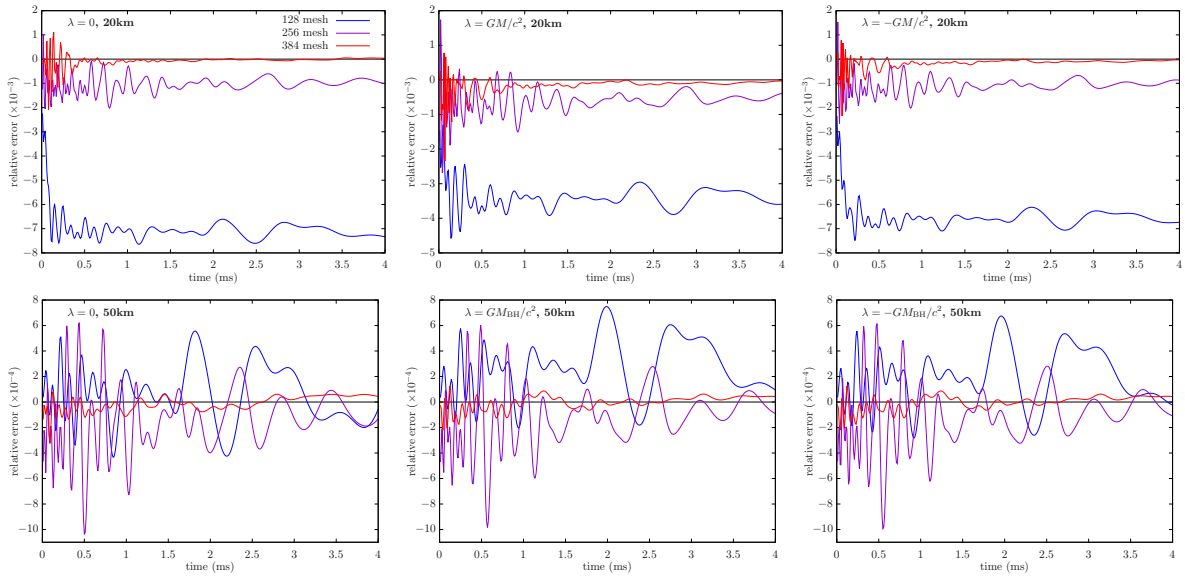

Figure D.5: Relative error of density for different specific angular momentum; non-rotating (left), prograde (middle), and retrograde (right). The spatial position are 20km (top) and 50km (bottom). Red, purple and blue lines denote the results for 384 mesh, 256 mesh, and 128 mesh, respectively.

Bibliography

Aartsen, M. G., Ackermann, M., Adams, J., et al. 2017, Journal of Instrumentation, 12, P03012, doi: 10.1088/1748-0221/12/03/P03012

Abbasi, R., Abdou, Y., Abu-Zayyad, T., et al. 2011, Astronomy & Astrophysics, 535, A109, doi: 10.1051/0004-6361/201117810

Abbott, B. P., Abbott, R., Adhikari, R., et al. 2009, Reports on Progress in Physics, 72, 076901, doi: 10.1088/0034-4885/72/7/076901

Abdikamalov, E., Pagliaroli, G., & Radice, D. 2022, Gravitational Waves from Core-Collapse Supernovae (Singapore: Springer Nature Singapore), 909–945, doi: 10.1007/978-981-16-4306-4_21

Abe, K., Bronner, C., Hayato, Y., et al. 2021, Phys. Rev. D, 104, 122002, doi: 10.1103/PhysRevD.104.122002

Abe, K., Bronner, C., Hayato, Y., et al. 2022, Nuclear Instruments and Methods in Physics Research A, 1027, 166248, doi: 10.1016/j.nima.2021.166248

Abe, S., Asami, S., Eizuka, M., et al. 2023, Physical Review Letters, 130, 051801, doi: 10.1103/PhysRevLett.130.051801

Abed Abud, A., Abi, B., Acciarri, R., et al. 2023, Physical Review D, 107, 112012, doi: 10.1103/PhysRevD.107.112012

Abi, B., Acciarri, R., Acero, M. A., et al. 2021, European Physical Journal C, 81, 423, doi: 10.1140/epjc/s10052-021-09166-w

Abrahamyan, S., Ahmed, Z., Albataineh, H., et al. 2012, Physical Review Letters, 108, 112502, doi: 10.1103/PhysRevLett.108.112502

Accadia, T., Acernese, F., Alshourbagy, M., et al. 2012, Journal of Instrumentation, 7, 3012, doi: 10.1088/1748-0221/7/03/P03012

Adhikari, D., Albataineh, H., Androic, D., et al. 2021, Physical Review Letters, 126, 172502, doi: 10.1103/PhysRevLett.126.172502

Akaho, R., Harada, A., Nagakura, H., et al. 2023, The Astrophysical journal, 944, 60, doi: 10.3847/1538-4357/acad76

Akutsu, T., Ando, M., Arai, K., et al. 2021, Progress of Theoretical and Experimental Physics, 2021, 05A103, doi: 10.1093/ptep/ptaa120

An, F., An, G., An, Q., et al. 2016, Journal of Physics G Nuclear Physics, 43, 030401, doi: 10.1088/0954-3899/43/3/030401

Arnett, W. D. 1977, The Astrophysical journal, 218, 815, doi: 10.1086/155738

Asakura, K., Gando, A., Gando, Y., et al. 2016, The Astrophysical journal, 818, 91, doi: 10.3847/0004-637X/818/1/91

Ashida, Y., Nakazato, K., & Tsujimoto, T. 2023, The Astrophysical journal, 953, 151, doi: 10.3847/1538-4357/ace3ba

Barrère, P., Guilet, J., Reboul-Salze, A., Raynaud, R., & Janka, H. T. 2022, Astronomy & Astrophysics, 668, A79, doi: 10.1051/0004-6361/202244172

Baumgarte, T. W., Montero, P. J., Cordero-Carrión, I., & Müller, E. 2013, Physical Review D, 87, 044026, doi: 10.1103/PhysRevD.87.044026

Bauswein, A., Just, O., Janka, H.-T., & Stergioulas, N. 2017, The Astrophysical journal Letters, 850, L34, doi: 10.3847/2041-8213/aa9994

Beacom, J. F., Farr, W. M., & Vogel, P. 2002, Physical Review D, 66, 033001, doi: 10.1103/PhysRevD.66.033001

Bethe, H. A., & Wilson, J. R. 1985, The Astrophysical journal, 295, 14, doi: 10.1086/163343

Bionta, R. M., Blewitt, G., Bratton, C. B., et al. 1987, Physical Review Letters, 58, 1494, doi: 10.1103/PhysRevLett.58.1494

Blondin, J. M., Mezzacappa, A., & DeMarino, C. 2003, The Astrophysical journal, 584, 971, doi: 10.1086/345812

Bollig, R., Janka, H. T., Lohs, A., et al. 2017, Physical Review Letters, 119, 242702, doi: 10.1103/PhysRevLett.119.242702

Bollig, R., Yadav, N., Kresse, D., et al. 2021, The Astrophysical Journal, 915, 28, doi: 10.3847/1538-4357/abf82e

Bruenn, S. W. 1985, The Astrophysical journal Supplement, 58, 771, doi: 10.1086/191056

Buras, R., Janka, H. T., Rampp, M., & Kifonidis, K. 2006, Astronomy & Astrophysics, 457, 281, doi: 10.1051/0004-6361:20054654

Burrows, A., Reddy, S., & Thompson, T. A. 2006, Nuclear Physics A, 777, 356, doi: 10.1016/j.nuclphysa.2004.06.012

Burrows, A., & Vartanyan, D. 2021, Nature, 589, 29, doi: 10.1038/s41586-020-03059-w

Burrows, A., Vartanyan, D., & Wang, T. 2023a, The Astrophysical journal, 957, 68, doi: 10.3847/1538-4357/acfc1c

Burrows, A., Wang, T., Vartanyan, D., & Coleman, M. S. B. 2023b, arXiv e-prints, arXiv:2311.12109, doi: 10.48550/arXiv.2311.12109

Cabezón, Rubén M., Pan, Kuo-Chuan, Liebendörfer, Matthias, et al. 2018, A&A, 619, A118, doi: 10.1051/0004-6361/201833705

Capozzi, F., Di Valentino, E., Lisi, E., et al. 2017, Physical Review D, 95, 096014, doi: 10.1103/PhysRevD.95.096014

Cardall, C. Y., Endeve, E., & Mezzacappa, A. 2013, Physical Review D, 87, 103004, doi: 10.1103/PhysRevD.87.103004

Chan, C., Müller, B., Heger, A., Pakmor, R., & Springel, V. 2018, The Astrophysical journal Letters, 852, L19, doi: 10.3847/2041-8213/aaa28c

Chandrasekhar, S. 1931, The Astrophysical journal, 74, 81, doi: 10.1086/143324

Chevalier, R. A. 1989, The Astrophysical journal, 346, 847, doi: 10.1086/168066

Christodoulou, D. 1991, Phys. Rev. Lett., 67, 1486, doi: 10.1103/PhysRevLett.67.1486

Colella, P., & Woodward, P. R. 1984, Journal of Computational Physics, 54, 174 , doi: http://dx.doi.org/10.1016/0021-9991(84)90143-8

Coleman, M. S. B., & Burrows, A. 2022, Monthly Notices of the Royal Astronomical Society, 517, 3938, doi: 10.1093/mnras/stac2573

Colgate, S. A. 1971, The Astrophysical journal, 163, 221, doi: 10.1086/150760

Colgate, S. A., & White, R. H. 1966, The Astrophysical journal, 143, 626, doi: 10.1086/148549

Couch, S. M. 2013, The Astrophysical journal, 775, 35, doi: 10.1088/0004-637X/775/1/35

Dasgupta, B., & Beacom, J. F. 2011, Physical Review D, 83, 113006, doi: 10.1103/PhysRevD.83.113006

Delfan Azari, M., Yamada, S., Morinaga, T., et al. 2020, Physical Review D, 101, 023018, doi: 10.1103/PhysRevD.101.023018

Dessart, L., Burrows, A., Livne, E., & Ott, C. D. 2006, The Astrophysical journal, 645, 534, doi: 10.1086/504068

Dexter, J., & Kasen, D. 2013, The Astrophysical journal, 772, 30, doi: 10.1088/0004-637X/772/1/30

Dighe, A. S., & Smirnov, A. Y. 2000, Physical Review D, 62, 033007, doi: 10.1103/PhysRevD.62.033007

Ehlers, J. 1971, in General Relativity and Cosmology, 1–70

Foglizzo, T., Galletti, P., Scheck, L., & Janka, H. T. 2007, The Astrophysical journal, 654, 1006, doi: 10.1086/509612

Friman, B. L., & Maxwell, O. V. 1979, The Astrophysical journal, 232, 541, doi: 10.1086/157313

Fryer, C. L. 2009, The Astrophysical journal, 699, 409, doi: 10.1088/0004-637X/699/1/409

Fryxell, B., Mueller, E., & Arnett, D. 1991, The Astrophysical journal, 367, 619, doi: 10.1086/169657

Fu, L., & Yamada, S. 2022, Phys. Rev. D, 105, 123028, doi: 10.1103/PhysRevD.105.123028

Fukuda, S., Fukuda, Y., Hayakawa, T., et al. 2003, Nuclear Instruments and Methods in Physics Research A, 501, 418, doi: 10.1016/S0168-9002(03)00425-X

Furusawa, S., & Nagakura, H. 2023, Progress in Particle and Nuclear Physics, 129, 104018, doi: 10.1016/j.ppnp.2022.104018

Furusawa, S., Togashi, H., Nagakura, H., et al. 2017, Journal of Physics G: Nuclear and Particle Physics, 44, 094001, doi: 10.1088/1361-6471/aa7f35

Glas, R., Janka, H. T., Capozzi, F., et al. 2020, Physical Review D, 101, 063001, doi: 10.1103/PhysRevD.101.063001

Goldberg, J. A., Bildsten, L., & Paxton, B. 2019, The Astrophysical journal, 879, 3, doi: 10.3847/1538-4357/ab22b6

Gossan, S. E., Fuller, J., & Roberts, L. F. 2020, Monthly Notices of the Royal Astronomical Society, 491, 5376, doi: 10.1093/mnras/stz3243

Hansen, R. S. L., Shalgar, S., & Tamborra, I. 2022, Physical Review D, 105, 123003, doi: 10.1103/PhysRevD.105.123003

Harada, A., & Nagakura, H. 2022, The Astrophysical journal, 924, 109, doi: 10.3847/1538-4357/ac38a0

Harada, A., Nagakura, H., Iwakami, W., et al. 2019, The Astrophysical Journal, 872, 181, doi: 10.3847/1538-4357/ab0203

Harada, A., Nagakura, H., Iwakami, W., et al. 2020, The Astrophysical journal, 902, 150, doi: 10.3847/1538-4357/abb5a9

Harada, A., Suwa, Y., Harada, M., et al. 2023a, The Astrophysical journal, 954, 52, doi: 10.3847/1538-4357/ace52e

Harada, M., Abe, K., Bronner, C., et al. 2023b, The Astrophysical journal Letters, 951, L27, doi: 10.3847/2041-8213/acdc9e

Harten, A., Lax, P. D., & van Leer, B. 1983, SIAM Review, 25, 35, doi: 10.1137/1025002

Herant, M., Benz, W., Hix, W. R., Fryer, C. L., & Colgate, S. A. 1994, The Astrophysical journal, 435, 339, doi: 10.1086/174817

Hirata, K., Kajita, T., Koshiba, M., et al. 1987, Physical Review Letters, 58, 1490, doi: 10.1103/PhysRevLett.58.1490

Horiuchi, S., & Kneller, J. P. 2018, Journal of Physics G Nuclear Physics, 45, 043002, doi: 10.1088/1361-6471/aaa90a

Horowitz, C. J. 2002, Physical Review D, 65, 043001, doi: 10.1103/PhysRevD.65.043001

Horowitz, C. J., Ahmed, Z., Jen, C. M., et al. 2012, Physical Review C, 85, 032501, doi: 10.1103/PhysRevC.85.032501

Hubeny, I., & Burrows, A. 2007, The Astrophysical journal, 659, 1458, doi: 10.1086/512179

Hyper-Kamiokande Proto-Collaboration, :, Abe, K., et al. 2018, arXiv e-prints, arXiv:1805.04163. https://arxiv.org/abs/1805.04163

Ikeda, M., Takeda, A., Fukuda, Y., et al. 2007, The Astrophysical journal, 669, 519, doi: 10.1086/521547

Iwakami, W., Okawa, H., Nagakura, H., et al. 2020, Simulations of the Early Post-Bounce Phase of Core-Collapse Supernovae in Three-Dimensional Space with Full Boltzmann Neutrino Transport. https://arxiv.org/abs/2004.02091

Janka, H. T. 1992, Astronomy & Astrophysics, 256, 452

Janka, H.-T., Wongwathanarat, A., & Kramer, M. 2022, The Astrophysical journal, 926, 9, doi: 10.3847/1538-4357/ac403c

Johns, L. 2023, Phys. Rev. Lett., 130, 191001, doi: 10.1103/PhysRevLett.130.191001

Johns, L., & Xiong, Z. 2022, Physical Review D, 106, 103029, doi: 10.1103/PhysRevD.106.103029

Johnston, S., Hobbs, G., Vigeland, S., et al. 2005, Monthly Notices of the Royal Astronomical Society, 364, 1397, doi: 10.1111/j.1365-2966.2005.09669.x

Johnston, S., Kramer, M., Karastergiou, A., et al. 2007, Monthly Notices of the Royal Astronomical Society, 381, 1625, doi: 10.1111/j.1365-2966.2007.12352.x

Juodagalvis, A., Langanke, K., Hix, W. R., Martínez-Pinedo, G., & Sampaio, J. M. 2010, Nuclear Physics A, 848, 454, doi: 10.1016/j.nuclphysa.2010.09.012

Just, O., Bollig, R., Janka, H.-T., et al. 2018, Monthly Notices of the Royal Astronomical Society, 481, 4786, doi: 10.1093/mnras/sty2578

Kato, C., Delfan Azari, M., Yamada, S., et al. 2015, The Astrophysical journal, 808, 168, doi: 10.1088/0004-637X/808/2/168

Kato, C., Ishidoshiro, K., & Yoshida, T. 2020, Annual Review of Nuclear and Particle Science, 70, 121, doi: 10.1146/annurev-nucl-040620-021320

Kato, C., Nagakura, H., Furusawa, S., et al. 2017, The Astrophysical journal, 848, 48, doi: 10.3847/1538-4357/aa8b72

Kato, C., Nagakura, H., & Johns, L. 2023, arXiv e-prints, arXiv:2309.02619, doi: 10.48550/arXiv.2309.02619

Kawaguchi, K., Fujibayashi, S., Shibata, M., Tanaka, M., & Wanajo, S. 2021, The Astrophysical Journal, 913, 100, doi: 10.3847/1538-4357/abf3bc

Keil, W., Janka, H. T., & Mueller, E. 1996, The Astrophysical journal Letters, 473, L111, doi: 10.1086/310404

Kuroda, T., Kotake, K., & Takiwaki, T. 2012, The Astrophysical Journal, 755, 11, doi: 10.1088/0004-637x/755/1/11

—. 2016, The Astrophysical Journal, 829, L14, doi: 10.3847/2041-8205/829/1/l14

Lang, R. F., McCabe, C., Reichard, S., Selvi, M., & Tamborra, I. 2016, Physical Review D, 94, 103009, doi: 10.1103/PhysRevD.94.103009

Langanke, K., & Martínez-Pinedo, G. 2000, Nuclear Physics A, 673, 481, doi: 10.1016/S0375-9474(00)00131-7

Langanke, K., Martínez-Pinedo, G., Sampaio, J. M., et al. 2003, Phys. Rev. Lett., 90, 241102, doi: 10.1103/PhysRevLett.90.241102

Latest Supernovae. 2024, Latest Supernovae

Lattimer, J. M. 2023, in Journal of Physics Conference Series, Vol. 2536, Journal of Physics Conference Series, 012009, doi: 10.1088/1742-6596/2536/1/012009

Lattimer, J. M., & Mazurek, T. J. 1981, The Astrophysical journal, 246, 955, doi: 10.1086/158989

Lattimer, J. M., & Swesty, D. F. 1991, N. Phys. A, 535, 331, doi: 10.1016/0375-9474(91)90452-C

Lentz, E. J., Bruenn, S. W., Hix, W. R., et al. 2015, The Astrophysical journal Letters, 807, L31, doi: 10.1088/2041-8205/807/2/L31

Levermore, C. 1984, Journal of Quantitative Spectroscopy and Radiative Transfer, 31, 149 , doi: https://doi.org/10.1016/0022-4073(84)90112-2

Li, S. W., Roberts, L. F., & Beacom, J. F. 2021, Physical Review D, 103, 023016, doi: 10.1103/PhysRevD.103.023016

Li, Y.-F., Vagins, M., & Wurm, M. 2022, Universe, 8, 181, doi: 10.3390/universe8030181

Liebendörfer, M., Mezzacappa, A., Thielemann, F.-K., et al. 2001, Physical Review D, 63, 103004, doi: 10.1103/PhysRevD.63.103004

Liebendörfer, M., Whitehouse, S. C., & Fischer, T. 2009, The Astrophysical Journal, 698, 1174, doi: 10.1088/0004-637x/698/2/1174

Lin, Y.-C., & Duan, H. 2023, Physical Review D, 107, 083034, doi: 10.1103/PhysRevD.107.083034

Lindquist, R. W. 1966, Annals of Physics, 37, 487 , doi: https://doi.org/10.1016/0003-4916(66)90207-7

Liu, J., Akaho, R., Ito, A., et al. 2023, Phys. Rev. D, 108, 123024, doi: 10.1103/PhysRevD.108.123024

Liu, J., Zaizen, M., & Yamada, S. 2023, arXiv e-prints, arXiv:2302.06263, doi: 10.48550/arXiv.2302.06263

MacFadyen, A. I., & Woosley, S. E. 1999, The Astrophysical journal, 524, 262, doi: 10.1086/307790

MacFadyen, A. I., Woosley, S. E., & Heger, A. 2001, The Astrophysical journal, 550, 410, doi: 10.1086/319698

Martinez, L., Bersten, M. C., Anderson, J. P., et al. 2022, Astronomy & Astrophysics, 660, A41, doi: 10.1051/0004-6361/202142076

Mezzacappa, A., & Bruenn, S. W. 1993, The Astrophysical journal, 405, 669, doi: 10.1086/172395

Mezzacappa, A., Calder, A. C., Bruenn, S. W., et al. 1998, The Astrophysical journal, 493, 848, doi: 10.1086/305164

Misner, Thorne, W. 1973, Gravitation (H Freeman & Co)

Morinaga, T. 2021, PhD thesis, Waseda University

Morinaga, T., Nagakura, H., Kato, C., & Yamada, S. 2020, Physical Review Research, 2, 012046, doi: 10.1103/PhysRevResearch.2.012046

Moriya, T., Tominaga, N., Tanaka, M., et al. 2010, The Astrophysical journal, 719, 1445, doi: 10.1088/0004-637X/719/2/1445

Moriya, T. J., Müller, B., Chan, C., Heger, A., & Blinnikov, S. I. 2019, The Astrophysical journal, 880, 21, doi: 10.3847/1538-4357/ab2643

Moriya, T. J., Terreran, G., & Blinnikov, S. I. 2018, Monthly Notices of the Royal Astronomical Society, 475, L11, doi: 10.1093/mnrasl/slx200

Mukhopadhyay, M., Cardona, C., & Lunardini, C. 2021, arXiv e-prints, arXiv:2105.05862, doi: 10.48550/arXiv.2105.05862

Murchikova, E. M., Abdikamalov, E., & Urbatsch, T. 2017, Monthly Notices of the Royal Astronomical Society, 469, 1725, doi: 10.1093/mnras/stx986

Murphy, J. W., Ott, C. D., & Burrows, A. 2009, The Astrophysical journal, 707, 1173, doi: 10.1088/0004-637X/707/2/1173

Müller, B., Janka, H.-T., & Marek, A. 2013, The Astrophysical Journal, 766, 43, doi: 10.1088/0004-637x/766/1/43

Nagakura, H. 2023, arXiv e-prints, arXiv:2301.10785, doi: 10.48550/arXiv.2301.10785

Nagakura, H., Burrows, A., Radice, D., & Vartanyan, D. 2019, Monthly Notices of the Royal Astronomical Society, 490, 4622, doi: 10.1093/mnras/stz2730

—. 2020, Monthly Notices of the Royal Astronomical Society, 492, 5764, doi: 10.1093/mnras/staa261

Nagakura, H., Burrows, A., & Vartanyan, D. 2021, Monthly Notices of the Royal Astronomical Society, 506, 1462, doi: 10.1093/mnras/stab1785

Nagakura, H., Ito, H., Kiuchi, K., & Yamada, S. 2011, The Astrophysical Journal, 731, 80, doi: 10.1088/0004-637x/731/2/80

Nagakura, H., Iwakami, W., Furusawa, S., et al. 2017, The Astrophysical Journal Supplement Series, 229, 42, doi: 10.3847/1538-4365/aa69ea

Nagakura, H., & Johns, L. 2021a, Physical Review D, 103, 123025, doi: 10.1103/PhysRevD.103.123025

—. 2021b, Physical Review D, 104, 063014, doi: 10.1103/PhysRevD.104.063014

Nagakura, H., Sumiyoshi, K., & Yamada, S. 2014, The Astrophysical Journal Supplement Series, 214, 16, doi: 10.1088/0067-0049/214/2/16

—. 2019, The Astrophysical Journal, 878, 160, doi: 10.3847/1538-4357/ab2189

Nagakura, H., & Vartanyan, D. 2022, Monthly Notices of the Royal Astronomical Society, 512, 2806, doi: 10.1093/mnras/stac383

Nagakura, H., & Yamada, S. 2009, The Astrophysical Journal, 696, 2026, doi: 10.1088/0004-637x/696/2/2026

Nagakura, H., & Zaizen, M. 2023, Physical Review D, 108, 123003, doi: 10.1103/PhysRevD.108.123003

Nakamura, K., Takiwaki, T., & Kotake, K. 2022, Monthly Notices of the Royal Astronomical Society, 514, 3941, doi: 10.1093/mnras/stac1586

Nakazato, K., Sumiyoshi, K., Suzuki, H., et al. 2013, The Astrophysical journal Supplement, 205, 2, doi: 10.1088/0067-0049/205/1/2

Nakazato, K., & Suzuki, H. 2019, The Astrophysical Journal, 878, 25, doi: 10.3847/1538-4357/ab1d4b

Nakazato, K., & Suzuki, H. 2020, The Astrophysical journal, 891, 156, doi: 10.3847/1538-4357/ab7456

Nakazato, K., Nakanishi, F., Harada, M., et al. 2022, The Astrophysical journal, 925, 98, doi: 10.3847/1538-4357/ac3ae2

Ng, C. Y., & Romani, R. W. 2007, The Astrophysical journal, 660, 1357, doi: 10.1086/513597

O'Connor, E., Bollig, R., Burrows, A., et al. 2018, Journal of Physics G: Nuclear and Particle Physics, 45, 104001, doi: 10.1088/1361-6471/aadeae

O'Connor, E. P., & Couch, S. M. 2018, The Astrophysical Journal, 854, 63, doi: 10.3847/1538-4357/aaa893

Odrzywolek, A., Misiaszek, M., & Kutschera, M. 2004, Astroparticle Physics, 21, 303, doi: 10.1016/j.astropartphys.2004.02.002

Padilla-Gay, I., Tamborra, I., & Raffelt, G. G. 2022, Physical Review D, 106, 103031, doi: 10.1103/PhysRevD.106.103031

Pascal, A., Novak, J., & Oertel, M. 2022, Monthly Notices of the Royal Astronomical Society, 511, 356, doi: 10.1093/mnras/stac016

Patton, K. M., Lunardini, C., & Farmer, R. J. 2017, The Astrophysical journal, 840, 2, doi: 10.3847/1538-4357/aa6ba8

Peres, B., Penner, A. J., Novak, J., & Bonazzola, S. 2014, Classical and Quantum Gravity, 31, 045012, doi: 10.1088/0264-9381/31/4/045012

Perna, R., Duffell, P., Cantiello, M., & MacFadyen, A. I. 2014, The Astrophysical journal, 781, 119, doi: 10.1088/0004-637X/781/2/119

Pons, J. A., Ma Martí, J., & Müller, E. 2000, Journal of Fluid Mechanics, 422, 125, doi: 10.1017/S0022112000001439

Pons, J. A., Miralles, J. A., Prakash, M., & Lattimer, J. M. 2001a, The Astrophysical journal, 553, 382, doi: 10.1086/320642

Pons, J. A., Steiner, A. W., Prakash, M., & Lattimer, J. M. 2001b, Physical Review Letters, 86, 5223, doi: 10.1103/PhysRevLett.86.5223

Raaijmakers, G., Greif, S. K., Hebeler, K., et al. 2021, The Astrophysical journal Letters, 918, L29, doi: 10.3847/2041-8213/ac089a

Radice, D., Perego, A., Zappa, F., & Bernuzzi, S. 2018, The Astrophysical journal Letters, 852, L29, doi: 10.3847/2041-8213/aaa402

Richers, S., Nagakura, H., Ott, C. D., et al. 2017, The Astrophysical Journal, 847, 133, doi: 10.3847/1538-4357/aa8bb2

Roberts, L. F. 2012, The Astrophysical journal, 755, 126, doi: 10.1088/0004-637X/755/2/126

Roberts, L. F., & Reddy, S. 2017, in Neutrino Signatures from Young Neutron Stars, ed. A. W. Alsabti & P. Murdin (Springer), 1605, doi: 10.1007/978-3-319-21846-5_5

Roberts, L. F., Shen, G., Cirigliano, V., et al. 2012, Physical Review Letters, 108, 061103, doi: 10.1103/PhysRevLett.108.061103

Ronchi, M., Rea, N., Graber, V., & Hurley-Walker, N. 2022, The Astrophysical journal, 934, 184, doi: 10.3847/1538-4357/ac7cec

Rybicki, G. B., & Lightman, A. P. 1986, Radiative Processes in Astrophysics (Wiley)

Sarbach, O., & Zannias, T. 2013, in American Institute of Physics Conference Series, Vol. 1548, IX Mexican School on Gravitation and Mathematical Physics: Cosmology for the XXIst Century: Gravitation and Mathematical Physics Division of the Mexican Physical Society DGFM-SMF, 134–155, doi: 10.1063/1.4817035

Sarbach, O., & Zannias, T. 2014a, in American Institute of Physics Conference Series, Vol. 1577, Recent Developments on Physics in Strong Gravitational Fields: V Leopoldo García-Colín Mexican Meeting on Mathematical and Experimental Physics, 192–207, doi: 10.1063/1.4861955

Sarbach, O., & Zannias, T. 2014b, Classical and Quantum Gravity, 31, 085013, doi: 10.1088/0264-9381/31/8/085013

Sasaki, H. 2019, PhD thesis, University of Tokyo

Sawyer, R. F. 2005, Physical Review D, 72, 045003, doi: 10.1103/PhysRevD.72.045003

Scholberg, K., Albert, J. B., & Vasel, J. 2021, SNOwGLoBES: SuperNova Observatories with GLoBES, Astrophysics Source Code Library, record ascl:2109.019. http://ascl.net/2109.019

Seto, N., Kawamura, S., & Nakamura, T. 2001, Physical Review Letters, 87, 221103, doi: 10.1103/PhysRevLett.87.221103

Shalgar, S., & Tamborra, I. 2023, Physical Review D, 107, 063025, doi: 10.1103/PhysRevD.107.063025

Shen, H., Toki, H., Oyamatsu, K., & Sumiyoshi, K. 1998, Nuclear Physics A, 637, 435 , doi: https://doi.org/10.1016/S0375-9474(98)00236-X

Shibagaki, S., Kuroda, T., Kotake, K., Takiwaki, T., & Fischer, T. 2023, arXiv e-prints, arXiv:2309.05161, doi: 10.48550/arXiv.2309.05161

Shibata, M. 2015, Numerical Relativity (WORLD SCIENTIFIC), doi: 10.1142/9692

Shibata, M., Kiuchi, K., Sekiguchi, Y.-i., & Suwa, Y. 2011, Progress of Theoretical Physics, 125, 1255, doi: 10.1143/PTP.125.1255

Shibata, M., Nagakura, H., Sekiguchi, Y., & Yamada, S. 2014, Physical Review D, 89, 084073, doi: 10.1103/PhysRevD.89.084073

Shibata, M., Zhou, E., Kiuchi, K., & Fujibayashi, S. 2019, Physical Review D, 100, 023015, doi: 10.1103/PhysRevD.100.023015

Simpson, C., Abe, K., Bronner, C., et al. 2019, The Astrophysical journal, 885, 133, doi: 10.3847/1538-4357/ab4883

Skinner, M. A., Burrows, A., & Dolence, J. C. 2016, The Astrophysical Journal, 831, 81, doi: 10.3847/0004-637x/831/1/81

Sugiura, K., Furusawa, S., Sumiyoshi, K., & Yamada, S. 2022, Progress of Theoretical and Experimental Physics, 2022, 113E01, doi: 10.1093/ptep/ptac118

Sumiyoshi, K., & Yamada, S. 2012, The Astrophysical Journal Supplement Series, 199, 17, doi: 10.1088/0067-0049/199/1/17

Sumiyoshi, K., Yamada, S., Suzuki, H., et al. 2005, The Astrophysical Journal, 629, 922, doi: 10.1086/431788

Suwa, Y., Sumiyoshi, K., Nakazato, K., et al. 2019, The Astrophysical journal, 881, 139, doi: 10.3847/1538-4357/ab2e05

Tamborra, I., & Shalgar, S. 2021, Annual Review of Nuclear and Particle Science, 71, 165, doi: 10.1146/annurev-nucl-102920-050505

Thorne, K. S. 1981, Monthly Notices of the Royal Astronomical Society, 194, 439, doi: 10.1093/mnras/194.2.439

Togashi, H., Nakazato, K., Takehara, Y., et al. 2017, Nuclear Physics A, 961, 78, doi: https://doi.org/10.1016/j.nuclphysa.2017.02.010

Vartanyan, D., Burrows, A., & Radice, D. 2019, Monthly Notices of the Royal Astronomical Society, 489, 2227, doi: 10.1093/mnras/stz2307

Vartanyan, D., Coleman, M. S. B., & Burrows, A. 2022, Monthly Notices of the Royal Astronomical Society, 510, 4689, doi: 10.1093/mnras/stab3702

Woosley, S. E., Heger, A., & Weaver, T. A. 2002, Reviews of Modern Physics, 74, 1015, doi: 10.1103/RevModPhys.74.1015

Woosley, S. E., & Weaver, T. A. 1995, The Astrophysical journal Supplement, 101, 181, doi: 10.1086/192237

Xiong, Z., Johns, L., Wu, M.-R., & Duan, H. 2023a, Physical Review D, 108, 083002, doi: 10.1103/PhysRevD.108.083002

Xiong, Z., Wu, M.-R., Martínez-Pinedo, G., et al. 2023b, Physical Review D, 107, 083016, doi: 10.1103/PhysRevD.107.083016

Yamada, S., Janka, H.-T., & Suzuki, H. 1999, Astronomy & Astrophysics, 344, 533. https://arxiv.org/abs/astro-ph/9809009

Yamasaki, T., & Yamada, S. 2005, The Astrophysical journal, 623, 1000, doi: 10.1086/428496

—. 2006, The Astrophysical journal, 650, 291, doi: 10.1086/507067

Yamasaki, T., & Yamada, S. 2007, in American Institute of Physics Conference Series, Vol. 937, Supernova 1987A: 20 Years After: Supernovae and Gamma-Ray Bursters, ed. S. Immler, K. Weiler, & R. McCray, 344–348, doi: 10.1063/1.3682927

Yoshida, T., Takahashi, K., Umeda, H., & Ishidoshiro, K. 2016, Physical Review D, 93, 123012, doi: 10.1103/PhysRevD.93.123012

Zaizen, M., & Nagakura, H. 2022, arXiv e-prints, arXiv:2211.09343, doi: 10.48550/arXiv.2211.09343

Zhang, W., Woosley, S. E., & Heger, A. 2008, The Astrophysical journal, 679, 639, doi: 10.1086/526404

List of research achievements for application of Doctor of Science, Waseda University

Full Name： 赤穂　龍一郎　seal or signature

Date Submitted(yyyy/mm/dd): 2024/2/5

種類別 (By Type)	題名、 発表・発行掲載誌名、 発表・発行年月、 連名者（申請者含む） (theme, journal name, date & year of publication, name of authors inc. yourself)
Academic papers	○ **Ryuichiro Akaho**, Hiroki Nagakura, Thierry Foglizzo, "Detectability of Late-time Supernova Neutrinos with Fallback Accretion onto Protoneutron star", The Astrophysical Journal, Volume 960, 116, 13pp, (2024) ○ **Ryuichiro Akaho**, Jiabao Liu, Hiroki Nagakura, Masamichi Zaizen and Shoichi Yamada, "Collisional and fast neutrino flavor instabilities in two-dimensional core-collapse supernova simulation with Boltzmann neutrino transport", Physical Review D 109, 023012 (2024) Jiabao Liu, **Ryuichiro Akaho**, Akira Ito, Hiroki Nagakura, Masamichi Zaizen and Shoichi Yamada, "Universality of the neutrino collisional flavor instability in core-collapse supernovae", Physical Review D 108, 123024 (2023) ○ **Ryuichiro Akaho**, Akira Harada, Hiroki Nagakura, Wakana Iwakami, Hirotada Okawa, Shun Furusawa, Hideo Matsufuru, Kohsuke Sumiyoshi and Shoichi Yamada, "Protoneutron Star Convection Simulated with a New General Relativistic Boltzmann Neutrino Radiation Hydrodynamics Code", The Astrophysical Journal, Volume 944, 60, 18pp (2023) Wakana Iwakami, Akira Harada, Hiroki Nagakura, **Ryuichiro Akaho**, Hirotada Okawa, Shun Furusawa, Hideo Matsufuru, Kohsuke Sumiyoshi and Shoichi Yamada, "Principal-axis Analysis of the Eddington Tensor for the Early Post-bounce Phase of Rotational Core-collapse Supernovae", The Astrophysical Journal, Volume 933, 91, 21pp (2022) ○ **Ryuichiro Akaho**, Akira Harada, Hiroki Nagakura, Kohsuke Sumiyoshi, Wakana Iwakami, Hirotada Okawa, Shun Furusawa, Hideo Matsufuru and Shoichi Yamada, "Multidimensional Boltzmann Neutrino Transport Code in Full General Relativity for Core-collapse Simulations", The Astrophysical Journal, Volume 909, 210, 17pp (2021)
Presentations	「ボルツマン輻射流体計算で探る超新星爆発と ニュートリノ集団振動」、理論天文学宇宙物理学懇談会シンポジウム、2023年12月27日、弘前大学 「超新星のボルツマン輻射輸送計算におけるニュートリノ集団振動の系統的解析」、日本天文学会2023年秋季年会、2023年9月22日、名古屋大学 "Fast and Collisional Neutrino Flavor Instabilities in Core-collapse Supernovae with Boltzmann Neutrino Transport", Microphysics in Computational Relativistic Astrophysics (MICRA), Sep 14th, 2023, Trento, Italy 「超新星のボルツマン輻射輸送計算におけるニュートリノ集団振動の系統的解析」、第9回超新星ニュートリノ研究会、2023年3月3日、九州大学 「ボルツマン輻射輸送計算で探る超新星爆発」、第3回地下宇宙若手研究会、2022年11月23日、つくば国際会議場

List of research achievements for application of Doctor of Science, Waseda University

Full Name： 赤穂　龍一郎　seal or signature

Date Submitted(yyyy/mm/dd): 2024/2/5

種類別 (By Type)	題名、 発表・発行掲載誌名、 発表・発行年月、 連名者（申請者含む） (theme, journal name, date & year of publication, name of authors inc. yourself)
	“Core-collapse Supernova Simulation with General Relativistic Boltzmann Neutrino Radiation-Hydrodynamics Code“, The 9th East Asian Numerical Astrophysics Meeting (EANAM9), Sep 27, 2022, Tenbusu Naha, Okinawa, Japan
	「冷え切った原始中性子星への降着によるニュートリノ放射とその観測可能性」、日本天文学会2022年秋季年会、2022年9月13日、新潟大学
	「冷え切った原始中性子星への降着によるニュートリノ放射とその観測可能性」、RCNP研究会「低エネルギー核物理と高エネルギー天文学で読み解く中性子星」、2022年8月5日、大阪大学
	"Core-collapse Supernova Simulation with Boltzmann Neutrino Transport", Unraveling the History of the Universe and Matter Evolution with Underground Physics (UGAP2022), Jun 14, 2022, Tokyo University of Science, Noda, Chiba, Japan
	「ボルツマンニュートリノ輻射流体コードによる原始中性子星冷却計算及び今後のコード開発の展望」第8回超新星ニュートリノ研究会、2022年1月7日、オンライン開催
	「一般相対論的ボルツマン輻射流体計算による原子中性子星冷却」、日本天文学会2021春季大会、企画セッション「富岳時代のシミュレーション天文学」、2021年3月16日、オンライン開催
	「多次元一般相対論的ボルツマンニュートリノ輸送コード開発」、第7回超新星ニュートリノ研究会、2021年1月7日、オンライン開催
	「大質量星の重力崩壊における多次元一般相対論的Boltzmannニュートリノ輸送」、第50回天文・天体物理夏の学校、2020年8月25日、オンライン開催
	「一般相対論的ボルツマン方程式の直接解法コード開発」、日本天文学会2020春季大会、3月19日、筑波大学
	「ニュートリノ輻射輸送計算のボルツマン方程式直接解法コード開発」、第一回地下宇宙若手研究会、2020年2月23日、東京大学宇宙線研究所神岡宇宙素粒子研究施設
	"General Relativistic Boltzmann Solver for Core-Collapse Supernovae"、CfCAユーザーズミーティング、2020年1月20日、国立天文台
	「一般相対論的Boltzmann方程式の直接解法によるニュートリノ輻射輸送計算」 、第49回天文・天体物理夏の学校、2019年7月31日、愛知県豊橋市